Universidad de Málaga

Escuela Técnica Superior de Ingeniería de Telecomunicación

TESIS DOCTORAL

Photonic Reflectometer on Silicon-on-Insulator

Autor:

ROBERT HALIR

Directores:

ÍÑIGO MOLINA FERNÁNDEZ
JUAN GONZALO WANGÜEMERT PÉREZ

SPICUM
servicio de publicaciones
ma

UNIVERSIDAD DE MÁLAGA
SPICUM servicio de publicaciones

AUTOR: Robert Halir

EDITA: Servicio de Publicaciones de la Universidad de Málaga

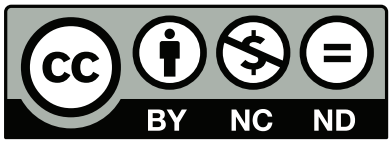

Esta obra está sujeta a una licencia Creative Commons:
Reconocimiento - No comercial - SinObraDerivada (cc-by-nc-nd):
Http://creativecommons.org/licences/by-nc-nd/3.0/es
Cualquier parte de esta obra se puede reproducir sin autorización
pero con el reconocimiento y atribución de los autores.
No se puede hacer uso comercial de la obra y no se puede alterar,
transformar o hacer obras derivadas.

Esta Tesis Doctoral está depositada en el Repositorio Institucional de
la Universidad de Málaga (RIUMA): riuma.uma.es

SPICUM servicio de publicaciones

Dr.D. Íñigo Molina Fernández y **Dr.D. Juan Gonzalo Wangüemert Pérez**, profesores doctores del Departamento de Ingeniería de Comunicaciones de la Universidad de Málaga

CERTIFICAN:

Que D. Robert Halir, Ingeniero de Telecomunicación, ha realizado en el Departamento de Ingeniería de Comunicaciones de la Universidad de Málaga bajo su dirección, el trabajo de investigación correspondiente a su TESIS DOCTORAL titulada:

Photonic Reflectometer on Silicon-on-Insulator

En dicho trabajo se han expuesto diversas aportaciones originales, entre las que cabe destacar una completa estrategia de diseño para acopladores de interferencia multimodal, que ofrecen altas prestaciones y buenas tolerancias de fabricación. Asimismo, se ha desarrollado una nueva técnica de medida de circuitos fotónicos integrados, que, haciendo uso de conceptos de fase mínima, permite una complete caracterización de dichos circuitos con un montaje de medida sencillo. Finalmente, cabe destacar el desarrollo de redes de acoplo eficientes chip-fibra para polarización TM, basadas en estructuras más pequeñas que la longitud de onda para la apodización de las mismas. Los resultados expuestos han dado lugar a publicaciones en revistas y aportaciones a congresos internacionales.

Por todo ello, consideran que esta Tesis es apta para su presentación al tribunal que ha de juzgarla. Y para que conste a efectos de lo establecido en el artículo 8° del Real Decreto 778/1998 Real Decreto 56/2005, regulador de los Estudios de Tercer Ciclo-Doctorado, AUTORIZAN la presentación de esta Tesis en la Universidad de Málaga.

Málaga, a 23 de Junio de 2010

Fdo.: Dr.D. Íñigo Molina Fernández

Fdo.: Juan Gonzalo Wangüemert Pérez

E.T.S.I.Telecomunicación, Campus de Teatinos, 29071-MÁLAGA, Tlf.: 952131440, Fax: 952132927

SPICUM servicio de publicaciones

SPICUM
servicio de publicaciones

Photonic Reflectometer on Silicon-on-Insulator

Robert Halir

SPICUM
servicio de publicaciones

SPICUM
servicio de publicaciones

To Leonor
and
my parents

SPICUM
servicio de publicaciones

SPICUM
servicio de publicaciones

Acknowledgements

First and foremost I want to thank my thesis supervisors Íñigo Molina Fernández and Gonzalo Wangüemert Pérez for their continued support, guidance and encouragement during the development of this thesis. Without their patience, solid ideas and resolve, this work would have been nothing short of impossible. Alejandro Ortega Moñux, though not officially my supervisor, has offered me countless helpful (and hourlong) discussions on many aspect of this work, for which I want to thank him.

Pavel Cheben, together with Siegfried Janz and Dan-Xia Xu, has supervised my work during several stays at the National Research Council of Canada, where I had the privilege to learn many aspect on the design of optical devices. Pavel also provided the core idea behind the grating concept presented here, and, beyond this, has proven a great person. Siegfried and Dan-Xia have dedicated much of their time to improve my understanding of device fabrication, and have given me many invaluable pieces of advice. My gratitude goes to all of them. I also gratefully acknowledge the assistance provided by all the staff of the Canadian Photonic Fabrication Centre, where most of the devices presented in this work were fabricated.

Gunther Roelkens supervised my work during my stay at the INTEC group in Ghent. I would like thank him not only for his instruction on polarisation diversity grating couplers, but also his continued drive and support. He furthermore provided one of the external reports on this work.

During a short stay at the Heinrich Hertz Institute in Berlin, Norbert Keil supervised my work, which has been followed by extensive collaboration with the group at Málaga. I highly appreciate his great mood, and want to thank him and Jin Wang for providing an external report on my thesis.

I am grateful for the long hours of joy (and sometimes sorrow) I have shared with all the colleagues in and out of the lab: Alejandro, Álvaro, Benito, Carlos, Elena, Juanma, Laureano, Luis, María, Sebastián, Yak...

I also wish to thank my parents for their continuing love, support and advice. And of course, Leonor whom I love and admire more every single day.

Finally, I acknowledge founding through a FPU scholarship from the Spanish Ministry of Education, which has enabled all this work.

Robert Halir
Málaga, Spain
September 2010

SPICUM
servicio de publicaciones

SPICUM
servicio de publicaciones

Nomenclature

a	Amplitude of a s-bend
ARDE	Aspect Ratio Dependent Etching
β	Propagation constant
BOX	Bottom Oxide
c	Speed of light in vacuum: $c = 3 \times 10^8$ m/s
c_m	Modal excitation coefficients
D	Etch depth
DUT	Device under test
DUV	Deep Ultraviolet
E_d	Dominant electrical field component. $E_d = E_x$ for horizontal (TE) polarization and $E_d = E_y$ for vertical (TM) polarization.
g	Minimum gap between waveguides
H	Substrate height
λ	Free-space wavelength. By default $\lambda = 1.55\,\mu$m.
L_{MMI}	Length of the multimode region
L_P	Length of two parallel waveguides.
L_π	Half beat length of the two lowest order modes
L_S	Length of a s-bend
L_T	Taper length
LTI	Linear time invariant (system)
M	Number of guided modes
m	Lateral (x direction) mode number
MPTF	Minimum Phase Temporal Filtering
MZI	Mach Zehnder Interferometer
N_c	Effective index of the cladding
n_c	Refractive index of the cladding

SPICUM servicio de publicaciones

N_g	Effective index of the guiding region
n_g	Refractive index of the guiding region or group index
n_s	Refractive index of the substrate
ν	Optical frequency: $\nu = c/\lambda$
OFDR	Optical Frequency Domain Reflectometry
p_g	Guidance factor
PIC	Photonic Integrated Circuit
PLC	Planar lightwave circuit
p_s	Symmetry factor
Q	Number of images
s	Centre to centre separation of the MMI access waveguides
s_I	Centre to centre separation between interconnecting waveguides
S_{ij}	S-parameter from port j to port i
SWG	Sub-wavelength Grating
TE	Transversal electric polarzation
TM	Transversal magnetic polarization
$\mathrm{TX}_{m,n}$	TE or TM mode with m half cycles in the lateral (x) direction and n half cycles in the vertical (y) direction.
φ	Scalar mode field profile
W	Width of the interconnecting waveguides
W_A	Width of the MMI access waveguides
W_{eff}	Effective width of the multimode region
W_{MMI}	Width of the multimode section

SPICUM servicio de publicaciones

Contents

SPICUM servicio de publicaciones

SPICUM servicio de publicaciones

SPICUM servicio de publicaciones

SPICUM servicio de publicaciones

The highest to which man can reach is amazement.
Johann Wolfgang von Goethe

1 Introduction

THIS work presents the implementation and characterisation of an optical six-port reflectometer on silicon-on-insulator, that will enable accurate magnitude and phase characterisation of photonic devices. Furthermore, we propose and demonstrate a novel grating coupler structure for silicon wire waveguides. In this introductory chapter, we will examine the relevance of optical technologies and their relation to silicon (section 1.1), and provide a brief context on optical measurement techniques (section 1.2) and fibre-to-chip coupling (section 1.3). A general outline of the goals and contributions of this thesis is given in section 1.4.

1.1. Silicon and The Harnessing of Light

The science of the harnessing of light. This is the definition of photonics given by Pierre Aigrain, when he coined the term in 1967. Just as electronics refers to the study of electrons, photonics aims at the manipulation of photons, the "elementary particle" of light. Some claim that the word electronics was introduced by McGraw-Hill, when they published the first issue of a magazine with that name in April 1930. In its beginnings the Electronics magazine mainly covered the technology of radio communications, that had been booming since the 1920's. Hence, it is not surprising that photonics is often related rather directly to another telecommunication milestone: the development of optical communications. With optical fibre based, long haul transmission systems providing the backbone of high speed internet with all its revolutionary services, it is hard to exaggerate the impact of this technology on our lives. In fact, the 2009 Nobel price recognises this in awarding the Nobel in physics to Charles Kao, the father of optical fibres. And recent developments, such as coherent 100 Gigabit/s transmission over systems initially design for 10 times smaller data rates [1–3], the introduction of optical networks into datacenters [4, 5], and the ever growing volume of internet traffic, confirm, among many other factors, that telecommunications continues to be the main driving force behind photonics. Then again, just as electronics were focused on radio communications in their beginnings, and have since then spread to many other aspects of daily live, the field of photonics extends beyond optical data transmission. Fibre Bragg gratings are widely used as temperature and strain sensors [6], optical coherence tomography provides imaging

SPICUM servicio de publicaciones

of microscopic structures inside tissues in medicine and biology [7], and frequency combs are used for the detection of exoplanets in astronomy [8], to name but a few applications.

The tremendous success of modern electronics is founded on Silicon [9]: being one of the most commons elements on earth, once purified, this semiconductor is the basis of CMOS (complementary metal-oxide semiconductor) technology, which, in turn, powers the vast majority of electronic devices. But silicon also exhibits interesting properties for integrated, chip scale, photonics [10]: it is transparent at wavelengths larger than 1.2µm so that it can act as a waveguide at the 1.3µm and 1.55µm wavelengths used for optical communications. Light is guided by total internal reflection inside a silicon core surrounded by silicon dioxide. The silicon dioxide layer has its origin in microelectronics, where it is used to reduce parasitics, and also gives this technology its name: Silicon-on-Insulator (SOI). The SOI platform offers a very high refractive index contrast of $\Delta n \sim 2$ (in optical fibres $\Delta n \sim 0.01$), that allows for the realisation of integrated photonic circuits with an overall size of only tens to a few hundreds of microns.

With electrical interconnects running out of bandwidth in future high speed microprocessors, silicon based optical interconnects, compatible with existing CMOS fabrication techniques, could provide a long term solution [11]. However, silicon is not well suited for light emission and modulation, both of which are required for on-chip optical communication [12]. These limitations are currently being overcome by Intel, IBM, and the European Wadimos project, among others: silicon modulators at 1 GHz and 10 GHz were demonstrated in 2004 and 2007 [13, 14], germanium high speed avalanche photodiodes were shown in 2008 and 2010 [15, 16], and lasers integrated with silicon were presented in 2006 and 2010 [17, 18]. Probably the first commercial silicon photonics products are active optical cables, i.e. optical fibres connected to miniaturised optical CMOS transceivers, offered by Luxtera [19].

The high index contrast, together with the volume production capabilities, make SOI an extremely attractive platform for photonic integrated circuits (PICs) in general. For instance, a high resolution spectrometer, consisting of an arrayed waveguide grating with extremely closely spaced waveguides, was described in [20]. Very compact and highly sensitive biosensors have been demonstrated in [21], making use of the strong evanescent field of transversal magnetic polarised light in silicon-wire waveguides. The high confinement that can be achieved in silicon waveguides was used in [22] to produce non-linear effects and construct an optical oscilloscope. Highly selective filters, based on interconnect resonators or echelle gratings, have been presented in [23–25]. These examples constitute only a tiny subset of the activity in the silicon photonics field.

The primary focus of this thesis is the implementation of an integrated reflectometer on SOI, that enables accurate magnitude *and* phase measurements of photonic devices. Furthermore, we present an efficient, yet easy to fabricate device for fibre-to-chip coupling, which, due to the miniature size of SOI waveguides, is far from trivial. We shall elaborate on these two points in the following sections.

SPICUM servicio de publicaciones

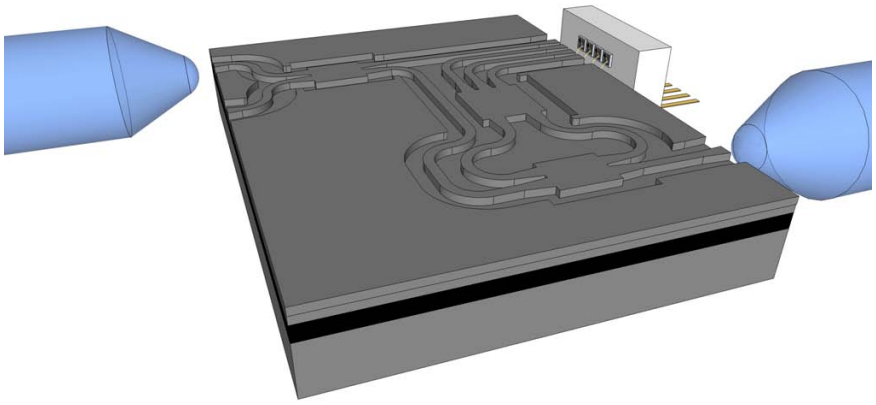

Figure 1.1.: Illustration of the integrated optical six-port.

1.2. Characterisation of photonic devices

The complexity of optical communication systems and photonic devices has grown over time, calling for more sophisticated measurement techniques. In classical long haul transmissions system where losses were the main concern, optical time domain reflectometry (OTDR) offered not only a convenient characterisation of propagation losses, but also served as a fault detection and location scheme. With increasing bit rates fibre dispersion became more critical, and the modulation phase shift method was introduced. This hybrid radiofrequency-optical technique, yields a direct measurement of the device's group delay [26]. It is, however, time consuming when applied to narrowband devices, such as dense wavelength division multiplexing filters, with a passband of around 50 GHz. For such devices, optical low coherence reflectometry (OLCR) and optical frequency domain reflectometry (OFDR) are better suited [27, 28]. Remarkably these techniques have spread beyond the scope of optical communication, and are applied in biology and medicine in the form of optical coherence tomography [7, 29]. OLCR and OFDR are interferometric techniques that produce direct measurements of the phase of optical devices [30, 31], which in a sense is a more fundamental characterisation than group delay and dispersion, since both are derivatives of optical phase. In fact, knowledge of the phase response enables the use of linear, time invariant system analysis, a technique that is widely used in the analysis of electrical systems. In the context optical signal processing, with interconnected, micro-meter size photonic devices, this type of analysis is becoming increasingly important [23].

Here, we focus on a novel six-port based measurement technique [32], which is actually an optical form of a well established microwave measurement technique. As opposed to OLCR and OFDR, which rely on the analysis of a complete interferogram to obtain the phase at a certain wavelength, the six-port technique directly measures phase at each wavelength and benefits from sophisticated calibration techniques to reduce measurement errors. The core of this technique is the integrated photonic circuit shown in figure 1.1, which we will call six-port in the following. It consists of

SPICUM servicio de publicaciones

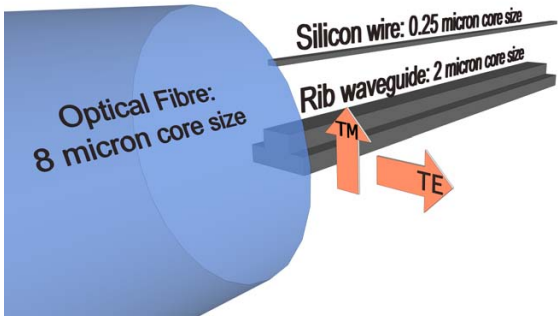

Figure 1.2.: Size comparison of the core of single-mode fibre, a rectangular silicon-wire waveguide and a micrometric rib waveguide (roughly to scale). The arrows indicate the convention of naming the horizontal and vertical linear polarisation states TE and TM respectively.

an interconnection of three multi-mode interference couplers, and is connected via optical fibres to a laser source and the device under test. The mission of the six-port is to combine the light incident from the laser and the light reflected from the device under test (DUT) at four external photodiodes. As we will show in section 2.4, the reflection coefficient of the DUT can be determined from the power readings of these four photodiodes. The implementation and characterisation of the optical six-port is the main goal of this thesis.

1.3. Fibre to chip coupling

The size reduction afforded by the high index contrast in the SOI platform comes at a price: the size mismatch of the integrated waveguides with fibres, which constitute the interface to the devices outside the optical chip, is enormous, which makes efficient coupling between them difficult. Figure 1.2 illustrates the size difference between an optical fibre and the two types of waveguides commonly used in SOI: a micrometer size rib waveguide, and a nanometric rectangular silicon-wire waveguide (typical cross-section: 220 nm × 500 nm). Using lensed fibres a reasonable coupling efficiency to micrometric waveguides can be achieved, but silicon-wire waveguides require special coupling structures. Grating couplers offer a good coupling efficiency to fibres situated above the chip [33], but require a two-etch step process to achieve a good matching to the fibre mode. Furthermore, efficient coupling is commonly achieved for transversal electric (TE) polarisation, whereas transversal magnetic (TM) polarisation is required for certain applications, such as biosensing; the orientation of the TE and TM polarisation states is shown in figure 1.2. Here, we will propose and demonstrate an efficient grating coupler for TM polarisation, that can be defined in the same etch step as the waveguides.

SPICUM servicio de publicaciones

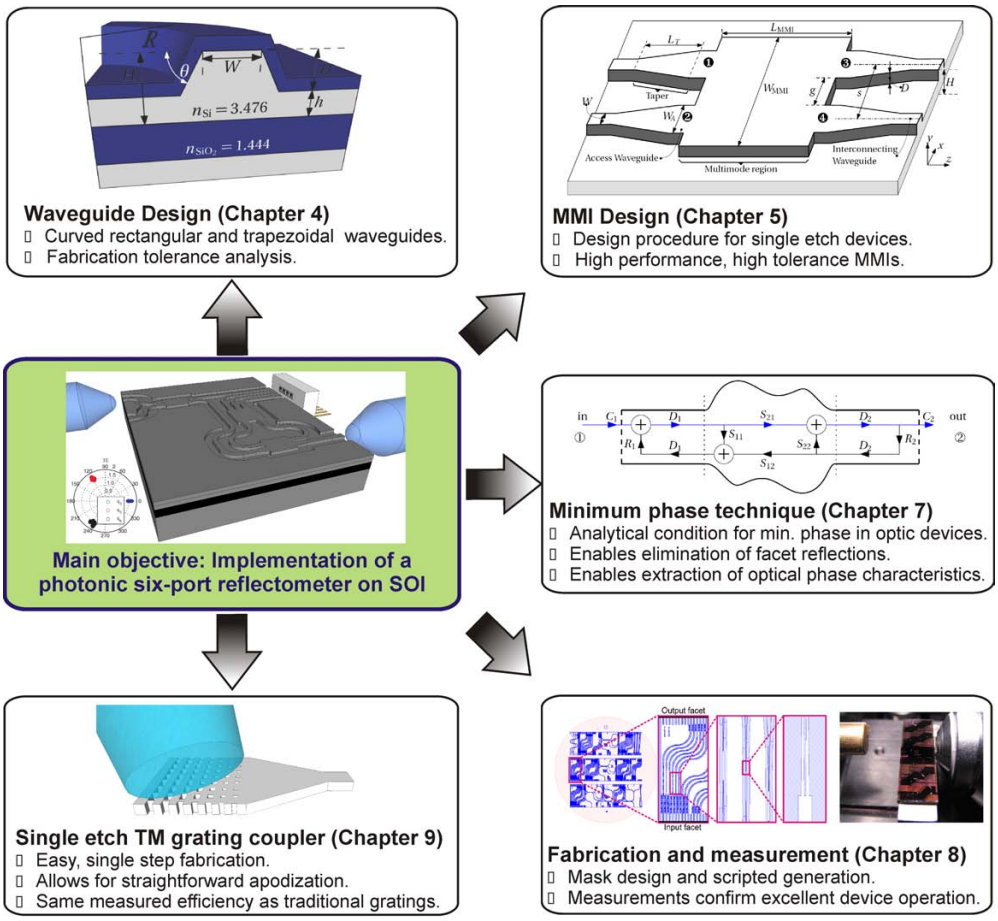

Figure 1.3.: Overview of the main contributions of this work.

1.4. Overview of this work

In this section we will briefly outline the main goals and contributions of this thesis, and give a general overview of the following chapters. As depicted in figure 1.3 the implementation of a photonic reflectometer is the main goal of this work. This basic objective has motivated a series of contributions, with applications spanning beyond the scope of this work.

The optical six-port reflectometer is based on silicon-on-insulator, micrometric rib waveguides. To achieve a cost effective design, we shall restrict the fabrication to a single etch step. This requires, in the first place, a thorough study of the interconnecting waveguides, and, particularly, of the effect of fabrication tolerances on curved waveguides [34, 35]. Both trapezoidal and rectangular waveguides are considered in the analysis, but since the latter are shown to provide tighter curvature radii, they are used throughout this work. The next step is the design of multi-mode interference couplers that maintain a high performance despite fabrication variations and shallow etch depth. A complete design procedure for such devices has been developed [36, 37], and applied successfully not only to MMIs on SOI but also on Indium-

SPICUM servicio de publicaciones

phosphide [3], although the latter are not described here. A complete mask, which included test structures of the individual MMIs as well as the six-port junctions, was designed, and fabricated at the Canadian Photonics Fabrication Centre. Characterisation of the devices poses two challenges: first, we need to remove facet reflections to accurately characterise the MMIs, and second, we need to measure the magnitude *and* phase response of the sixport. We have proposed a minimum phase technique that *computes* the phase of integrated optical devices from their power transmission spectrum, and established an analytical criterion to assess when such devices exhibit the required minimum phase characteristics [38,39]. This allowed us to overcome both challenges using a simple setup, based solely on power transmission measurements of the devices. As a result, we were able to demonstrate MMIs with an unprecedented combination of performance, tolerances and compact size [40], as well as a six-port reflectometer with almost ideal magnitude and phase performance in a broad bandwidth [41].

The general problem of coupling light from an optical fibre to an optical chip is also briefly addressed in this work. Butt-coupling a fibre to micrometric waveguides still yields reasonable coupling efficiencies, which is why this approach was used for the implementation of the reflectometer. However, as discussed before, smaller Si-wire waveguides call for different solutions. Here we have proposed an efficient fibre-to-chip grating coupler for silicon wire waveguides that operates with TM polarisation, and can be fabricated in a single etch step. To achieve this we use, for the first time, subwavelength gratings to match the field radiated by the grating to the fibre mode [42]. Recent measurement show an excellent agreement with simulation results.

The organisation of this work is as follows. In chapter 2, we review some optical measurement techniques, and present the operation and calibration of the six-port reflectometer. Since the device benefits from a compact size, implementing it in SOI is a natural choice, which is why this platform is briefly described in chapter 3. The design of the interconnecting waveguides is discussed in chapter 4, including tolerances issues of waveguide bends, and important considerations on waveguide coupling. Chapter 5 is devoted to multi-mode interference couplers, the fundamental component of the six-port. This chapter examines the approximations intrinsic to the self-imaging effect that governs the operation of MMIs, and presents several key aspects to the design of high performance devices with large tolerances. A complete design procedure for such devices is developed, and the resulting tolerances are thoroughly analysed. The design and simulation of the complete six-port reflectometer is described in chapter 6, showing that an excellent performance can be expected from the fabricated device. Chapter 7 formulates a novel measurement technique that produces OFDR like information based solely on wavelength swept power transmission measurements. We establish a closed form expression to assess the applicability of this technique, and examine its practical requirements. The measurement technique is subsequently used both to eliminate the effect of facet reflections from MMI measurements, and to obtain the phase characterisation of the six-port. Some important considerations on mask design are given at the beginning of chapter 8, which presents the experimental performance of the MMIs and the six-port. Particularly, we demonstrate high-performance 2×2 MMIs with large tolerances, and a complete six-port junction with excellent performance in a large bandwidth. In chapter 9, we

SPICUM servicio de publicaciones

describe the realisation of effective media via sub-wavelength gratings, and detail the design and simulation of a silicon-wire fibre-to-chip grating coupler based on these structures. Measurements confirm not only the feasibility but also the excellent performance of this approach. Conclusions are drawn in chapter 10.

SPICUM servicio de publicaciones

SPICUM
servicio de publicaciones

2

Phase and magnitude measurement techniques for passive optical devices

OPTICAL phase measurements are of growing importance in modern optical communication systems. We will start this chapter by giving a short introduction to linear system analysis (section 2.1). This technique is extensively used for the design of electrical systems, and provides some interesting insight on optical phase. Section 2.2 describes the classical modulation phase shift method for group delay and dispersion measurement of passive devices, and points out some of its shortcomings. Optical frequency domain reflectometry, an established phase measurement technique, is discussed to some extent in section 2.3, providing a basis of comparison for the six-port technique, and illustrating some concepts that we will use for the characterisation of our devices. Section 2.4 is devoted to the operation of the six-port reflectometer, and outlines some of the desirable characteristics of its implementation.

2.1. Linear time invariant systems

The aim of this section is to provide a brief review of linear time invariant (LTI) systems and some of their properties in the context of optics. This will not only provide a better understanding of optical phase, but will also facilitate and simplify the understanding of the measurement techniques that we will discuss in the following. The concepts we present here are commonly used in electrical engineering [43], so that the reader who is familiar with LTI systems may skip this section.

2.1.1. General concepts

Figure 2.1 depicts a LTI system, with $x(t)$ as a input (or excitation) and $y(t)$ as an output (or response). As indicated by its name, a LTI system has two fundamental

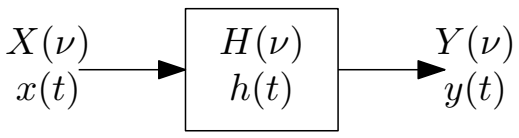

Figure 2.1: Schematic representation of a LTI system.

SPICUM servicio de publicaciones

properties: a superposition of inputs yields a superposition of outputs, and the behaviour of the system does not change over time. Note that passive optical devices usually exhibit these properties, including optical fibres, fibre Bragg gratings, resonators and filters. A LTI system is completely characterised by its impulse response function, $h(t)$. This function is obtained by applying a Dirac delta function at the input, $x(t) = \delta(t)$, and observing the output, $y(t) = h(t)$. Optically, the impulse response can be thought of as the temporal *amplitude* response of the system when excited with an extremely narrow optical pulse. We emphasise the term amplitude, because in optics it is common to detect optical power, which corresponds to the time averaged, squared *magnitude* of the impulse response function: $\langle |h(t)|^2 \rangle$.[1] The impulse response relates input and output through a convolution:

$$y(t) = x(t) * h(t) = \int_{-\infty}^{\infty} x(u)h(u-t)\mathrm{d}u. \tag{2.1}$$

By Fourier transforming the impulse response, the frequency response is obtained:

$$H(\nu) = \mathscr{F}\{h(t)\} = \int_{-\infty}^{\infty} h(t)\exp(-\mathrm{j}2\pi\nu t)\mathrm{d}t. \tag{2.2}$$

Here we have denoted optical frequency by ν, which is related to wavelength by $\nu = c/\lambda$, with $c = 3\times10^8$ m/s the speed of light in vacuum. By Fourier transforming (2.1), we see that spectrum of the system's output can be calculated as:

$$Y(\nu) = H(\nu)X(\nu) \tag{2.3}$$

For example, the frequency response of a span of optical fibre of length L is $H(\nu) = \exp(-\alpha L)\exp[\mathrm{j}\beta(\nu)L]$, where α accounts for the attenuation, and β is the propagation constant. Note that knowledge of the magnitude and phase response allows for a simple yet complete description of complex systems, e.g. the concatenation of several spans of fibres and filters, via equation (2.3). When performing swept laser measurements and detecting the transmitted signal with a power detector, the information that is obtained is only the squared magnitude of the frequency (or wavelength) response, $|H(\lambda)|^2$. Using a broad-band source as input and observing the output in an optical spectrum analyser yields the same result. The impulse response can be obtained from the frequency response by an inverse Fourier transform:

$$h(t) = \mathscr{F}^{-1}\{H(\nu)\} = \int_{-\infty}^{\infty} |H(\nu)|\exp\left(\mathrm{j}\angle H(\nu)\right)\exp(\mathrm{j}2\pi\nu t)\mathrm{d}\nu \tag{2.4}$$

We have expressed $H(\nu) = |H(\nu)|\exp[\mathrm{j}\angle H(\nu)]$ to highlight that this computation requires knowledge of both the magnitude, $|H(\nu)|$, and the phase, $\angle H(\nu)$, of the frequency response. In optics, the impulse response is often encountered in terms of a reflectogram, which is essentially $\langle |h(t)|^2 \rangle$.

[1] Time averaging here refers to low pass filtering, or averaging, of optical frequencies, like the optical carrier and its harmonics.

SPICUM servicio de publicaciones

2.1.2. Group delay and dispersion

Group delay and dispersion are widely used to characterise optical components. These concepts arise when we examine the transmission of a narrowband signal through a LTI system, i.e. when using $x(t) = a(t)\cos(2\pi\nu_0 t)$ as input. By narrowband we understand that the bandwidth of $A(\nu) = \mathscr{F}\{a(t)\}$ is small both compared to the carrier frequency, ν_0, and to bandwidth of $H(\nu)$, the frequency response of the LTI system. The first constraint applies to almost any optical system, because optical frequencies are orders of magnitude higher than the communication frequencies with which their are modulated. The second restriction means that, within the bandwidth of $A(\nu)$, the response of the system, $H(\nu)$, is well approximated by its first order Taylor expansion, i.e. $H(\nu) = H(\nu_0) + (\mathrm{d}H(\nu)/\mathrm{d}\nu)|_{\nu=\nu_0} \times (\nu - \nu_0)$. If both conditions hold, the output of the system is given by:

$$y(t) = |H(\nu_0)|a(t-\tau_g)\cos\left(2\pi\nu_0(t-\tau_\phi)\right) \tag{2.5}$$

where τ_g is the group delay, and τ_ϕ is the phase delay. These two delays are computed directly from the phase response of the system:

$$\tau_g(\nu_0) = -\frac{1}{2\pi}\left.\frac{\mathrm{d}\angle H(\nu)}{\mathrm{d}\nu}\right|_{\nu=\nu_0} \qquad \tau_\phi(\nu_0) = -\frac{1}{2\pi}\frac{\angle H(\nu_0)}{\nu_0}. \tag{2.6}$$

Dispersion is then defined as the variation of the group delay with wavelength:

$$D(\lambda_0) = \frac{1}{L}\left.\frac{\mathrm{d}\tau_g}{\mathrm{d}\lambda}\right|_{\lambda=\lambda_0}, \tag{2.7}$$

where L is the length of the component. Expression (2.6) shows that group delay is only a first order approximation to the phase response of a system at a certain wavelength. The complete description of the system is only available through its phase and amplitude response. This becomes apparent when characterising DWDM (Dense wavelength division multiplexing) components, such as optical filters with a passband width comparable to the bandwidth of the communication signals are employed. A group delay based analysis of such devices requires measuring the group delay in frequency intervals much smaller than the bandwidth of the communication signal, and integrating the results to obtain the phase response. Direct measurement of the optical phase thus seems to be a much more straightforward approach.

2.2. Modulation phase shift method

The modulation phase shift method produces a direct measurement of the group delay of an optical component, and is widely used to determine the dispersion of optical fibres [26]. It is based on the transmission of a narrowband signal through the DUT, as described in section 2.1. The apparatus employed by the modulation phase shift method is shown in figure 2.2, and consists in modulating a tunable optical carrier with frequency ν_0 with a sinusoidal radiofrequency signal with frequency f_m. The bandwidth of the modulated signal is thus $2f_m$ (see right hand side of figure 2.2), and f_m is adjusted to ensure that the response of the DUT can be considered linear in this

SPICUM servicio de publicaciones

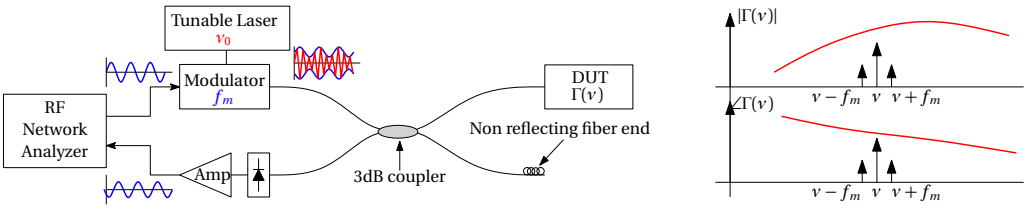

Figure 2.2.: Basic setup for group delay measurement using the modulation phase shift method.

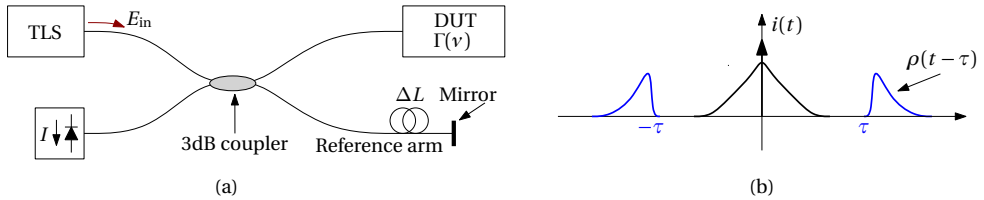

Figure 2.3.: (a) Schematic setup for OFDR and (b) spectrum of the photocurrent.

bandwidth. The test signal is reflected by (or travels through) the DUT, and is detected by a photodiode, that recovers the radiofrequency envelope. A vector network analyser is used to measure the phase shift, $\Delta\phi$, of the reflected envelope with respect to the modulating signal, from which the group delay of the device at ν_0 can be calculated as $\tau_g = \Delta\phi/(2\pi f_m)$. A phase characterisation of the device can only be achieved by measuring the group delay at several optical frequencies ν_i and integrating the results. While this yields excellent results in broadband devices such as spans of optical fibre, it is less optimum for the characterisation of narrowband devices [28], because many time consuming measurements must be taken.

2.3. Coherent Optical Frequency Domain Reflectometry

Coherent optical frequency domain reflectometry (OFDR) is a fully optical technique for amplitude and phase characterisation of passive photonic components, which has been developed over the last few decades [31, 44]. Commercial instruments based on OFDR are available since around 2003 from Luna technologies [45] and others, and achieve insertion loss and return loss accuracies of ±0.15 dB and a group delay accuracy of ±0.25 ps. OFDR consists in recording the wavelength swept interference of a reference beam and the signal reflected from (or transmitted through) the DUT. Upon Fourier transformation of this interference signal, the complete device characteristics can be extracted. In the next section we will examine operation of OFDR more closely, but, for the sake of clearness, we will first skip some practical restrictions, to which we will come back in section 2.3.2.

2.3.1. Basic operation of OFDR

Figure 2.3(a) illustrates a fibre based OFDR setup operating in reflection, where we are interested in determining the complex reflectivity of the DUT, $\Gamma(\nu)$. A 3 dB cou-

SPICUM servicio de publicaciones

pler divides the light from the tunable laser source (TLS) between the DUT arm and a reference arm which is terminated in a mirror. Both the DUT and the mirror reflect the light back into the coupler, from where it is directed to a photo-detector. As the wavelength (or frequency) of the TLS is swept, the optical field incident on the photodetector is:

$$E_T(\nu) = \frac{E_{\text{in}}}{2}[\exp(-\text{j}2\pi\nu\tau) + \Gamma(\nu)]. \tag{2.8}$$

where $\Gamma(\nu)$ is the reflectivity of the device, the mirror is supposed to be a perfect reflector, and the amplitude of the TLS signal (E_{in}) is assumed to be constant with frequency. Note that the laser sweep varies the optical frequency with time, so that E_T is actually a function of time, i.e. $E_T = E_T(\nu(t))$. The delay of the reference arm with respect to the DUT arm is $\tau = 2\Delta L n_g/c$, where ΔL is the extra length of the reference arm, n_g the group index of the fibre and c the speed of light in vacuum. The current produced by the photo-detector is directly proportional to the incident optical power, i.e., $I = \mathscr{R}\langle|E_T|^2\rangle$, where $\mathscr{R}$ is the responsivity of the photodiode, so that

$$I(\nu) = \mathscr{R}\frac{P_{\text{in}}}{4}[1 + |\Gamma(\nu)|^2 + \text{Re}\{\Gamma(\nu)\exp(-\text{j}2\pi\nu\tau)\}] \tag{2.9}$$

where P_{in} is the output power of the TLS and Re{} stands for the real part of its argument. The device's frequency response, $\Gamma(\nu)$, cannot be directly obtained from $I(\nu)$. However, upon inverse Fourier transformation of (2.9) we obtain

$$i(t) = \mathscr{R}\frac{P_{\text{in}}}{4}\left[\delta(t) + \rho(t) * \rho(-t) + \frac{\rho(t-\tau) + \rho(-t-\tau)}{2}\right], \tag{2.10}$$

where $\rho(t)$ is the device's impulse response, $\delta(t)$ is Dirac's delta function, and $*$ denotes convolution. Provided that the delay τ much larger than the duration of $\rho(t)$, a delayed version of the impulse response, $\rho(t-\tau)$, is well separated from all the other terms of (2.10) [see figure 2.3(b)]. By filtering the unwanted terms, $\rho(t-\tau)$ can be isolated, and by Fourier transforming it, the desired frequency response $\Gamma(\nu)$ can be obtained.

2.3.2. Practical considerations

Let us now come back to some practical considerations on OFDR we have not taken into account so far.

First, we are considering a completely coherent interference scheme, so that the coherence length of the tunable laser source must be much larger than any physical length in the setup.[2] With modern lasers having linewidths below 100 KHz and thus coherence lengths of several hundred meters, this is usually not a mayor issue. Also, in writing equation 2.8 we are assuming precise knowledge of the instantaneous frequency of the TLS during the sweep. While most modern instrumentation lasers provide this information, it can also be determined with an auxiliary interferometer [44].

Furthermore, we are assuming that the polarisation states of the signals coming from the two arms of the interferometer are aligned. In practice this may not be the

[2] The coherence length is directly related to the linewidth, ν_Δ, of the laser by $L_{\text{coh}} = c/(\pi\nu_\Delta)$, with c the speed of light in vacuum.

SPICUM servicio de publicaciones

case, because of optical fibres are generally not polarisation maintaining. Polarisation alignment can be achieved with a polarisation controller in one of the arms, or, alternatively, a polarisation diversity receiver instead of single photodetector can be used [31].

In the above analysis, we have not placed any restrictions on the bandwidth of the laser sweep. The finite bandwidth of tunable lasers limits the temporal resolution with which the impulse response, $\rho(t)$, can be computed. Specifically, if the measurement bandwidth is $\Delta\nu$ (in Hertz), the temporal resolution is limited to $\Delta t = 1/\Delta\nu$. The minimum distance between two reflectors than can then be resolved is $\Delta z = \Delta t c/(2n_g)$, where the factor 2 comes from the fact that the light has to travel forth and back between the reflectors. Using the relation $|\Delta\nu| = \Delta\lambda c/\lambda_0^2$ we can express this result in terms of the laser's wavelength span, $\Delta\lambda$:

$$\Delta z = \frac{\lambda_0^2}{2n_g\Delta\lambda}, \tag{2.11}$$

where λ_0 is the central wavelength. With 100 nm laser span, and a group index of ~ 1.45 in fibre, a spacial resolution of about 8.3 µm is achieved. In a silicon chip, where the group index can be as high as 3.6, resolutions down to 3.3 µm are possible.

Finally, the processing of the photocurrent is usually carried out with digital signal processors, so that the current signal, $I(\nu)$, must be sampled. If the laser is swept linearly with a speed γ_{Hz} Hz/s, so that $\nu(t) = \nu_0 + \gamma_{\mathrm{Hz}} t$, the highest frequency in $I(\nu)$ [Equation 2.9], comes from the exponential term and is given by $\gamma_{\mathrm{Hz}}\tau$. Taking into account that the sampling frequency has to be at least twice this frequency we find

$$f_{\mathrm{sample}} \geq \gamma_{\mathrm{m}} \frac{4\Delta L n_g}{\lambda_0^2}, \tag{2.12}$$

where γ_{m} is the sweep speed expressed in m/s. Analysing a fibre assembly with a 30 m long fibre and a 40 nm/s scan requires a sampling frequency of 3 MHz. A pigtailed photonic device, with a much shorter fibre of, say, 30 cm would only require a sampling rate of 30 KHz.

2.4. Six-port technique

At microwave frequencies, a six-port is a passive device that produces linear combinations of its two input waves at four output ports. By detecting the output powers, the complex ratio, i.e. the relative magnitude and phase, of the input waves can be precisely computed [46]. Traditionally, the six-port has been used as a measurement device. In its basic configuration as a reflectometer, proposed by Engen in the 1970s [47], it combines the incident and reflected waves from a DUT with relative amplitudes of 1.5 and 120° phase shifts at three different outputs, while a fourth output provides a power reference. The complex ratios (amplitude and phase) between the incident and reflected waves are referred to as six-port centres. From the power readings at the four outputs at a single frequency the complex reflection coefficient of the DUT at that frequency can be determined, without any frequency sweeps. This facilitates

SPICUM servicio de publicaciones

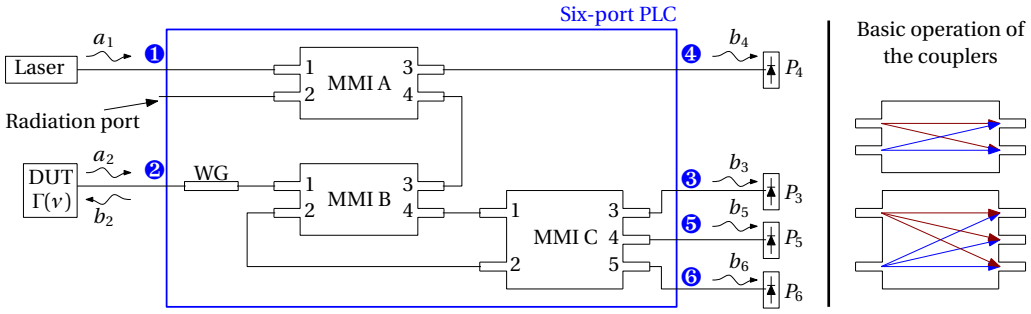

Figure 2.4.: Architecture of an optical six-port junction.

the use of sophisticated hardware calibration techniques, which yield reduced measurement errors in spite of reflectometer hardware imperfections. More recently, the six-port has also been used as a coherent microwave receiver [48, 49].

In 2005, an optical realisation of the sixport reflectometer, that benefits from similar calibration techniques as its microwave counterpart, was proposed [32]. A preliminary design on low contrast silica-on-silicon proved the feasibility of implementing an optical high-performance reflectometer. A calibration technique suitable to the particularities of the optical domain was developed in [50], and the effects of limited laser linewidth were analysed in [51]. Simulations of realistic hardware and calibration techniques showed that a six-port based measurement system achieves return loss accuracy of ±0.01 dB and group delay errors below ±0.2 ps in the characterisation of a fibre Bragg grating, using a 5 nm wavelength span. Hence, the six-port technique has the potential to outperform existing OFDR techniques. This potential is strengthened by the fact that calibration accuracy improves as the size of the six-port junction is reduced. This will be achieved by moving from a low contrast silica-on-silicon design to a more compact silicon-on-insulator design. Just as OFDR, the six-port technique requires polarisation alignment, or polarisation diversity detection. While the latter is out of the scope of this work, we will require the six-port to operate with both TE and TM polarisation.

We shall now analyse the six-port technique in some detail: the basic operation of the optical sixport reflectometer is explained in section 2.4.1, and the calibration of the device will be discussed in section 2.4.2.

2.4.1. Operation principle

Figure 2.4 shows a schematic of the six-port measurement system. The light source is an external narrow line-width laser, which, in principle, need not be tunable. However, in order to be able to perform characterisation at different wavelengths, a tunable source is of course required. Detection of the interference signals is performed with four power detectors at the six-port outputs. The passive six-port junction is realised with a planar lightwave circuit (PLC), that provides the necessary magnitude and phase relations between the waves incident on the DUT and reflected from the DUT. The PLC consists of three interconnected multimode interference couplers, that split light as illustrated on the right hand side of figure 2.4. The element labelled “WG” is a

SPICUM servicio de publicaciones

waveguide that accounts for the length difference between the path of the reference signal, and the path of the signal reflected back from the DUT.[3] The six ports of the PLC are identified with circled numbers, whereas the ports numbers of the individual couplers are indicated inside each coupler. We will denote the complex amplitude transmission from port j to i of the complete six-port by the scattering parameter S_{ij}.

To understand the operation of the six-port lets us examine its four output waves, $b_{\{3,4,5,6\}}$. Port 4 act as a power reference, providing a sample of the input wave: $b_4 = a_1 S_{41}$. The waves at outputs 3, 5 and 6 are a superposition of the wave transmitted directly to the output ($a_1 S_{\{3,5,6\}1}$) and the wave reflected from the DUT ($a_1 S_{21} \Gamma S_{\{3,5,6\}2}$), so that

$$b_{\{3,5,6\}} = a_1 S_{\{3,5,6\}1} + a_1 S_{21} \Gamma S_{\{3,5,6\}2}, \tag{2.13}$$

where $\Gamma = a_2 / b_2$ is the DUT's reflection coefficient. In defining the six-port centres as

$$q_{\{3,5,6\}} = -\frac{S_{\{3,5,6\}1}}{S_{21} S_{\{3,5,6\}2}}, \tag{2.14}$$

we can re-express (2.13) as:

$$b_{\{3,5,6\}} = a_1 S_{\{3,5,6\}1} \left(1 - q^{-1}_{\{3,5,6\}} \Gamma\right). \tag{2.15}$$

Note that at each output we have a directly transmitted wave and a sample of the reflection from DUT, that is, three OFDR like outputs are generated.[4] The six-port techniques exploits the differences between these outputs to directly determine Γ, without requiring wavelength swept measurements. In fact, by normalising the output powers of ports 3, 5 and 6 with respect to the reference port 4 we find the equations:

$$\left| \frac{b_{\{3,5,6\}}}{b_4} \right|^2 = \left| \frac{S_{\{3,5,6\}1}}{S_{41}} \right|^2 \left| \left(1 - q^{-1}_{\{3,5,6\}} \Gamma\right) \right|^2, \tag{2.16}$$

each of which defines a circle in the complex plane, centred at $q_{\{3,5,6\}}$ and with a radius proportional to power measured at each six-port output. As illustrated in figure 2.5, the intersection of these circles uniquely determines the reflection coefficient of the DUT.

The optimum centres of a six-port reflectometer in terms of measurement precision have a magnitude of 3/2 and relative phases of 120° [47]. We will now analyse how the architecture shown in figure 2.4 implements these centres. The three six-port S-parameters that define the centres through (2.14) can be expressed in terms of the S-parameters of the individual MMIs A, B and C, which we shall denote with superscripts:

$$\begin{aligned} S_{\{3,5,6\}1} &= S^A_{41} S^B_{23} S^C_{\{3,4,5\}2} \\ S_{21} &= S^A_{41} S^B_{13} \exp(-\mathrm{j}\theta_{\mathrm{WG}}) \\ S_{\{3,5,6\}2} &= \exp(-\mathrm{j}\theta_{\mathrm{WG}}) S^B_{41} S^C_{\{3,4,5\}} \end{aligned} \quad , \tag{2.17}$$

[3] This is equivalent to the τ delay between the reference arm and the DUT arm in OFDR.

[4] In fact, (2.15) is analogous to (2.8), the basic equation describing OFDR.

SPICUM servicio de publicaciones

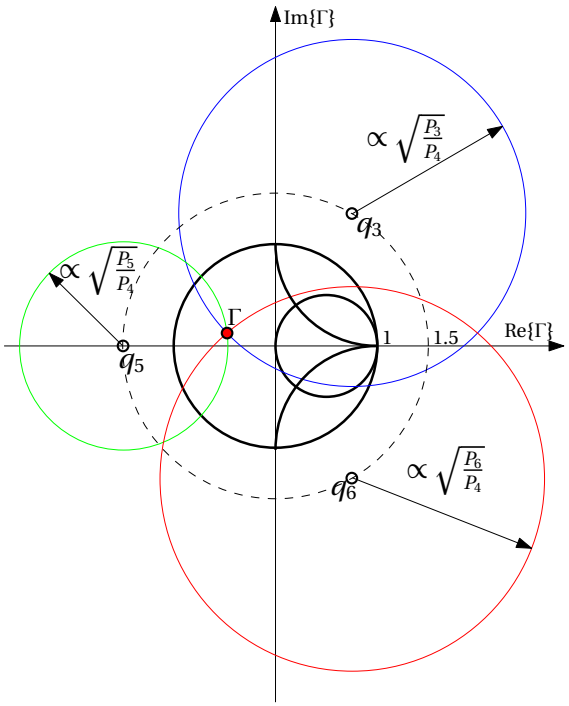

Figure 2.5.: Graphical representation of the reflection coefficient determination.

where $\exp(-j\theta_{WG})$ stands for the wavelength dependent phase shift introduced by waveguide "WG". Substitution of (2.17) in (2.14) yields:

$$q_{\{3,5,6\}} = -\frac{S^{B}_{23} S^{C}_{\{3,4,5\}2}}{S^{B}_{13} S^{B}_{41} S^{C}_{\{3,4,5\}1}} \exp(j2\theta_{WG}) \overset{\text{ideal}}{=} \sqrt{2}\exp(j2\theta_{WG} + j\{0, \tfrac{\pi}{3}, \tfrac{2\pi}{3}\}). \tag{2.18}$$

Assuming ideal MMIs, the 2×3 MMI coupler C introduces exactly the required 120° phase shifts, while the 2×2 MMI coupler B provides the near optimum magnitude $\sqrt{2} \approx 3/2$. The behaviour of the MMI couplers will be studied in detail in section 5.2.6. Due to the wavelength dependent phase shift θ_{WG} the centres will rotate with wavelength at a constant speed. However, this rotation, as well as other hardware imperfections, is readily cancelled out by calibration.

2.4.2. Calibration

Calibration of a measurement system essentially consists in determining its systematic errors at each frequency before carrying out the actual measurement, so that these errors can be cancelled from the final results. Sophisticated calibration techniques exist for microwave domain six-port reflectometers and were extended to the optical regime in [50]. An exhaustive analysis and justification of this technique is out of the scope of this work and can be found in [52]. However, the performance of the calibration technique, and consequently the accuracy of the measurements, partially relies

SPICUM servicio de publicaciones

on some physical properties of the six-port junction. Thus, we will briefly review the calibration technique and point out its main requirements on the six-port hardware.

In the microwave domain, calibration of the six-port is carried out, at each measurement frequency, in two steps known as W plane calibration and Γ plane calibration. W plane calibration consists in connecting five different loads whose reflection coefficients have the same, unknown, amplitude and arbitrary, but well distributed, phases. A sliding mirror that produces reflection coefficients $\Gamma_k = \exp(\mathrm{j}k2\pi/5)$, $k = 1,2,\ldots,5$ constitutes an ideal calibration standard for this step. For the Γ plane calibration a matched load ($\Gamma = 0$), a short circuit ($\Gamma = -1$) and a open circuit ($\Gamma = 1$) are needed. We will now discuss how the W and Γ plane calibration can be realised in the optical domain.

2.4.2.1. Optical W plane calibration

Optical W plane relies on a virtual sliding mirror (VSL), that is, a physically fixed mirror connected to the DUT port with a fibre of length L_f. As wavelength is varied, the reflection coefficient seen through the DUT port varies according to $\Gamma = -\exp(-\mathrm{j}2\pi n_{\mathrm{eff}} L_f/\lambda)$, with n_{eff} the effective index of the fibre. Hence, five loads with different phases and equal amplitude are easily generated by selecting a proper fibre length and using five wavelength steps. However, these loads are only useful for W plane calibration if the response of the six-port can be considered flat in the wavelength range needed to generate them.

The smallest wavelength range in which the five loads can be synthesised is ultimately limited by the smallest wavelength step in the system. If we assume a 10 nm/s laser sweeping speed with a 100 KHz sampling, we achieve a minimum wavelength step of $\delta\lambda = 0.1$ pm. This means that $5 \times \delta\lambda = 0.5$ pm are required to generate the five phases, and the six-port response thus has to vary in a scale much larger than 0.5 pm. Since the MMIs are broadband devices, the fast variations of the six-port response only arise from Fabry-Perot cavities that form either inside the PLC or between the PLC and the photo-detectors. The beating period of a Fabry-Perot cavity is inversely proportional to its length, i.e. $\Delta\lambda = \lambda^2/(2\Delta L n_g)$, and from the condition $\Delta\lambda \geq 10 \times 0.5$ pm we find $\Delta L n_g \leq 24$ cm.

Clearly, cavities of this size will not form within the PLC, but rather between the PLC and the power detectors if these were attached to the PLC with optical fibres. Thus, it is clearly preferable to situate the power detectors very close to the chip, through some kind of hybrid integration scheme. The fastest variations in the six-port response will then come from the PLC itself, meaning that any size reduction of the device will result in an easier generation of the calibration loads, or a greater calibration accuracy.

2.4.2.2. Optical Γ plane calibration

While the matched load ($\Gamma = 0$) and the short circuit ($\Gamma = -1$) are easily implemented at optical frequencies with a fibre wrapped tightly around a pencil, and a mirror, respectively, an open circuit ($\Gamma = 1$) is harder to realise. Fortunately, the open circuit is not needed for calibration if the reference port (port number 4) can be considered

SPICUM servicio de publicaciones

ideal, in the sense that the output wave b_4 contains no contribution from the signal reflected back from the DUT. Well designed MMIs exhibit very low back reflections, so that the S_{42} parameter of the six-port junction can be assumed to be zero; this is confirmed by simulations of the complete junction in chapter 6. Consequently, the main path from the DUT to the reference port is via reflection at port 1 or the radiation port. The magnitude of this reflection will essentially be determined by the quality of the anti-reflective coating deposited on the chip facet.

As shown in [50], imperfect Γ plane calibration results in spurious reflections in the temporal response. Hence, the residual errors arising from an Γ plane imperfect calibration can be cancelled by temporal gating (or filtering) of these artifacts. Of course, this requires taking measurements with bandwidths and resolutions comparable to those of OFDR.

2.4.3. Conclusions

The six-port technique has the potential to improve the measurement accuracy of existing OFDR techniques, owing to sophisticated calibration techniques imported from the microwave domain. Calibration accuracy has been shown to improve as the size of the circuit is reduced, which makes silicon-on-insulator the preferred choice for its implementation, since this platform allows for drastic size reduction compared to more established silica-on-silicon technologies. Being an interferometric technique, the six-port has to be able to handle both TE and TM polarised light, since the DUT may, in principle, rotate the polarisation state.

SPICUM servicio de publicaciones

SPICUM
servicio de publicaciones

3

Silicon on Insulator Technology

DESIGNING practical devices requires a basic knowledge of the process by which they are made. Thus, here we will briefly study the general fabrication process of silicon on insulator waveguide devices (section 3.1), as well as the limitations that this process imposes on device geometry (section 3.2). In sections 3.3 and 3.4 we will analyse the advantages and drawbacks of the two light-guiding paradigms in SOI: silicon wire waveguides, which have a guiding region of only 250 nm × 500 nm, and micrometre scale rib waveguides, with a size of around 2 µm × 2 µm. The latter will be chosen for the realisation of the six-port.

This chapter aims to give a basic overview of silicon-on-insulator technology, so that a reader who is already familiar with it, may want to proceed directly to section 3.4.

3.1. Waveguide fabrication

Silicon-on-insulator waveguides are defined on wafers, which have typical diameters between 100 mm and 200 mm and are composed of three layers, as illustrated in figure 3.1(a). The substrate solely provides mechanical support, with no light propagating

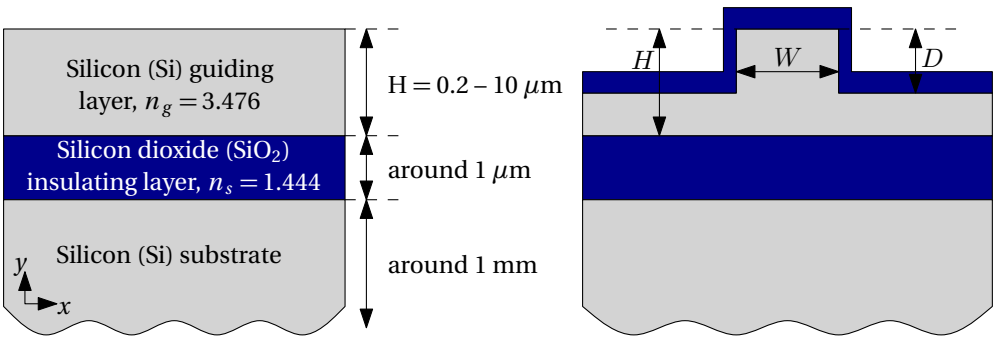

(a) Cross section of a SOI wafer. **(b)** Etched rib waveguide.

Figure 3.1.: (a) Cross-section of an unprocessed wafer and (b) finished rib waveguide on SOI. Material refractive indexes are given at $\lambda = 1.55\,\mu m$.

SPICUM servicio de publicaciones

through it. Light is guided by the top silicon layer, the middle silicon dioxide layer or bottom oxide (BOX), and the cladding, which may be air, silicon dioxide or a polymer such as benzo-cyclo-butene (BCB) and SU-8. The refractive index of silicon is much higher than that of silicon dioxide and the cladding, so that light is confined by internal reflection. This guiding mechanism is only effective if the BOX layer is thick enough to act as an optical *insulator*; otherwise light would leak into the substrate, causing losses. For photonic applications silicon layer thicknesses between 220 nm and 10 µm are typically used; the thickness uniformity of this layer is around ±5% [53]. The thickness of the BOX layer ranges between 0.5 µm for silicon layers with a thickness of several micrometers, up to 2 µm or 3 µm for silicon wires.

While the top silicon layer naturally provides confinement in the vertical (y) direction, confinement in the horizontal (x) direction is achieved by selectively removing (or *etching*) material. This generally results in a rib waveguide structure as shown in figure 3.1(b), where the silicon layer has been partially etched to a depth D, and a silicon dioxide cladding, which acts as protection, has been added. In order to avoid etching large areas of silicon, waveguides are usually defined by etching trenches along them instead of removing all the silicon that does not guide light. The basic steps involved in the fabrication of this structure are depicted in in figure 3.2, and will be succinctly described in the following.

1. The pattern is first written on a high resolution mask plate.
2. The wafer is spin-coated with a layer of photo-sensitive resist.
3. The pattern is transferred optically (by illumination with light) from the mask plate to the photo-resist [figure 3.2(a)].[1] This process is called optical lithography. Usually the pattern is smaller than the wafer, so that after an exposure, the spot can be moved (or *stepped*) and the pattern can be repeated. The machine that performs this task is called a *stepper*.
4. The photo-resist is then developed, and the exposed area is chemically removed. Hence, only the silicon under the remaining photo-resist is protected [figure 3.2(b)].
5. The silicon is then attacked either with an ionised gas in a reactor (reactive ion etching) or by submerging the chip in an acid (wet etching), so that the material that is not protected by photo-resist is etched away [figure 3.2(c)]. The main difference between the two etching techniques is the sidewall angle, which is vertical in the case of reactive ion etching, and approximately 54.74° in the case of wet etching [55]; this is further discussed in chapter 4.
6. Finally, the resist is removed [figure 3.2(d)] and a protective layer is added on top of the structure [figure 3.2(e)].

If a second etch depth is required, the above process has to be repeated, thus significantly increasing fabrication complexity and costs. This is why designs that rely only on a single etch depth are preferable.

[1] Other transfer techniques such as contact lithography or electron beam lithography exhibit advantageous characteristics such as higher resolution, but are not suited for high volume production [54, Ch. 7].

SPICUM servicio de publicaciones

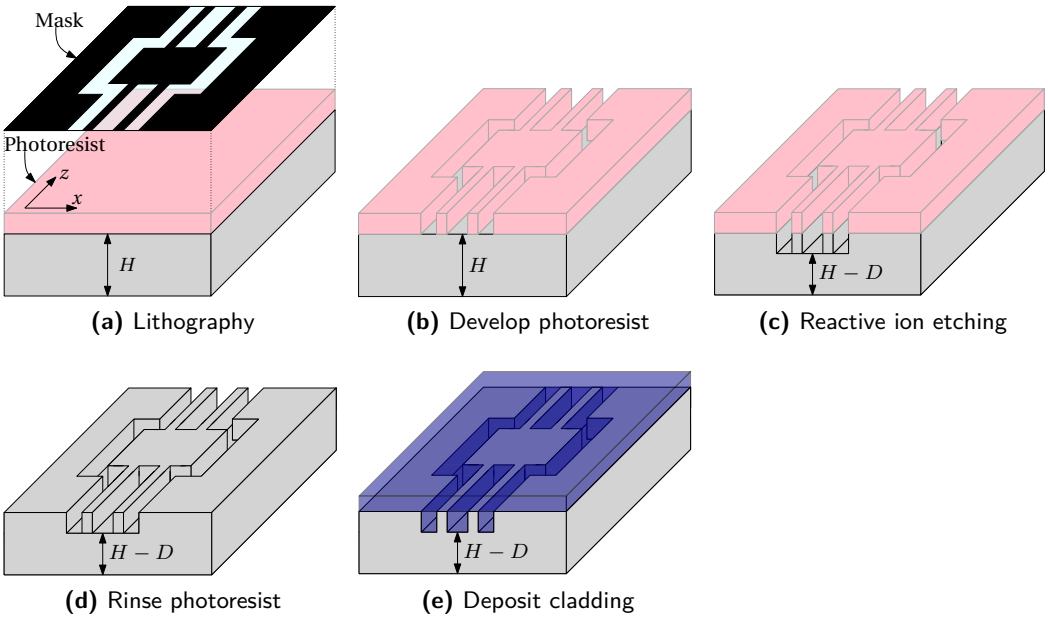

(a) Lithography **(b)** Develop photoresist **(c)** Reactive ion etching

(d) Rinse photoresist **(e)** Deposit cladding

Figure 3.2.: Basic steps in SOI waveguide fabrication.

3.2. Fabrication tolerances and limitations

When designing a device, it is crucial to take into account the limitations of the process by which it will be fabricated. In this section we will describe these limitations and their effect on waveguide geometry.

Lithographic resolution Lithography is performed by illuminating the photo resist with an ultraviolet light sources. The wavelength which is employed thus fundamentally limits the smallest feature that can be faithfully reproduced.

ARDE (Aspect ratio dependent etching) Etching of grooves with different aspect ratios, as illustrated in figure 3.3(a), yields different etch depths [54, Ch. 7]. This phenomenon occurs because less etch gas enters the smaller opening of the narrow groove, thus reducing its etch depth. When placing two parallel waveguides close together, this results in a reduced etch depth in the gap between them [see figure 3.3(b)]. This effect, which is also known as microloading, can become critical, since it increases unwanted coupling between the waveguides.

Dishing When not etching fully through the silicon layer, i.e. when $D < H$, the etch depth decreases slightly close to the waveguides, as illustrated in figure 3.3(b). While this can be controlled to below 10% of the etch depth, it has to be taken into account when specifying etch depth for fabrication.

Sidewall angle Reactive ion etching usually results in sidewalls with an angle of around 1° (see figure 3.3(b)). This translates into devices with a slightly increased effective width.

SPICUM servicio de publicaciones

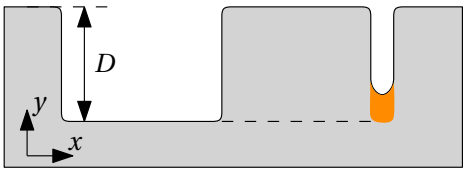

(a) Aspect ratio dependent etching.

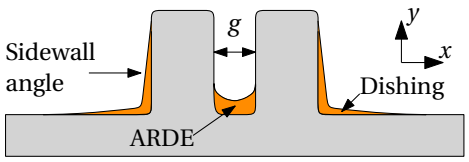

(b) Two parallel rib waveguides, with ARDE, dishing and non-vertical sidewalls.

Figure 3.3.: Effects of different fabrication impairments on waveguide geometry.

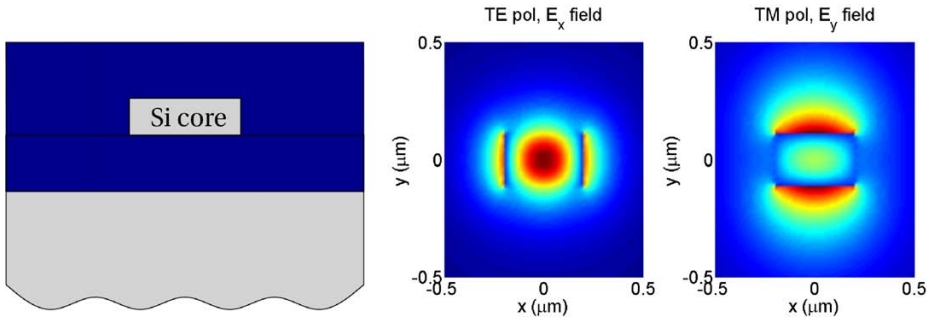

Figure 3.4.: Basic geometry of a silicon wire waveguides and its fundamental TE and TM modes.

Etch depth tolerances Etch depth will exhibit variations both on different spots on the wafer, as well as from one fabrication run to the next. These need be taken into account in the device design to optimise yield.

Lateral device dimensions Device length and width also experience slight deviations as a combined result of limited lithographic resolution and non-ideal etching. Again, these variations have to be considered during the design phase.

Some typical tolerance values are given in sections 3.3 and 3.4 for silicon wire and micrometric rib waveguides, respectively.

3.3. Silicon wire waveguides

Silicon wire waveguides have a very small core of typically 250 nm × 500 nm, which ensures that the waveguides are always vertically single-moded. Consequently they are usually completely etched, i.e. $D = H$, to optimise lateral confinement. The definition of waveguides this small requires deep ultraviolet (DUV) lithography, with an illumination wavelength of 193 nm or 248 nm. The pattern is then transferred to the silicon with reactive ion etching. Since the waveguides are completely etched, with the BOX acting as an etch-stop layer, etch depth tolerances and dishing effects are usually not an issue. If a second shallow etch step is used, they do, however, become of importance. The smallest feature size that can be faithfully reproduced with state of the art 193 nm lithography is between 120 nm and 150 nm [56, 57].

SPICUM servicio de publicaciones

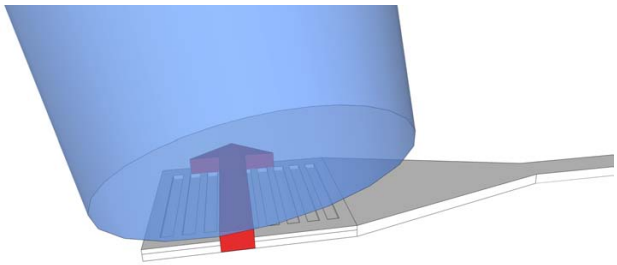

Figure 3.5: Coupling TE polarised light into a silicon wire waveguide with a grating coupler.

Figure 3.4 shows the TE and TM modefields in a silicon-wire-waveguide, which have a size of only a few hundred nanometres. On the other hand, the mode field diameter of an optical fibre is around 10 µm, so that direct butt-coupling of a fibre to the waveguide would yield very high coupling losses. One solution to this problem is the use of inverse tapers [58], which increase the size of the waveguide mode field by reducing the confinement. However, these structures require stringent fabrication control of the taper tip. A widely used alternative are grating couplers [59, 60], which scatter the light out of the waveguide plane into an optical fibre situated above the chip, as shown in figure 3.5. However, these couplers only operate with either TE or TM polarisation. Coupling losses of less than 2 dB have been reported using special fabrication steps [61], but standard couplers exhibit losses of around 5 dB and a 3 dB bandwidth of 60 nm [57].

The strong lateral confinement of silicon wire waveguides allows for the use of bending radii as low as 5 µm [62]. On the other hand, the small waveguide cross-section also imposes very different boundary conditions for the TE and TM modes (see figure 3.4). This generates a strong polarisation dependence, both in terms of polarisation dependent losses and fibre to chip coupling [63]. While low polarisation dependence can, in principle, be implemented with 2D gratings and polarisation diversity techniques, this is a topic of ongoing research at the time of writing [64]. Since we want the six-port circuit to operate at both polarisations, silicon-wire waveguides were not deemed the most adequate choice at the time of design. Nonetheless, chapter 9 is devoted to the design of a single etch step fibre-to-chip coupling grating in silicon-wires.

3.4. Micrometric rib waveguides

A rib geometry as shown in figure 3.1 is typically used for micrometre scale SOI waveguides, because if $D < H/2$ the waveguide is vertically single-moded despite the large waveguide height (see section 4.2). With dimensions ranging from $\sim 1.5\,\mu m \times 1.5\,\mu m$ to $\sim 4\,\mu m \times 4\,\mu m$, these waveguide can be defined with standard i-line lithography, with an illumination wavelength of 365 nm. The minimum feature size is then approximately 0.4 µm [54, 65, Ch. 7]. Since the silicon layer is not completely etched, the etch depth is not controlled by the BOX, so that tolerances of around $\pm 0.1\,\mu m$ arise. Device width can typically be controlled down to $\pm 0.1\,\mu m$. In principle, both reactive ion etching and wet etching can be used for the definition of the waveguides, yielding rectangular and trapezoidal rib waveguides, respectively.

Due to the relatively large waveguide size, the shapes of the TE and TM polarised

SPICUM servicio de publicaciones

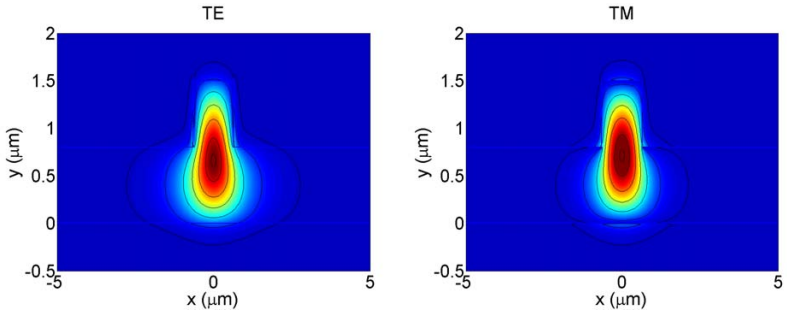

Figure 3.6.: Fundamental TE and TM modes of a singlemode SOI rib waveguide with $H = 1.5\mu m$, $D = 0.7\mu m$ and $W = 1.3\mu m$.

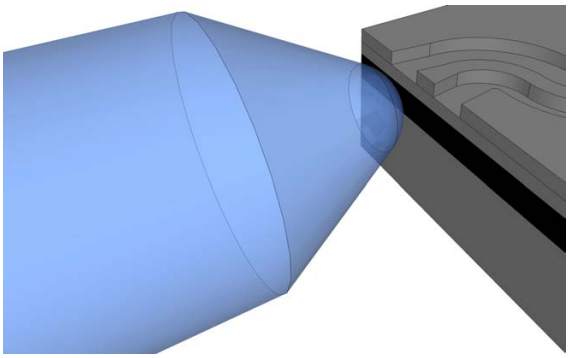

Figure 3.7: Butt coupling between a lensed fibre and a micrometric rib waveguide.

modes are rather similar, as shown in figure 3.6. As a consequence, devices with a low polarisation sensitivity are readily achieved [66, 67]. However, in choosing a shallow etch depth ($D < H/2$) for single mode operation, lateral confinement is sacrificed, so that the waveguides can only be bent with radii of several hundred microns, unless a second, deep etch is used for the curves [68]. Light is coupled into the chip by simply butt coupling a lensed fibre to the waveguides, which are widened at the facets to improve the modal overlap (see figure 3.7). Coupling losses depend on the curvature radius of the fibre lens as well as the waveguide size, but are virtually wavelength independent.

Owing to the low polarisation dependence and the straightforward coupling scheme, micrometric rib waveguides were chosen for the implementation of the six-port junction. Fabrication was carried out at the Canadian Photonic Fabrication Center (CPFC) [69] on a commercial SOI wafer with a $1.5\mu m$ thick silicon layer and $1\mu m$ thick bottom oxide. The devices were coated with a SiO_2 passivation and cladding layer with a thickness of about $0.5\mu m$.

SPICUM servicio de publicaciones

4
Waveguide design

WAVEGUIDES are the natural starting point for the design of the sixport junction. In this chapter, we will consider both rectangular and trapezoidal waveguides (section 4.1), and will study their single-mode behaviour (section 4.2) and curvature losses (section 4.3). The fabrication tolerance analysis carried out in section 4.4 will reveal that, for the same dimensional variations, rectangular waveguides offer tighter bending radii, and will thus be used in the sixport. Based on the results of the tolerance analysis, the design of the waveguide dimensions is then described in section 4.5. The problem of waveguide coupling is analysed in section 4.6, both in terms of two parallel waveguides maintaining a high extinction ratio (all the power in one waveguide), and maintaining a low imbalance (equal power in both waveguides), the latter of which is actually more critical. Finally, a simple design rule for s-bends is derived (section 4.7) and conclusions are drawn.

4.1. Introduction

The general waveguide geometry for rectangular and trapezoidal rib waveguides is shown in figure 4.1. H stands for the silicon layer height, h for the height of the lateral slab, and D for the etch depth, so that $D+h=H$. The sidewall angle θ depends on the etch technique used to partially remove the silicon layer. Dry etching uses ion bombardment to etch away the silicon, yielding rectangular ribs ($\theta = 90°$), whereas wet or chemical etching produces sidewalls along one of the crystalline planes of silicon, so that $\theta = \arctan\sqrt{2} \approx 54.74°$. We shall denote the upper width of the trapezoidal waveguide by W_u to distinguish it from the width of the rectangular waveguide, W. The the lower rib width (W_l) of the trapezoidal waveguide is related to the top width by:

$$W_l = W_u + \frac{2D}{\tan\theta} \tag{4.1}$$

Assuming that the silicon layer height (H) is fixed, we wish to design the waveguide cross-section, i.e. the width W, etch depth D, and the curvature radius R, so that:

1. Single mode operation is achieved and
2. The bending radius is as small as possible.

SPICUM servicio de publicaciones

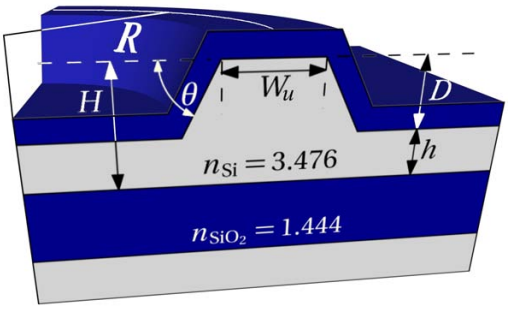

Figure 4.1: Geometry of the waveguide curves, with refractive indexes at $\lambda = 1.55\,\mu m$. θ is either 90° or 54.74°.

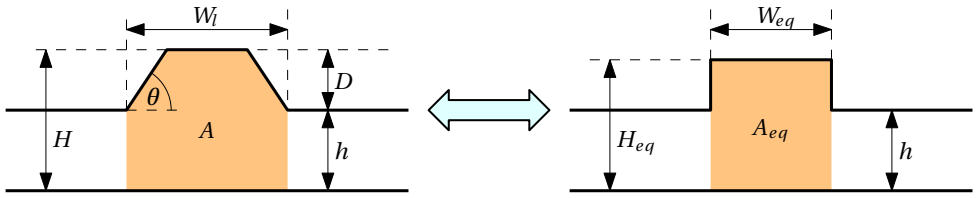

Figure 4.2.: Equivalent rectangular waveguide according to Marcatili's method.

The reduction of the curvature radius is limited by the insertion losses of a 90° turn, which we will require not to exceed 0.2 dB. We will find that in the single mode region fabrication tolerances have a strong impact on the curvature losses of both rectangular and trapezoidal waveguides, so that they need be incorporated into the design process.

4.2. Single mode operation

The single mode condition for rectangular rib waveguides ($W_u = W_l = W$), was established by Soref in [70], and basically sets an upper limit for the waveguide width and etch depth:

$$\frac{W}{H} \leq 0.3 + \frac{\frac{h}{H}}{\sqrt{1-\left(\frac{h}{H}\right)^2}} \tag{4.2}$$

$$\frac{D}{H} \leq \frac{1}{2} \tag{4.3}$$

While it has been recently found that there are some combinations of D and W which should yield single-mode waveguides according to these expressions and nevertheless seem to support higher order modes [71], Soref's formulae can still be used as a basis of design [72]. Furthermore, in most practical applications, waveguides have to be curved, so that higher order modes would be filtered.

In [73] it was shown that trapezoidal waveguides with $\theta = 54.74°$ exhibit the same single mode behaviour as Marcatili's equivalent rectangular waveguides. Marcatili's method is illustrated schematically in figure 4.2, and consists in replacing the trapezoidal waveguide with a rectangular waveguide that has the same width to height ratio ($W/H = W_{eq}/H_{eq}$) and the same area under the rib ($A = A_{eq}$). This yields the

SPICUM servicio de publicaciones

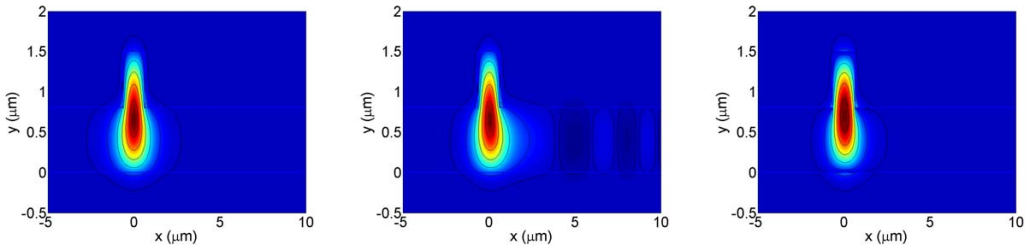

(a) TE, straight waveguide. **(b)** TE, $R = 300\,\mu m$. **(c)** TM, $R = 300\,\mu m$.

Figure 4.3.: Fundamental mode fields of a straight and a bent waveguides for TE and TM polarisation ($H = 1.5\,\mu m$, $D = 0.7\,\mu m$, $W = 1.3\,\mu m$, $\lambda = 1.55\,\mu m$).

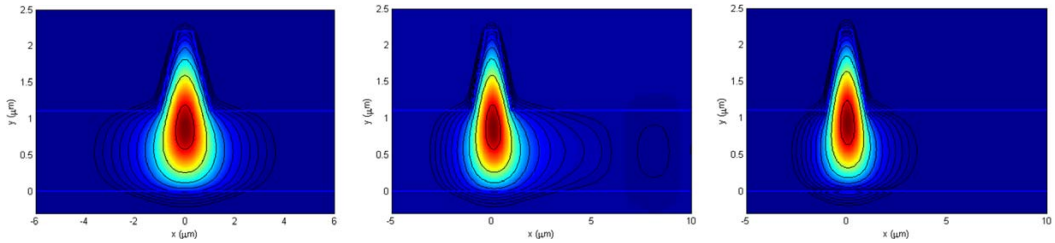

(a) TE, straight waveguide. **(b)** TE, $R = 900\,\mu m$. **(c)** TM, $R = 900\,\mu m$.

Figure 4.4.: Fundamental mode fields of a straight and a bent trapezoidal waveguides for TE and TM polarisation ($H = 2.2\,\mu m$, $D = 1.1\,\mu m$, $W_l = 2.1\,\mu m$, $\lambda = 1.55\,\mu m$).

following dimensions for the equivalent waveguide:

$$W_{eq} = \sqrt{W_l^2 - \frac{W_l}{H}\frac{D^2}{\tan\theta}} \tag{4.4}$$

$$H_{eq} = \sqrt{H^2 - \frac{H}{W_l}\frac{D^2}{\tan\theta}}. \tag{4.5}$$

Introducing (4.4) and (4.5) in (4.2), with $\theta = 54.74°$, the single mode condition for trapezoidal waveguides becomes

$$\frac{W_l}{H} \leq 0.3 + \frac{\frac{h}{H}}{\sqrt{1 - \left(\frac{h}{H}\right)^2 - \frac{\left(1-\frac{h}{H}\right)^2}{\frac{W_l}{H}\sqrt{2}}}} = \frac{W_{l,max}}{H}, \tag{4.6}$$

together with (4.3).

4.3. Curvature losses

The insertion losses of a 90° bend are made up of transition losses and pure bending losses. Transition losses occur at the junction of the straight waveguide and the bent

SPICUM servicio de publicaciones

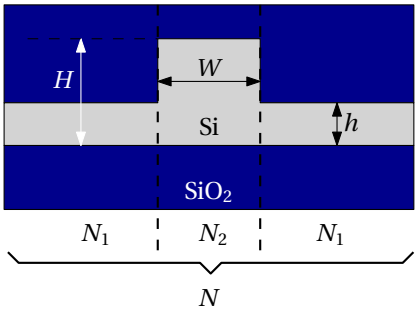

Figure 4.5.: Effective indexes of a rectangular rib waveguide.

waveguide, because their mode fields are dissimilar. This is illustrated in figure 4.3 for a rectangular waveguide and figure 4.4 for a trapezoidal waveguides. Note that the mode fields of curved waveguides slightly "skid" out of the curve, and that this effect is much more pronounced for TE than for TM polarisation. If reflections are negligible, the transition losses that result from the mode field deformation can be computed as:

$$\mathrm{L_T[dB]} = -10\log_{10}\frac{|\langle\Psi_B,\Psi_S\rangle|^2}{|\langle\Psi_B,\Psi_B\rangle||\langle\Psi_S,\Psi_S\rangle|} \tag{4.7}$$

where $\langle\Psi_B,\Psi_S\rangle$ is the overlap integral between the mode fields of the bent waveguide and the straight waveguide, which can be defined as:

$$\langle\Psi_B,\Psi_S\rangle = \frac{1}{2}\iint_{\Omega}\left(\mathbf{E}_S\times\mathbf{H}_B^*+\mathbf{E}_B^*\times\mathbf{H}_S\right)\cdot\hat{\mathbf{z}}\mathrm{d}\Omega, \tag{4.8}$$

with Ω the waveguide's cross section. Pure bending losses arise from the leaky nature of the bent mode, which radiates part of its power outwards the curve; this is clearly visible in figure 4.3(b). Pure bending losses can be calculated directly from the mode attenuation constant α, and for a 90° turn they are given by:

$$\mathrm{L_{90^\circ}}\left[\frac{\mathrm{dB}}{90^\circ}\right] = -20\log_{10}\left(\exp\left(-\frac{\pi}{2}R\alpha\right)\right) \approx 13.64R\alpha, \tag{4.9}$$

where R is the radius of curvature. A rigorous calculation of α requires a full-vectorial mode solver for bent waveguides and PML boundary conditions. For a preliminary analysis Marcuse's approximation is useful, because even on high index contrast waveguides it gives a good estimation of the attenuation constant of the fundamental mode of a bent rectangular rib waveguide [74]:

$$\alpha = \frac{1}{2}\frac{\alpha_y^2}{k_0^3 N\left(1+\alpha_y\frac{W}{2}\right)}\frac{k_y^2}{\left(N_2^2-N_1^2\right)}\exp(\alpha_y W)\exp\left(-\frac{2\alpha_y^3}{3N^2k_0^2}R\right) \tag{4.10}$$

where $\alpha_y = k_0\sqrt{N^2-N_1^2}$, $k_y = k_0\sqrt{N_2^2-N^2}$, $k_0 = \frac{2\pi}{\lambda}$, and N_1, N_2 and N are the effective indexes defined in figure 4.5.

From the designers point of view, the parameter of interest are the total bending losses along a 90° turn, which are the sum of the pure bending losses and the transition losses at each interface:

$$L_B[\mathrm{dB}] = L_{90^\circ} + 2L_T \tag{4.11}$$

SPICUM servicio de publicaciones

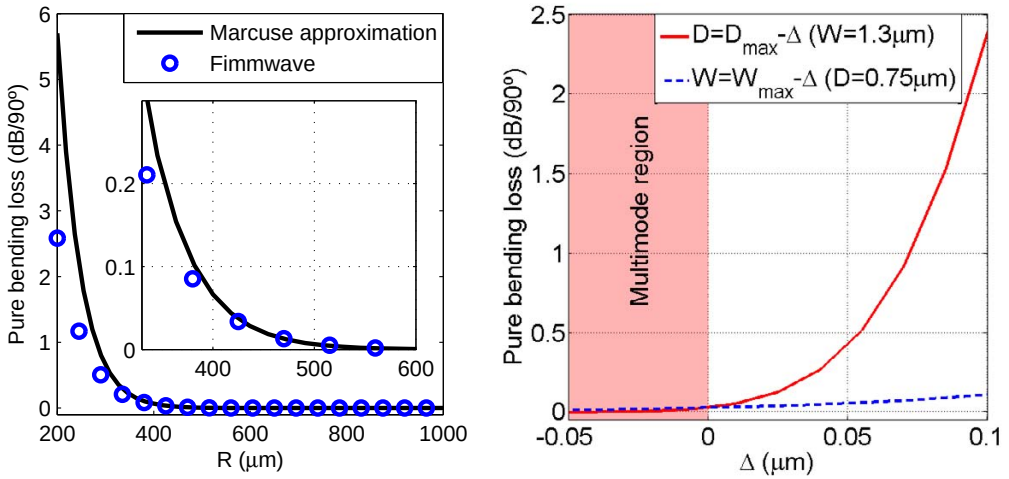

(a) $D = 0.7\,\mu m$, $W = 1.3\,\mu m$ **(b)** $R = 300\,\mu m$

Figure 4.6.: Variation of the pure bending losses of the fundamental quasi-TE mode with (a) curvature radius, R, and (b) the rib width, W, and etch depth, D. The waveguide is rectangular and has a silicon height of $H = 1.5\,\mu m$.

For the waveguides considered in this work, TM polarised modes always exhibit lower bending losses than TE polarised modes, so we will focus our analysis on the latter. While the modes of a bent waveguide are, generally speaking, hybrid in nature [75], our full vectorial simulations showed that for the radii of curvature of interest the modes remain quasi-TE or quasi-TM and virtually no polarisation coupling occurs.

Let us now analyse how bending losses depend on the geometrical parameters of the waveguide, namely curvature radius (R), waveguide width (W) and etch depth (D). Figure 4.6(a) shows the pure bending losses of a rectangular rib waveguide as a function R. While for $R > 400\,\mu m$ the losses are virtually zero, they increment exponentially for lower radii. A good agreement between the semi-analytical Marcuse approximation and the simulated losses is observed. In figure 4.6(b) the curvature radius is kept constant and the waveguide width and etch depth are varied around the maximum values that allow for singlemode operation according to Soref's conditions (4.2) and (4.3). It is apparent that the waveguide width has only a moderate impact on curvature losses, whereas etch depth reduction is critical, especially in the single mode region: a decrement of 100 nm can results in an increase of pure bending losses of around 2.5 dB. Given the high sensitivity of the curvature losses to the dimensions of the waveguide, in the next section we carry out a comprehensive tolerance analysis, for both rectangular and trapezoidal waveguides.

4.4. Fabrication tolerance analysis

In this section we rigorously analyse the effects of fabrication tolerances in a practical waveguide design and compare the performance of rectangular and trapezoidal rib waveguides. The study presented in this section was carried out for a substrate height

SPICUM servicio de publicaciones

of $H = 2.2\,\mu m$. However, its conclusions extend directly to the silicon height of $H = 1.5\,\mu m$ that was used in the final design. For the tolerance analysis in this section we shall consider the following specifications:

- single mode waveguide with minimum bending radius.
- total losses per 90° turn must not exceed 0.2dB ($L_B \leq 0.2dB$).
- silicon layer height: $H = 2.2\,\mu m$
- tolerances: ±10% in upper rib width (W) and $\pm 0.1\,\mu m$ in etch depth (D).

As a reduced bending radius is desired, waveguide dimensions are chosen at the limit of the single mode condition, i.e., we use the maximum etch depth and the maximum waveguide width allowed for this etch depth. This yields $D = 1.1\,\mu m$, $W = 1.93\,\mu m$ for the rectangular waveguide and $D = 1.1\,\mu m$, $W_l = 2.12\,\mu m$ ($\rightarrow W_u = 0.56\,\mu m$) for the trapezoidal one. However, if fabrication tolerances are taken into account, these dimensions no longer ensure single-mode behaviour, and more restrictive values have to be chosen, so that the waveguides remain single-moded even in a worst case. The nominal dimensions are thus: $D_{nom} = (1.1 - 0.1)\,\mu m = 1\,\mu m$, $W_{nom} = (1.93/1.1)\,\mu m = 1.75\,\mu m$ and $W_{u,nom} = (0.56/1.1)\,\mu m = 0.51\,\mu m$. When this waveguide is fabricated, its dimensions will lay somewhere within the domain defined by all the possible combinations of variations of either the waveguide width, or the etch depth, or both of them. Therefore we have to calculate the minimum bending radius (MBR) of nine different rectangular and nine different trapezoidal waveguides in order to carry out a tolerance analysis. The determination of the MBR in turn may require a large number of simulations to find the radius that exactly matches the specified level of losses. This is why we use the following strategy to calculate the MBR with a reduced number of simulations.

1. The total losses are divided equally between transition losses and pure bending losses; this division will be justified later on. In our design example this means: $L_{90°} = 0.1dB$ and $L_T = 0.05dB$, because the latter occur twice (4.11).

2. In order to obtain an approximation of the MBR, the pure bending losses are first estimated as a function of the curvature radius by means of (4.10) and (4.9). In this way the curvature radius that yields the pure bending losses established in step 1) serves as an initial guess of the MBR. Note that, because (4.10) is analytical, the pure bending losses can be calculated in a wide range of curvature radii with negligible computational cost, so that it is easy to find the region of interest. This is illustrated for the trapezoidal waveguide with nominal dimensions in figure 4.7, where the estimated MBR is about 1600 µm. In this case, the waveguide was first converted into its equivalent rectangular waveguide, using (4.4) and (4.5).

3. In order to obtain the accurate mode attenuation constant (α) and the bent mode profile in the region of interest, the real waveguides (not the equivalent ones) are then simulated with about four or five different curvature radii around

SPICUM servicio de publicaciones

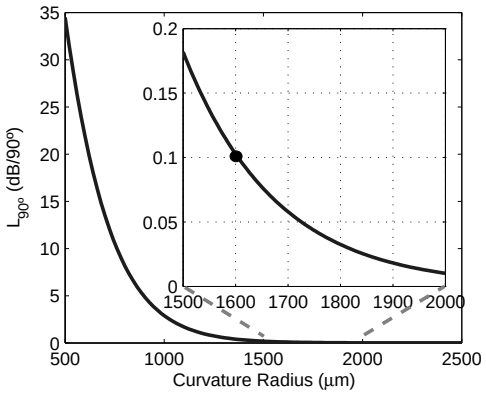

Figure 4.7: Estimation of the MBR using Marcuse's approximation (trapezoidal waveguide with nominal dimensions).

the initial guess obtained in step 2). Without this starting point, it can be a rather cumbersome task to find the correct radius by means of simulations. In this step the Fimmwave mode solver[1] for bent waveguides with 5μm thick lateral PML boundary conditions has been used.
The software is based on the Film Mode Matching technique [76], which makes it particularly suitable for the analysis of the rectangular rib waveguides, because these only need be divided into three vertical slices. On the contrary, in the case of the trapezoidal rib waveguides, it is necessary to finely discretise the slated sidewalls, which combined with the use of the complex solver makes simulations quite lengthy.

4. Expression (4.9) is then used to calculate the pure bending losses from the simulated mode attenuation constant, and the transition losses are obtained from the simulated mode fields by means of (4.8) and (4.7).
In order to facilitate interpolation, the pure bending losses per 90° turn are then fitted to the model:

$$\mathrm{L}_{90^\circ}\,[\mathrm{dB}] = aR\exp(-bR) \tag{4.12}$$

where a and b are degrees of freedom; this model is easily deduced from (4.10) and (4.9). Transition losses are simply fitted to a straight line.

5. Figure 4.8 shows that a good fitting of both types of losses is achieved, so that the total losses can be obtained by just adding up the fitted curves of pure bending losses and transition losses. The minimum bending radius is then easily determined for range of total losses; in our example it is 1740μm.
Note that for this radio the pure bending losses are slightly above 0.1dB, whilst the transition losses are a little bit lower than 0.05dB, but the equal division which was assumed in step 1) is a good approximation. We found that it also works fine with other substrate heights: for two rectangular rib waveguides with $H = 3.5\,\mu$m and $H = 5\,\mu$m the initial guesses obtained in step 2) are 3350μm and 8000μm, and simulations yield MBRs of 3400μm and 8200μm, respectively. Anyhow, if a different division is made in step 1), the estimated radio does not

[1] Fimmwave is a product by Photon Design: `www.photond.com`

SPICUM servicio de publicaciones

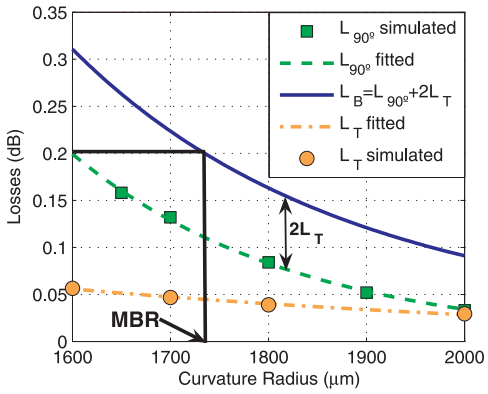

Figure 4.8: Fitting of pure bending losses and transition losses, and determination of the MBR for the trapezoidal waveguide with nominal dimensions.

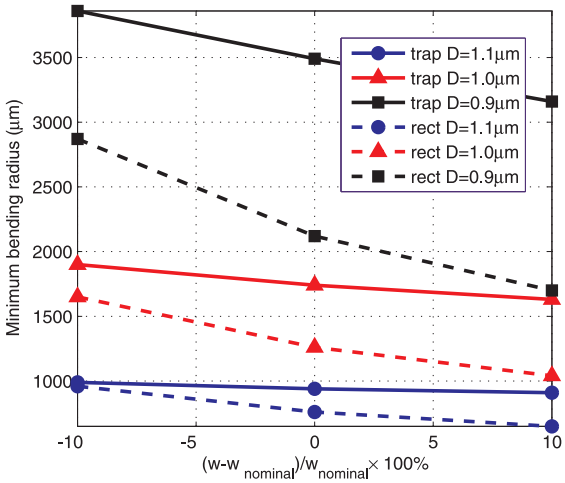

Figure 4.9: Variation of the MBR as a function of fabrication tolerances for rectangular and trapezoidal rib waveguides.

change substantially (see figure 4.7), so that the initial guess is still good enough and only a few more simulations would be necessary.

Repeating this strategy for the remaining 17 waveguides, we finally obtain the chart shown in figure 4.9, which summarises the dependence of the MBR on the fabrication tolerances. From this figure it is clear that the minimum bending radius of both rectangular and trapezoidal single-mode waveguides is extremely sensitive to etch depth variations. The MBR of the former increases with about a factor 1.5 each time the etch depth is reduced in 0.1µm, and in nearly a factor 2 for the latter. The rectangular waveguides seem to be more sensitive to width variations than the trapezoidal waveguides, but they always support lower curvature radii than their trapezoidal counterparts with the same etch depth. Another important conclusion is that the design has to be carried out in a worst case, i.e., radii of 2870µm and 3860µm would have to be chosen for the rectangular and trapezoidal waveguides respectively. This is because although not shown in figure 4.9, if the MBR for the nominal dimensions were chosen and the fabricated waveguide had an etching 0.1µm shallower than expected (i.e. 0.9µm instead of 1.0µm), pure bending losses would augment up to 5dB, which is far beyond the loss specifications.

Three main conclusions can be drawn from this analysis:

SPICUM servicio de publicaciones

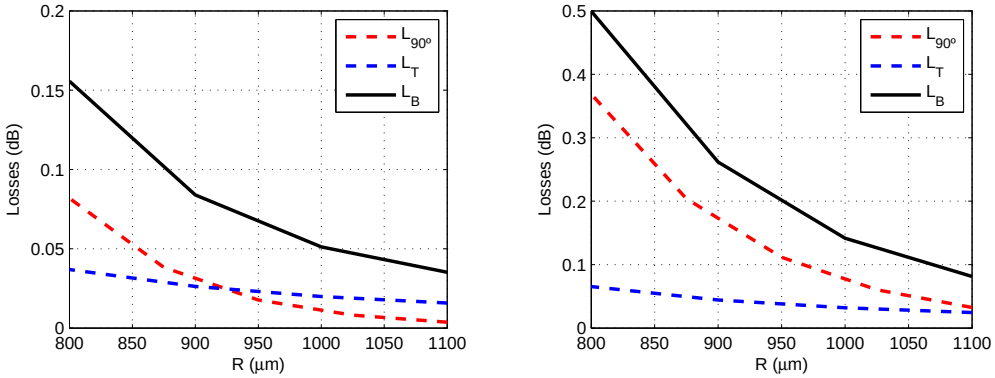

(a) $W = 1.3\,\mu m$ **(b)** $W = 1.2\,\mu m$

Figure 4.10.: Total bending losses as a function of curvature radius for $H = 1.5\,\mu m$, $D = 0.6\,\mu m$.

- For the same total curvature loss specification rectangular waveguide support smaller curvature radii than their trapezoidal counterparts.
- The minimum bending radius is very sensitive to etch depth, increasing in a factor of about 1.5 per 0.1 µm decrement in etch depth. Hence, the curvature radius has to be designed for the shallowest expected etch depth.
- As a consequence of the etch depth sensitivity, choosing a shallow etch depth, that ensures single-mode behaviour in the full tolerance range, results in large curvature radii.

4.5. Waveguide design for $H = 1.5\,\mu m$

Since rectangular waveguides offer smaller curvature radii than trapezoidal waveguides, the former are chosen for the design of the sixport. Furthermore, a substrate height of $H = 1.5\,\mu m$ is adopted to allow for smaller curvature radii. The expected fabrication tolerances in the reactive ion etching process are $\Delta D = \pm 0.1\,\mu m$ and $\Delta W = \pm 0.1\,\mu m$.

For the substrate height of $H = 1.5\,\mu m$, the maximum allowed etch depth and width for single-mode operation are $D = 0.75\,\mu m$ and $W = 1.32\,\mu m$ according to (4.2) and (4.3). The nominal width is set to $W_{nom} = 1.3\,\mu m$. To achieve a reasonably small curvature radius, we choose the nominal etch depth as $D_{nom} = 0.7\,\mu m$, even though this means that strict single-mode operation will not be ensured in the complete tolerance range. This is because for the maximum expected etch depth $D_{max} = 0.7\,\mu m + |\Delta D| = 0.8\,\mu m$ the single mode condition (4.3) is violated; we will analyse this in more detail below. On the other hand, the bending radius has to be designed for the minimum etch depth $D_{min} = 0.7\,\mu m - |\Delta D| = 0.6\,\mu m$. The total curvature losses (L_B) for this etch depth are shown in figure 4.10. A nominal radius of $R_{nom} = 900\,\mu m$ is a reasonable choice, since it yields total losses below 0.1 dB for a waveguide width of $W = 1.3\,\mu m$

SPICUM servicio de publicaciones

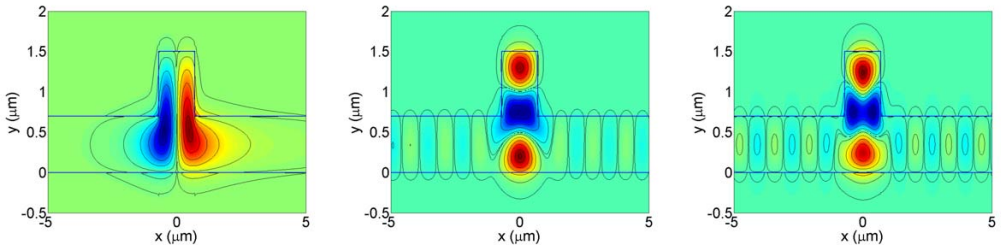

(a) TM_{21}: $L_{90°} = 0.11\,dB$ **(b)** $TE_{1,3}$: $L_{90°} = 39\,dB$ **(c)** $TM_{1,3}$: $L_{90°} = 44\,dB$

Figure 4.11.: Higher order modes for $H = 1.5\,\mu m$, $D = 0.8\,\mu m$, $W = 1.4\,\mu m$, $R = 900\,\mu m$.

[figure 4.10(a)], which increase to about 0.25 dB in the worst case of a 1.2 µm wide waveguide [figure 4.10(b)]

Since we have chosen nominal dimensions that do not ensure single-mode behaviour for all possible combinations of fabrication tolerances, we need to examine the behaviour of higher order modes in the worst case, that is $D = D_{max} = 0.8\,\mu m$ and $W = W_{max} = 1.3\,\mu m + |\Delta W| = 1.4\,\mu m$. The higher order modes supported by a waveguide with these dimensions are shown in figure 4.11 for a curvature radius of $R_{nom} = 900\,\mu m$. The mode fields in the straight waveguide do not differ appreciable from those of figure 4.11. The $TE_{1,3}$ and $TM_{1,3}$ in figures 4.11(b) and (c) exhibit strong leakage into both sides of the slab waveguide and exhibit around 40dB of propagation losses per 90° turn. This means that even if they were excited, they would be strongly attenuated and would not interfere in the practical operation of the waveguide. The $TM_{2,1}$ mode shown if figure 4.11(a) is more critically since it is not leaky in a straight waveguide and exhibits only reduced curvature losses of 0.1 dB per 90°. Consequently, in a worst case scenario this mode could potentially propagate with low losses. However, if the waveguide width is nominal ($W_{nom} = 1.3\,\mu m$) the $TM_{2,1}$ suffers an attenuation of $L_{90°} = 15\,dB$ per 90° turn, even if the etch depth is maximum ($D_{max} = 0.8\,\mu m$). In fact, in the practical measurements described in section 8.4 no higher order mode effects were observed.

4.6. Waveguide coupling

Two parallel waveguides support a pair of even and odd supermodes, as shown in figure 4.12 for a rib waveguide. When light is launched in only one of the waveguides, both supermodes are excited. Since these modes have slightly different propagation constants, their relative phase changes as they propagate, and energy is transferred between the two waveguides, i.e., directional coupling occurs. Generally, the interconnecting waveguides in a integrated optical circuit have to be decoupled, i.e., power transfer between them should be negligible. Specifically, for two parallel waveguides this means that:

1. They have to maintain a high extinction ratio: if is light is launched in only one of the waveguides, the amount of light that couples into the other waveguide

SPICUM servicio de publicaciones

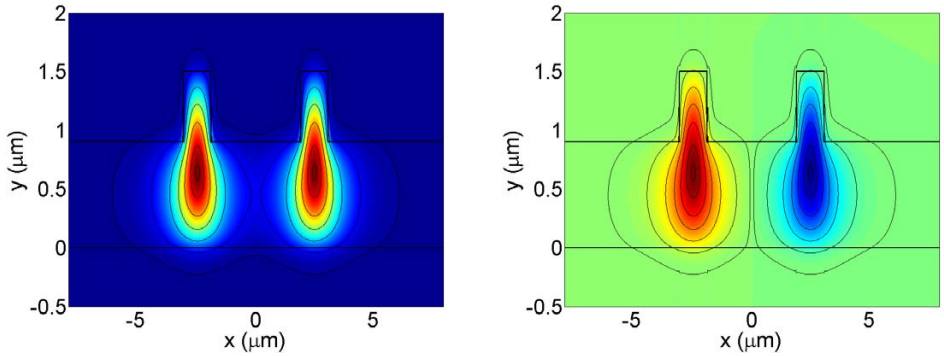

(a) Even TE supermode. **(b)** Odd TE supermode.

Figure 4.12.: Supermodes of two straight parallel waveguides with $H = 1.5\mu m$, $D = 0.6\mu m$, $W = 1.2\mu m$.

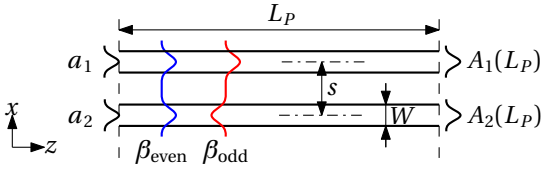

Figure 4.13.: Schematic representation of waveguide coupling calculations.

must be negligible. Let us denote by P_{in} the power launched into one of the waveguides, and by P_C the power coupled into the other waveguide after a certain propagation distance. We may then define the coupling between them as

$$C = P_C / P_{in}. \tag{4.13}$$

2. They must keep the power balance: if an equal amount of light is launched into both waveguides, as will typically be the case at the output of an MMI, the power imbalance due to waveguide coupling must also be negligible. If the same power is launched into two waveguides and after a certain propagation distance the powers in waveguides 1 and 2 are P_1 and P_2, the imbalance due to waveguide coupling is

$$u = P_1 / P_2. \tag{4.14}$$

We can study these two situations assuming that the waveguides are weakly coupled. In this case, and referring to figure 4.13, when two fields of amplitude a_1 and a_2 are launched into each of the waveguides, the field amplitude along each of the waveguides is given by [77, Ch. 2.6.3]:

$$\begin{aligned} A_1(z) &= \exp(j\bar{\beta}z)\left[a_1 \cos\left(\frac{\pi}{2}\frac{z}{L_\pi}\right) + j a_2 \sin\left(\frac{\pi}{2}\frac{z}{L_\pi}\right)\right] \\ A_2(z) &= \exp(j\bar{\beta}z)\left[a_2 \cos\left(\frac{\pi}{2}\frac{z}{L_\pi}\right) + j a_1 \sin\left(\frac{\pi}{2}\frac{z}{L_\pi}\right)\right] \end{aligned}, \tag{4.15}$$

SPICUM servicio de publicaciones

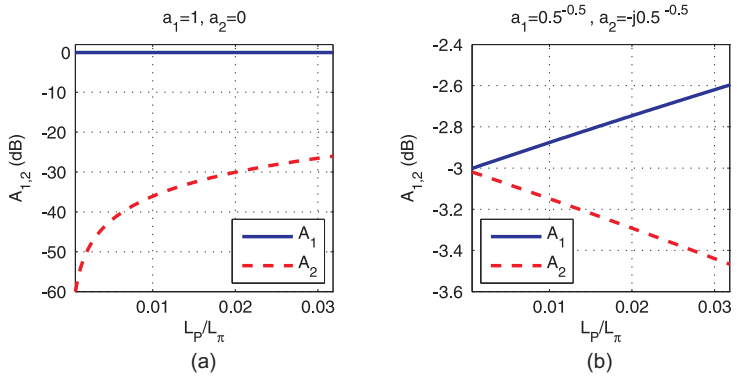

Figure 4.14.: (a) Power coupled from one waveguide to the other. (b) Power exchange between two waveguides with identical initial power.

where $\bar{\beta} = (\beta_{\text{even}} + \beta_{\text{odd}})/2$, $L_\pi = \pi/(\beta_{\text{even}} - \beta_{\text{odd}})$, and β_{even} and β_{odd} are the propagation constants of the even and odd supermodes of the two parallel waveguides. Generally, we denote the length of the two parallel waveguides by L_P, and their centre to centre separation by s.

To analyse situation 1, we set $a_1 = 1$ and $a_2 = 0$ in (4.15), so that $P_{in} = |a_1|^2 = 1$ and $P_C = |A_2(z)|^2$. The evolution of the power in each waveguide is shown in figure 4.14(a), from where it is clear that a coupling lower than −30 dB is maintained for electrical lengths $L_P/L_\pi < 0.03$. To analyse situation 2, where both waveguides carry equal power, we set $a_1 = 1/\sqrt{2}$ and $a_2 = -\mathrm{j}/\sqrt{2}$ in (4.15), because this emulates the 90° phase shift that is present at the output of a 2 × 2 MMI (see section 5.2.6). The power in each waveguide is simply $P_1 = |A_1(z)|^2$ and $P_2 = |A_2(z)|^2$, which is plotted in figure 4.14(b). Note that a rather high imbalance of around 0.6 dB for is obtained for $\bar{\Delta}\beta L_P = 0.03$, even though the same waveguides yielded a low coupling ($C < -30$ dB) in situation 1. Clearly the coupling in situation 2 is more critical than the coupling in situation 1.

From (4.15) it is straightforward to establish a relation between the coupling (C) of situation 1, and the imbalance (u) in situation 2:

$$u = \frac{|A_2|^2}{|A_1|^2} = \frac{1-\sin(\pi L_P/L_\pi)}{1+\sin(\pi L_P/L_\pi)} \approx \frac{1-2\sqrt{C}}{1+2\sqrt{C}} \approx 1-4\sqrt{C}, \tag{4.16}$$

the approximation holding for $\sqrt{C} \ll 1$. This means that to achieve an imbalance better than 0.1 dB one has to design the waveguide so that the extinction ratio is better than $C = (1-u)^2/16$, which yields −45 dB.

To design two uncoupled interconnecting waveguides, we simply have to choose a centre to centre separation (s_I) between them that ensures $C < -45$ dB over a propagation distance L_P larger than the lengths we expect in our final circuit. Coupling increases appreciable as etch depth is reduced, so the design has to be carried out for the shallowest expected etch depth, which is $D = 0.6\,\mu$m in our case. We used full vectorial 3D simulations of the supermodes in Fimmwave to determine the necessary separation, and found that $s_I = 10\,\mu$m is sufficient to produce negligible coupling ($C = -47$ dB) over a length $L_P = 3$ cm.

SPICUM servicio de publicaciones

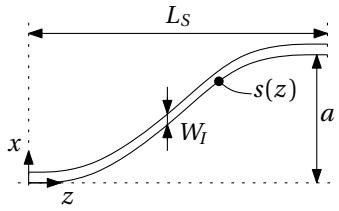

Figure 4.15.: Schematic top view of a s-bend.

4.7. Design of the S-bends

S-bends are required in several parts of the circuit to separate waveguides, mainly at the input and the output of the MMIs, to avoid coupling between them, and at the chip facets, to allow easy access with butt-coupled fibres, detectors, etc. We shall consider the s-bends to have to same width (W) and etch depth (D) as the interconnecting waveguides, because they are used only with these waveguides.

A top view of a s-bend is schematically shown in Fig. 4.15, with its shape given by the function $s(z)$ defined as:

$$s(z) = \frac{a}{2}\left(1 - \cos\frac{\pi}{L_S}z\right), \tag{4.17}$$

where a is the amplitude and L_S the length in the propagation direction. This cosenoidal shape provides a smooth transition, which is why it is commonly used in in integrated optics.

Given the desired offset, a, designing the s-bend reduces to determining the necessary length, L_S, which provides a sufficiently slow transition to keep losses below a certain desired level. For small amplitudes of a few micrometers, L_S may be determined by simulation. But for large amplitudes (several tens of microns), which are required for the output waveguides, simulations grow increasingly challenging, because the required windows size in the lateral (x) direction becomes very large compared to the size of the waveguide, so that very high spatial resolutions are required.

However, some simplifications can be made to facilitate the design of the s-bend length, L_S. In the first place, we may neglect transition losses between the straight waveguide and the sbend. This is because the shape of the s-bend is cosenoidal, which provides a smooth transition to the waveguide, i.e. there is no discontinuity in the waveguide shape and its first derivative. Second, since the s-bend is single-moded its losses may be seen as the product of the radiation losses of its fundamental mode per unit length and its total length. Hence, the sbend will exhibit less losses than a 90° waveguide bend, if we ensure that:

1. The *local* curvature radius of the s-bend is never smaller than the minimum curvature radius of a waveguide bend, and

2. The s-bend is shorter than a 90° curve.

SPICUM servicio de publicaciones

The local curvature radius $R(z)$ of a certain function $s(z)$ is given by

$$\frac{1}{R(z)} = \frac{\frac{\mathrm{d}^2 s}{\mathrm{d}z^2}}{\left[1+\left(\frac{\mathrm{d}s}{\mathrm{d}z}\right)^2\right]^{3/2}}. \tag{4.18}$$

Inserting (4.17) into (4.18) it is straightforward to show that the minimum local curvature radius of an s-bend is

$$R_{\min} = \frac{2}{a}\frac{L_S^2}{\pi^2},$$

which gives the desired criterion:

$$\boxed{L_S \geq \frac{\pi}{\sqrt{2}}\sqrt{R_{\min} a} \approx 2.22\sqrt{R_{\min} a}.} \tag{4.19}$$

The path length of the s-bend is given by an elliptic integral of the second kind,[2] but for our design a simple approximation is sufficient: by inspection of Fig. 4.15 it is clear that the s-bend is always shorter than $L_S + a$. Taking into account (4.19), the second condition may then be may be expressed as

$$\frac{\pi}{\sqrt{2}}\sqrt{R_{\min} a} + a \leq \frac{\pi}{2} R_{\min},$$

which yields the following bound for the amplitude:

$$a \leq 0.318 R_{\min}. \tag{4.20}$$

Note that this is not a strong restriction since normally $a \ll R_{\min}$.

4.8. Conclusions

In this chapter we have compared the fabrication tolerances of rectangular and trapezoidal waveguides, and have found that etch depth variations have a stronger impact on trapezoidal waveguides than on rectangular waveguides, so that the latter are chosen for the design of the sixport. The design of the waveguide dimensions that achieve a low curvature radius while maintaining single mode behaviour in the expected range of fabrication variations was then described. We have highlighted that waveguide coupling is particularly critical when both waveguides carry the same amount of power, which is often the case at the output of an MMI. Finally a design formula for the length of s-bends has been given.

[2] $L_{\text{path}} = \int_0^{L_S} \sqrt{1+\left(\frac{\mathrm{d}s(z)}{\mathrm{d}z}\right)^2}\mathrm{d}z = \frac{2L_S}{\pi}\int_0^{\pi/2}\sqrt{1+\left(\frac{a\pi}{2L_S}\right)^2\sin^2 u}\,\mathrm{d}u = \{(4.19)\} = \sqrt{2R_{\min}a}\,E\left[\frac{\pi}{2}; \frac{-a}{2R_{\min}}\right]$

SPICUM servicio de publicaciones

The engineer's first problem in any design situation is to discover what the problem really is.

Unknown

5

Multimode interference coupler design

MULTIMODE interference couplers in a 2×2 and 2×3 configuration are the key components of the optical sixport junction, providing both the splitting and routing of the optical signals, as well as the required phase relations between them. In this chapter we provide an in depth analysis of multi-mode interference couplers (MMIs) and propose a complete methodology for their design on rib type waveguides. Beyond their application in the six-port, MMIs are also fundamental to many other integrated optical devices; in fact the design methodology developed here has also proven useful for the development of a coherent optical receiver [3].

We start with a short historical review and some applications of MMIs in section 5.1, and then review the operation principle of these devices, with special emphasis on the assumptions made therein (section 5.2). After briefly defining the main performance parameters of MMIs (section 5.3), a succinct review of the state of the art in MMI design is given in section 5.4, and the design problem is defined (section 5.5). The particularities of imaging in rib waveguides are examined in section 5.6, yielding a simple design formula for the width of the MMI access waveguides that enables high performance operation. A design procedure for the complete device is then developed in section 5.7, and applied to 2×2 MMIs. An exhaustive fabrication tolerance analysis ensures the fabricability of these devices (section 5.8), so that we proceed with the design of the 2×3 MMI in section 5.9. The main results of this chapter are summarised in section 5.10.

5.1. Introduction

The self-imaging effect, which underlies the operation of MMIs, was discovered by Henry Talbot, who reported on it in the "London and Edinburgh Philosophical Magazine and Journal of Science" in December 1836 [78]. Figure 5.1(a) schematically shows his experiment, which he described as follows:

> *"In order to see these appearances in their perfection, it is requisite to have a dark chamber and a radiant point of intense solar light, which, for the sake of convenience, should be reflected horizontally by a mirror. I will relate a few, out of several experiments which were made in this manner.*

SPICUM servicio de publicaciones

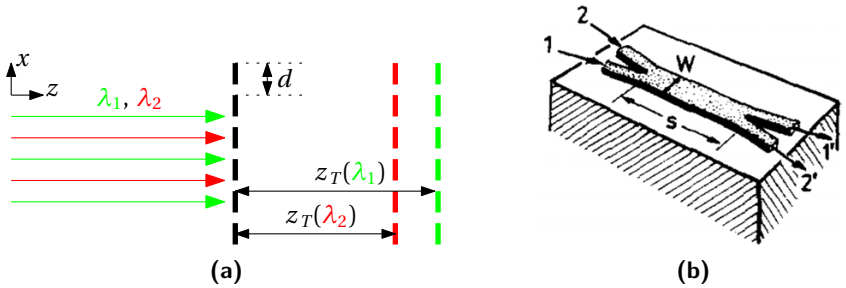

Figure 5.1.: From (a) Talbot's experiment in 1836 to (b) the conception of MMIs in 1973 [79].

> *1. About ten or twenty feet from the radiant point, I placed in the path of the ray an equidistant grating[a] made by Fraunhofer, with its lines vertical. I then viewed the light which had passed through this grating with a lens of considerable magnifying power. The appearance was very curious, being a regular alternation of numerous lines or bands of red and green colour, having their direction parallel to the lines of the grating. On removing the lens a little further from the grating, the bands gradually changed their colours, and became alternately blue and yellow. [...]*
>
> *It was very curious to observe that though the grating was greatly out of the focus of the lens, yet the appearance of the bands was perfectly distinct and well defined. [...]*
>
> *2. Another grating was then placed at right angles to the first, and light transmitted trough both was examined by the lens. The appearance now resembled a tissue woven with red and green threads."*

[a] *A plate of glass, covered with gold-leaf, on which several hundred parallel lines are cut, in order to transmit the light at equal intervals.*

It was only in 1880 that Lord Rayleigh gave a first mathematical description of the self-imaging effect in [80], where he deduced that images or replicas of the grating formed periodically at distances

$$z = \frac{\lambda}{1 - \sqrt{1 - (\lambda/d)^2}}, \tag{5.1}$$

with λ being the wavelength and d the period of the grating. Since $\lambda \ll d$, the Taylor expansion $\sqrt{1-x^2} \approx 1 - x^2/2$ may be used, yielding

$$z_T = 2d^2/\lambda, \tag{5.2}$$

which is commonly known as the Talbot distance. The wavelength dependence of z_T explains Talbot's observation of the changing colours of the bands, as the wavelength which is imaged varies as the lens is moved.

In 1973, Bryngdahl published a paper, [81], in which he suggested, for the first time, the possibility of "image formation with a single *light pipe*," that is, a multimode waveguide. The length of this waveguide would be given by equation (5.2), with d being

SPICUM servicio de publicaciones

the side of its square cross-section. Such "light pipe" based imaging was experimentally demonstrated two years later by Ulrich and Ankele [79], who obtained not only a double image of an excitation launched into a multimode waveguide, constituted by a liquid and two plates of glass, but also suggested its use in integrated optics for the first time. Figure 5.1(b) shows the device as proposed by the authors, which we would call today a 2×2 MMI (two input and two output waveguides). In this configuration the light enters the wide, multimode waveguide through one of the input waveguides, and a double image is formed at the output plane. Each of these images then couples into one of the output waveguides, so that the optical input power is split equally between them. Among the first experimental demonstrations of integrated MMIs we may cite [82] and [83], which were published in 1991 and 1992, respectively.

Due to their good performance and ease of fabrication MMIs have, since then, become key components in many integrated optical devices, such Mach-Zehnder interferometers (MZI) [84, 85], switches [86] and as ring resonators [66], to cite a few. They are also driving the first coherent optical receivers for high speed (100Gbits/s per channel) optical communication based on QPSK (Quadrature Phase Shift Keying) [3, 67, 87], and possibly OFDM (Orthogonal Frequency Division Multiplexing) in the near future [88].

5.2. The self-imaging principle

The self-imaging principle which, in the context of integrated optics, was described completely for the first time by Bachmann in 1994 [89], explains the formation of images in multi-mode waveguides as well as their position and phase. In the following we shall study this theory in detail, following mainly [89, 90]. Special attention will be paid to the assumptions it is based on, since it is from the fulfilment of these that the different strategies for improved MMI designs arise.

Let us consider the 2×2 coupler shown in figure 5.2. It is composed of two input and two output waveguides with a certain cross section in the xy plane —a rib in this case— and a portion of a wider waveguide, which constitutes the multi-mode section. The width of the input and output waveguides is W_A and the multi-mode section is W_{MMI} wide and L_{MMI} long. The refractive indexes of the cladding, the guiding region and the substrate are respectively given by n_c, n_g and n_s, with $n_g > n_c, n_s$.

If light is launched from either from waveguide 1 or 2, a twofold image is produced at the end of the multimode section which then couples into waveguides 3 and 4. Depending on the length of the device not only two, but generally Q images can be obtained. The Self Imaging Theory predicts the position and the phase of these Q-fold images by expanding the input field in the eigenmodes of the multi-mode section. These are then propagated with their respective propagation constants and superposed to study the formation of images. The starting point for the derivation is a two dimensional device model, which will be defined in section 5.2.1. The approximate eigenmodes of this two dimensional structure are calculated in section 5.2.2 and their propagation along the multimode section is analysed in section 5.2.3. A new approach to the calculation of the self-images is presented in section 5.2.4. Two special types of imaging are discussed in section 5.2.5, and as an application example of the

SPICUM servicio de publicaciones

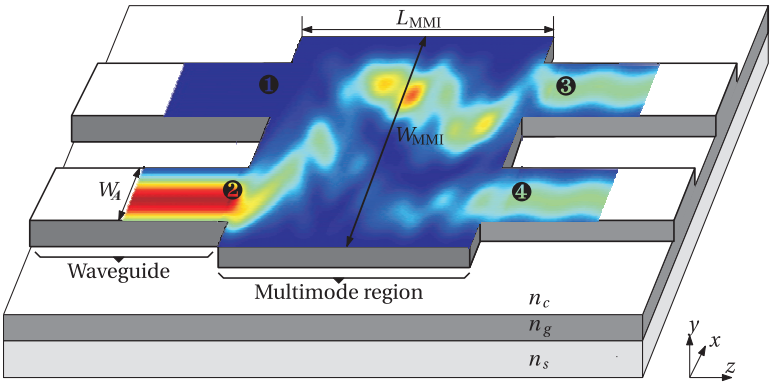

Figure 5.2.: Schematic view of a 2×2 MMI.

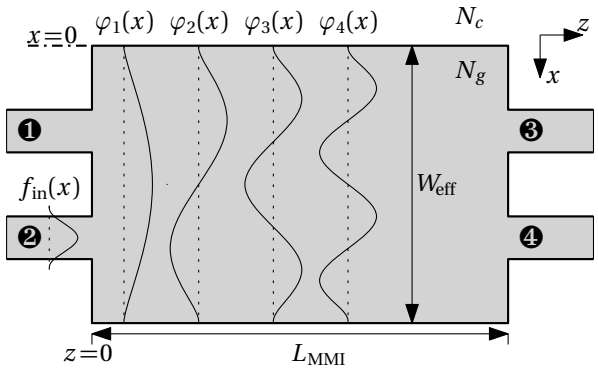

Figure 5.3.: Two dimensional model of a MMI.

theory, a 2×2 MMI and a 2×3 MMI are analysed in section 5.2.6.

Imaging properties are generally slightly different for TE and TM polarisations. In the following the two polarisations will be treated separately.

5.2.1. Two dimensional device model

While the eigenmode approach can obviously be applied to three dimensional structures, Self Imaging Theory is based upon a two dimensional model of the device.[1] This constitutes the first assumption of the theory.

Assumption 1: The three dimensional device shown in figure 5.2 is converted into a two dimensional structure as shown in figure 5.3.

This two dimensional model is obtained by applying the effective index method in the vertical (y) direction, so that the refractive index of the guiding region is substituted by the *effective* index N_g and the refractive indexes of the cladding and the substrate are condensed into N_c. Please note that N_g and N_c are different for TE and TM polarisation.[2]

[1] Self-Imaging in three dimensions has been investigated (see for example [91]), but is essentially an extension of the theory presented here.

[2] A description of the effective index method can be found, for example, in [92, pp. 60-64]

SPICUM servicio de publicaciones

5.2.2. Eigenmodes of the multimode section

One of the key points of the Imaging Theory is to approximate the $\varphi_m(x)$ modes of the multimode section by sine functions (see figure 5.3):

$$\varphi_m(x) = \sin\left(\frac{m\pi}{W_{\text{eff},m}}x\right), \quad m = 1,2,3,\ldots \tag{5.3}$$

While the actual modes do generally have a sine-like shape, their effective width, W_{eff}, depends on the mode number m. However, the Imaging Theory assumes that

Assumption 2: The effective width of the multimode section (W_{eff}) is independent of the mode number.

The concept of effective width may be understood as follows. Since the effective lateral index contrast, $N_g - N_c$, is finite, the modes of the waveguide and the multimode section will have evanescent tails outside the guiding region, so that they "see" an effective waveguide that is wider than the physical one.[3] Higher order modes have wider tails and thus their effective width is larger, too. Usually W_{eff} is estimated as the effective width of the fundamental mode which is approximately given by $W_{\text{eff}} \approx W_{\text{MMI}} + (\lambda/\pi)\left(N_c/N_g\right)^{2\sigma}(N_g^2 - N_c^2)^{-1/2}$, where $\sigma = 0$ for TE and $\sigma = 1$ for TM polarisation [90].

We will now calculate the propagation constants β_m of the modes of the multimode section. Since the modes are assumed to be given by (5.3), and are thus completely confined in the guiding region, we have

$$k_{x,m}\hat{\mathbf{x}} + \beta_m\hat{\mathbf{z}} = k_0 N_g\hat{\mathbf{k}}, \tag{5.4}$$

where $k_{x,m} = \pi m/W_{\text{eff}}$, $k_0 = 2\pi/\lambda$ and $\hat{\mathbf{k}}$ is the direction of the wave vector. Hence, the dispersion relation is given by $\beta_m^2 + k_{x,m}^2 = k_0^2 N_g^2$, and the β_m propagation constants are:

$$\beta_m = k_0 N_g\sqrt{1 - \left(\frac{k_{x,m}}{k_0 N_g}\right)^2}. \tag{5.5}$$

Please notice that the propagation angle θ_m of the ray that represents the m-th mode is

$$\cos\theta_m = \beta_m/(k_0 N_g). \tag{5.6}$$

It is now assumed that:

Assumption 3: Only the paraxial modes of the multi-mode section, i.e., those with small propagation angles, or equivalently, those which fulfil $k_{x,m} \ll k_0 N_g$, are relevant.[4]

This allows us to use a Taylor expansion to find a simple expression for β_m from (5.5), and after some algebra the following relation between the propagation constants is arrived at:

$$\beta_m = \beta_1 - (m^2 - 1)\frac{\pi}{3L_\pi}, \tag{5.7}$$

[3] This is also known as the Goos-Hänchen shift.

[4] Please notice that this is equivalent to $\lambda/N_g \ll 2W_{\text{eff}}/m$, which, in turn, is similar to the condition which allows for the deduction of the Talbot distance (5.2).

SPICUM servicio de publicaciones

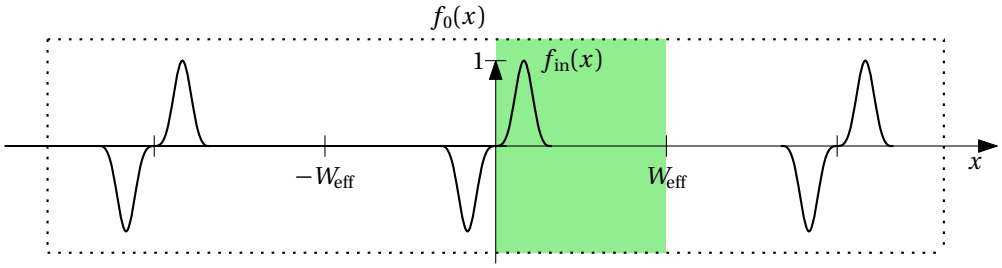

Figure 5.4.: Periodic extension of the input field.

where L_π is the half beat length of the two lowest order modes,

$$L_\pi \stackrel{\text{def}}{=} \frac{\pi}{\beta_1 - \beta_2} \approx \frac{4 N_g W_{\text{eff}}^2}{3\lambda}. \tag{5.8}$$

From this equation an important property of MMIs becomes apparent: their length is directly proportional to the square of their width. That means that devices with many input/output ports will be necessarily very long.

5.2.3. Field propagation along the multi-mode section

We will now expand the input field, $f_{\text{in}}(x)$, in the $\varphi_m(x)$ eigenmodes of the multimode section. Since the φ_m modes are sine functions with fundamental period $2W_{\text{eff}}$, it is mathematically convenient to define a periodically extended input field with the same period, and the same odd symmetry as the sine functions:

$$f_0(x) = \sum_{k=-\infty}^{+\infty} f_{\text{in}}(x - k2W_{\text{eff}}) - f_{\text{in}}(-x + k2W_{\text{eff}}). \tag{5.9}$$

Figure 5.4 illustrates how $f_0(x)$ is constructed from $f_{\text{in}}(x)$.

The electromagnetic field at the discontinuity between the input waveguide and the multi-mode section at $z = 0$ (see figure 5.3) has to be continuous. If the input field is well confined in the access waveguide, it does not "see" any refractive index change at this facet, so that reflections are generally negligible. This means that $f_0(x)$ must be completely expanded into the guided and radiated modes of the multi-mode section:

$$f_0(x) = \sum_{m=1}^{\infty} c_m \varphi_m(x),$$

where the summation symbolically includes radiative modes. The Fourier coefficients c_m are given by the well known overlap integral:

$$c_m = \langle f_0(x), \varphi_m(x) \rangle = \frac{2}{W_{\text{eff}}} \int_0^{W_{\text{eff}}} f_0(x) \varphi_m(x) \mathrm{d}x. \tag{5.10}$$

At this point a further simplification is made.

Assumption 4: The input field can be faithfully represented by the guided paraxial modes of the multimode section.

SPICUM servicio de publicaciones

This implies that $f_0(x)$ can be written as

$$f_0(x) = \sum_{m=1}^{M} c_m \varphi_m(x), \tag{5.11}$$

with M being the mode number of the highest order guided mode which can be considered paraxial. In other words, when the input field distribution is launched into the multi-mode section it only excites guided paraxial modes.

With the propagation constants of the *paraxial* φ_m modes given by (5.7), the field at an arbitrary z position is then simply given by

$$f(x,z) = \exp(-\mathrm{j}\beta_1 z) \sum_{m=1}^{M} c_m \varphi_m(x) \exp\left(\mathrm{j}(m^2-1)\frac{\pi}{3L_\pi} z\right). \tag{5.12}$$

In order to illustrate image formation let us consider the field $f(x,z)$ at $z = 6L_\pi$. Then the complex exponential in (5.12) becomes unity, so that $f(x,6L_\pi) = \exp(-\mathrm{j}\beta_1 6L_\pi) f(x,0)$, that is, the extended input is replicated or *imaged*. In the following we will show that this phenomenon occurs at other propagation distances, too. Specifically, Q images are formed at $z = 3L_\pi/Q$.

5.2.4. Multiple self-Images: A Fourier series approach

The mathematical derivation of the position and phase of the multiple self images given in [89] is not easy to follow, which is why a more straightforward derivation will be presented here. While giving some interesting insight into the relation between MMI imaging and Fourier series, this section is not essential to the understanding of MMIs, so that a reader who is not interested in the mathematical details may directly proceed to its main result: equation 5.24. Since the new derivation is heavily based on Fourier series properties, it is convenient to introduce a few changes in notation at this point.

We shall denote the extended field at $z_Q = 3L_\pi/Q$ as $f_Q(x)$. Furthermore, we define $T = 2W_{\text{eff}}$, $\omega = 2\pi/T$, and use complex exponentials instead of sine functions in the expansion of the extended input field. Equations (5.11) and (5.10) then read

$$f_0(x) = \sum_{m=-M}^{M} F_0[m] \exp(\mathrm{j}m\omega x) \tag{5.13}$$

$$F_0[m] = \frac{1}{T}\int_T f_0(x) \exp(-\mathrm{j}m\omega x)\mathrm{d}x, \tag{5.14}$$

which are the classical Fourier series expressions. The $F_0[m]$ coefficients are related to the c_m coefficients by: $c_m = (F_0[m] - F_0[-m])/2$.

Dropping the common phase factor $\exp(-\mathrm{j}\beta_1 z)$ from (5.12), the propagation along the multi-mode region may be seen as a change in the Fourier coefficients. Specifically, the spectrum at the imaging distances $z_Q = 3L_\pi/Q$ can be identified as

$$F_Q[m] = F_0[m]\Phi_Q[m], \tag{5.15}$$

with

$$\Phi_Q[m] = \exp\left(\mathrm{j}\frac{\pi}{Q}\left(m^2-1\right)\right). \tag{5.16}$$

SPICUM servicio de publicaciones

It is easy to check that

$$\Phi_Q[m-Q] = \Phi_Q[m](-1)^Q. \tag{5.17}$$

In the space domain, (5.15) becomes

$$f_Q(x) = f_0(x) * \phi_Q(x), \tag{5.18}$$

where $*$ is the convolution operator defined as $g(x) * h(x) = \frac{1}{T}\int_{\langle T\rangle} g(\xi)h(x-\xi)\mathrm{d}\xi$. According to (5.17), for general Q, $\Phi_Q[m]$ is periodic with period $2Q$, which means that $\phi_Q(x)$ is given by

$$\phi_Q(x) = \sum_{k=-\infty}^{+\infty} \phi_Q[k]\delta\left(x - k\frac{T}{2Q}\right), \tag{5.19}$$

$$\phi_Q[k] = \frac{T}{2Q}\sum_{m=\langle 2Q\rangle} \Phi_Q[m]\exp\left(\mathrm{j}k\frac{2\pi}{2Q}m\right). \tag{5.20}$$

A proof of (5.19) and (5.20) can be found in appendix A.1. By inserting (5.19) into (5.18), and using the Delta function property $g(x) * \delta(x-x_0) = \frac{1}{T}g(x-x_0)$, we get:

$$f_Q(x) = f(x, z_Q) = \frac{1}{T}\sum_{k=0}^{2Q-1} \phi_Q[k] f_0\left(x - k\frac{T}{2Q}\right). \tag{5.21}$$

At the imaging distances $z_Q = 3L_\pi/Q$ the field inside the multimode region is a superposition of several replicas of the *extended* input field, whose phases are given by $\phi_Q[k]$. Thus, to complete our analysis, we need to compute $\phi_Q[k]$. By using (5.20) together with (5.17) it is straightforward to show that

$$\phi_Q[k] = \frac{1+(-1)^{Q+k}}{2}\frac{T}{Q}\sum_{m=\langle Q\rangle} \Phi_Q[m]\exp\left(\mathrm{j}mk\pi/Q\right), \tag{5.22}$$

which only is non-zero if Q and k have the same parity, i.e., if they are both odd or both even. In these cases we show in appendix A.2 that $\phi_Q[k]$ can be reduced to:

$$\phi_Q[k] = \frac{T}{\sqrt{Q}}\exp\left(j\frac{\pi}{4} - j\frac{\pi}{Q}\right)\exp\left[-j\frac{\pi}{Q}\left(\frac{k}{2}\right)^2\right], \quad k \text{ and } Q \text{ same parity} \tag{5.23}$$

From (5.21) and (5.23), by recalling that $\phi_Q[k]$ is zero for Q and k of different parity, and by substituting $T = 2W_{\text{eff}}$, the phase and position of the Q-fold images, which are formed at distances $z_Q = 3L_\pi/Q$, is readily derived as

$$f_Q(x) = \frac{\exp(\mathrm{j}\pi/4 - \mathrm{j}\pi/Q)}{\sqrt{Q}}\sum_{l=0}^{Q-1} f_0(x - x_l)\exp(-\mathrm{j}\theta_l), \tag{5.24}$$

where $f_0(x)$ is the *extended* input field defined by (5.9), and x_l and θ_l are given in table 5.1.[5]

[5] Seemingly, from (5.24), all images have equal power $(1/Q)$. However, there are special cases where two overlapping images interfere, yielding nonuniform power splitting [93]. Arbitrary power splitting ratios have also been reported [94, 95], but are out of the scope of this work.

SPICUM servicio de publicaciones

Table 5.1.: Phase and position of the Q-fold images in an MMI.

	θ_l	x_l
Q even	$l^2\pi/Q$	$2lW_{\text{eff}}/Q$
Q odd	$(l-\frac{1}{2})^2\pi/Q$	$2(l-\frac{1}{2})W_{\text{eff}}/Q$

5.2.5. Restricted imaging

Until now we have placed no restrictions on the excitation of the MMI, $f_{\text{in}}(x)$. However, by doing so, we can select which types of modes of the multimode section are excited, and this can result in length reduction of the device. There are two types of restricted imaging: symmetric imaging and paired imaging.

5.2.5.1. Symmetric Imaging

Symmetric imaging takes place when only the even φ_m modes of the multimode section are excited, i.e., $\varphi_m(x) = \varphi_m(-x)$, which holds for all φ_m with m odd. In this case, the factor (m^2-1) in (5.12) is always a multiple of 4, so that the imaging distances z_Q are reduced in a factor 4. In order to excite only even modes, $f_{\text{in}}(x)$ needs be symmetric with respect to the centre of the MMI, which in practice means that a single, centred input waveguide, with a symmetric mode field, has to be employed. Q images, with equal spacing W_{eff}/Q, are then formed at $z_Q = 3L_\pi/(4Q)$.

5.2.5.2. Paired Imaging

If φ_m modes with mode numbers $m = 3,6,9,\ldots$ are *not* excited, the factor (m^2-1) in (5.12) is always a multiple of 3, so that the imaging distances z_Q are reduced in a factor 3. From figure 5.3 we can see that φ_3 is antisymmetric with respect to $x = W_{\text{eff}}(\frac{1}{2}\pm\frac{1}{6})$, a property which also holds for $\varphi_6, \varphi_9, \ldots$. Thus, by placing two input waveguides, with a symmetric mode field, at $x = W_{\text{eff}}(\frac{1}{2}\pm\frac{1}{6})$, the desired excitation can be achieved, and images will form at $z_Q = L_\pi/Q$. Please note that this does not mean that a 2×2 MMI based on paired imaging is always be shorter than a 2×2 MMI based on general imaging, since in the former the mandatory $\frac{1}{3}W_{\text{eff}}$ spacing between the input waveguides increases the coupler's width, which, according to (5.8), increases its length.

5.2.6. Examples: The 2 × 2 and 2 × 3 MMI

Since in this work we will deal with 2×2 and 2×3 MMIs, we shall now briefly review their basic properties.

Starting with the 2×2 MMI, from (5.24), with $Q=2$, we find that

$$f_2(x) = \frac{1}{\sqrt{2}}\left[f_0(x) + \mathrm{j}f_0(x - W_{\text{eff}})\right],$$

which is illustrated in figure 5.5. The periodically extended input field, $f_0(x)$, is shown in figure 5.5(a), while the extended field at the two-fold image distance, $f_2(x)$, is shown

SPICUM servicio de publicaciones

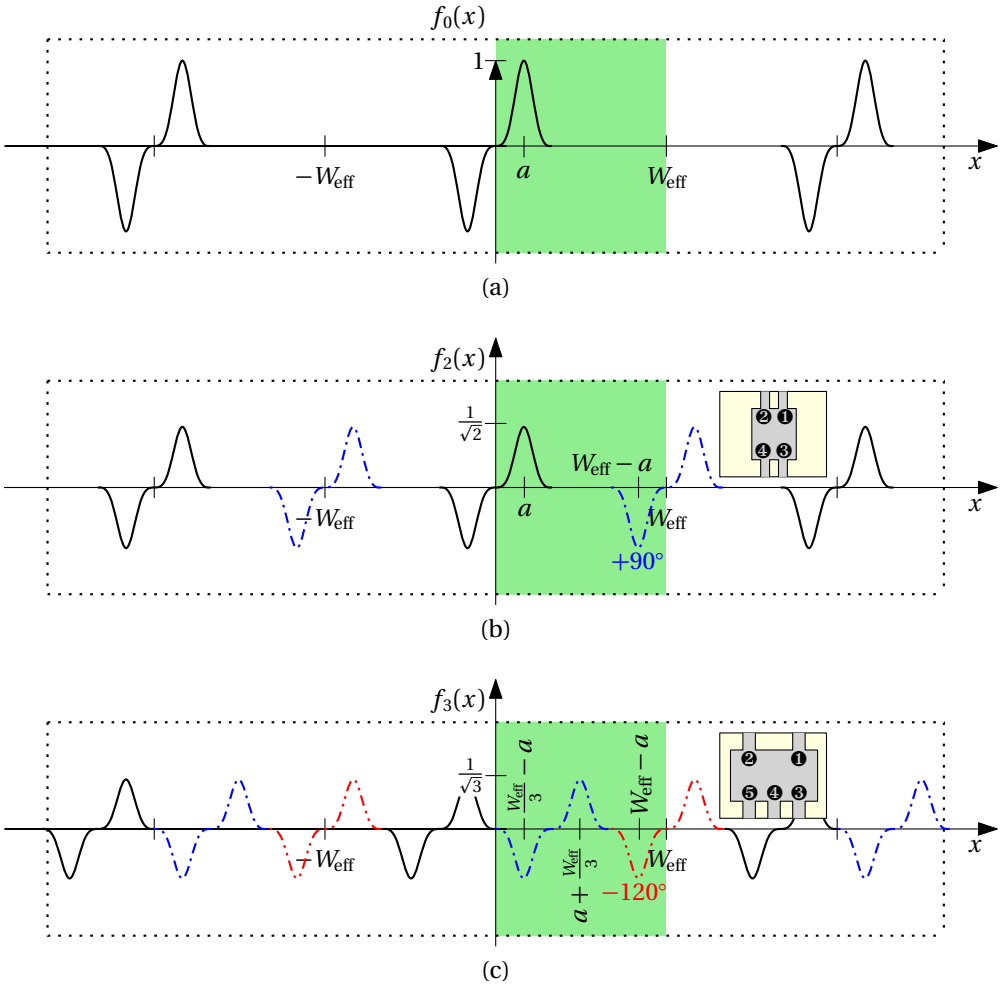

Figure 5.5.: Two-fold and three fold image formation.

in figure 5.5(b); a sketch of the device is displayed in the inset. As expected, two images are formed: one of them at the same position as the original input, and another one whose position is mirrored with respect to the centre of the MMI. The mirrored image is both inverted and 90° phase shifted, so that it is actually a copy of the input, multiplied by −j. Consequently, a 2×2 MMI acts as 90°hybrid: it divides a single input into two 3 dB outputs, with a 90° phase shift between them. From this point of view, one may define S-parameters for this device, which, according to the port numbering shown in the inset of figure 5.5(b), would be

$$S_{11} = S_{22} = 0 \quad S_{31} = S_{42} = \frac{1}{\sqrt{2}} \quad S_{41} = S_{32} = -\frac{\mathrm{j}}{\sqrt{2}} \ .$$

The parameter S_{ij} represents the complex transmission from port j to port i.

The geometry of the 2 × 3 MMI is shown schematically in the inset of figure 5.5(c). From (5.24), with $Q = 3$, we find that the extended field at the three-fold image distance is

SPICUM servicio de publicaciones

$$f_3(x) = \frac{\exp(-\mathrm{j}\frac{1}{6}\pi)}{\sqrt{3}}[f_0(x+W_{\mathrm{eff}}/3) + f_0(x-W_{\mathrm{eff}}/3) + f_0(x-W_{\mathrm{eff}})\exp(-\mathrm{j}\tfrac{2}{3}\pi)].$$

This means that with the input field centred at distance a from the device edge [see figure 5.5(a)], the output images form at the positions shown in figure 5.5(c). It is then clear that for the middle image to appear at the centre of the MMI, we have to choose $a = W_{\mathrm{eff}}/6$. Using the port numbering shown in the inset of figure 5.5(c), the theoretical transmission coefficients of the device are given by:

$$S_{31} = S_{52} = \tfrac{-1}{\sqrt{3}} \quad S_{41} = S_{42} = \tfrac{1}{\sqrt{3}} \quad S_{51} = S_{32} = \tfrac{1}{\sqrt{3}}\exp(\mathrm{j}\pi/3).$$

The relative phases with which the two inputs interfere at each output are then

$$\angle\frac{S_{31}}{S_{32}} = \frac{2\pi}{3} = 120° \quad \angle\frac{S_{41}}{S_{42}} = 0 \quad \angle\frac{S_{51}}{S_{52}} = \frac{2\pi}{3} = -120°,$$

which will yields the desired 120° phase shifts between the six-port centres (see section 2.4).

5.3. MMI performance metrics

We have so far considered the general theory that governs the operation of MMIs, and have also analysed the ideal 2×2 and 2×3 MMI. In order to be able to compare actual designs, we will now present the parameters that are generally used to assess the performance of MMI devices, namely, excess loss, imbalance and phase error. We will define these parameters in terms of the S_{ij} parameters, that express the complex transmission coefficients from the fundamental mode of port j to the fundamental mode of port i. Referring to the port numbering shown in figure 5.5, for both the 2×2 and the 2×3 MMI the input port numbers are $j = \{1,2\}$, whereas the outputs are $i = \{3,4\}$ for the 2×2 and $i = \{3,4,5\}$ for the 2×3. The performance metrics are then defined as follows:

Excess loss: For each input, j, the excess loss is the amount of power relative to the input power, that is not transferred to any output:

$$\mathrm{EL}_j[\mathrm{dB}] = -10\log_{10}\left(\sum_i |S_{ij}|^2\right) \tag{5.25}$$

Imbalance: Imbalance is the power difference between two outputs i and k (for each input j):

$$\mathrm{IB}_j[\mathrm{dB}] = 10\log_{10}(|S_{ij}|^2/|S_{kj}|^2) \tag{5.26}$$

Phase error: This parameters accounts for the deviation from the ideal phase with which the waves coming from the two inputs combine at each output:

$$\mathrm{PE}_i = \angle\frac{S_{i1}}{S_{i2}} - \theta_i \tag{5.27}$$

where θ_i is the ideal relative phase, e.g., in the 2×2 MMI $\theta_3 = 90°$.

SPICUM servicio de publicaciones

5.4. State of the art MMI design

In this section we will briefly review the state of the art in MMI design, that is, we will focus our attention on design techniques rather than specific experimental results, some of which can be found in section 8.5. Fabricability of the devices will, however, be a fundamental factor in our analysis.

One approach to the design of MMIs is using a strong lateral confinement to make the modes of the multimode section as sine-like as possible [96–98]. In silicon-on-insulator waveguides such a high contrast is readily achieved by completely etching the multi-mode region. However, for the thick SOI situation on which we are focusing, a second, shallow etch step is still required for the single-mode interconnecting waveguides. Furthermore, as we will discuss in section 5.6.3, widening of the MMI access waveguides, which does not require special fabrication steps, produces the same effect as increasing the etch depth. Simulated excess losses below 0.1 dB and imbalance of 0.03 dB are reported for a 1×4 splitter in [98].

As highlighted in section 5.2.2, the quadratic relationship between the propagation constants of the modes of the multimode region is crucial to the formation of images. Depending on the lateral index contrast, this relationship is fulfilled to a certain degree, and sizeable phase errors can be incurred, resulting in poor image quality and performance degradation. In [99] an exhaustive analysis of the origin of these phase errors is presented, and the etch depth is adjusted to minimise them. In [100] a graded index profile is employed to reduce the phase errors, and in [101] the refractive index in the complete MMI region is optimised. While application especially of the latter technique achieves drastic performance improvements in Silicon-wire technology [102], we will find in section 5.6 that phase errors are not the most critical issue when using larger rib waveguides.

Widening of MMI access waveguides has been shown to improve MMI performance and tolerances [103, 104]. The studies carried out in the literature so far report 0.1 dB of excess loss and imbalance. However, they are simulation based and do neither offer physical insight into why such a widening produces the aforementioned improvements nor provide a design procedure. Since widening of the access waveguides requires no additional fabrication steps, this is the option that will be further investigated in the next sections.

Furthermore, several techniques to reduce the length of MMIs have been proposed [105–107]. The most classical consist of using a parabolic tapering of the multimode section, which reduces the average width of the device, and thus, by virtue of equation (5.8), its length. While this technique can produce devices which are only half as long as their non-tapered counterparts, it also introduces higher excess losses (~ 1 dB) and imbalance, as well as decreased fabrication tolerances [107]. Careful design of the multimode region tapering is required to achieve lower losses, but also results in less attractive length reductions [106]. Other techniques include the definition of slots in the multimode region, which exhibit a slightly different refractive index [108]. While this readily halves the length of this devices, and does not produce higher excess loss if the refractive index value is chosen properly, it does present difficulties in its practical implementation. Defining waveguide holograms to adjust to length of MMIs is another option that has been recently proposed in [109].

SPICUM servicio de publicaciones

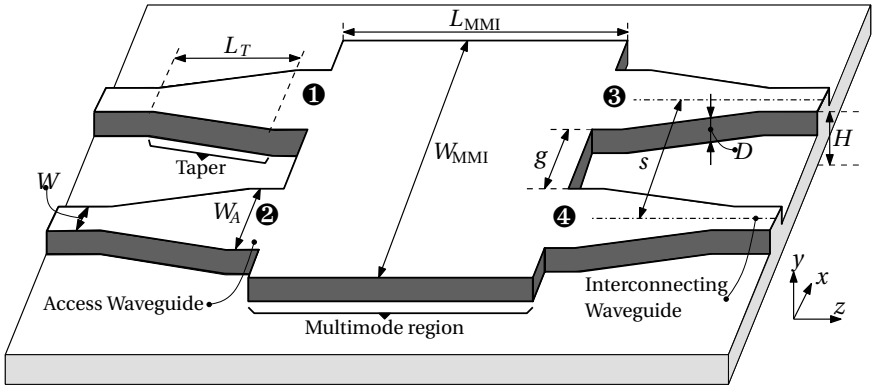

Figure 5.6.: Geometry of the proposed MMI design.

Finally, it is noteworthy that "extraneous" self images, not predicted by the conventional, have been found in low contrast waveguides [110], and that MMIs in both metallic as well as periodic waveguides are being investigated [111, 112].

5.5. Problem definition

Our goal is to design high performance MMIs on thick Silicon-on-Insulator that can be connected to singlemode rib waveguides. Since we are interested in reducing fabrication costs, the device has to be kept as simple as possible. That means that etch depth variations need to be avoided, and only the lateral dimensions of the elements can be freely adjusted. Thus, from the various options to improve device performance presented in section 5.4, we choose to widen the access waveguides, which does not require any additional fabrication steps. This yields a device geometry as shown in figure 5.6. Our objective is then threefold:

1. So far, other authors have determined the optimum width of the access waveguides by simulation, and little physical insight on how this widening improves device performance is available. In section 5.6 we shall not only provide a better understanding of the underlying phenomena, but also give a simple expression for the required access waveguide width.

2. A complete design procedure, that allows for the determination of all the design variables shown in figure 5.6, will be derived in section 5.7. It has to be highlighted that even though we will focus on 2×2 couplers, this procedure is easily extended to more general configurations.

3. Since the designed devices shall ultimately be fabricated, it is important to know their sensitivity to fabrication tolerances, which will be analysed in section 5.8.

Nevertheless, we shall first give a closer description of all the design variables and device specifications.

The device geometry that we shall consider is shown in figure 5.6. The design of the single-mode interconnecting waveguides detailed in section 4.5 fixes the width

SPICUM servicio de publicaciones

Table 5.2.: Effective indexes at $\lambda = 1.55\,\mu m$ for $H = 1.5\,\mu m$, $D = 0.7\,\mu m$.

	N_g	N_c	$N_g - N_c$
TE	3.4444	3.3567	0.088
TM	3.4375	3.2981	0.139

of the interconnecting waveguides to $W = 1.3\,\mu m$, and sets the overall etch depth and substrate height to $D = 0.7\,\mu m$ and $H = 1.5\,\mu m$, respectively. The access waveguides are widened to a width W_A by means of an adiabatic transition of length L_T. The centre to centre separation between the input/output waveguides is s, so that the minimum gap, g, is given by $g = s - W_A$.

From the analysis of the state of the art (section 5.4), simulated excess loss and imbalance are targeted to be as low as 0.1 dB and 0.05 dB, respectively. Due to micro-loading effects the minimum fabricable separation between adjacent waveguides is limited to $1\,\mu m$ (section 3.2). Furthermore, the device should support dimension variations due to fabrication tolerances of $\pm 100\,nm$ in width and length, and $\pm 100\,nm$ in etch depth (see section 3.4).

As a reference, the effective indexes of the cladding and the guiding region for a rib waveguide with the above dimensions are given in table 5.2.

5.6. Imaging in rib waveguides

In this section we shall derive a simple design criterion for the access waveguide width, W_A, that enables high quality image formation in rib waveguide based MMIs. To do so, we need to examine under which conditions single-mode rib waveguides can comply with the assumptions made by the self-imaging theory (section 5.2). Figure 5.7 outlines the analysis that will be carried out in this section.

Assumptions 1 (2D approximation) and 4 (decomposition of the input field in guided, paraxial modes only), will be studied in sections 5.6.1 and 5.6.2, respectively. Our goal is to *express in numbers* to which extent the two assumptions are fulfilled. In doing so, we will show that device losses depend on the degree of symmetry and the width of the input mode field. Furthermore, it will become apparent why wider input waveguides reduce device losses, and ultimately we will be able to give a simple expression for the necessary input waveguide width, W_A.

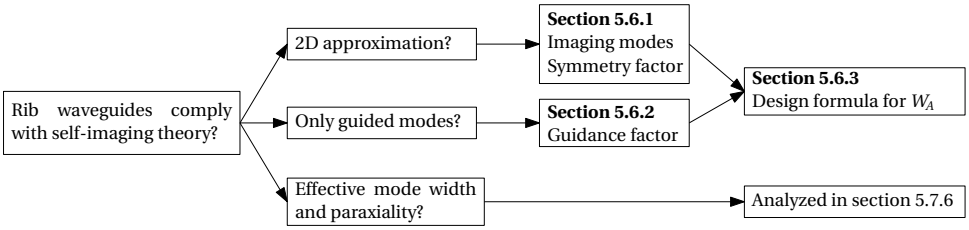

Figure 5.7.: Analysis of self-imaging in rib waveguides.

SPICUM servicio de publicaciones

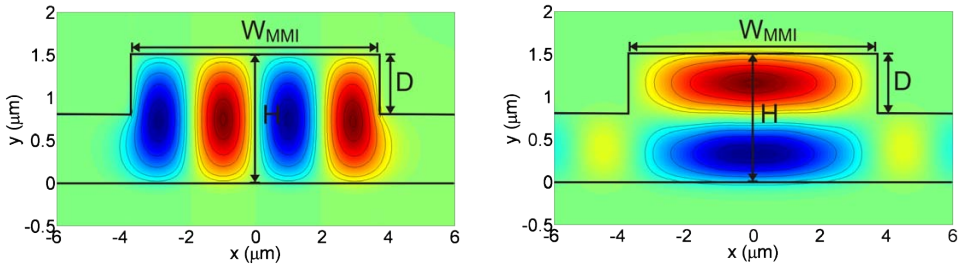

(a) Example of an imaging mode ($TE_{4,1}$). **(b)** Example of a non-imaging mode ($TE_{1,2}$).

Figure 5.8.: Two modes of a shallowly etched multimode section ($W_{MMI} = 7.5\mu m$, $D = 0.7\mu m$, $H = 1.5\mu m$).

The two remaining assumptions are number 2 (effective width of the multimode region does not depend on the mode number) and 3 (paraxial approximation). The phase error that arises from the violation of these conditions depends on the effective lateral index contrast $N_g - N_c$, and increases with increasing mode number [99]. Since in the considered technology platform the lateral index contrast only depends on the etch depth (D), which is fixed by other considerations, the only way to reduce this error is by exciting a reduced number of modes. Thus, we will skip these two assumptions for the moment, but we will come back to them in section 5.7.6.

5.6.1. Two dimensional model

Assumption 1 states that the three dimensional device is well approximated by a two dimensional effective index model (see figures 5.2 and 5.3 on page 44). To check if this holds, we need examine both the modes of the multimode section and the mode of the access waveguide that is launched into the device.

We will first classify the modes of the multimode section in *imaging* and *non-imaging* modes, and then analyse which of them are excited by the input waveguide mode. We will derive an expression that allows us to measure the amount of power that couples into non-imaging modes, and we will study its dependence on the rib aspect ratio, i.e., W_A and D.

In the following, guided rib waveguide modes of both polarisations (TE and TM) with m half cycles in the lateral (x) direction and n half cycles in the vertical (y) direction, will be referred to as $TX_{m,n}$ modes.

5.6.1.1. Imaging and non-imaging modes

Figure 5.8 shows two TE modes of a typical rib multimode section. In the effective index method, where the height of the device is "compressed" to zero, the $TE_{4,1}$ mode in figure 5.8(a) would be well approximated by a sine-type mode like $\varphi_4(x)$ (see (5.3) and figure 5.3). Since this is true for all guided $TX_{m,1}$ modes, these modes can be denominated *imaging modes*. If only these types of modes were excited in the multimode region, the 2D approximation would be a valid one.

On the contrary, the $TE_{1,2}$ mode in figure 5.8(b) is a *non-imaging mode*. This is

SPICUM servicio de publicaciones

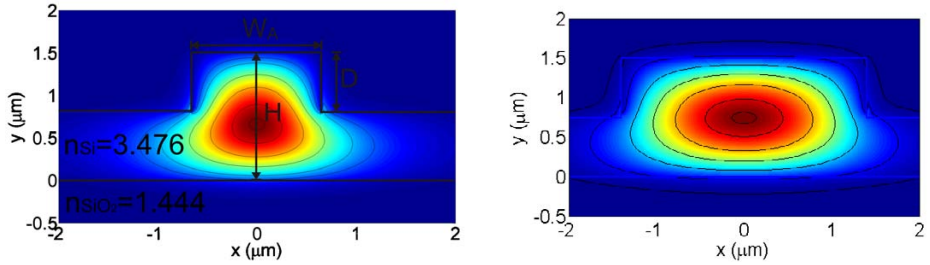

(a) $W_A = 1.3\mu m$, $D = 0.7\mu m$, $H = 1.5\mu m$ **(b)** $W_A = 2.4\mu m$, $D = 0.7\mu m$, $H = 1.5\mu m$

Figure 5.9.: TE_{11} mode of two rib access waveguides with different aspect ratios.

because due to its two half cycles in the vertical (y) direction, its propagation constant cannot generally fit into the parabolic law required for image formation in the desired horizontal direction. This also holds for all other modes with more than one half cycle in the vertical (y) direction, i.e., all $TX_{m,n}$ modes with $n \geq 2$ are non-imaging modes. Power that is coupled into non-imaging modes will not properly focus in the images, thus causing excess losses and imbalance.

The amount of power that couples into imaging and non-imaging obviously depends on the input field, which will be analysed in the next section.

5.6.1.2. The symmetry factor

We will now derive a condition for the input mode which ensures that only imaging modes are excited in the multimode region. The input excitation is the fundamental mode of the access waveguide, which is shown for TE polarisation and $W_A = W = 1.3\mu m$ in figure 5.9(a).

In order to find out what kind of modes this field excites inside the imaging region, one option is to solve the discontinuity between the access waveguide and the imaging section. This calculation can be performed with mode matching techniques, as implemented, for example, in Fimmprop,[6] but while this yields the rigorous result, it gives little insight into the problem. This is why we use a different approach, based on an idealised, rectangular imaging section of width W_{MMI} and height H that supports an infinite number of sine like modes

$$\varphi_{m,n}(x,y) = \sin\left(\frac{m\pi}{W_{\mathrm{MMI}}}x\right)\sin\left(\frac{n\pi}{H}y\right), \quad m,n = 1,2,3,\ldots \tag{5.28}$$

whose excitation coefficients are given by

$$c_{m,n} = \frac{4}{HW_{\mathrm{MMI}}}\int_0^{W_{\mathrm{MMI}}}\int_0^{H} E_d(x,y)\varphi_{m,n}(x,y)\mathrm{d}x\mathrm{d}y \tag{5.29}$$

where E_d is the dominant field component of the mode, that is, E_x for TE polarisation and E_y for TM polarisation. Note that (5.28) and (5.29) are simply extension of (5.3)

[6] Fimmprop is an eigenmode expansion based tool and is part of the Fimmwave package by Photon Design: `www.photond.com`

SPICUM servicio de publicaciones

and (5.10) and that $\varphi_{m,1}$ are the imaging modes. Since the $c_{m,n}$ coefficients can be interpreted as the (bi-dimensional) Fourier coefficients of E_d, the quantities

$$p_n = \frac{\sum_m |c_{m,n}|^2}{\sum_m \sum_n |c_{m,n}|^2} \tag{5.30}$$

are the fraction of power of the input field that, in an idealised imaging region, would couple into all modes that have n half-cycles in the vertical direction. Particularly, the fraction of power that would couple into the imaging modes $\varphi_{m,1}$ is given by p_1.

If we analyse the mode of a typical single mode rib waveguide as the one in figure 5.9(a) we get $p_1 = 0.93$, $p_2 = 0.066$ and $p_3 = 0.001$. That means that even in a idealised imaging section only 93% of the power would couple into imaging modes so that a power loss of *at least* $-10\log_{10}(0.93) \approx 0.3\,\mathrm{dB}$ is to be expected.

For other waveguide geometries similar power distributions are observed, i.e., nearly all the power that does not couple in $\varphi_{m,1}$ modes couples into $\varphi_{m,2}$ modes, that is, modes of the same type as the one shown in figure 5.8(b). This fact can be exploited to estimate more easily the fraction of power that couples into imaging modes. All the $\varphi_{m,n}$ modes with n odd are symmetrical with respect to $y = H/2$, whereas the modes with n even are antisymmetrical. Since virtually all the power that couples into symmetric modes couples into the imaging modes ($p_1 \gg p_3$), their power may be estimated as the power in the symmetric part of the input field:

$$p_s = \frac{\iint_\Omega \left|\frac{1}{2}\left[E_d(x,y) + E_d(x,H-y)\right]\right|^2 \mathrm{d}x\mathrm{d}y}{\iint_\Omega \left|E_d(x,y)\right|^2 \mathrm{d}x\mathrm{d}y} \tag{5.31}$$

where Ω is the waveguide's cross-section and p_s will be called the *symmetry factor*. Please note that given the p_s value of a certain input field, the excess loss (in dB) due to coupling to higher order vertical modes is directly

$$\mathrm{EL}_s = -10\log_{10} p_s. \tag{5.32}$$

In conclusion, for all the power of the input excitation to couple into imaging modes, its symmetry factor has to be unity. This result is actually rather intuitive: since all the imaging modes are symmetric with respect to $y = H/2$, their superposition can only represent excitations with the same kind of symmetry.

Naturally, the above analysis applies to both TE and TM modes.

5.6.1.3. Influence of waveguide geometry on the symmetry factor

Figure 5.9(b) shows the fundamental mode of an access waveguide which is wider than the interconnecting waveguide shown in figure 5.9(a). By comparison of these two figures it is apparent that shape of E_d, and thus the value of p_s, depends on the rib's aspect ratio, that is, W_A/H and D/H. In fact, by computing the fundamental mode of rib waveguides with different aspect ratios, and calculating the symmetry factor via (5.31), we can quantify this dependency. Figure 5.10 shows the values of $-10\log_{10} p_s$ as a function of rib aspect ratio for two different substrate heights. We can see that symmetry improves as the waveguides become wider or more deeply etched. Furthermore, the symmetry factor depends only weakly on the substrate height, H,

SPICUM servicio de publicaciones

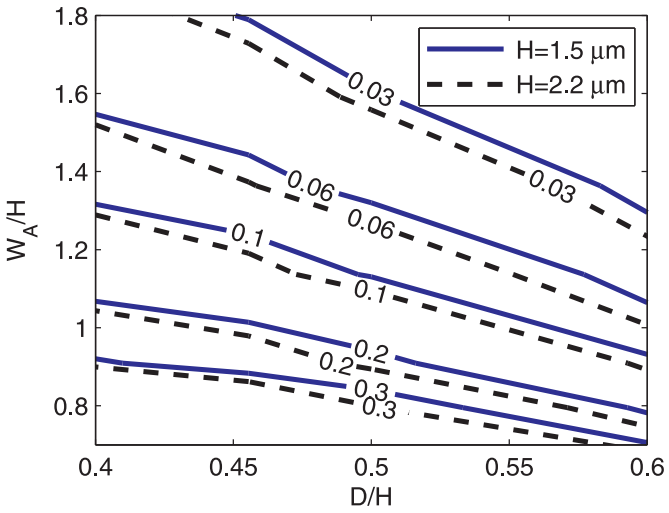

Figure 5.10: Symmetry factor, $-10\log_{10} p_s$, as a function of rib aspect ratio for substrate heights $H = 1.5\mu$m and $H = 2.2\mu$m.

since the values for $H = 1.5\mu$m and $H = 2.2\mu$m are close together. Thus, for a given etch depth, D, p_s can be improved by increasing the waveguide width, W_A.

For TM polarisation the symmetry factor exhibits the same behaviour as displayed in figure 5.10, but with slightly better values, which are probably due to the stronger modal confinement of this polarisation.

5.6.2. Guided modes approximation

In the preceding section we have discussed under which conditions rib waveguide based MMIs conform to the two dimensional device model used in the self-imaging theory. We shall now concentrate on another important assumption, namely that only guided modes should be excited in the multimode region (assumption 4 in section 5.2).

Using the concept of the (bi-dimensional) Fourier expansion introduced in section 5.6.1, it is clear that an input field which is narrow in the lateral (x direction), will excite a large number of higher order lateral modes, because its spatial spectrum is broad. However, the effective lateral index contrast of the multimode region is finite, and consequently it only supports a limited number of such higher order lateral modes. If the input field spectrum is "wider" than the spatial frequency of the highest supported mode, part of the input power will couple into radiative modes and will be lost.

In the following we will introduce a measurement of the amount of power that is lost as radiation, and we will analyse how it varies with W_A and D.

5.6.2.1. The guidance factor

We will now define a *guidance factor*, which quantifies the fraction of power that remains guided. In principle, this factor will depend on the effective lateral index contrast, $N_g - N_c$, the aspect ratio of the input waveguide, that is, on W_A/H and D/H,

SPICUM servicio de publicaciones

and on the width of the multimode section W_{eff}, which determines the number of modes that it supports.

We already account for excess losses in the form of power coupling to higher order vertical (y direction) modes, which occurs because of the partial invalidness of the two dimensional device model, through the symmetry factor (5.32). Hence, we may now restrict ourselves to a two dimensional analysis, via the effective index method. Under this simplification the guidance factor, p_g, may be defined as:

$$p_g = \frac{\text{power coupled into guided modes of an equivalent slab}}{\text{total power of 2D excitation}}. \tag{5.33}$$

Note that using the symmetry factor, p_s, and the guidance factor, p_g, we can compute the amount of power that couples from the input excitation into the 2D, guided modes on which the operation of MMIs is based:

$$P_{\text{2D,guided}} = (\text{power coupled to 2D}) \cdot \frac{\text{power guided in 2D}}{\text{power coupled to 2D}} = P_{\text{MMI input}}\, p_s\, p_g.$$

To compute p_g we proceed as follows. We approximate the multimode section's modes by the $\varphi_m(x)$ functions defined in section 5.2.2, setting $W_{\text{eff}} \approx W_{\text{MMI}}$ for the sake of simplicity. We then calculate the c_m expansion coefficients, defined by equation (5.10), of a "flattened" and power normalised version of a perfectly symmetric input field,

$$f_{\text{in}}(x) = \begin{cases} \sqrt{\frac{W_{\text{MMI}}}{W_A}} \sin\left(\frac{\pi}{W_A}(x - W_{\text{MMI}}/2)\right) & |x - W_{\text{MMI}}/2| \le W_A \\ 0 & \text{elsewhere} \end{cases}. \tag{5.34}$$

Due to the power normalisation the resulting c_m coefficients fulfil $\sum_{m=1}^{\infty} |c_m|^2 = 1$. The next step is to calculate the number of guided modes, M, supported by the multimode region:

$$M = \left\lfloor \frac{W_{\text{MMI}}}{\lambda} 2\sqrt{N_g^2 - N_c^2} \right\rfloor. \tag{5.35}$$

Please note that the effective indexes depend on the rib geometry (N_g depends on H and N_c depends on $H - D$), so that for a fixed substrate height (H), M depends not only on W_{MMI} but also on the etch depth (D). The guidance factor is then given by

$$p_g = \sum_{m=1}^{M} |c_m|^2, \tag{5.36}$$

and the excess losses (in dB) due to power coupling to radiative modes are simply given by

$$\text{EL}_g = -10 \log_{10} p_g. \tag{5.37}$$

5.6.2.2. Influence of waveguide geometry on the guidance factor

In principle, p_g depends both on the access waveguide geometry and on the dimensions of the multimode section. Since we are assuming that the multimode region has the same substrate height and etch depth as the access waveguides, it actually only introduces one additional variable: W_{MMI}. Figure 5.11 illustrates the variation

SPICUM servicio de publicaciones

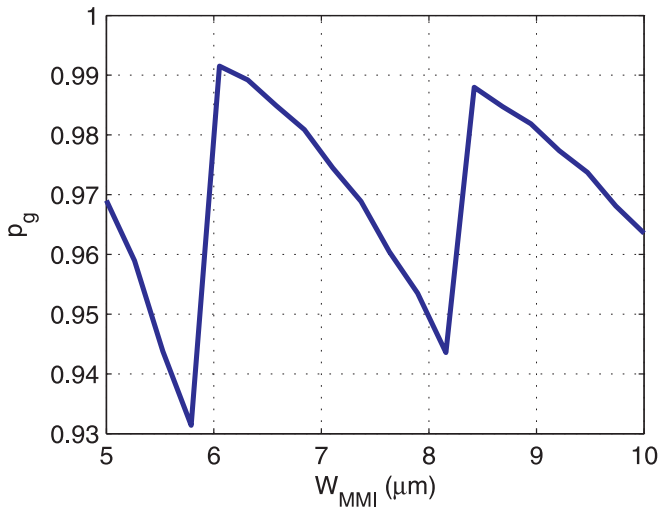

Figure 5.11: Guidance factor as a function of MMI width ($W_A = 2.4\mu m$, $D = 0.7\mu m$, $H = 1.5\mu m$).

of p_g when W_{MMI} is changed. We can see that p_g exhibits oscillations, which may be understood as follows. When W_{MMI} is slightly increased, the lobes of the modes it supports become wider. Since the width of the input field is constant, it is represented worse by these wider modes and consequently p_g decreases. As W_{MMI} is further incremented, the multimode section begins to support a new higher order mode, which has a narrower lobe, and thus the input field can again be faithfully represented, so that p_g increases abruptly. Since a local maximum can always be found by slightly adjusting W_{MMI} (see section 5.7.4), in the present analysis we eliminate this dependence by considering only the maximum values, i.e., $\max_{W_{\mathrm{MMI}}}\{p_g\}$. Hence, for a given substrate height (H), p_g only depends on W_A and D (through the effective lateral index contrast $N_g - N_c$).

Figure 5.12 shows the excess loss due to coupling to radiative modes, EL_g, as a function of rib aspect ratio for TE polarisation. We see that losses decrease as W_A or D are increased. This is expected, since a wider input field has a narrower spectrum, and therefore requires less modes to be correctly expanded. On the other hand, a deeper etching yields an increase effective lateral index contrast, thus increasing the number of modes, M, available for the expansion. Finally it is worth notice that p_g scarcely depends on the substrate height, H.

Again, very similar results are obtained for the TM polarisation, with a slight improvement, which comes from the higher effective lateral index contrast.

5.6.3. Design criterion for the access waveguides width

In this section we derive a design criterion for the access waveguides that ensures minimum losses. From sections 5.6.1 and 5.6.2 we already know that by widening the access waveguides device performance should increase. However, excessively widening the access waveguides is not desirable, as it brings the MMI access waveguides closer together (refer to figure 5.6 on page 53) so that coupling between them becomes stronger. Alternatively, we could increase the access waveguide separation, s, but this would also increase the MMI width, resulting in a larger device. Furthermore, we have

SPICUM servicio de publicaciones

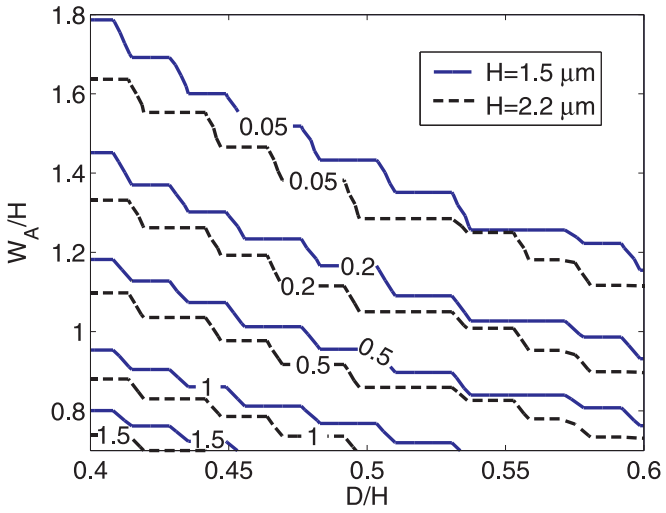

Figure 5.12: EL_g as a function of rib aspect ratio for substrate heights $H = 1.5\mu m$ and $H = 2.2\mu m$.

learned that an increased etch depth has similar advantageous effects as access waveguide widening, and consequently the optimum access waveguide width will depend on the chosen etch depth. Hence, our objective is to find the minimum value of W_A that yields excess losses of 0.1 dB or below, as a function of etch depth.

In order to derive the desired values of W_A we estimate MMI excess losses as the combination of symmetry losses and guidance losses:

$$EL_{est} = EL_s + EL_g = -10\log_{10}(p_s p_g). \tag{5.38}$$

EL_s accounts for the losses due to the partial invalidness of the two dimensional device model, and EL_g represents the losses due coupling to radiative modes in this two dimensional model. Figure 5.13 shows EL_{est} as a function of rib aspect ratio. By simple inspection it is apparent that there is a certain region, above the red solid line, where the desired performance is achieved. From the equation of that line we obtain the condition

$$\boxed{W_A \geq 3(H-D),} \tag{5.39}$$

which allows for the direct calculation of W_A and is one of the main results of this chapter. Equation (5.39) controls the spatial spectrum of the input field in a twofold way. On the one hand, it ensures that the fundamental mode is symmetric enough so as not to excite higher order vertical modes. On the other hand, it guarantees that the expansion of the input field does not require spatial frequencies higher than those supported by the MMI.[7] Please note that even though the derivation of this formula is based on results only for TE polarisation, it will also be valid for TM polarisation, since the estimated excess losses for the latter will be lower then for the former, due to the somewhat higher symmetry and guidance factors.

[7] The highest supported spatial frequency, or maximum propagation angle (see section 5.2.2), does *not* depend on the MMI width, but only on the effective refractive index contrast (also refer to section 5.7.6).

SPICUM servicio de publicaciones

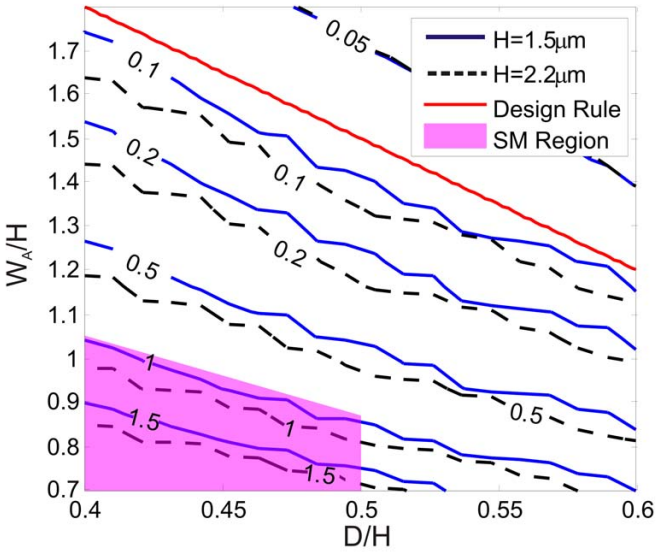

Figure 5.13: Estimated excess loss, EL_{est}, as a function of rib aspect ratio for substrate heights $H = 1.5\mu m$ and $H = 2.2\mu m$. The single mode region is shaded.

Some other interesting conclusions can also be drawn from figure 5.13. First, EL_{est} exhibits only a small dependence on substrate heights, so that a designer can directly apply equation (5.39) and does not need to calculate p_s or p_g. Second, given a fixed W_A, the excess loss can also be reduced by increasing the etch depth, which explains the high performance of the deeply etched devices reported in [98] (also see section 5.4). Finally, it is clear that waveguides fulfilling Soref's single-mode condition, which is represented as the shaded area in figure 5.13, are inadequate as MMI access waveguide, as they yield excess losses of at least 1 dB.

5.7. Design procedure

We will now present a procedure that allows for the design of the complete MMI (see figure 5.6 on page 53), which will be developed by means of an example based on the specifications given in section 5.5.

5.7.1. Access waveguide width (W_A)

The design of this dimension is now rather trivial, thanks to equation (5.39). For a substrate height of $H = 1.5\mu m$ and a nominal etch depth of $D = 0.7\mu m$, we get $W_A \geq 2.4\mu m$. However, when taking into account fabrication tolerances, the worst case occurs for $D = 0.6\mu m$. In this case we find $W_A \geq 2.7\mu m$, so that we finally set $W_A = 2.8\mu m$ to ensure good etch depth tolerances.

5.7.2. Taper length (L_T)

The next step is to design an adiabatic transition (or taper) between the interconnecting waveguides (W_I) and the access waveguides (W_A). Since this taper starts with a single mode waveguide, initially no coupling between guided modes can take place,

SPICUM servicio de publicaciones

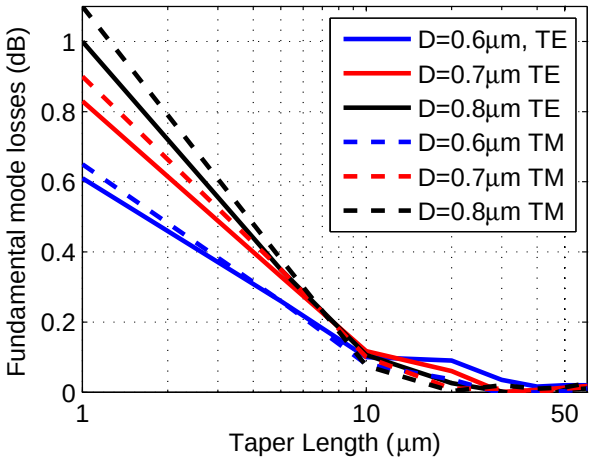

Figure 5.14: Losses of the fundamental mode as a function of taper length, L_T.

so that the main loss mechanism is expected to be radiation. Thus, eigenmode expansion is not well suited to analyse this problems, as a very large number of modes would be required. Furthermore, perfectly matched layer (PML) boundary conditions are needed to absorb the outgoing radiation. Consequently, a full vectorial 3D Beam Propagation Method with PML boundary conditions is probably the best choice to design this taper. In this work, we used the software described in [113] to perform the taper analysis. Both a linear and a cosenoidal taper profile were considered, yielding very similar results, which is why the simpler linear profile was adopted.

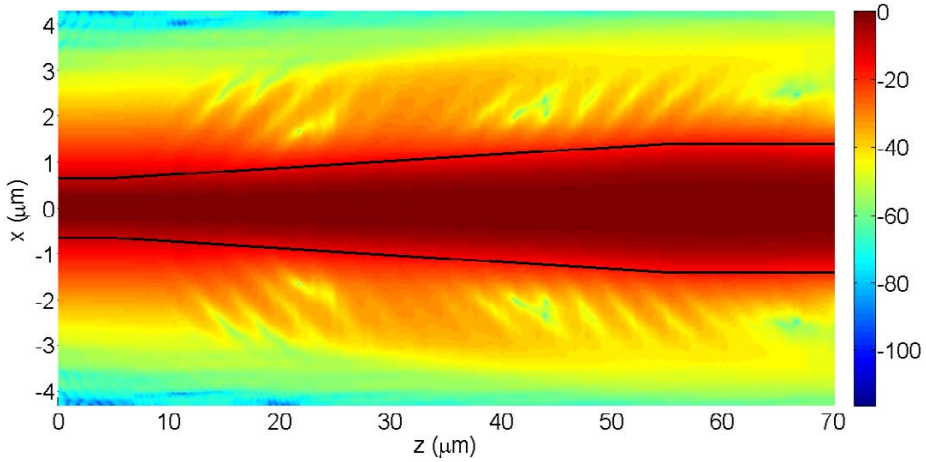

Figure 5.15.: Light intensity (in dB) along the taper of length $L_T = 50\,\mu m$.

Returning to our design example, figure 5.14 shows the losses of the fundamental TE and TM modes as a function of taper length, when the waveguide width is widened from $W_I = 1.3\,\mu m$ to $W_A = 2.8\,\mu m$. As modal confinement varies appreciably with etch depth, the taper has to be simulated for the maximum typical fluctuations ($\pm 0.1\,\mu m$) around the nominal value. First consider the curves for the nominal value, $D = 0.7\,\mu m$. For a very short taper, the calculated losses match the overlap integral between the fundamental modes of the narrow and the wide waveguides. These are

SPICUM servicio de publicaciones

slightly higher for the TM polarisation, because the mode confinement is stronger, so that the difference in shape between these two modes is slightly bigger. As the taper length is increased, losses decrease quite fast reaching less than 0.1 dB for $L_T = 20\,\mu m$. Now, for $D = 0.6\,\mu m$ one might expect higher losses due to weaker confinement. However, for this value of D the fundamental modes of the narrow and the wide waveguide resemble each other more than those for $D = 0.7\,\mu m$, which is why losses are lower when the taper is very short. As the taper length increases, losses decrease, but with a slower rate than in the $D = 0.7\,\mu m$ case, and that is because of the weaker confinement. For $D = 0.8\,\mu m$ the behaviour may be explained just the other way around. For a taper length of only $L_T = 50\,\mu m$ losses are lower than 0.05 dB in all cases. Finally, figure 5.15 shows a top view of the light distribution along the taper for the chosen length of 50 µm in decibels. The radiation leaving the guiding region is clearly visible and confirms the initial assumption that radiation is the main loss mechanism in this type of tapers.

5.7.3. Access waveguide separation (*s*)

Once the length of the taper, L_T, is known, the separation of the access waveguides, s, can be designed. This separation obviously influences the width of the MMI (W_{MMI}), which in turn determines its length. Consequently, in order to achieve a compact device, s has to be kept as low as possible. However, it also has to be large enough to ensure that:

1. the gap between the access waveguides (g) can be fabricated, i.e. is not smaller than 1 µm (also refer to section 3.2).

2. there is no coupling between the parallel input and output waveguides. The two parallel tapered waveguides act as a directional coupler, and thus a certain amount of power will be transferred between them.

Since the taper has been designed to be adiabatic, at each point z along it virtually only the fundamental local normal mode carries power [114, Ch. 28]. This means that the coupling between the two tapered waveguides may be estimated as the coupling between their fundamental modes. And this in turn can be bound by the coupling that takes place between two sets of two straight parallel waveguides, whose widths are the maximum and minimum width of the taper, $W_A = 2.8\,\mu m$ and $W = 1.3\,\mu m$ respectively. Consequently, we may design the separation between the MMI access waveguides using the same criteria as for the interconnecting waveguides (see section 4.6). As discussed in section 4.6, a coupling $C < -45\,dB$ is required to minimise imbalance at the MMI output. However, in the design phase the separation between waveguides was (erroneously) chosen to yield $C = -30\,dB$. As we will show below, owing to a conservative design, and the fact that the etch depth specified for fabrication was slightly increased with respect to the design values, this slip had no practical impact on device performance.

Figure 5.16 shows the maximum length ($L_{P\max}$) of two parallel waveguides with a coupling C better than $-30\,dB$ as a function of the waveguide centre to centre separation (s) for two different etch depths. Note that there is only a minor difference in

SPICUM servicio de publicaciones

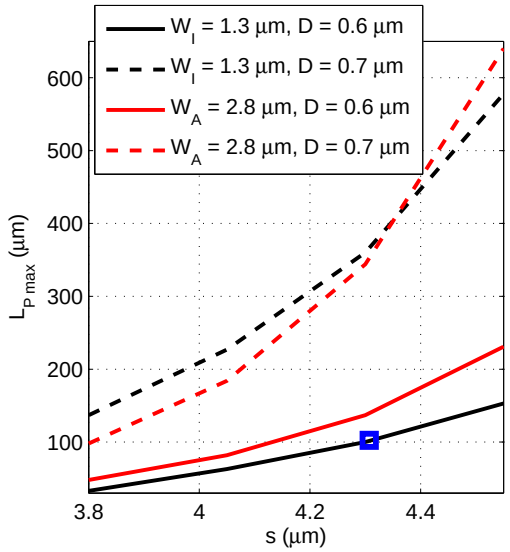

Figure 5.16: Maximum length of parallel input/output waveguides for coupling to be lower than −30 dB. Here $H = 1.5\,\mu$m.

coupling length between the narrow and the wide waveguides, but that etch depth has a strong impact on coupling and thus on the maximum allowed length. This is because as etch depth is decreased the modes of the individual waveguides are less confined and thus their interaction is stronger. As the taper is 50 µm long a separation of about $s = 4\,\mu$m would be enough to make sure that coupling is below the desired level. However, to leave some degree of freedom —for example, for an s-bend of the interconnecting waveguides—, a slightly bigger separation of $s = 4.3\,\mu$m needs be chosen, which gives a maximum allowed length of 100 µm. Note that for this separation the gap between the waveguides is $g = 1.5\,\mu$m which can be easily fabricated.

As we discuss in section 8.2, for the final fabrication etch depth was increased from 0.7 µm to 0.75 µm, and the measurements described in chapter 8 indicate that the error in etch depth is low. It is thus sensible to assume that the etch depth is not lower than 0.7 µm, and in this case the maximum coupling between both the 1.3 µm and the 4.3 µm wide waveguides is −41 dB, which yields a maximum imbalance of 0.16 dB. Since experimental precision is around ±0.2 dB, we may conclude that the waveguide coupling had no notable impact on device performance.

If more than two input or output waveguides are required, the coupling analysis can still be performed on pairs of adjacent waveguides, since the interaction between non-adjacent waveguides will be negligible.

5.7.4. Multimode region dimensions (W_{MMI} and L_{MMI})

So far we have determined the width of the access waveguides (W_A), the length of the taper (L_T) which joins them with the interconnecting waveguides, and the necessary separation (s) between a pair of tapered waveguides. This section deals with the design of the two remaining dimensions, namely the MMI's width, W_{MMI}, and its length, L_{MMI}. In principle these are given by the type of imaging which is desired (see section 5.2.5 on page 49), but they need to be optimised around their theoretical values to maximise performance. Since we have dimensioned the tapers to be adia-

SPICUM servicio de publicaciones

Algorithm 5.1 Optimisation of W_{MMI} and L_{MMI}

1. Start with the width, W_{MMI}, and length, L_{MMI} , determined by imaging theory.
2. By simulation, find the optimum length of the device, in the sense of a tradeoff between minimum excess loss and minimum imbalance for both polarisations.
3. Decrease the width by 0.1 µm and again find the optimum length of the device.
4. If the tradeoff between excess losses and imbalance is improved, repeat steps 3 and 4 until no further improvement is achieved. If the performance is worsened, increase the width.

Table 5.3.: MMI dimensions in µm and their design criteria.

	H	D	W_I	W_A	L_T	s		W_{MMI}	L_{MMI}
$D =$ 0.7 µm	1.5	0.7	1.3	2.8	50	4.3	gen.	7.5	274
							pair.	12.8	256
$D =$ 0.75 µm	1.5	0.7	1.3	2.8	50	4.3		12.85	255
Criterion	—	Section 4.5		Eq. (5.39)	Section 5.7.2	Section 5.7.3		Algorithm 1	

batic, and have separated them enough to minimise coupling between them, we can carry out this optimisation by simulating only the W_A wide access waveguides and the central multimode region. This structure can again be readily analysed by eigenmode expansion, especially because the access waveguides have already been designed so as to excite virtually only the guided modes within the multimode section. Thus, we may again use Fimmprop, with which the effect of variation of L_{MMI} can be analysed swiftly. This enables us to use algorithm 5.1 to perform the optimisation. Please note that through steps 3 and 4 we are iteratively determining the effective width of the multimode region, W_{eff}.

We will now apply this algorithm to the design of two 2×2 MMIs, one based on general imaging, and another one based on paired imaging (see section 5.2.5 on page 49). If we assume that the access waveguides should not stick out over the edge of the multimode region, the minimum possible width of a general interference based MMI is given by $W^G_{\mathrm{MMI}} = 2W_A + g = 7.1\,\mu\mathrm{m}$, whereas for a paired interference based device it is $W^P_{\mathrm{MMI}} = 3(W_A + g) = 12.9\,\mu\mathrm{m}$. After optimisation, the following dimensions are arrived at: $W^G_{\mathrm{MMI}} = 7.5\,\mu\mathrm{m}$, $L^G_{\mathrm{MMI}} = 274\,\mu\mathrm{m}$ and $W^P_{\mathrm{MMI}} = 12.8\,\mu\mathrm{m}$, $L^P_{\mathrm{MMI}} = 256\,\mu\mathrm{m}$. As we have already mentioned before, the etch depth specification was finally increased to 0.75 µm (see section 8.2), and due to timing constraints it was not possible to redesign the MMIs for the first fabrication run. For the second run, only paired interference MMIs were used, since both theoretical tolerance analysis (see section 5.8) and our experimental results (see section 8.5) showed that it outperformed the general interference device. The optimised width and length of the paired interference MMI with

SPICUM servicio de publicaciones

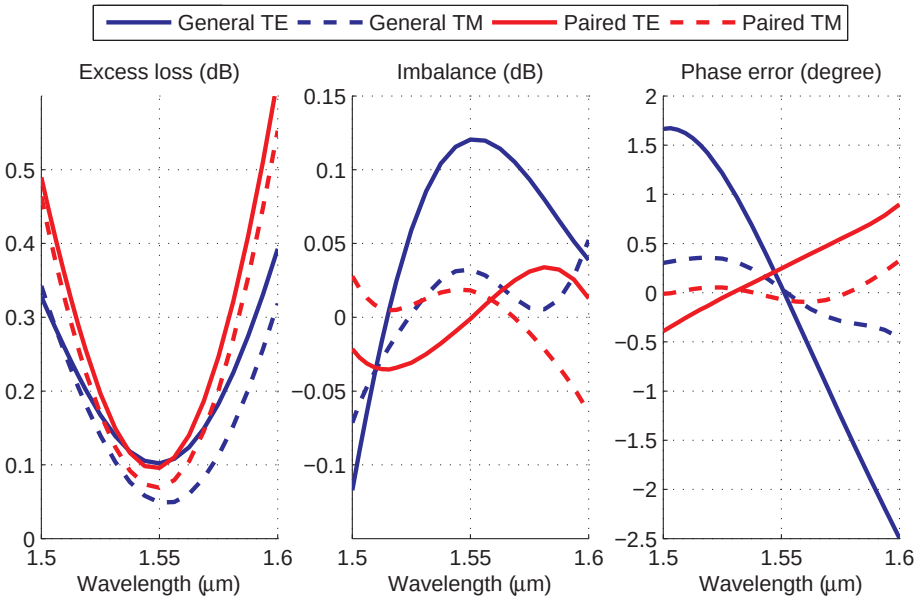

Figure 5.17.: Comparison of the bandwidth of the paired and general interference MMIs.

Table 5.4.: Performance of the optimised devices at $\lambda = 1.55\,\mu m$.

	Excess Loss [dB]		Imbalance [dB]		Phase Error [degree]	
	TE	TM	TE	TM	TE	TM
General	0.1	0.05	0.11	0.02	0.02	−0.02
Paired	0.1	0.07	< 0.01	0.02	0.3	−0.07

an etch depth of $D = 0.75\,\mu m$ are $W^P_{MMI} = 12.85\,\mu m$, $L^P_{MMI} = 255\,\mu m$.

This completes our design process; the final dimensions and their design criteria are summarised in table 5.3.

5.7.5. Device performance and bandwidth

The performance of the optimised devices is shown table 5.4, where excess loss, imbalance and phase error are defined as in section 5.3.

Please note that the excess losses for TE polarisation are exactly 0.1 dB, which was the level we set when deriving the design formula for the access waveguide width (5.39). The slightly lower losses for TM polarisation are also expected, as the symmetry and guidance factors are slightly higher for this polarisation due to the higher modal confinement. Both imbalance and phase error are very low, especially for the paired interference based device.

Figure 5.17 shows the excess loss, imbalance and phase error as a function of wavelength. In the 1.5 µm – 1.6 µm wavelength band excess losses remain below 0.6 dB for the paired interference based device, and below 0.4 dB for the general interference based device. However, the imbalance and phase error of the latter are slightly higher.

SPICUM servicio de publicaciones

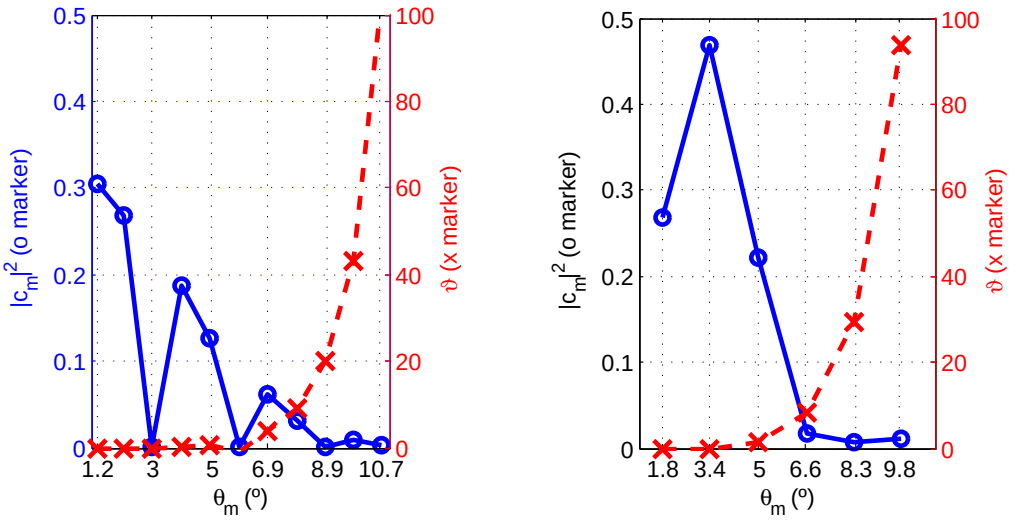

(a) Paired Interference MMI.

(b) General Interference MMI.

Figure 5.18.: Modal phase deviation (in degrees) and normalised modal excitation coefficients for the general and paired interference based MMI.

5.7.6. Propagation constants error

In our design we have ignored the effect of the non-ideal distribution of the propagation constants, i.e., their deviation from the parabolic law (5.7). This error depends on the lateral refractive index contrast, which, in our case, cannot be altered. However, we shall now check that in the designed devices this error is low.

The accumulated phase deviation (in degrees) of the m-th mode is given by

$$\vartheta_m = \left(\beta_m - \beta_m^{\text{ideal}}\right) L_{\text{MMI}} \times 180/\pi, \tag{5.40}$$

where β_m is the real (simulated) propagation constant, and β_m^{ideal} is calculated from equation (5.7). Figure 5.18 shows this deviation for both devices, as a function of mode propagation angle as defined by equation (5.6). We can observe that the deviation is very large, up to 100° for the highest order modes. However, since the input waveguides are relatively wide, the excitation coefficients (c_m) of these modes are very low (see figure 5.18). Actually, if we define an average phase deviation, $\overline{\vartheta} = \sum_m |c_m|^2 \vartheta_m$, we find $\overline{\vartheta} = 1.83°$ for the general interference based device, and $\overline{\vartheta} = 1.25°$ for the paired interference based device, which explains their satisfactory performance.

From figure 5.18 we also see that the highest order modes of both devices propagate with similar angles, and that, as expected, in the paired device c_3, c_6 and c_9 are virtually zero (compare with section 5.2.5.2).

Finally, it is apparent from figures 5.18(a) and (b), that the phase error of each mode is determined by its propagation angle rather than its mode number. For example, the sixth mode of the paired device has a propagation angle of 6.9° and its phase error is comparable to the fourth mode of the general interference device, which has a similar

SPICUM servicio de publicaciones

propagation angle of 6.6°.The fifth mode of the paired interference device has a much smaller phase error than the fifth mode of the general interference device, because the propagation angle of the former is much smaller.

5.8. Tolerance analysis

When designing the access waveguide width (W_A), the taper length (L_T) and the waveguide separation (s), fabrication tolerances were taken into account. However, the optimisation of W_{MMI} and L_{MMI} does not yield much information about fabrication tolerances. Besides, these values are optimal only for the nominal etch depth. This is why a thorough fabrication tolerance analysis, including length, width and etch depth variations, will be carried out in this section.

From equation (5.8) we can find a relation between the variation of coupler length, width and operating wavelength [115]:

$$\left|\frac{\Delta L_{\mathrm{MMI}}}{L_{\mathrm{MMI}}}\right| = 2\left|\frac{\Delta W_{\mathrm{MMI}}}{W_{\mathrm{MMI}}}\right| = \left|\frac{\Delta\lambda}{\lambda}\right| \tag{5.41}$$

We see that $\Delta L = \Delta\lambda\frac{L_{\mathrm{MMI}}}{\lambda}$, so that length variations should have a similar impact on performance as wavelength variations scaled by a factor L_{MMI}/λ, which, for the general interference based device, is 177. Since the device exhibits an acceptable performance for wavelength variations of ±50 nm, it should also support length variations of approximately $\pm 0.05 \times 177 \approx 9\,\mu\mathrm{m}$. On the other hand, $\Delta L_{\mathrm{MMI}} = \Delta W_{\mathrm{MMI}}\frac{2L_{\mathrm{MMI}}}{W_{\mathrm{MMI}}}$, which means that width variations are equivalent to length variations but enhanced by a factor $2L_{\mathrm{MMI}}/W_{\mathrm{MMI}}$, which in our case is 73 for the general interference based device. Thus, width variations larger than $9/73 \approx 0.12\,\mu\mathrm{m}$ must be expected to be critical. As discussed in section 5.2.5.2, in the paired interference MMI only a subset of the multimode region's modes is excited, reducing the distances at which the images form by a factor of three. As shown in [115], this also results in a threefold increment in the width tolerance, so that the paired interference MMI is expected to much less affected by the fabrication tolerances than the general interference MMI.

5.8.1. Length variations

Figure 5.19 shows the performance variations when the the length (L_{MMI}) of the device is changed. We can see that the device supports length fluctuations of ±5 µm without appreciable changes in its characteristics, which is expected from the above analysis. In fact, the shape of the curves in figure 5.19 clearly resembles those in figure 5.17. It is also noticeable that while excess losses increase as soon as the length deviates from its optimum value, imbalance remains almost invariant in a range of approximately ±5 µm. Thus, we may conclude that length variations are not critical, since during fabrication this dimension can be easily controlled below 0.5 µm.

5.8.2. Width variations

Device performance as a function of multimode section width (W_{MMI}) is illustrated in figure 5.20. As expected from equation (5.41), excess losses increase rapidly as

SPICUM servicio de publicaciones

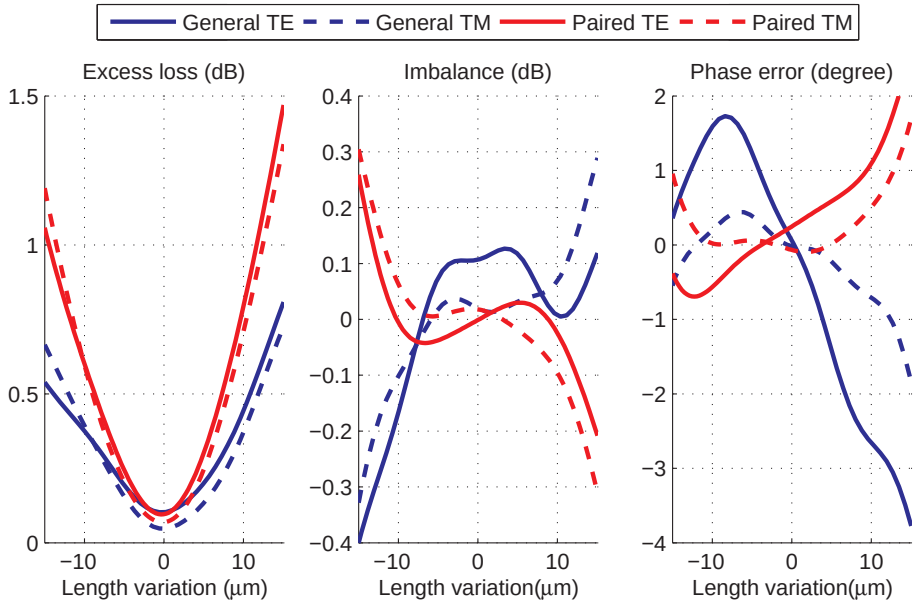

Figure 5.19.: Effect of length variations.

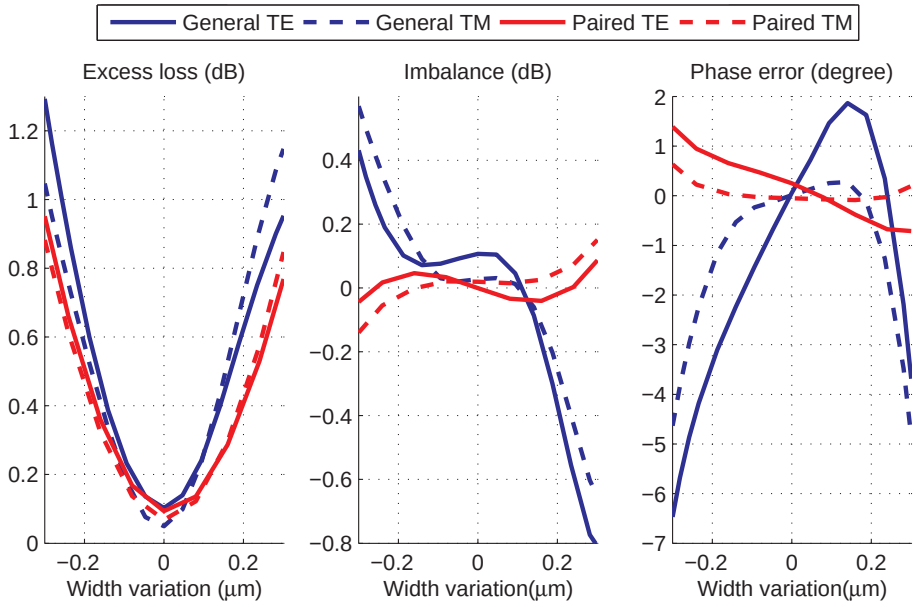

Figure 5.20.: Effect of width variations.

SPICUM servicio de publicaciones

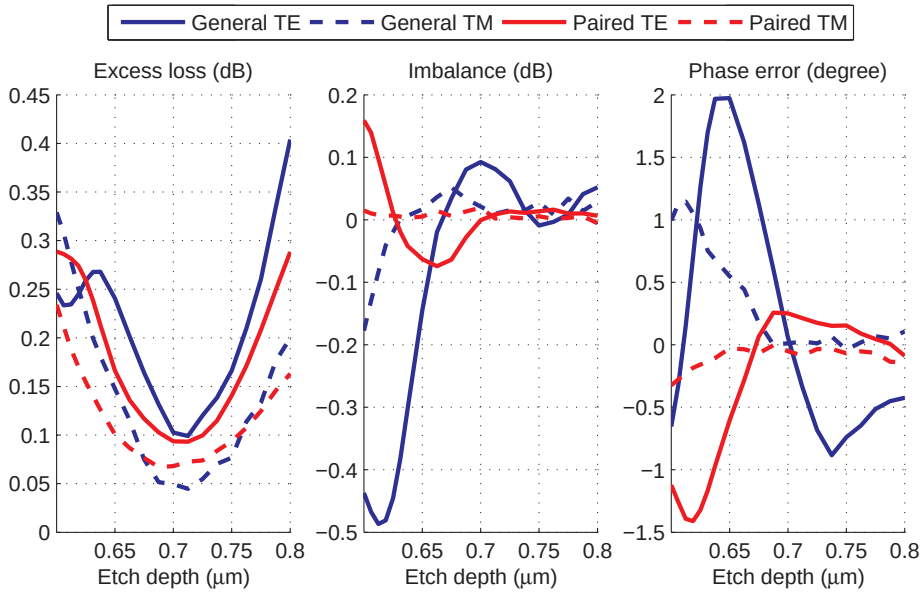

Figure 5.21.: Effect of etch depth variations.

W_{MMI} deviates from its nominal value: for a width variation of only 300 nm they reach around 1 dB, the paired device being slightly more insensitive than the general one. For width variations around 100 nm both devices exhibit excess losses of about 0.3 dB. Imbalance and phase error exhibit quite different behaviour for the paired and the general interference devices. As depicted in the central plot of figure 5.20, imbalance is much more insensitive to width variation in the paired interference MMI than in the general interference MMI, staying below 0.2 dB in former, and reaching 0.8 dB in the latter. The phase error (right plot in figure 5.20) remains below 2° for variations of ±300 nm for the paired device, but increases up to 7° in the general device. Hence, with ±100 nm being a reasonable value for fabrication fluctuations, it seems to difficult to achieve a coupler with excess losses below 0.2 dB. However, the paired configuration still allows for reduced imbalance (0.1 dB) and small phase errors (1°).

Finally, it is noteworthy that the shape of the curves in figure 5.20, resembles the mirror image of those in figure 5.19. This is because widening the MMI results in a larger imaging length (see equation (5.8)), which is equivalent to a smaller device length.

5.8.3. Etch depth variations

The etch depth of fabricated devices typically varies in ±100 nm. By examining figure 5.21 we find that excess losses remain below 0.3 dB for the paired device, and below 0.4 dB for the general device. This good tolerance probably comes from the fact that the access waveguide width (W_A) was designed with this etch depth variations in mind. As for imbalance, we see that the paired configuration again outperforms the general one. The maximum phase error of the paired interference based device is about −1.5° and 2° for the general configuration.

SPICUM servicio de publicaciones

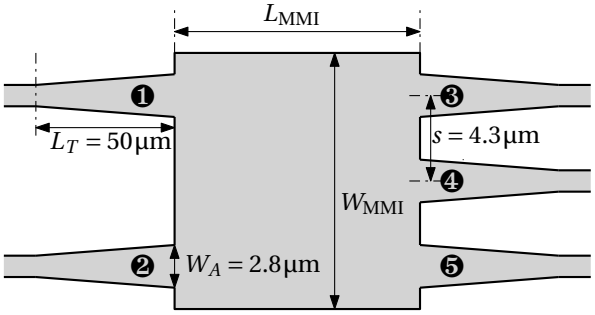

Optimized multimode region dimensions

D	W_{MMI}	L_{MMI}
0.70 µm	12.8 µm	512 µm
0.75 µm	12.8 µm	506 µm

Figure 5.22.: Geometry of the 2×3 MMI.

5.8.4. Conclusions

The main conclusion than can be drawn from this tolerance analysis is that , in terms of imbalance and phase error the paired interference MMI is considerably more robust to fabrication tolerances than the general interference MMI. Consequently we will use this device in the sixport. Even with the maximum expected variations of $\pm 0.1\,\mu\mathrm{m}$ in device width and $\pm 0.1\,\mu\mathrm{m}$ in etch depth, this MMI still offers a good performance: $\sim 0.2\,\mathrm{dB}$ of imbalance and $\sim 1.5°$ of phase error.

5.9. Design of the 2×3 MMI

As discussed in chapter 2, the sixport requires not only the 2×2 MMI, whose design we have discussed in the previous sections, but also a 2×3 MMI. With the design procedure that we have developed, the design of the latter is straightforward. The width of the access waveguides, their separation and the length of the adiabatic taper is the same as in the 2×2 design (see figure 5.22), so that only the width (W_{MMI}) and the length (L_{MMI}) of the device have to determined. Note that increasing the MMI width will not substantially increase the average phase error, because, as discussed in section 5.7.6, this error depends on the propagation angle of the modes excited inside the multimode region, and not so much on their mode number. Since we are keeping the same input waveguide width as in the 2×2 MMI, we are also maintaining the angular spectrum of the input excitation, so that the phase error should not increase appreciably.

As outlined in section 5.2.6, in order to have a uniform spacing between the output waveguides, the centres of the input waveguides has be situated at a distance $W_{\mathrm{eff}}/6$ from the edges of the multi-mode section. Assuming $W_{\mathrm{eff}} = W_{\mathrm{MMI}}$, i.e., ignoring the Goos-Hänchen shift, and by inspection of figure 5.22 we find that the approximate width of the device is $W_{\mathrm{MMI}} = 3s = 12.9\,\mu\mathrm{m}$. Using this as starting point for the optimisation of MMI width and length (algorithm 5.1), the optimum dimensions shown on the right hand side of figure 5.22 are arrived at.

Apart from insertion loss and imbalance, the phase error is of particular importance in the 2×3 MMI, since it determines the accuracy of the position of the sixport centres. Specifically, we are interested in the relative phases with which the waves from both input ports combine at each output port, so that we define the phase er-

SPICUM servicio de publicaciones

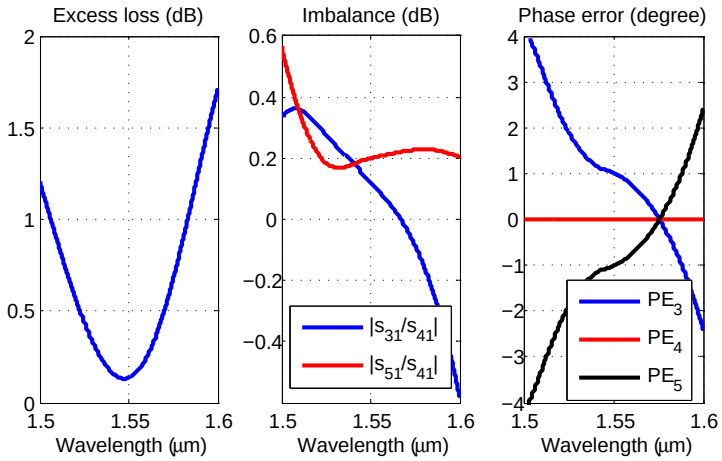

(a) TE polarisation

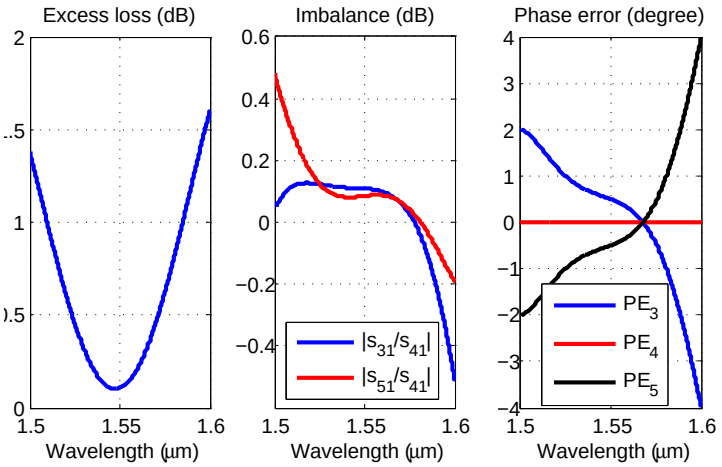

(b) TM polarisation

Figure 5.23.: Performance of the 2 × 3 MMI as a function of wavelength for (a) TE polarisation and (b) TM polarisation.

rors of the 2 × 3 MMI as:

$$\begin{aligned} \mathrm{PE}_3 &= \angle\frac{s_{32}}{s_{31}} - \frac{2\pi}{3} \\ \mathrm{PE}_4 &= \angle\frac{s_{42}}{s_{41}} \\ \mathrm{PE}_5 &= \angle\frac{s_{52}}{s_{51}} + \frac{2\pi}{3} \end{aligned} \tag{5.42}$$

The performance of the device in the 1500 nm to 1600 nm band is shown in figure 5.23 for both polarisations. The maximum insertion loss of the device is about 2 dB for TE polarisation at $\lambda = 1.6\,\mu$m, which is considerably higher than the 0.6 dB insertion losses of the paired 2 × 2 MMI. Similarly, the maximum imbalance of 0.6 dB of the 2 × 3

SPICUM servicio de publicaciones

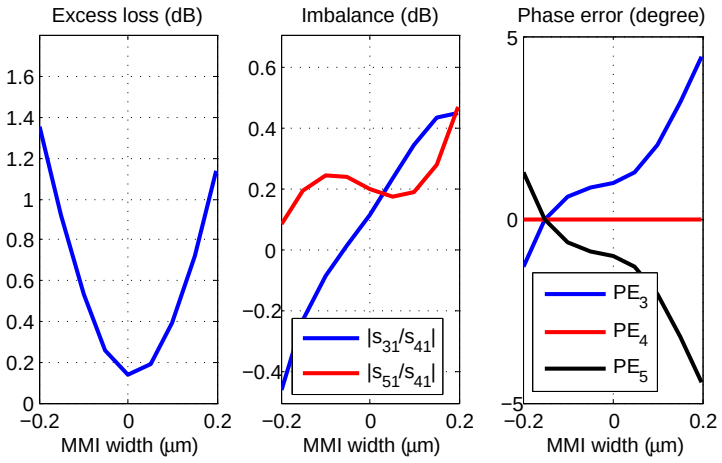

(a) TE polarisation

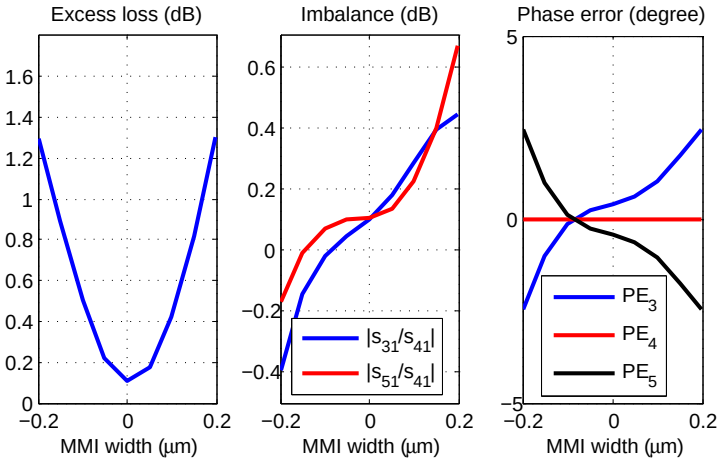

(b) TM polarisation

Figure 5.24.: Width tolerance of the 2×3 MMI as for (a) TE polarisation and (b) TM polarisation.

MMI clearly exceeds the 0.15 dB obtained in the 2×2 coupler. Also, the phase error is considerably larger in the 2×3 MMI (4°) than in the 2×2 MMI (1°).

From the tolerance analysis of the 2×2 MMI carried out in section 5.8 we now that the width of the MMI is critical to the operation of the device, so that it is convenient to examine also the width tolerance of the 2×3. This is shown in figure 5.24, revealing that for width variation in the range of $\pm 0.1\,\mu$m the 2×3 MMI exhibits insertion losses of about 0.6 dB, and a maximum imbalance of 0.3 dB for TE and TM polarisations, both of which are appreciably higher than the 0.2 dB insertion loss and 0.1 dB imbalance that were calculated for the same width variation for the paired 2×2 MMI. Similarly, the phase error of $\sim 3°$ is significantly higher than in the paired 2×2 MMI, which showed an error of $\sim 1°$.

Consequently, the 2×3MMI is be the most critical part of the sixport, and will determine the performance of the circuit in both bandwidth and fabrication tolerances.

SPICUM servicio de publicaciones

5.10. Conclusions

The main goal of this chapter was to design shallowly etched, rib waveguide based multi-mode interference couplers, that can be fabricated in the same lithographic step as the single-mode interconnecting waveguides.

Our starting point has been the self-imaging theory that governs the operation of multi-mode interference couplers. We have quantitatively analysed what restrictions this theory poses on the design of MMIs based on shallowly etched rib waveguides. As a result, we have established the presence of imaging and non-imaging modes in the multimode section, and have derived the design formula (5.39) for the width of the access waveguide, that ensures high performance operation. We have studied the design of an adiabatic taper to join the interconnecting waveguides and the MMI access waveguides and we have developed a complete design procedure to optimise all geometrical parameters of the coupler.

Using this procedure, a paired interference and a general interference based 2×2 MMI have been designed, both offering almost ideal performance (imbalance and excess loss of ~ 0.1 dB) when nominal dimensions are considered. As expected, device width was found to be the most critical parameter regarding tolerances. However, as predicted by theory, the paired interference device exhibits much larger tolerances to fabrication fluctuations and will thus be used in the six-port junction. We have furthermore described the design of the 2×3 MMI, which has a smaller bandwidth and tighter fabrication tolerances than the 2×2 MMI, and will thus be determine the overall performance of the sixport.

SPICUM servicio de publicaciones

SPICUM
servicio de publicaciones

6
Sixport design

ONCE the design of waveguides and the MMIs is completed, the design if the six-port is relatively straightforward. In this brief chapter we will discuss the general layout of the junction (section 6.1) and assess its overall performance via simulation (section 6.2).

6.1. Layout

Both fabrication, measurement and a possible packaging of the final chip have to be taken into account in the layout of the device. The fabricated device will be part of a rectangular optical chip. Two opposite sides (or facets) of the chip will be polished to optical quality, and can thus be employed for light input and output, whereas the remaining two sides cannot be used for this purpose. For measurement, a fibre and a microscope objective have to be precision aligned to the input and output waveguides. Since the alignment blocks are relatively large mechanical parts, input and output cannot be on the same facet of the chip, since it would be impossible to align both. For packaging, it is mandatory to separate the DUT port from the four outputs that would be connected to a photodetector array by at least 5 mm. Otherwise, mechanical alignment of the photo-detectors and the output fibre would not be feasible. Furthermore, in order to avoid coupling of straylight from the input to the outputs, they should be vertically offset by about 2 mm. Finally, the circuit should introduce as little imbalance as possible between the light travelling from the input and from the DUT port to each of the outputs of the 2×3 MMI. This means that the layout of this part should be symmetrical, so that curvature losses are identical for both paths.

The most compact layout we found to fulfil all the above considerations is shown in figure 6.1. In this figure tapers and s-bends, which are needed at the MMI inputs and outputs to decouple the waveguides, are not shown for the sake of clarity. As discussed in section 5.10, the 2×2 MMI is paired interference based. Port 1 is the input port, and the DUT port is port number 2. The power reference is provided through port 4, and the three sixport outputs are ports 3, 5 and 6. The left hand side waveguide that is not numbered is the radiation port. The length of the interconnecting waveguides is also shown in figure 6.1. For the moment, we will assume that both facets have a perfect anti-reflective coating, and in this case only the length of the DUT port

SPICUM servicio de publicaciones

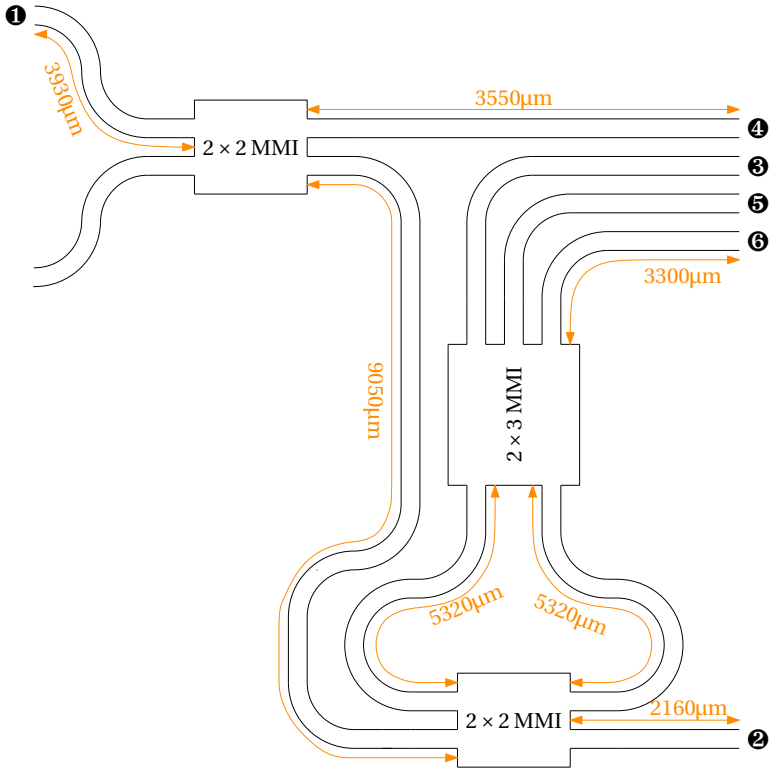

Figure 6.1.: Schematic layout of the sixport junction (not to scale). The port numbering and the length of the interconnecting waveguides is also shown.

(number 2) is relevant, because, as discussed in section 2.4, it determines the rotation rate of the sixport centres. In section 8.6, when we discuss the characterisation of the fabricated device, the remaining distances have to be taken into account, since they determine the interference produced by the reflections from the uncoated facets.

6.2. Simulation of the complete circuit

A full electromagnetic simulation of the complete circuit is computationally unfeasible. However, since all the interconnecting waveguides are single-moded, a S-matrix based simulation can be carried out. This approach assumes that the input and output waveguides of all devices support only the fundamental TE and TM mode, so that, for each wavelength and polarisation, the device is completely defined by a matrix of complex transmission (and reflection) coefficients that relate the optical field at every pair of input and output ports. Additionally, we do not consider polarisation cross-talk, which is reasonable, since no polarisation coupling was observed in the electromagnetic simulation of the individual devices.

With this approach a waveguide of length L is simply characterised by the effective indices of both polarisations, $n_{\text{eff}}^{\text{TE}}(\lambda)$ and $n_{\text{eff}}^{\text{TM}}(\lambda)$, as a function of wavelength, its S-matrix being:

SPICUM servicio de publicaciones

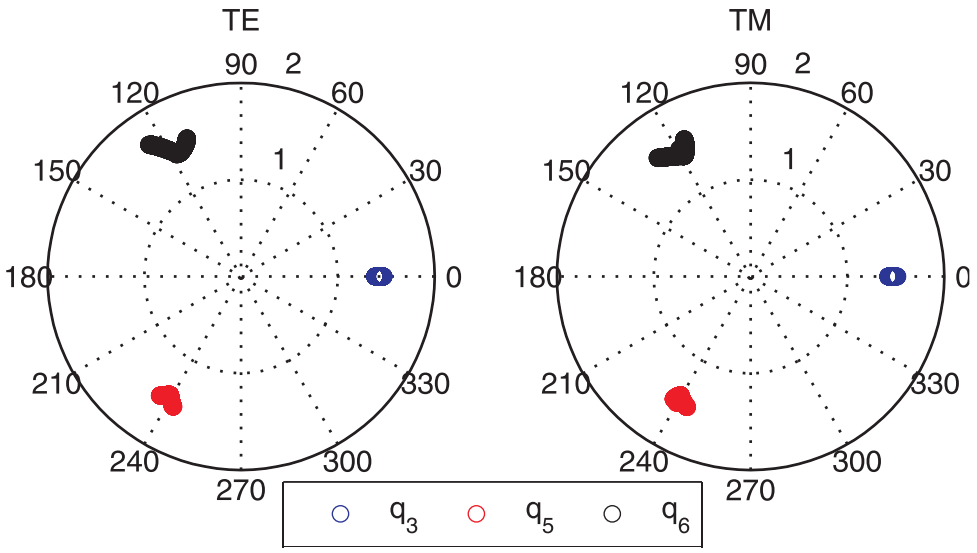

Figure 6.2.: Simulated sixport centres in the 1500 nm – 1600 nm band for both TE and TM polarisation..

$$\mathbf{S}_{wg}^{\mathrm{TE,TM}}(\lambda) = \begin{bmatrix} S_{11} & S_{12} \\ S_{21} & S_{22} \end{bmatrix} = \begin{bmatrix} 0 & \exp(-\mathrm{j}2\pi L n_{\mathrm{eff}}^{\mathrm{TE,TM}}/\lambda) \\ \exp(-\mathrm{j}2\pi L n_{\mathrm{eff}}^{\mathrm{TE,TM}}/\lambda) & 0 \end{bmatrix} \tag{6.1}$$

The S_{11} and S_{22} elements of the matrix are zero, because no reflection is expected from the waveguide. It is noteworthy that while the effective indices, $n_{\mathrm{eff}}^{\mathrm{TE}}(\lambda)$ and $n_{\mathrm{eff}}^{\mathrm{TM}}(\lambda)$, vary slowly with wavelength, the transmission parameters, S_{12} and S_{21}, can vary very rapidly depending on the length (L) of the waveguide. In order to avoid undersampling of the phase response of these terms, it is convenient to interpolate $n_{\mathrm{eff}}^{\mathrm{TE}}(\lambda)$ and $n_{\mathrm{eff}}^{\mathrm{TM}}(\lambda)$ to a much smaller wavelength step than the one used for electromagnetic simulation.

The electromagnetic simulation results of the MMIs are also stored in S-matrices. Again, the MMI response varies slowly with wavelength, but in order to avoid phase uncertainties when connecting two or more MMIs with a waveguide, the response of this devices was interpolated to the same wavelength step used for the waveguides.

The S-matrices of the MMIs and the waveguides were then connected according to the schematic shown in figure 6.1 using the algorithm described in [116, Ch. 10]. This yields a 7×7 S-matrix (because the sixport has a total of 7 ports) for each polarisation that contains all the amplitude and phase information of the complete junction. The sixport centres are then readily computed using equation (2.14). As mentioned in section 2.4.1, the centres of the sixport will actually rotate with wavelength, because of the wavelength dependent phase difference introduced by the ~ 2.2 mm long DUT waveguide. Since this effect is easily accounted for by calibration, and in order to facilitate visualisation, we will cancel out this rotation when plotting the centres. Figure 6.2 shows the simulated centres of the six-port junction for both TE and TM polarisation. Clearly, the centres are located at the desired amplitude (~ 1.5) and with 120°

SPICUM servicio de publicaciones

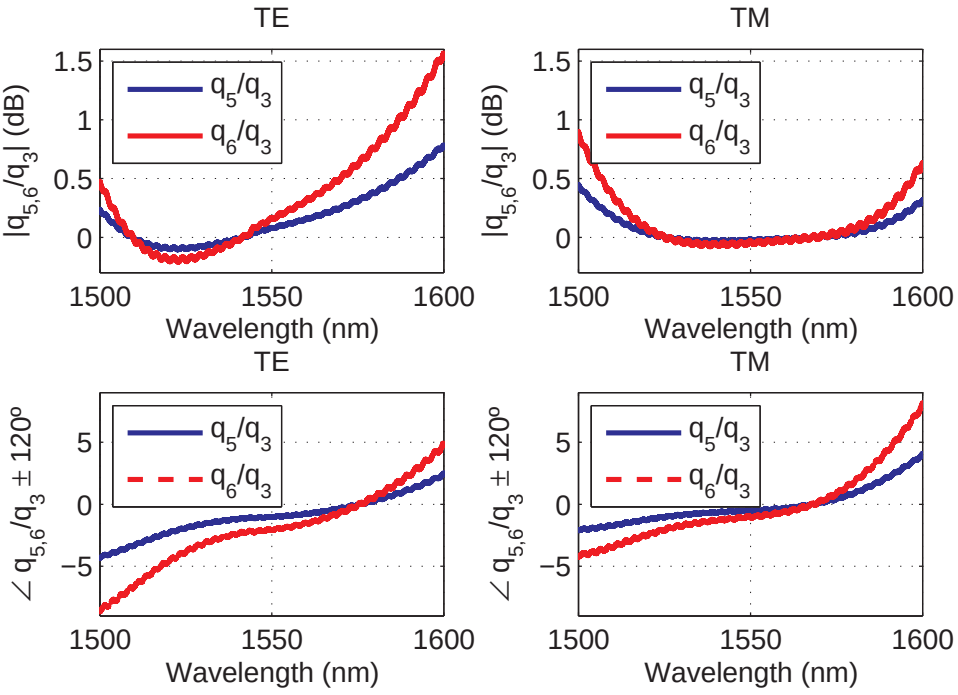

Figure 6.3.: Relative amplitude and phase of the six-port centres.

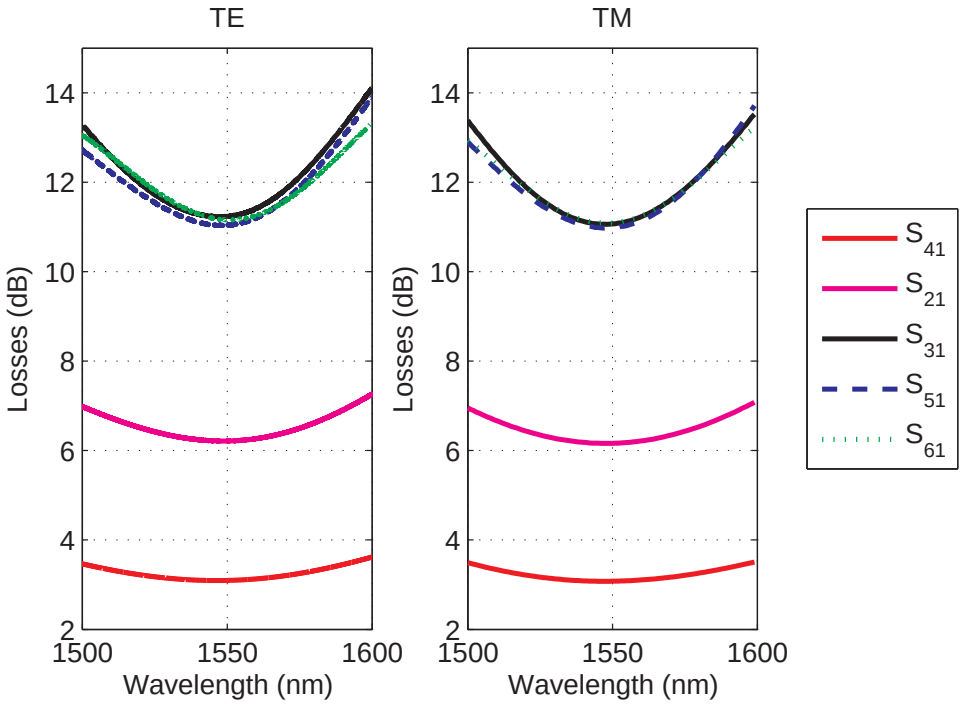

Figure 6.4.: Sixport losses.

SPICUM servicio de publicaciones

phase shifts, both of which vary only slightly with wavelength. From figure 6.3 we see that the centres are well balanced, with a maximum amplitude and phase error of 1.5 dB and 10° in the 1500 nm – 1600 nm band. Within the C-band, these errors are well below 1 dB and 5°. As discussed in section 5.10 these errors can be mainly attributed to the 2×3 MMI. When discussing the calibration of the sixport in section 2.4.2, we highlighted the importance of the six-port not coupling any power from the DUT port (port number 2) to the reference pot (port number 4). Indeed, the simulated S_{42} parameter is below −68 dB in the 1500 nm – 1600 nm band, so that power can only couple between these ports by reflection in port 1, which, in turn, depends on the quality of the anti-reflective coating deposited on the chip facets.

Finally, the expected losses of the device are given in figure 6.4, and found to be very similar for TE and TM polarisation. The reference port (number 4), exhibits the expected 3 dB losses at $\lambda = 1550$ nm, and has the flattest response, as the signal only travels through a single MMI. At the DUT port (number 2) around 6 dB are obtained, due to the two 2×2 splitters. At $\lambda = 1550$ nm the losses at the sixport outputs (port numbers 3, 5 and 6) are close to the ideal $-10\log_{10}(0.5 \times 0.5 \times 0.33) = 10.8$ dB and increase up to 14 dB at the band edges due to the combined wavelength response of the three MMIs.

SPICUM servicio de publicaciones

SPICUM
servicio de publicaciones

To define it rudely but not inaptly, engineering is the art of doing that well with one dollar which any bungler can do with two after a fashion.

Arthur M. Wellington.

7

Minimum Phase in Photonic Devices

THE FOCUS of this chapter and the next is on the characterisation of photonic devices. Here, we develop a general theory of minimum phase in photonic devices, that will be applied to the measurements in chapter 8. Minimum phase is particularly relevant to the characterisation of photonic devices, because unless sophisticated OFDR techniques are employed, the optical phase response cannot be measured. However, if a certain device exhibits minimum phase, its phase response can be directly computed from its wavelength-swept power response. Once the complete (amplitude and phase) response is known, it can be converted to the time domain by means of an inverse Fourier transform, yielding the impulse response, or reflectogram, of the device. While we have also proposed the use of this technique to detect spurious reflections [39], here we centre our attention on the removal of reflection artifacts that appear when a photonic device is measured without anti-reflective coating, as will be the case in the next chapter. This is achieved by filtering (or gating) of the impulse response, and is termed from now on as minimum phase temporal filtering (MPTF).

We outline the problem of facet reflections, as well as some previous results on minimum phase in optics in section 7.1. The concept of MPTF is rigorously defined in section 7.2 and mathematically analysed in section 7.3. As a result of this analysis we are able to establish a mathematical condition that assesses whether a photonic device is or not minimum phase. Section 7.4 deals with the practical requirements of the new technique, such as measurement bandwidth and resolution, and presents simulated and experimental results for multi-mode interference couplers in SOI without anti-reflective coating. Finally conclusions are drawn.

7.1. Introduction

Characterisation of integrated optical devices in research environments is often performed with a tunable laser source (TLS) as input and a detector at the device output which records the transmitted optical power as a function of wavelength. When a high refractive index platform, such as InP or SOI, is used, power reflections at the chip facets can be very strong (~ 30% of the power is reflected at SOI facets). In a waveguide this results in the well known Fabry-Perot fringes, which can be used to calculate pro-

SPICUM servicio de publicaciones

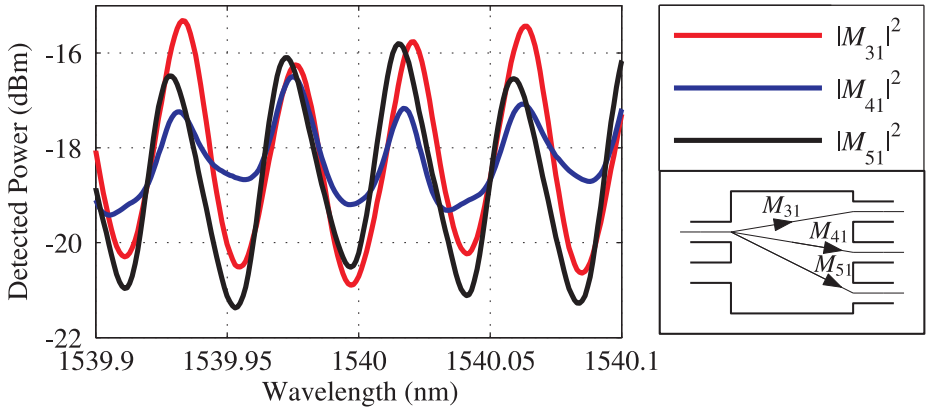

Figure 7.1.: Measured transmittance of a 2×3 MMI in SOI without AR coating.

pagation losses (see section 8.4 or reference [117]). However, for devices with several inputs and outputs more complicated interference patterns arise, because of the multiple sources of reflection. As an example, figure 7.1 shows the experimental response of the SOI 2×3 MMI designed in section 5.9, when measured without anti-reflective coating. The amplitude of the interference fringes is of 5 dB, thus completely obscuring the actual device response which is only expected to vary approximately 1 dB in the $1520 - 1580$ nm band. Hence it is often necessary to cover the chip facets with an anti-reflective coating prior to measurement. Nevertheless, the ability to measure propagation losses of reference waveguides on the chip, using the Fabry-Perot technique, is then lost. Furthermore, from cost point of view, it might be preferable to coat only those devices which are known to function correctly. This is why several methods have been proposed to characterise devices without anti-reflective coating [118, 119]. These are however limited to specific coupler configurations and depend on the value of the facet reflection coefficient.

Here we will show that using minimum phase techniques it is possible to compute a meaningful temporal (impulse) response of the device from wavelength swept power transmission measurements. The temporal response can then be filtered to eliminate the reflection artifacts and recover the desired device characteristics. The temporal data constitutes a reflectogram that is conceptually analogous to that obtained by Optical Frequency Domain Reflectometry (OFDR) [31], and can also be used for other time domain characterisation techniques, such as [120]. On the other hand, minimum phase techniques have been applied to the characterisation of Fibre Bragg Gratings [121–123], optical tomography [124] and the characterisation of nonlinear films [125], among others. The key issue of these techniques is to ensure that the system which is being analysed actually exhibits minimum phase characteristics [126–128]; if these are not fulfilled the accuracy of the technique is often affected negatively. This is why we eventually need to derive a condition that establishes if a certain photonic device exhibits minimum phase.

SPICUM servicio de publicaciones

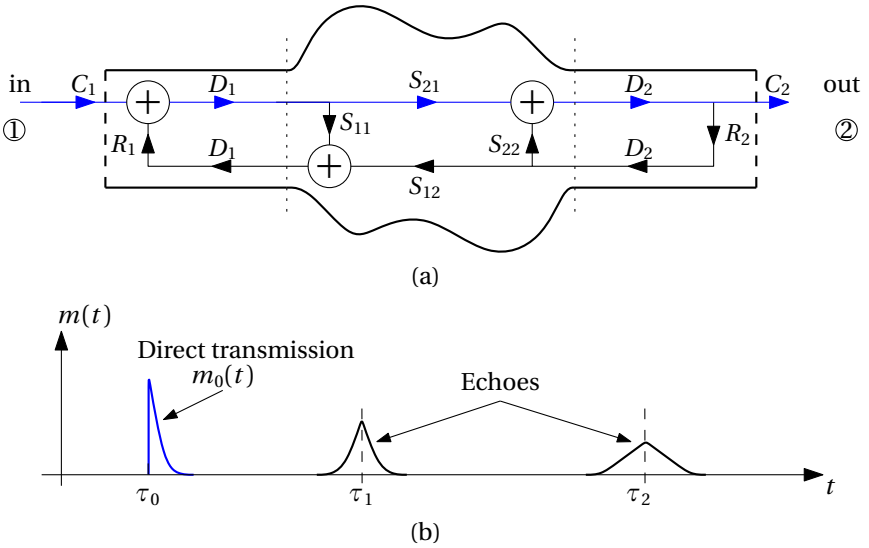

Figure 7.2.: Concept of minimum phase filtering.

7.2. MPTF concept

To illustrate the concept of MPTF, we will make use of the concept of impulse response, which we briefly reviewed in section 2.1. Let us consider light propagation inside a chip with reflecting facets as shown in Fig. 7.2(a). C_1 and C_2 are the input and output coupling efficiencies, and R_1, R_2 are the facet amplitude reflectivities. S_{21} and S_{12} represent the device's forward and backward amplitude response, whereas S_{11} and S_{22} are the device's input and output amplitude reflection coefficients. The single mode input and output waveguides are modelled as

$$D_i(\nu) = \exp(-\alpha L_i)\exp(-\mathrm{j}2\pi\nu n_{\mathrm{eff}} L_i/c), \tag{7.1}$$

with L_i the length of the waveguides, n_{eff} the effective index and α the loss coefficient. For simplicity, here we are neglecting waveguide dispersion. This does not affect our analysis, as long as the temporal effect of a waveguide can be considered to be a delay, i.e. its impulse response is much shorter than the impulse response of the device. The impulse response of the system in Fig. 7.2(a) is shown schematically in Fig. 7.2(b). It will typically consist of a direct transmission term, $m_0(t)$ corresponding to the first transmission through the chip, and a subsequent series echoes arising from internal reflections and facet reflections. The delay of the direct transmission term is τ_0, and the echoes occur at τ_i, $i > 0$.

When measuring an integrated optical system with a TLS and recording the optical output power, we obtain its power frequency response $|M(\nu)|^2$ (or, equivalently, the power wavelength response $|M(\lambda)|^2$). To recover the device's forward response, $|S_{21}(\nu)|^2$ from measurement data, we apply MPTF as follows:

- Calculate the *minimum* phase response, $\angle\tilde{M}(\nu)$, from $|M(\nu)|$. This is accomplished either by logarithmic Hilbert transformation [129, 130], or using iterative error reduction algorithms [125,131]. A detailed discussion of the former as well as a Matlab implementation can be found in appendix C.

SPICUM servicio de publicaciones

- Compute the minimum phase impulse response, $\tilde{m}(t)$, as the inverse Fourier transform of $|M(\nu)|\exp(\mathrm{j}\angle\tilde{M}(\nu))$.
- Filter the unwanted echoes from $\tilde{m}(t)$ and Fourier transform the direct transmission term, $\tilde{m}_0(t)$. As we show in the section 7.3, the square magnitude of the Fourier transform of $\tilde{m}_0(t)$ yields the direct power transmission through the chip:

$$|\tilde{M}_0(\nu)|^2 = |C_1|^2|C_2|^2\exp(-2\alpha(L_1+L_2))|S_{21}(\nu)|^2. \tag{7.2}$$

- The coupling and waveguide losses are obtained by measuring a reference waveguide and repeating steps 1-3, which yields $|\tilde{W}_0(\nu)|^2 = |C_1|^2|C_2|^2\exp(-2\alpha(L_1+L_2))$. The quotient $|\tilde{M}_0(\nu)|^2/|\tilde{W}_0(\nu)|^2$ then gives the desired parameter $|S_{21}(\nu)|^2$.

Naturally, filtering the direct transmission term is only possible if it is properly separated from the first echo. As discussed in section 7.4.1 this is usually the case if the device is not narrow-band, and will be assumed in the following. It is also noteworthy that instead of preserving only the direct transmission term, we could also isolate any of the echoes or a combination of both.

7.3. Theoretical framework

In this section we will provide the theoretical background of the MPTF technique. We proof the applicability of the MPTF algorithm for devices with a single optical path from input to output, as illustrated in Fig. 7.2(a). In the presence of multiple input and output waveguides, and hence multiple optical paths from input to output, the validity of the technique depends on the minimum phase nature of the device. A sufficient condition for such devices to exhibit minimum phase is derived, assuming, as above, that the separation between echoes be large.

7.3.1. Laplace transform and minimum phase

Before analysing the MPTF technique, it is convenient to recall some properties of the Laplace transform. Given a certain impulse response $m(t)$, its Laplace transform,which we will also refer to as transfer function, is defined as

$$M(s) = \int_{-\infty}^{+\infty} m(t)\exp(-st)\mathrm{d}t, \tag{7.3}$$

where $s = \sigma + \mathrm{j}2\pi\nu$ is the complex Laplace variable. Note that by setting $s = \mathrm{j}2\pi\nu$ in (7.3) the transfer function reduces to the Fourier transform of $m(t)$, that is, the frequency response $M(\nu)$.

In the following we will use two well known properties of the Laplace transform [126, 130]: i) A transfer function $M(s)$ is a minimum phase function, if and only if, all its poles and zeros are in the left-hand half plane. ii) If $M(s)$ is not minimum phase, it can be factored into a minimum phase function, $\tilde{M}(s)$, and an all pass function, $\bar{M}(s)$. The latter accounts for all the zeros of $M(s)$ in the right-hand half-plane and has unit magnitude, i.e., $|\bar{M}(\nu)| = 1$. From now on the $\tilde{}$ and $\bar{}$ symbols will be used to denote minimum phase and allpass functions, respectively.

SPICUM servicio de publicaciones

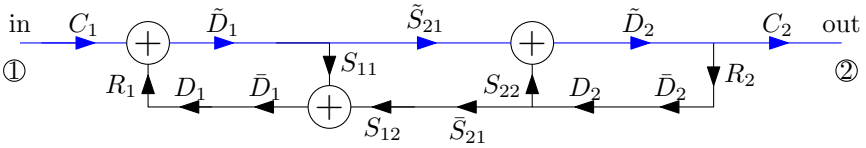

Figure 7.3.: Minimum phase signal flow graph.

7.3.2. Analysis of MPTF

Consider again the basic device with one input and one output waveguide and reflecting facets shown in Fig.7.2(a). We will now analytically examine the application of the MPTF algorithm to this system.

The transfer function of the system in Fig.7.2(a) can be obtained using Mason's rule [132], yielding

$$M(s) = \frac{C_1 D_1(s) S_{21}(s) D_2(s) C_2}{\Delta(s)} \tag{7.4}$$

The denominator is given by $\Delta = 1 - Q_1 - Q_2 - Q_3 + Q_1 Q_2$, the loop gains being $Q_{1,2} = D_{1,2}^2 S_{11,22} R_{1,2}$ and $Q_3 = D_1^2 D_2^2 S_{21} S_{12} R_1 R_2$, where the s dependence has been dropped for simplicity. The numerator is the gain of the only forward path from input to output. In a signal flow graph, a forward path is a path from input to output along which no node is encountered more than once. In an optical device this condition can be understood as the lightwave not travelling through the same waveguide in the same direction more than once. We shall now factor $M(s)$ into a minimum phase function and an all-pass function. Since $M(s)$ is the transfer function of a passive system, it is stable, so that all its poles are in the left-hand half-plane. The zeros of $M(s)$ arise from the zeros of its numerator and the poles of its denominator, $\Delta(s)$. All poles of $\Delta(s)$ are in the left-hand half-plane, since all transfer functions involved in the denominator are stable. Hence, the only right-hand half-plane zeros of $M(s)$ are those of its numerator. Thus, $M(s)$ may be factored as $M(s) = \tilde{M}(s)\bar{M}(s)$, with

$$\tilde{M}(s) = \frac{C_1 \tilde{D}_1(s) \tilde{S}_{21}(s) \tilde{D}_2(s) C_2}{\Delta(s)} \tag{7.5}$$

$$\bar{M}(s) = \bar{D}_1(s) \bar{S}_{21}(s) \bar{D}_2(s). \tag{7.6}$$

The minimum phase and all-pass parts of $D_{1,2}$ are $\tilde{D}_{1,2}(s) = \exp(-\alpha L_{1,2})$ and $\bar{D}_{1,2}(s) = \exp(-s n_{\text{eff}} L_{1,2}/c)$, because $\bar{D}_{1,2}(s)$ has a zero at $\sigma = +\infty$, and $|\bar{D}_{1,2}(s = \mathrm{j}2\pi\nu)| = 1$ (see also [133, Eq. 7]).

From (7.5) and (7.6) we see that $M(s)$ is not a minimum phase function. Consequently, the minimum phase information recovered from the measurement data, $|M(\nu)|^2$, is not the physical phase of the measurement setup, but the phase of a system with transfer function $\tilde{M}(s)$. The signal flow graph of $\tilde{M}(s)$, which is obtained by simple comparison of (7.4) and (7.5), is shown in Fig. 7.3. Note that the forward path contains the minimum phase terms, whose product yields the numerator of (7.5). The all-pass terms have been moved to the lower part of the loops, so that the loops gains (Q_i) that compose the numerator of (7.5) do not change. From Fig. 7.3 it is clear that the minimum phase impulse response, $\tilde{m}(t)$, is composed of a direct transmission term

$$\tilde{m}_0(t) = C_1 C_2 \exp(-\alpha(L_1 + L_2))\tilde{s}_{21}(t), \tag{7.7}$$

SPICUM servicio de publicaciones

and a series of echoes from the different feedback loops. If the waveguides are long enough to ensure that the echoes do not overlap with the direct transmission term, which in practical situations is often the case (see Section 7.4.1), the spurious echoes can be filtered. Fourier transforming the remaining $m_0(t)$ term, and taking the square magnitude of the result we find

$$|\tilde{M}_0(\nu)|^2 = |C_1|^2|C_2|^2 \exp(-2\alpha(L_1+L_2))|S_{21}(\nu)|^2, \tag{7.8}$$

since $|\tilde{S}_{21}(\nu)| = |S_{21}(\nu)|$. This equation is one the main results of this chapter. It shows that using the minimum phase information computed from the measurement data, $|M(\nu)|^2$, it is possible to recover the device's magnitude response, $|S_{21}(\nu)|^2$, multiplied by the total waveguide losses, $\exp(-2\alpha(L_1+L_2))$, and the total coupling losses, $|C_1|^2|C_2|^2$. As discussed in Section 7.2, these losses can be determined by measuring a reference waveguide, so that they can be cancelled from the device measurement. Naturally, this cancellation requires repeatable coupling characteristics, which are achieved if the reference waveguide and the device are close to one another, and their facets are polished to similar quality.

7.3.3. Minimum phase condition for general device configurations

In the previous section we have shown that in systems with a single forward path the MPTF technique successfully recovers the device response. Let us now consider more complex configurations with multiple forward paths, such as the 2×2 coupler shown in Fig. 7.4. To determine the minimum phase nature of such a system, it would be possible to explicitly compute the overall transfer function of the device with the reflecting facets and then study the position of its zeros. However, with the signal flow graph approach employed in the previous section, a general minimum phase condition, which provides a better insight into the problem, can be derived. Mason's rule for graphs with N forward paths reads [132]:

$$M(s) = \frac{1}{\Delta(s)}\left[\sum_{k=0}^{N} F_k(s)[1+\sum_{q_k} P_{q_k}(s)]\right], \tag{7.9}$$

where F_k is the gain of the k-th forward path, N is the number of forward paths, and $P_{q_k}(s)$ is a product of loop gains of those loops that do not touch the k-th forward path. Since the numerator of $M(s)$ is now a sum of several terms, $M(s)$ cannot be easily factored into a minimum phase and an all-pass function as in (7.5) and (7.6). However, in many practical situation, including multi-mode interference couplers (see Section 7.4.1), the delay introduced by the waveguides is much larger than the impulse response of the device. As we show in appendix B, this fact can be exploited to derive a sufficient condition for the minimum phase part of $M(s)$ to contain all the relevant information on the device. This condition is given by

$$\boxed{|F_0| > \sum_{k=1}^{N}|F_k| + \sum_{k=0}^{N}|F_k|\sum_{q_k}|P_{q_k}|,} \tag{7.10}$$

and constitutes an important result of this chapter. It states that *if the gain of the shortest forward path (or direct transmission) is larger then the sum of the gains of the*

SPICUM servicio de publicaciones

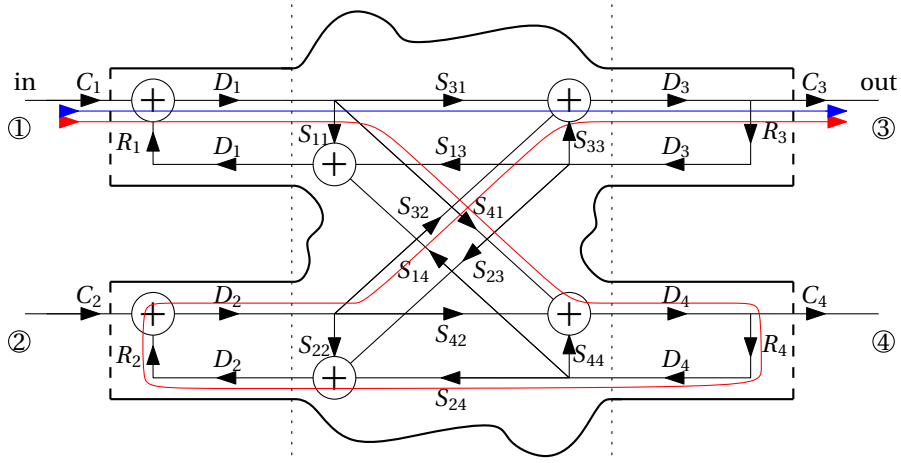

Figure 7.4.: 2×2 coupler with signal flow graph. The two forward paths are shown as blue and red lines.

remaining paths (and the relevant loop gains), the associated impulse response is a minimum phase function (with exception of the initial delay). In the case of a device with a single forward path such as the one analysed in section 7.3.2, (7.10) holds always, since it reduces to $|F_0| > 0$. This is because if there is only one forward path $N = 0$ and $P_{q_k} = 0$ because all loops touch the forward path.

As an application example of (7.10) consider the 2×2 coupler illustrated in figure 7.4 . Using Mason's rule and dropping the common delay of both forward paths ($D_1 D_3$), we find $V = F_0 + F_1 + F_0 P_0$,where $F_0 = S_{31} C_1 C_3$, $P_0 = R_2 R_4 S_{42} S_{24} D_2^2 D_4^2$ and $F_1 = S_{41} S_{24} S_{32} R_4 R_2 D_2^2 D_4^2 C_1 C_3$. Neglecting waveguide losses and setting $S_{ij} = 1/\sqrt{2}$ ($i \neq j$), $S_{ii} = 0$, $R_i = 0.56$, which is the approximate Fresnel reflection coefficient for a silicon-air interface as encountered in SOI technology, we find: $|F_0| \approx 0.71|C_1 C_3| > |F_1| + |F_0||P_0| \approx (0.11 + 0.11)|C_1 C_3|$. Hence, the measured data corresponds to a minimum phase function.

While the derivation of the minimum phase condition (7.10) is focused on integrated optical devices, it is expected to hold for more general systems, too, as long as the impulse response consists of short, well separated pulses. In fact, it agrees well with previously published results in other areas. In [125] it was found by simulation that an impulse response with two peaks of comparable magnitude could still be successfully processed using minimum phase techniques, whereas in the presence of a third peak the results were less accurate. Neglecting the P_{q_k} terms in (7.10) and setting $N = 2$, we find $|F_0| > |F_1|$, that is, the impulse response actually remains minimum phase as long as the second peak is only marginally smaller than the first one. On the other hand, for $N = 3$ we have $|F_0| > |F_1| + |F_2|$, which is obviously not fulfilled with three peaks of comparable magnitude, so that the impulse response can no longer be assured to be a minimum phase function. In another paper [134] it is shown experimentally that by artificially adding an impulse at the origin to an arbitrary impulse response function, the sum becomes a minimum phase function. In the treatment presented here this technique consist in increasing the value of $|F_0|$ until (7.10) holds.

SPICUM servicio de publicaciones

7.4. Application

The practical application of the MPTF technique is discussed in this section. First, measurement setup requirements are studied and found to be readily realisable. Simulations for MMIs on SOI are carried out and confirm the accuracy of the technique. Finally a 2 × 3 MMI on SOI without AR coating is experimentally characterised, and some considerations on the extension of the technique to narrow band devices are given.

7.4.1. Practical Considerations

In this section we will address some practical limitations which have to be taken into account to assure that the algorithm presented in the previous section yields accurate results.

First, and referring to figure 7.2(b), the separation of the first echo and the direct transmission has to be large enough for the two pulses to be clearly separated. The duration of the direct transmission pulse is approximately given by the reciprocal of the couplers bandwidth, whereas the delay of the first echo is bound by the shortest input or output waveguide. From this, the minimum waveguide length is found to be:

$$L_{\min} \gg \frac{\lambda_0^2}{\mathrm{BW}_{\mathrm{DUT}} n_g}, \tag{7.11}$$

where $\mathrm{BW}_{\mathrm{DUT}}$ is the DUT's 3 dB bandwidth, and n_g is the group index. In micrometer scale SOI rib waveguides the group index is approximately $n_g \approx 3.6$. Assuming a coupler bandwidth $\mathrm{BW}_{\mathrm{DUT}} = 30\,\mathrm{nm}$ at $\lambda_0 = 1550\,\mathrm{nm}$, we find $L_{\min} \gg 20\,\mu\mathrm{m}$, which is verified in virtually any practical layout.

Second, measuring $|M(\nu)|^2$ in a limited bandwidth determines the temporal resolution with which the impulse response can be computed. Equivalently it limits the minimum spatial separation of two reflections that can still be distinguished. Imposing that this separation be the physical length of the device under test, the following criterion for the measurement bandwidth is readily derived:

$$\mathrm{BW}_{\mathrm{meas}} \gg \frac{\lambda_0^2}{L_{\mathrm{DUT}} n_g}. \tag{7.12}$$

Note that (7.12) is very similar to the equation (2.11) that determines the spatial resolution of a OFDR measurements. For a coupler length of $L_{\mathrm{DUT}} = 300\,\mu\mathrm{m}$, and the same parameters as before, we find $\mathrm{BW}_{\mathrm{meas}} \gg 2\,\mathrm{nm}$. With most moderns lasers sweeping 60 nm or 100 nm of bandwidth is unproblematic, so that condition (7.12) can be readily fulfilled.

Finally, the required spectral resolution of the measurement is determined by the Nyquist criterion: the sampling of the frequency response has to be fine enough to avoid temporal aliasing of the impulse response, $m(t)$. Taking into account that $m(t)$ consist of a series of echoes from the chip facets, we find:

$$\Lambda \ll \frac{\lambda_0^2}{L_{\max} n_g}, \tag{7.13}$$

SPICUM servicio de publicaciones

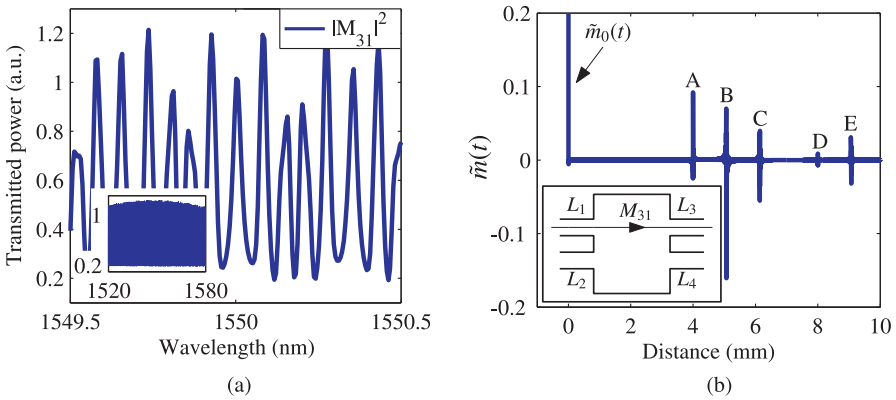

Figure 7.5.: (a) Simulated power transmission of a 2×2 MMI in SOI without AR coating. The device layout is shown schematically in the inset of figure 7.5(b). (b) Computed minimum phase impulse response.

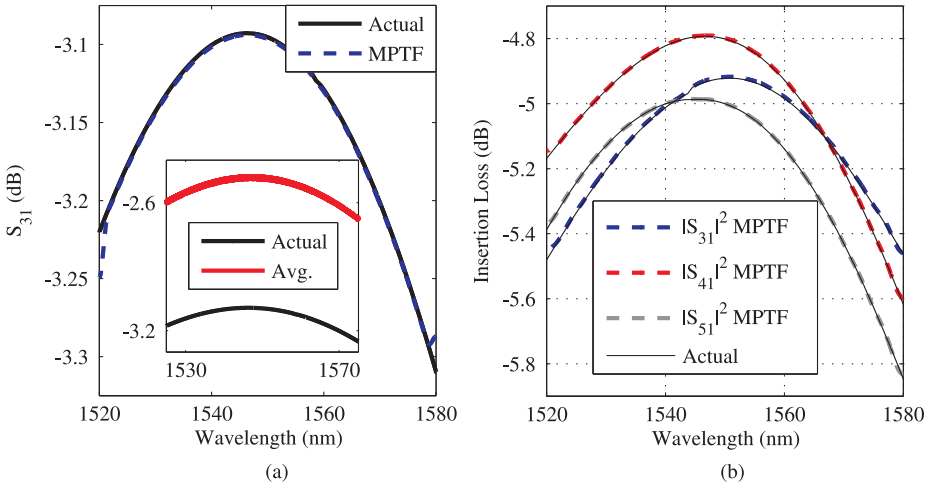

Figure 7.6.: Recovered coupler parameters for (a) a 2×2 MMI and (b) a 2×3 MMI.

where Λ is the spectral resolution and $L_{\max}$ is the length of the longest round-trip in the device. A chip length of 1 cm (and an associated round-trip of 2 cm), would require $\Lambda \ll 0.04$ nm. The adequate spectral resolution is also easily identified experimentally by ensuring that the interference fringes are smoothly sampled.

7.4.2. Simulations

We shall now assess the performance of the MPTF technique in two simulated scenarios: the paired 2×2 MMI and the 2×3 MMI designed in chapter 5, both with strong facet reflections from the silicon-air facets.

The transmission and reflection of the couplers and the dispersion characteristics of the input and output waveguides were simulated with the Fimmwave tool. The reflecting facets were simply modelled as a constant Fresnel reflection amplitude coefficient $R = 0.56$, and perfect coupling was assumed for simplicity. Using the S-matrix

SPICUM servicio de publicaciones

approach described in section 6.2, the waveguides, the reflecting facets and the MMI were then connected. The overall spectral response consists of 12000 data points in the 1520 nm to1580 nm band, i.e., a spectral resolution of 0.005 nm. As expected, the resulting power transmission ($|M_{31}|^2$) through the 2×2 coupler exhibits strong and complex fringes, as shown in figure 7.5(a). The minimum phase of $|M_{31}(\nu)|$ was computed using the logarithmic Hilbert transform approach (see appendix C for details) and the minimum phase impulse response, $\tilde{m}(t)$, was obtained by an inverse Fast Fourier Transform (FFT). The processing time for these two operations is about 30 ms using Matlab on a 1.6 GHz notebook. Figure 7.5(b) shows $\tilde{m}(t)$, where the time axis has been conveniently scaled to represent propagation distance.

The length of the input and output waveguides of the the MMI are $L_1 = 1$ mm, $L_2 = 2$ mm, $L_3 = 3$ mm and $L_4 = 4$ mm [see inset of figure 7.5(b)], and they were chosen to illustrate that $\tilde{m}(t)$ has indeed physical meaning. Specifically, the echoes labelled A through E can be associated with different round trips in the coupler. Echo A arises from the propagation through waveguides $1 \rightarrow 3 \rightarrow 1 \rightarrow 3$, which is delayed4 mm with respect to direct path $1 \rightarrow 3$. Echo B results from the trips $1 \rightarrow 3 \rightarrow 2 \rightarrow 3$ and $1 \rightarrow 4 \rightarrow 1 \rightarrow 3$, and C from $1 \rightarrow 4 \rightarrow 2 \rightarrow 3$. D is the echo of the echo of A, and E is a combination of A and B.

A 5 ps wide smooth Kaiser window was used to filter the unwanted echoes and the remaining direct transmission, $m_0(t)$, was Fourier transformed, yielding the recovered response shown in figure 7.6(a). An excellent agreement between the original response and the MPTF processed data is achieved. The minor deviations at the band edges are an artifact of the Fourier expansion. The inset of figure 7.6(a) demonstrates that simple averaging of the measurement data ($|M_{31}|^2$) does not generally yield accurate results. The 2×3 coupler was simulated with 5.4 mm long input waveguides and 1.9 mm long output waveguides to emulate the physical device layout, and with the same bandwidth and resolution as the 2×2 coupler. The coupler response recovered by MPTF is plotted in figure 7.6(b), and overlaps almost perfectly with the original data, hence confirming the validity of the technique for this coupler configuration, too.

7.4.3. Experiment

As a practical example of MPTF we will now apply it to the characterisation of the 2×3 MMI coupler designed in section 5.9. Here we will focus on the use of the MPTF technique, rather than how the measurements were carried out. The latter are described in detail in section 8.3. The power transmission of the coupler without anti-reflective coatings was measured by injecting light into one of its inputs with a lensed fibre, and collecting the output with a microscope objective. The Fresnel power reflection coefficient at the facets is estimated to be 30%. Measurements of the coupler were taken in the 1480 nm to 1580 nm band, with a resolution of 0.001 nm, which takes about one minute using swept measurements. The strong interference patterns in the measurement data were shown in figure 7.1, and completely mask the coupler response. For calibration purposes a reference waveguide on the same chip as the coupler was also measured. Figure 7.7(a) shows the MPTF processed transmission of the reference waveguide, which includes coupling and waveguide losses, as well as laser sweep power

SPICUM servicio de publicaciones

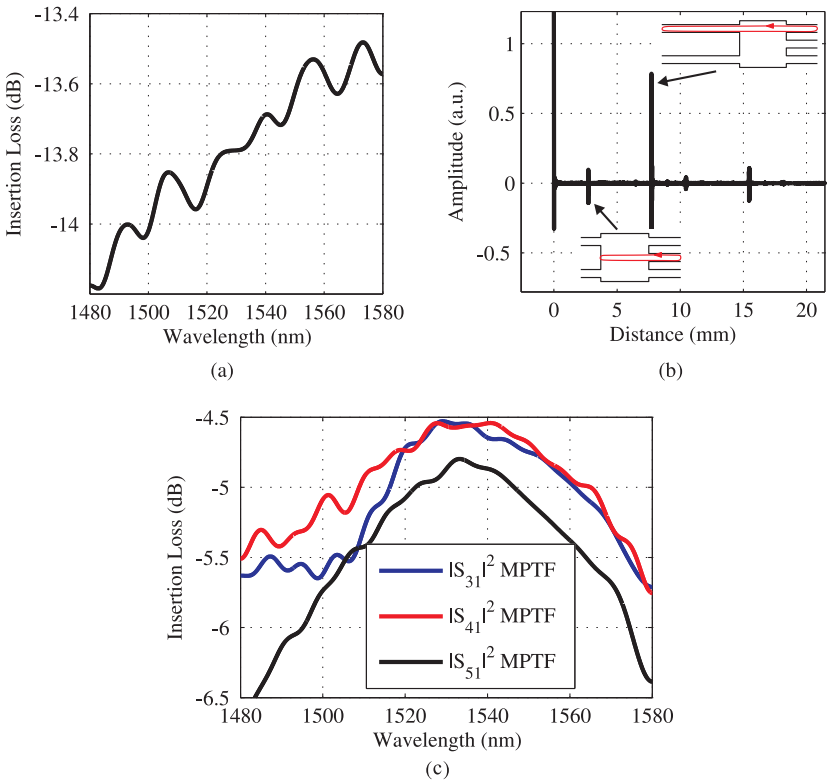

Figure 7.7.: (a) MPTF processed calibration data. (b) Minimum phase impulse response or reflectogram (c) Recovered coupler response.

nonlinearities. The minimum phase impulse response is plotted in figure 7.7(b). This reflectogram clearly shows the facet reflection at a distance of ~ 7.7 mm (which corresponds to the length of the chip), and also reveals a weak reflection at ~ 2.7 mm. The latter arises as follows: the input light travels through the MMI, is reflected back at the chip output facet, and is re-reflected at the beginning of the MMI multimode region [see inset in figure 7.7(b)]; the distance between beginning of the multimode region and the chip output facet is ~ 2.7 mm. The processed coupler data divided by the reference data is plotted in figure 7.7(c). Due to fabrication tolerances the experimental wavelength response is slightly shifted with respect to the simulated data given in figure 7.6(b), but both the absolute insertion loss as well as the shape of the curves are in good agreement with the simulations.

7.4.4. Application to narrow band devices

While we have focused our discussion on broadband devices, the MPTF technique could be extended to narrow band devices such as ring resonators. Naturally, these devices must exhibit minimum phase, which for ring-resonators is only the case if the coupling coefficient is smaller than the roundtrip losses. Since the impulse response of ring resonators is long, the length of the input and output waveguides must be such that there is no overlap between the direct transmission and the echoes. Finally, the

SPICUM servicio de publicaciones

temporal filtering window has to be chosen adequately. If the passband information is of particular importance, smooth temporal windows should be employed. Good reproduction of the resonances requires rectangular windows, which exhibit higher spectral resolution [135, Ch. 11.2].

7.5. Conclusions

If a device exhibits minimum phase, its optical phase response can be directly computed from the wavelength swept power transmission measurement. In this chapter we have derived a sufficient condition, equation (7.10), to assess the minimum phase behaviour of photonic devices. MMI couplers have been shown to be essentially minimum phase devices, which enables the computation of their complete (amplitude and phase) transfer function only from power transmission measurements. The impulse response or reflectogram of the device can then be computed via an inverse Fourier transform. While this reflectogram could be employed in a variety of ways, here we have focused on filtering unwanted artifacts arising from the facet reflections in uncoated devices. This typically requires power transmission measurements in a bandwidth of around 60 nm with a spectral resolution of ~ 0.005 nm, both of which are readily achieved with swept measurements. We have demonstrated that with this technique both 2×2 and 2×3 MMIs can be characterised accurately without need for anti-reflective coatings.

SPICUM servicio de publicaciones

8
Fabrication and Measurements

THE EXPERIMENTAL results of this thesis are presented here. While device fabrication was carried out in an external foundry (the Canadian Photonic Fabrication Center), we will give some important considerations regarding the design of the mask, i.e. the "blueprint" of the photonic circuit, in section 8.1. The specifications for the fabrication of the devices are given in section 8.2, and a brief description of the experimental setup will be provided in section 8.3. Waveguide losses are measured in section 8.4 and found to be as low as 0.25 dB/cm. Characterisation of the 2×2 MMIs confirms the high performance and good fabrication tolerance that are anticipated by simulation (section 8.5). A simple technique to measure the six-port centres is presented in section 8.6, and the amplitude and phase imbalance of the centres is determined to be below 0.5 dB and 5°, respectively.

8.1. Mask design

The mask is the starting point for fabrication and contains all the geometrical features (or patterns) that will be transferred to the wafer by lithography, i.e. by shining light through the mask onto the photoresist covering the wafer (see also section 3.1). A mask typically consist of a number of images, that can be transferred to the wafer independently from each other. This is achieved by covering the remaining images with metal blades that block the light, so that the photoresist is only exposed by the desired image. For instance, the mask shown on the left hand side of figure 8.1 contains three images (called A, B and C), which appear as the large rectangular areas filled with finer blue structures. Normally, each image, once transferred to the wafer, makes up a chip or die. Since the size of the wafer is typically much larger than the size of the mask (in our case the mask diameter is 31 mm and the wafer diameter is 6" = 152.4 mm), each image can be repeated several times on the wafer, resulting in a number of (nominally) identical chips. In our case, the three types of chips were distributed on the wafer as shown in figure 8.2. This layout was motivated by two reasons. First, lens distorsion is minimal in the centre of the wafer, so image B, which contains the most important test structures, was placed there. Second, the height of the silicon layer on the wafer, as well as the etching conditions vary on a centimetre scale, so that in

SPICUM servicio de publicaciones

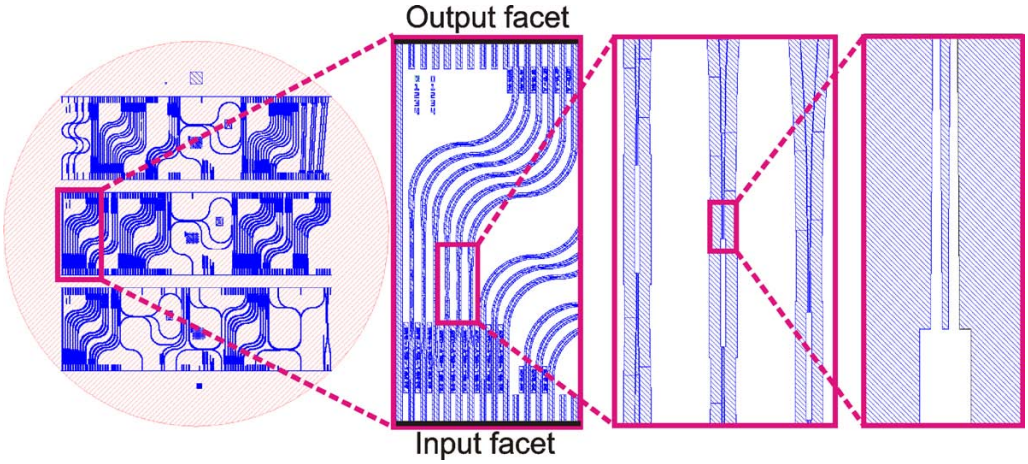

Figure 8.1.: Mask design for six-port, MMIs and several test structures. The different levels of zoom show, from left to right, the complete mask, a set of MMI test structures, three adjacent MMIs with input and output s-bends, and the tapered output waveguides of a MMI (shown as white space).

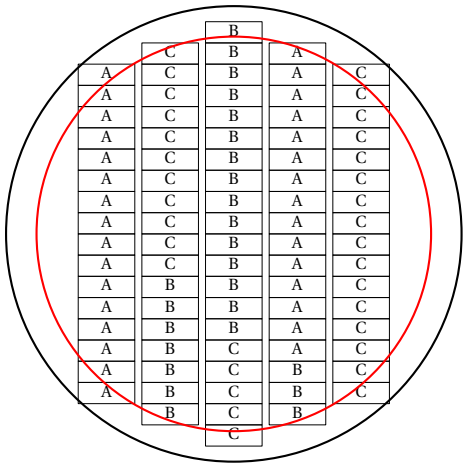

Figure 8.2: Layout of the images on the wafer. Only the images inside the red line yield valid chips.

principle it is interesting to have images of every type everywhere on the wafer. This is why some of the B images were placed on the left and right of the central column.

Each chip has two optical facets through which light is coupled in and out the waveguides (see second image from the left in figure 8.1). In order to make these facets accessible, the wafer has to be cut (or diced) along the lines shown in figure 8.2. Note that a cut in the vertical direction (between columns) merely separates the strips of chips, whereas a cut in the horizontal direction (along the long side of the chips) give access to the facet of the chip above the cut and the facet of the chip below it. However, the cut is produced with a mechanical saw that is relatively thick (of the order of 50µm), so that the position of the cut cannot be controlled very precisely. If the cut is made too far above the junction of the chips, the waveguides of the lower chip may not reach facets, which renders the chip useless. To avoid this, within each image waveguide stubs are placed opposite each waveguide end, as shown in figure 8.3. Several

SPICUM servicio de publicaciones

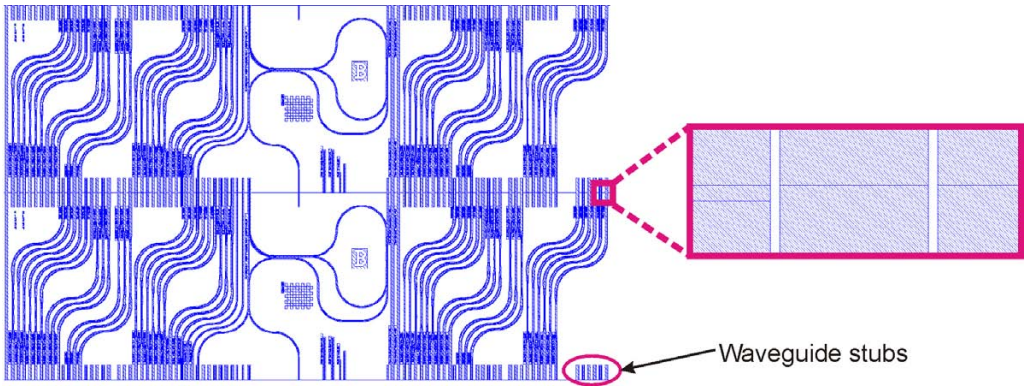

Figure 8.3.: "Stitching" of two identical images placed one below the other. The magnified area shows how two waveguides from different chips are joined together. The waveguides are shown as white space.

images of the same type can then be "stitched" together below one another, with the stubs providing an extension of the waveguides of one chip into the next chip, so that even if the cut is slightly misaligned, the waveguides of both chip reach the facet. This, of course, does not work for chips corresponding to different images. After dicing, the chip facets are polished to optical quality.

A further important consideration is etch density, i.e., the relative amount of wafer surface that is removed by etching. In this particular fabrication process it should be kept around 30 %, so that only trenches around the waveguides are etched away. Consequently, in the mask layout, instead of drawing the actual waveguides, the trenches around them are specified (see the two rightmost images in figure 8.1).

Due to the large amount of components in the mask, as well as the added complexity of generating the waveguide stubs and the trenches, manually drawing the mask did not seem a feasible approach. Instead, we made use of the scripting capabilities of Autocad and, using Visual Basic, we developed a simple library of functions to draw waveguides, curves, s-bends, tapers, and MMIs. Each function takes a pair of start coordinates and the dimensions of the device as parameters, draws the structure, and returns one or more pairs of end coordinates that can be used to connect new devices. The short piece of code below, which draws a MMI connected to a s-bend, illustrates this.

```
md.origin(0) = 0
md.origin(1) = 0
md.rotationAngle = 0
mmi2x2cp = drawMMI2x2(md)

sd.origin(0) = mmi2x2cp.downRight(0)
sd.origin(1) = mmi2x2cp.downRight(1)
sd.type = "downRight"
sd.rotationAngle = 0
scp = drawSbend(sd)
```

Here, `md` is a register that has been initialised with the dimensions of the MMI, and `sd`

SPICUM servicio de publicaciones

is a register with the dimensions of a standard s-bend. First, we define the origin of the MMI to be (0,0), and indicate that it should not be rotated. The function `drawMMI2x2` draws the MMI, and returns the coordinates of its endpoints in `mmi2x2cp`. We then initialise the starting coordinates of the s-bend with the lower right input waveguide of the MMI, and indicate that we want to draw the sbend down and to the right, and with zero rotation. `drawSbend` then draws the s-bend at the desired position and returns its endpoint in the variable `scp`. With this approach, the number of non-systematic errors in the layout is reduced, and, once all the functions are in place, mask generation is relatively fast and flexible.

8.2. Fabrication specifications

The specification that were passed on to the foundry for the fabrication of the circuits will be briefly enumerated here.

While the etch depth that was considered for the design of both the waveguides and the MMIs is $D = 0.70\mu m$, for final fabrication $D = 0.75\mu m$ was specified. This was done to compensate both for waveguide dishing and microloading between the MMI access waveguides (see section 3.1). The latter is of particular importance since it avoids coupling that could arise from too shallowly etched MMI input and output waveguides. The MMIs themselves are not expected to affected by this change, since they are relatively etch depth tolerant. Regarding the interconnecting the waveguides, no indication of multi-mode behaviour was found in the measurements (section 8.4).

Normally rib sidewalls are not perfectly vertical, but present a small angle, which makes the waveguide a little bit wider at the bottom. This has no sizeable impact on waveguide performance, but MMIs have been shown to be very sensitive to width variations. We found by simulation that if there is a small sidewall angle, it is preferable that the bottom width of the waveguide (instead of the top width) matches the specifications. Thus all widths were specified as bottom widths.

The most critical dimension in our design is the width of the 2×3 MMI, which is, however, to large to measure it directly. Instead a waveguide close to the 2×3 MMI is used to monitor the width offset during fabrication.

The thickness of the bottom oxide layer was $1\mu m$, which, owing to the $1.5\mu m$ thick silicon layer, is enough to prevent substrate leakage. The top cladding of the chip was a $0.5\mu m$–$1\mu m$ thick silicon dioxide (SiO_2) layer produced with plasma enhanced chemical vapour deposition (PECVD).

8.3. Measurement setup

The measurement setup employed to characterise the designs is illustrated schematically in figure 8.4. Linearly polarised light from a tunable laser source is rotated to horizontal (TE) or vertical (TM) with a polarisation controller. To launch light into the circuit, a polarisation maintaining lensed fibre mounted on a micro-positioning block is aligned in front of the chip, as shown in figure 8.5. At the output light is collected with a microscope objective, and the orthogonal polarisation state is filtered with a polarisation analyser. Using a flip down mirror the light can then be directed

SPICUM servicio de publicaciones

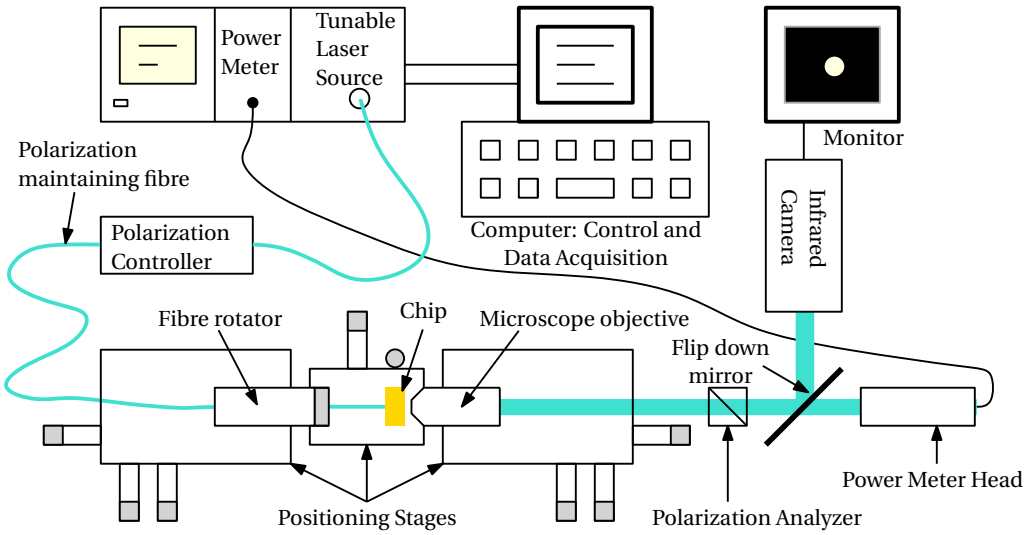

Figure 8.4.: Sketch of the measurement setup used to characterise the devices.

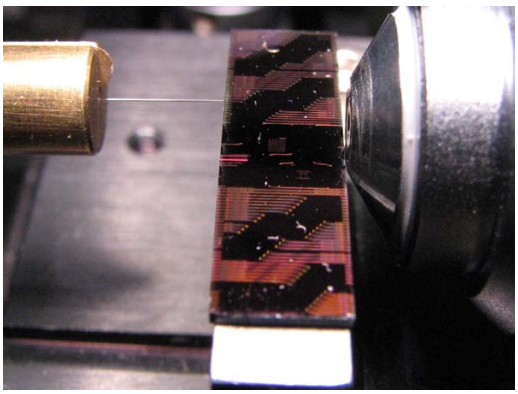

Figure 8.5: A tapered fibre (left hand side) is used to launch light into the circuit (centre), and the output light is collected with a microscope objective (right hand side).

either to a power detector or a infrarad camera connected to a monitor. The latter is used for the coarse alignment of the chip with the input fibre and the microscope objective. For fine tuning of the alignment as well as the actual measurements the photodetector is used. The wavelength response of the device that is being tested is then obtained by sweeping the wavelength of the tunable laser source.

Since we directly detect the light output from the chip, without having it interfere with the input light, only the power response of the devices is recorded, while the optical phase information is lost. Since the chips have no anti-reflective coating, and approximately 31 % of the optical power is reflected from the silicon-air facet, the measurements are obscured by Fabry-Perot fringes. However, as discussed in chapter 7, by using minimum phase techniques the actual optical phase can be recovered for the devices considered here. This, in turn, enables reconstruction of the impulse response and effective filtering (or gating) of the reflection artifacts. Still, a proper, high resolution sampling of the fringes is required for the processing to yield correct results. This is why using swept, i.e. continuous measurements as opposed to stepped measurements is crucial, since it allows for measurements in a large wavelength range (~ 100 nm) with a high spectral resolution (~ 0.001 nm) in a reasonable amount

SPICUM servicio de publicaciones

of time (~ 1 min). Unless otherwise stated, all measurements presented in this chapter have been adequately processed with the minimum phase technique presented in chapter 7 to remove the effect of facet reflections.

8.4. Waveguides

In this section we will verify the single-mode behaviour of the interconnecting waveguides and compute their propagation losses, which are found to be ~ 0.25 dB/cm for TE polarisation and ~ 2 dB/cm for TM polarisation.

There is probably no direct experimental method to proof that a rib waveguide is actually single-moded. However, there are two checks that are usually performed. The first one consists in aligning the waveguide and examining the output profile of the waveguide on a monitor. The input fibre is then slightly moved from its optimum position; if the waveguide is single moded this simply results in an attenuation of the output field. If, on the contrary, the shape of the output field changes, higher order modes can be present. The waveguide examined here showed a smooth attenuation of the output field as the input fibre was moved, which signals that they are single-moded. In a second test, the transmission spectrum of the waveguide is recorded and the Fabry-Perot fringes arising from facet reflections are examined. If several modes propagate along the waveguide, the fringes will exhibit anomalous peaks, due to the interference of modes with different propagation constants. The fabricated waveguide had simple, clean Fabry-Perot fringes as shown in figure 8.6(a), which again indicates that only a single mode is propagating.

Facet reflections also facilitate the measurement of waveguide losses via the well known Fabry-Perot resonance method [117]: the losses are computed from the maxima and minima of the fringes as:

$$L[\mathrm{dB}] = -10\log_{10}\left[\frac{1}{\Gamma^2}\frac{\sqrt{P_{\max}}-\sqrt{P_{\min}}}{\sqrt{P_{\max}}+\sqrt{P_{\min}}}\right] \tag{8.1}$$

where Γ^2 is the power reflectivity of the waveguide facets. We may estimate Γ^2 as the Fresnel reflection coefficient $\Gamma^2 = [(n_{\mathrm{Si}} - n_{\mathrm{air}})/(n_{\mathrm{Si}} + n_{\mathrm{air}})]^2 = 0.31 = 5.1$ dB, because the input and output waveguides are adiabatically tapered to a width at 3 µm at the facets, so that it is reasonable to say that the light is completely confined within the silicon waveguide. Applying equation (8.1) for several wavelength, we obtain the propagation losses shown in figure 8.6(b). Alternatively, MPTF can be used to calculate the transfer function of the direct transmission, $D(\lambda)$, and of the "echo", $R(\lambda)$. Since the echo is first reflected by the end facet, then travels back the waveguide, is reflected by the input facet and travels again to the output, we have $R(\lambda)/D(\lambda) = \Gamma\sqrt{L}\Gamma\sqrt{L} = \Gamma^2 L$. The losses obtained by this method coincide with those shown in figure 8.6(b). It has to be highlighted that for TE polarisation a consistently low loss of around 0.25 dB/cm is obtained. TM polarisation exhibits losses of ~ 2 dB/cm, which is still a very practical value. We were not able to determine the exact cause of the loss difference between the two polarisation states, but a certain polarisation dependence is observed in other micrometric rib waveguides, too [136].

Waveguides with several 90° curves with a 900 µm radius, s-bends and tapers were also measured and the insertion loss of these elements was found to be negligible.

SPICUM servicio de publicaciones

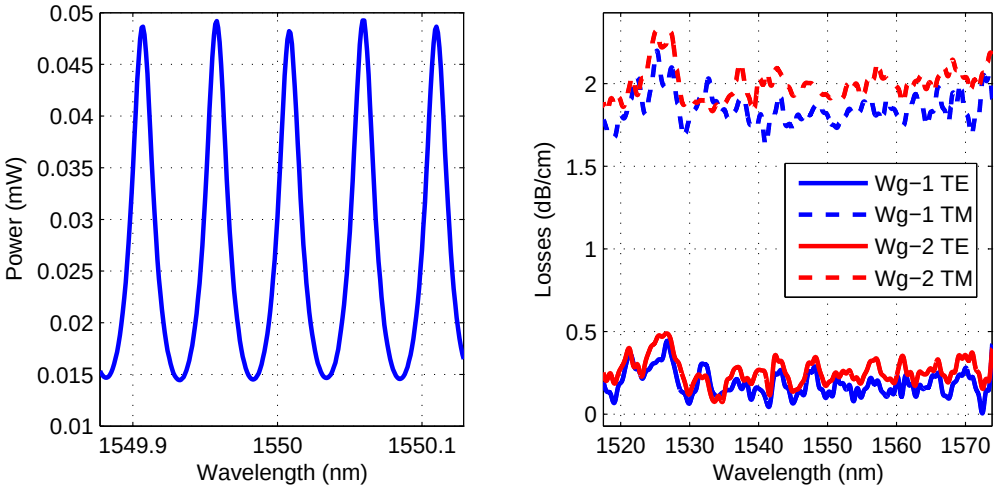

(a) Fabry-Perot fringes. **(b)** Extracted waveguide losses.

Figure 8.6.: Results of waveguide characterisation.

8.5. MMIs

We will now demonstrate that with the design technique presented in chapter 5, shallowly etched MMIs with high performance and relaxed fabrication tolerances are indeed attained. Both single MMIs as well two back-to-back MMIs in a Mach-Zehnder (MZI) configuration are employed for device characterisation. Some considerations on the design of the test structures will be given in section 8.5.1, before we present the experimental results in section 8.5.2.

8.5.1. Design of test structures

For device characterisation, both test structures with a single MMI and MZI consisting of two couplers (see figure 8.7) were used. When launching light into a planar lightwave circuit waveguide with an optical fibre, the mismatch between their optical fields and optical scattering result in stray light which can degrade the performance of MMIs [137]. To mitigate this effect, all test structures included two bends, with a lateral offset of ~ 1.8 mm between the input and output waveguides, reducing the amount of stray light detected at the output. After the MMI the waveguides are sufficiently separated to exhibit negligible coupling over several centimetres, using small s-bends not shown in the schematic in figure 8.7. Reference waveguides with the same bends as the test structures were also included on each chip.

When measuring the MZI structure shown in figure 8.7, we found that stray light originating at the output facets of the second MMI can distort the weak bar output. Hence, it is important to ensure that the output is not only offset with respect to the input waveguide, but also with respect to the MMIs. Measurement of the extinction ratio (P_C/P_B) between the cross and bar outputs of the MZI provides simultaneous information on phase error and imbalance of the individual couplers. Using the am-

SPICUM servicio de publicaciones

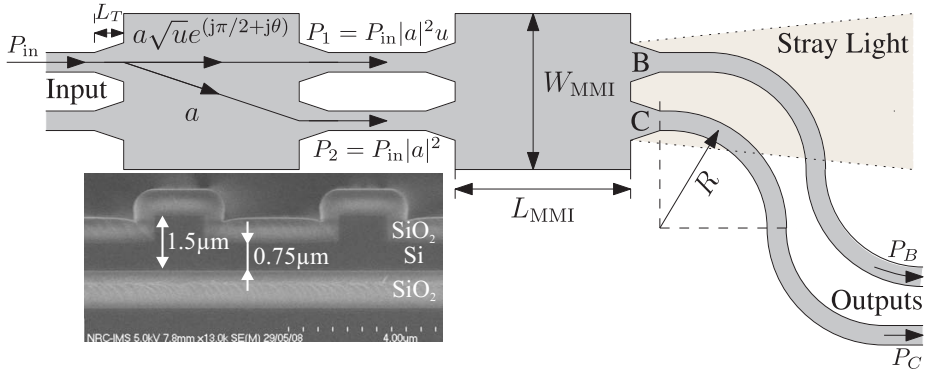

Figure 8.7.: Schematic of the back to back MMI test structure. A scanning electron microscope image of the interconnecting waveguides is shown in the inset. Interference is constructive in the cross arm labelled "C" and destructive in the bar arm labelled "B". θ denotes the MMI phase error, $u = P_1/P_2$ its imbalance, and a the nominal splitting ratio.

plitude coupling coefficients shown in figure 8.7, where $u = P_1/P_2$ is the power imbalance, and θ the phase error with respect to the ideal 90° shift between the MMI outputs, it is straightforward to show that the extinction ratio of the MZI is given by:

$$\mathrm{ER\,[dB]} = 10\log_{10}\frac{P_C}{P_B} = 10\log_{10}\frac{4}{u+u^{-1}-2\cos(2\theta)}. \tag{8.2}$$

A contour plot of (8.2) is shown in figure 8.8. Given a certain extinction ratio, from this chart maximum values for the imbalance and phase error can be obtained.

As discussed in section 5.8 device width (W_{MMI}) is the most critical dimension in MMI couplers. The expected maximum fabrication variations being 150 nm, for the experimental tolerance study devices with nominal dimensions and width variations of −300 nm, −150 nm and +150 nm were fabricated.

8.5.2. Measurements

All devices were measured in the 1520 nm – 1580 nm band. The MPTF technique presented in chapter 7 was used to remove the spurious reflections from the silicon-air facets, that cause complex Fabry-Perot fringes in the transmission spectra. The MPTF techniques involves comparing the devices losses with a reference waveguide. Since measurements for each polarisation state (TE and TM) are compared with the corresponding polarisation state in the reference waveguide, polarisation dependent losses of the devices' input and output waveguides are taken into account.

Excess loss and imbalance of the paired and general excitation based devices with nominal dimensions are shown in figure 8.9. The paired interference MMI (P-MMI) exhibits imbalance below 0.5 dB in the complete bandwidth, for both polarisations. A similar level of imbalance has been reported in [138], albeit for much larger devices on 4 µm silicon substrate, where polarisation dependence and fabrication tolerances are less stringent than in the 1.5 µm substrate used here. For TE polarisation the performance of the G-MMI is similar to the P-MMI, whereas for TM polarisation the im-

SPICUM servicio de publicaciones

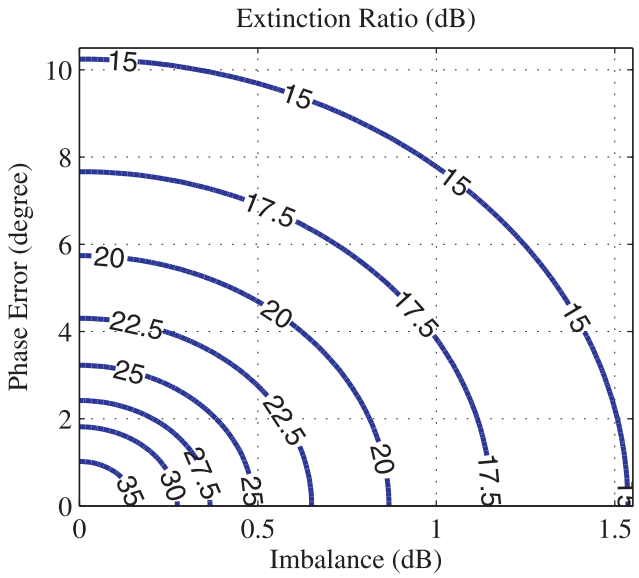

Figure 8.8: Extinction ratio of the MZI shown in figure 8.7 as a function of imbalance and phase error of the individual couplers computed from (8.2).

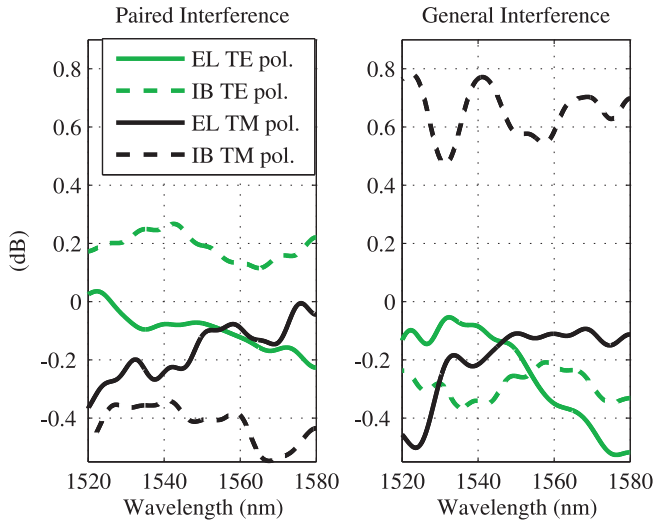

Figure 8.9: Excess loss (EL) and imbalance (IB) of the general and paired excitation based MMIs with nominal dimensions.

balance of the former is slightly higher when compared to the latter. This is attributed to the combined effect of lower fabrication tolerances of the G-MMI observed in simulation and stress induced birefringence [139] that modifies the optimum coupling length of the MMI. Excess losses of the P-MMI are below 0.4 dB in the 1520 nm to 1580 nm band for both polarisations. In [140], excess losses of approximately 0.5 dB per coupler (1 dB for a MZI configuration) were reported in five times longer MMIs on a 4 µm silicon substrate. The G-MMI exhibits similar losses. Both types of MMI exhibit slightly better performance for TE polarisation, while in simulations TM polarisation was found to yield somewhat better results (see 5.7.5). This variation is attributed to stress effects that were not included in the simulations.

The extinction ratio of the MZI composed of P-MMIs with nominal dimensions was found to be above 22 dB in the complete measurement bandwidth and for both polarisations, which again compares favourably with much larger devices reported

SPICUM servicio de publicaciones

in [84, 138] and [140]. Referring to figure 8.8, this extinction ratio ensures imbalances below 0.7 dB, which is in good agreement with the maximum measured imbalance of 0.5 dB, and indicates phase errors < 4°. The G-MMI exhibits a minimum extinction ratio of 25 dB for TE polarisation and 20 dB for TM polarisation. From figure 8.8 we see that this is again in agreement with the maximum measured imbalance of 0.8 dB for this polarisation.

To study the fabrication tolerances of the paired and general excitation based MMIs, the extinction ratios of MZIs composed of devices with widths varying between −300 nm and +150 nm around the nominal value were measured. Figure 8.10 shows the minimum extinction ratio in the 1520 nm – 1580 nm band of the MMIs, as a function of device width. The extinction ratio averaged over the wavelengths in the 1520 nm – 1580 nm band is also given. For TE polarisation, the P-MMI exhibits a minimum extinction ratio of 22 dB in the complete bandwidth and MMI width interval. This shows that in terms of imbalance and phase error the device design is highly fabrication tolerant, as we predicted in section 5.8.2. Comparable tolerances have, to the best of our knowledge, only been reported at a single wavelength and for much larger devices [141]. The extinction ratio for TM polarisation is slightly lower (20 dB) for the widest device.

For the device geometry considered here, the G-MMI is expected to be less fabrication tolerant, from MMI theory, and simulation (section 5.8). In fact, figure 8.10 shows that the minimum extinction ratio of the G-MMI in the 1520 nm to 1580 nm band drops to below 14 dB for width variations of −300 nm. Such a low extinction ratio indicates imbalance or phase errors of more than 1.5 dB and 10°, respectively (see figure 8.8). This highlights the importance of using the paired interference mechanism for this devices, as opposed to the general interference mechanism.

Finally it is observed that the average extinction ratio in the 1520 nm – 1580 nm band is several decibels above the minimum value for both coupler configurations, and that even higher extinction ratios are found at specific wavelengths.

8.5.3. Conclusion

From the measurements we can conclude that the 2 × 2 paired interference MMI, when fabricated with nominal dimensions, offers excellent performance despite of its shallow etch and compact size. Furthermore, power imbalance and phase error tolerate fabrication variations in MMI width in a range of 450 nm. To the best of our knowledge, this combination compact size, high performance and large fabrication tolerances had not been reported so far.

8.6. Sixport

In this section the sixport junction will be characterised, i.e. its centres and insertion losses will be measured, and shown to be very close to the simulated values (also see chapter 6). Since determination of the six-port centres relies on the knowledge of the relative optical phase between the reference wave and the wave reflected from the DUT, we start by elaborating, in section 8.6.1, a measurement technique based on MPTF. This technique allows for the determination of the complex (amplitude

SPICUM servicio de publicaciones

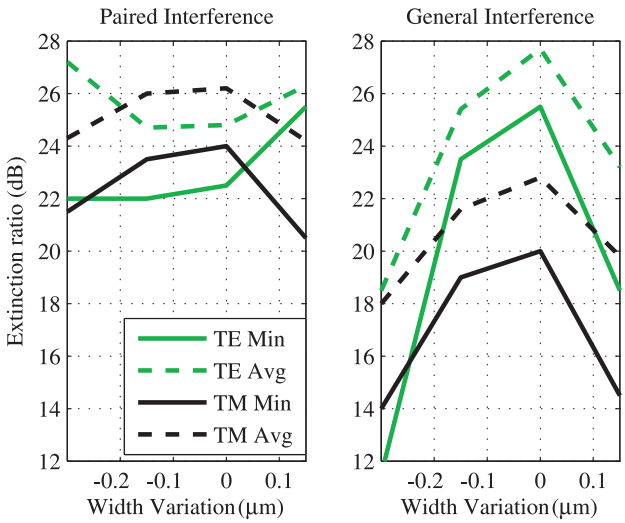

Figure 8.10.: Minimum and average extinction ratio in the 1520 nm – 1580 nm band for general and paired excitation MMIs and TE and TM polarisations. Actual device widths are $W_{\text{G-MMI}} = 7.5\,\mu\text{m} + (\text{Width Variation})$ and $W_{\text{P-MMI}} = 12.8\,\mu\text{m} + (\text{Width Variation})$.

and phase) response, solely from power measurements. The experimental results will then be presented in section 8.6.2.

8.6.1. Measurement Technique

For convenience the layout and port numbering of the six-port junction is replicated in figure 8.11. The centres of the six-port are given by (see section 2.4):

$$q_{\{3,5,6\}} = -\frac{S_{\{3,5,6\}1}}{S_{21} S_{\{3,5,6\}2}}. \tag{8.3}$$

Hence, determination of each six-port centres would involve measurement of the three complex S-parameters in (8.3). However, this would require both deposition of an anti-reflective coating, and, more importantly, a complex measurement setup. Such a setup would have to be able to access ports on several sides of the chip, as well as measuring both magnitude and phase of the transmission, as is done, for example, in Optical Frequency Domain Reflectometry (OFDR) [31]. Here, we work out a technique based on MPTF that exploits the reflections from the uncoated chip facets to determine each six-port centre with a single power transmission measurement from the input (port 1) to the corresponding output (ports 3, 5 and 6). We shall denote these power transmission measurements as $|M_{\{3,5,6\}1}(\lambda)|^2$ or, equivalently, $|M_{\{3,5,6\}1}(\nu)|^2$, where $\nu = c/\lambda$ is optical frequency, and c is the speed of light in vacuum.

To conceptually introduce the measurement technique, let us first consider that all ports of the six-port are covered with perfect anti-reflective coating, and only the DUT port exhibits a non-zero reflection coefficient equal to the Fresnel amplitude coefficient of the facet, $\Gamma_{\text{DUT}} = (n_{\text{Si}} - n_{\text{air}})/(n_{\text{Si}} + n_{\text{air}}) \approx 0.56$. In this case the complex

SPICUM servicio de publicaciones

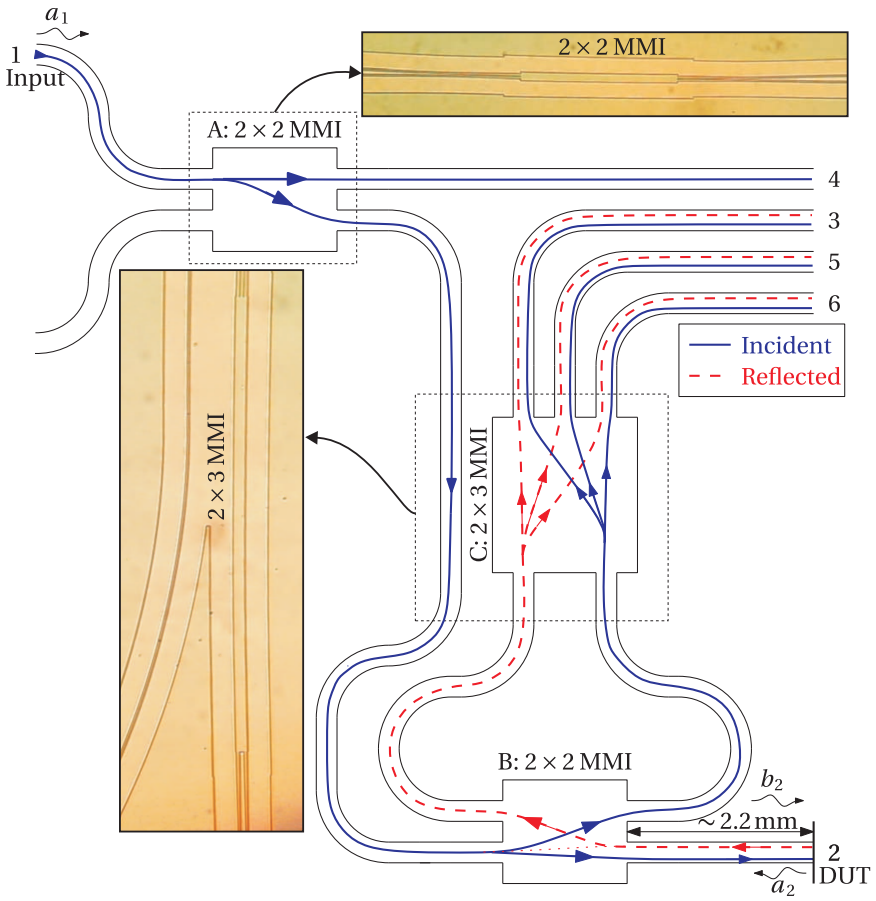

Figure 8.11.: Schematic layout of the six-port (not to scale). The insets show microscope images of the 2×2 MMI and the 2×3 MMI. The footprint of the circuit is 6.7 mm $\times$ 6.7 mm.

amplitude transmission from port 1 to any of the outputs (ports 3, 5 and 6) is

$$M_{\{3,5,6\}1}(\nu) = S_{\{3,5,6\}1}(\nu) + S_{21}(\nu)\Gamma_{\mathrm{DUT}}S_{\{3,5,6\}2}(\nu), \tag{8.4}$$

where the first term is the direct transmission from input to output (solid line in figure 8.11), and the second term corresponds to the reflection from the DUT (dotted line in figure 8.11). The key point is that these two contributions, while completely mixed in the frequency domain (ν) measurement, are well separated in the time domain (t). This is because the wave reflected from the DUT port is delayed with respect to the direct transmission by the 2.2 mm long DUT port waveguide (see figure 8.11). Hence, in the inverse Fourier transform of (8.4), $m_{\{3,5,6\}1}(t)$, the direct transmission, $d(t)$, and the reflection from the DUT, $r(t)$, appear as two peaks, which can be completely separated by gating (filtering). This yields $d(t) = s_{\{3,5,6\}1}(t)$ and $r(t) = \Gamma_{\mathrm{DUT}}s_{21}(t) * s_{\{3,5,6\}2}(t)$, where $*$ denotes convolution. By dividing the individual Fourier transforms, $D(\nu)$ and $R(\nu)$, of $d(t)$ and $r(t)$ we obtain

$$\frac{D(\nu)}{R(\nu)} = \frac{S_{\{3,5,6\}1}(\nu)}{\Gamma_{\mathrm{DUT}}S_{21}(\nu)S_{\{3,5,6\}2}(\nu)} = -\frac{q_{\{3,5,6\}}(\nu)}{\Gamma_{\mathrm{DUT}}}, \tag{8.5}$$

SPICUM servicio de publicaciones

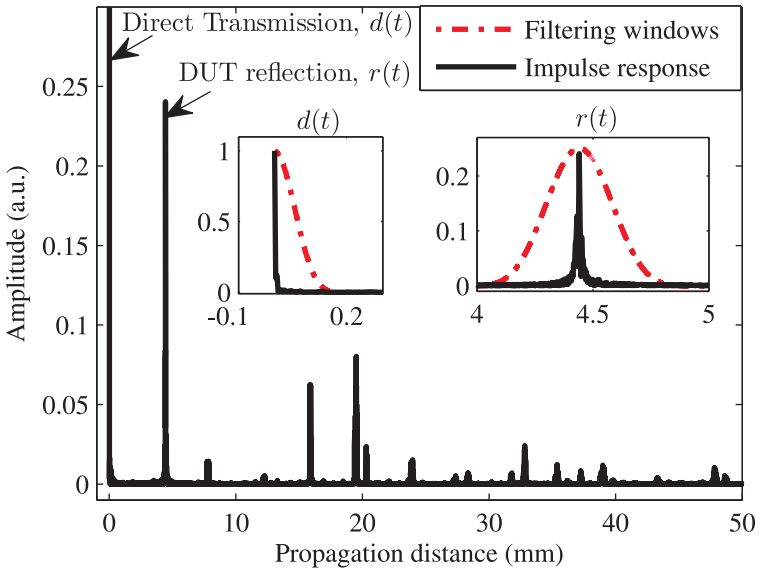

Figure 8.12.: Minimum phase impulse response from port 1 to port 3, $m_{31}(t)$, computed from the measured power transmission. The time axis has been scaled to represent propagation distance. The gating (filtering) windows for $d(t)$ and $r(t)$ are shown in the insets.

that is, by comparison with (8.3), the centre of the six-port normalised by the reflection coefficient of the DUT.

Naturally, the real measurements contain not only the direct transmission and the reflection from the DUT, but also spurious reflections from the other uncoated ports. These can, however, be eliminated in the gating process. What is more critical is that in the actual measurement process only the power transmission, $|M_{\{3,5,6\}1}(\nu)|^2$, is recorded, while the phase information is lost, so that, in principle, taking the inverse Fourier transform of the measurement results does not yield any meaningful time domain information at all. However, we showed in chapter 7 that optical systems in which the magnitude of direct transmission is sufficiently large compared to the reflected waves, are minimum phase systems, so that the phase information can be calculated directly from the measured power transmission. In the six-port, all reflections are attenuated by the Fresnel reflection coefficient of the facets, as well as several passes through the MMI power splitters. Hence, it is reasonable to assume that the six-port exhibits minimum phase, as we will also show by simulations below.

Using the setup described in section 8.3, we measured the power transmissions $|M_{\{3,5,6\}1}(\lambda)|^2$ in the 1480 nm – 1580 nm with a resolution of 1 pm to achieve a good sampling of the rapidly varying fringes arising from the multiple reflections. The minimum phase of $|M_{\{3,5,6\}1}(\nu)|^2$ was then computed, and $m_{\{3,5,6\}1}(t)$ was obtained with an inverse Fourier transform. The resulting reflectogram, or impulse response, is shown in figure 8.12. As expected, the reflection from the DUT occurs at a distance of ~ 4.4 mm, corresponding to the round trip through the DUT waveguide (see figure 8.11). Furthermore, the direct transmission and the DUT reflections are well separa-

SPICUM servicio de publicaciones

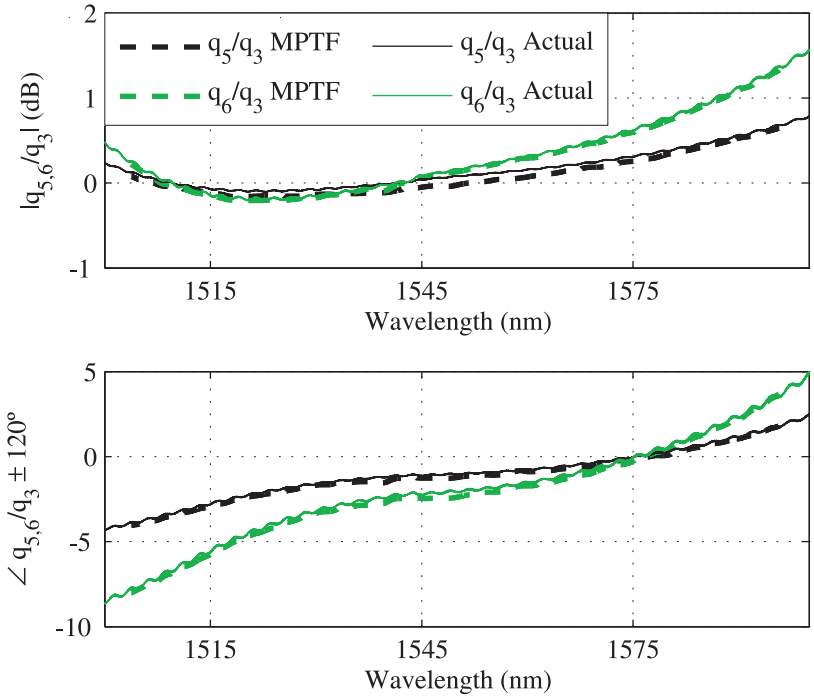

Figure 8.13.: Simulation of the relative magnitude (upper figure) and phase (lower figure) of the actual six-port centres and those computed with the minimum phase approach. TE polarisation is assumed.

ted from the spurious reflections, so that the six-port centres can be computed from $d(t)$ and $r(t)$.

In order to verify that the six-port actually exhibits the required minimum phase characteristics, reflecting facets ($\Gamma_{\text{Facet}} = 0.56$) were added to all input and output ports in the simulation of the complete device carried out in chapter 6. The minimum phase approach described above was then applied to the simulated detected powers in the presence of reflecting facets. The results are compared with the sixport centres obtained via equation (8.3) from simulations without reflecting facets in figure 8.13. It is clear that the sixport indeed exhibits minimum phase characteristics, since an excellent accuracy in both the magnitude and phase of the centres obtained with the minimum phase approach.

Summarising, measurement of each six-port centre involves three steps. 1) Measure the power transmission between input port 1 and outputs 3, 5 or 6. 2) Compute the minimum phase of this power transmission. 3) Perform the time domain filtering, and divide the spectra of the direct transmission and the DUT reflection.

8.6.2. Experimental results

In this section we present the measured six-port centres, as well as the device's overall losses for both TE and TM polarisation.

The measured six-port centres for both TE and TM polarisation are shown in figure 8.14(a) in the 1485 nm – 1575 nm band. A constant value of $\Gamma_{\text{DUT}} = 0.56$ has been

SPICUM servicio de publicaciones

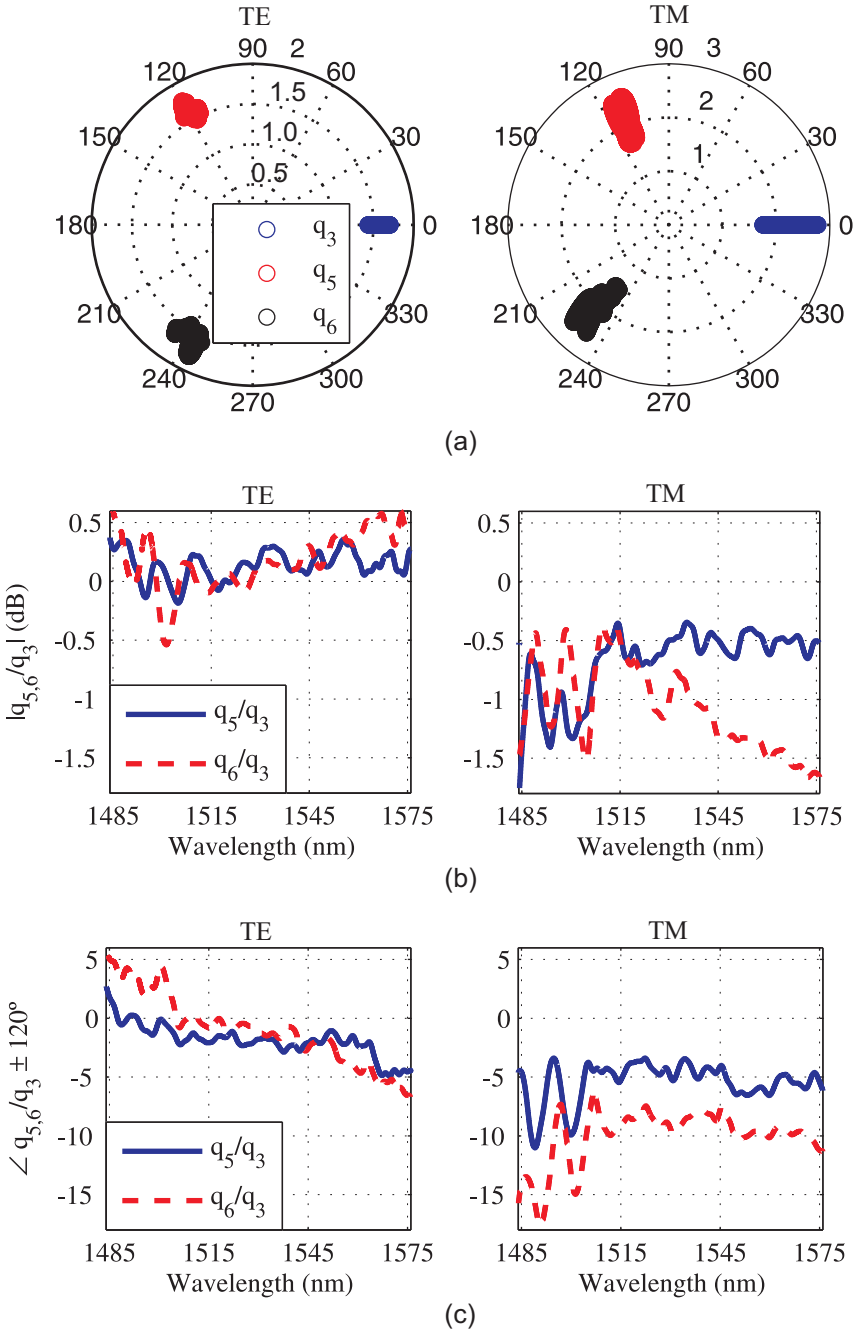

Figure 8.14.: Performance of the fabricated six-port in the 1485 nm –1575 nm band. (a) Position of the centres. (b) Imbalance between centres. (c) Phase error.

SPICUM servicio de publicaciones

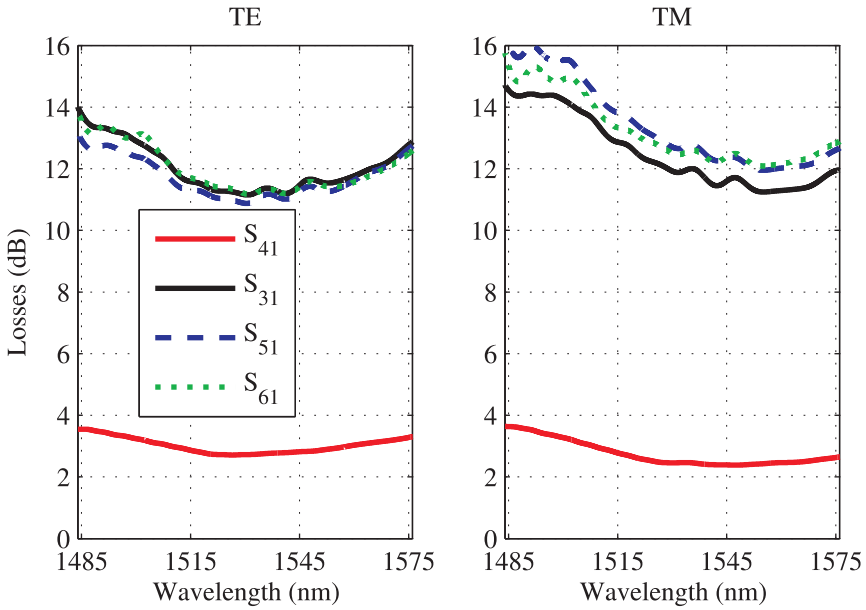

Figure 8.15.: Losses of the six-port junction in the1485 nm – 1575 nm band, for TE and TM polarisation. The $S_{\{3,4,5,6\},1}$ parameters refer to the ports of the circuit in figure 8.11.

assumed. Due to the 4.4 mm path imbalance between the incident and reflected waves, the centres actually rotate with wavelength, while maintaining their relative 120° phase. This rotation does not affect the operation of six-port as a reflectometer, since it can be accounted for by calibration, and has been cancelled in figure 8.14(a) for the sake of visualisation. While for TE polarisation the position of the centres is almost ideal, the deviations are slightly higher for TM polarisation. This is attributed to the polarisation dependence of the 2×3 MMI, since the performance of the 2×2 MMIs was found to be excellent for both polarisations (see section 8.5). The imbalance between centres is shown in figure 8.14(b), and for TE polarisation it is better than ±0.5 dB in the complete measurement range, which is in reasonable agreement with the simulations shown in figure 8.13. While simulations indicate a similar behaviour for TM polarisation, the measurements indicate that the 2×3 introduces a larger imbalance for this polarisation, which can, however, still be well compensated by calibration. Finally, the phase error of the centres is below ±6° for TE polarisation [see figure 8.14(c)], which is again in good agreement with simulations. A slightly higher phase error is observed for TM polarisation.

Figure 8.15 depicts the overall losses of the six-port junction. These are also obtained from the power transmission measurements with reflecting facets, by retaining only the direct transmission, and normalising with respect to the power transmission of a reference waveguide, as described in section 7.2. The reference port (port 4), provides a stable reference of the input power, with the expected 3 dB losses from the 2×2 MMI. The losses at ports 3, 5 and 6 are due to the concatenation of the three MMIs (see figure 2.4), and theoretically amount to $10 \log_{10}(0.5 \times 0.5 \times 0.33) \approx 10.8$ dB. This is in good agreement with the maxima of the measured curves. The slight polarisation

SPICUM servicio de publicaciones

dependence is attributed mainly to the 2 × 3 MMI.

8.6.3. Conclusions

Using MPTF is possible to determine each centre of the six-port junction with a single power transmission measurement. The measured centres lie on a circle of amplitude 1.5 with a separation of 120°. The error in the relative amplitude and position of the centres is less than ±0.5 dB and ±5° in the 1485 nm – 1575 nm for TE polarisation. For TM polarisation higher errors of ±1.5 dB and ±15° were measured, which are mainly attributed to the 2 × 3 MMI.

8.7. Conclusions

In this chapter we have given a general overview of the mask design process and have described the measurement setup used to characterise the devices. Waveguides, MMI and the complete six-port were then measured. Waveguide losses were found to be only ~ 0.25 dB/cm for TE polarisation and ~ 2 dB/cm for TM polarisation. The paired 2 × 2 MMI excess loss clearly below 0.5 dB in the 1520 nm – 1580 nm band and in a MZI maintains an extinction ratio above 22 dB for width variations of 450 nm. The combination of such performance and tolerances, exceeds, to the best of our knowledge, the current state of the art. The measured six-port centres are in excellent agreement with simulations, especially for TE polarisation, and deviate from their nominal positions in less than ±0.5 dB and 5°.

SPICUM servicio de publicaciones

SPICUM
servicio de publicaciones

9

Single etch grating coupler

COUPLING light in and out of photonic chips through their facets provides an almost wavelength independent coupling efficiency, as well as low losses when the size of the waveguide mode is matched to that of the input fibre. However, it also requires time consuming facet polishing, and becomes increasingly inefficient as the waveguides are shrunk. This is why, especially for silicon-wire waveguides, grating couplers, which scatter the light out of the waveguide plane to inject it into a fibre positioned *over* the chip, are widely used. They offer a series of advantages over facet coupling, including better mode matching, no need for facet polishing and improved accessibility of devices, since they can be placed anywhere on the chip.

In this chapter we turn our attention to the design of fibre-to-chip grating couplers in silicon wire technology. Although this chapter is not directly related to the design of the sixport in micrometric rib waveguides, it is relevant insofar the sixport, as well as any other silicon PLC, could be implemented in Silicon-wire technology in the future. Our design proposal is based on effective media, implemented with subwavelength gratings (SWG), that control the strength of the gratings. We will see that this considerably simplifies fabrication since the grating and waveguides are defined in a single etch step.

A brief introduction on grating theory, as well as a discussion of the state of the art in grating design is given in section 9.1. Some results of the effective medium theory are reviewed in section 9.2. In section 9.3, three diffractive gratings are designed and compared by simulation: a completely etched grating without SWG, a grating with a uniform SWG, and a grating with a variable SWG. The grating with uniform SWG offers an improvement in coupling efficiency of more than 3 dB with respect to the design without SWG, while still being compatible with DUV fabrication. Measurements of the uniform grating are presented in section 9.4, and confirm its performance. The chapter is summarised in section 9.5.

9.1. Introduction

Figure 9.1 shows a schematic view of a waveguide grating, with the input waveguide on the left hand side and the grating region on the right. The grating scatters light both

SPICUM servicio de publicaciones

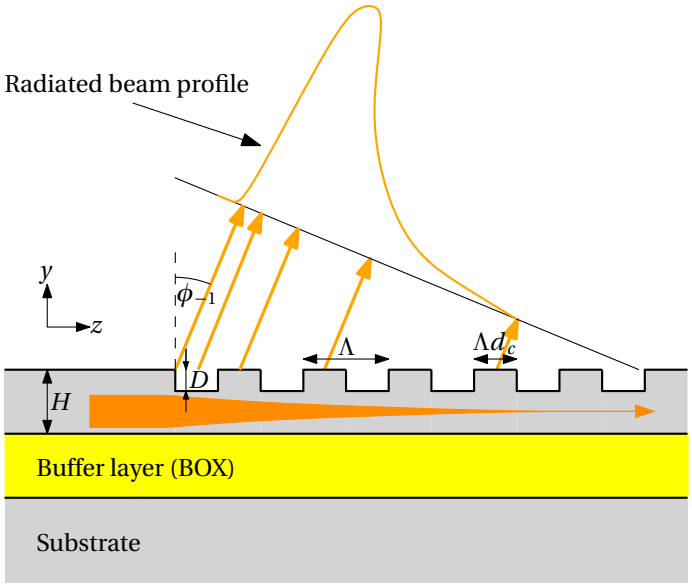

Figure 9.1.: Schematic view of a generic grating coupler

upwards as well as into the substrate, but we will here focus solely on the upward radiation. The input waveguide is assumed to be vertically (y direction) single-moded, which in Silicon-wire waveguides is always the case, since their height ($H \sim 250\,\text{nm}$) is chosen for this condition to be fulfilled. Likewise, the grating supports a single Bloch mode, with effective index n_B. We will denote the etch depth of the grating by D, its pitch (or period) by Λ and its duty cycle, which is defined as the ratio between the length of a silicon tooth and the pitch, by d_c. The k-th space harmonic of the Bloch mode has an effective index given by

$$n_k = n_B + k\frac{\lambda}{d} \tag{9.1}$$

and radiates into the upper region with an angle

$$\phi_k = \arcsin(n_k/n_a), \tag{9.2}$$

where n_a is the refractive index of the region covering the grating (usually air) [59]. Of course, only those harmonics with $|n_k/n_a| < 1$ can actually propagate, so that in most designs operate with the $k = -1$ harmonic. The strength of the grating, that is, the amount of light it scatters per period, depends on the etch depth. Generally, the deeper the grating grooves, the more power is extracted from the waveguide. Note that a grating with uniform strength will produce a radiated beam with an approximately exponential shape.

If a fibre, tilted with the radiation angle ϕ_{-1}, is placed closely over the grating surface, light will couple from the waveguide into the fibre. The chip-to-fibre coupling efficiency of the grating can be estimated as:

$$C = P_u(1 - R_f)O_f, \tag{9.3}$$

SPICUM servicio de publicaciones

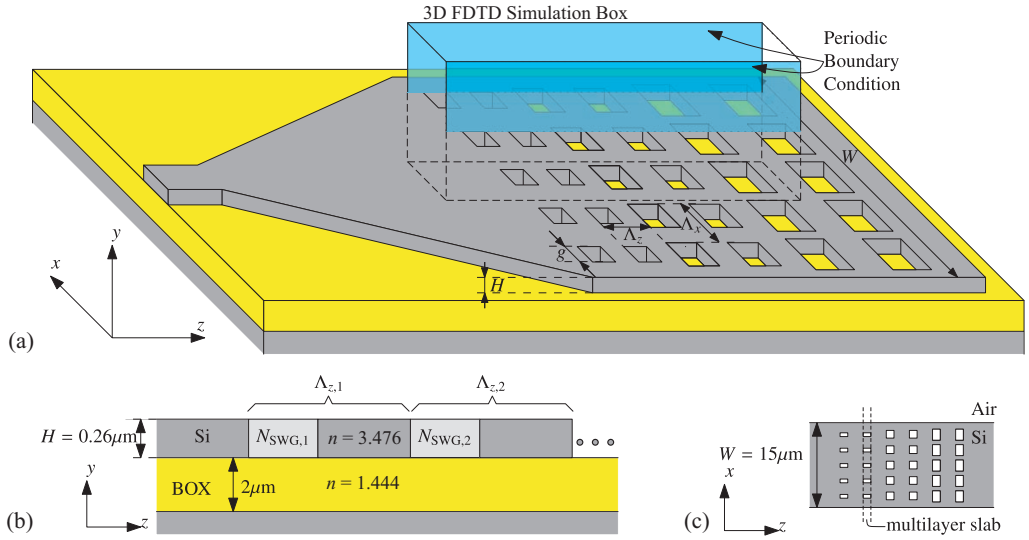

Figure 9.2.: (a) Fibre to chip grating coupler with sub-wavelength grating in lateral direction. Decoupled model schematics for (b) the vertical dimension showing the first two periods of the grating and (c) the lateral dimension.

where P_u is the power fraction of the incident waveguide mode that is directed towards the optical fibre, R_f is the Fresnel reflection coefficient between the fibre and the cladding medium, and O_f is the overlap between the radiated field and the fibre mode. In the usual case of an air-SiO_2 interface the Fresnel loss is $R_f \sim 4\,\%$. To maximise grating efficiency several techniques can be employed. These include the use of Bragg mirrors [60], metal layers [142], sub-wavelength mirrors [143] or high refractive index claddings [61] to enhance the fraction of power that is radiated upwards (instead of into the substrate). Back reflections due to second order Bragg diffraction in vertically radiating structures can be suppressed with an extra trench with distinct etch depth [144] or using slanted grating teeth [145]. Finally, using the same etch depth for the grating region as for the definition of the rectangular waveguides ($D = H$) yields a grating that is too strong, and consequently exhibits a poor overlap with the fibre mode. This can be improved by using a shallow etch to make the grating weaker. A Gaussian like radiated beam that further improves the overlap with the Gaussian fibre mode can be achieved with duty cycle apodisation [60, 61, 146], or by exploiting etch-lag effects to produce grooves with variable depth along the grating [147]. Fabrication and tolerance control of such structures can however be challenging.

Here we propose a new method to control the grating strength, which allows for the use of a single full etch ($D = H$) to define both the waveguides and the grating. This is achieved with effective media created by sub-wavelength gratings as shown schematically in figure 9.2(a). The diffraction grating is formed in the longitudinal (z) direction, whereas the non-diffractive SWG structure in the lateral (x) direction acts as effective medium thereby controlling the strength of the grating. The waveguide core layer is fully etched to the bottom oxide (BOX) cladding. Before detailing the design of the structure we will briefly review the theory of effective media.

SPICUM servicio de publicaciones

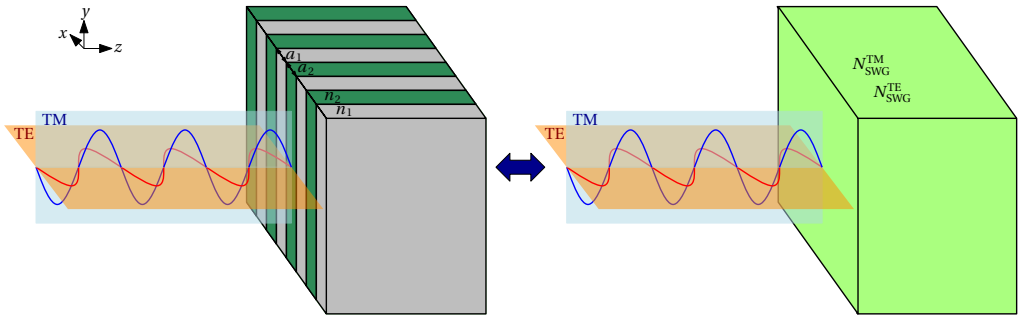

Figure 9.3.: Effective medium when the alternating media are stratified parallel to the propagation direction.

9.2. Effective medium theory

In 1956 Rytov described a rather general theory on the "Electromagnetic Properties of a Finely Stratified Medium" [148], where the equivalence between a medium composed of thin layers of two materials and an effective homogeneous medium is studied. Of the several cases examined in this paper, the one that is of particular interest to this work is shown in figure 9.3 . If the period of the alternating media, $\Lambda_x = a_1 + a_2$, is smaller than the wavelength, we call the alternating layers a sub-wavelength grating. A SWG is macroscopically equivalent to a homogeneous medium, with a refractive index N_{SWG}, which depends on the polarisation. This effective medium is shown to have refractive indices

$$N_{\mathrm{SWG}}^{\mathrm{TE}} = \sqrt{\frac{a_1}{a_1+a_2}n_1^2 + \frac{a_2}{a_1+a_2}n_2^2}, \tag{9.4}$$

$$N_{\mathrm{SWG}}^{\mathrm{TM}} = \sqrt{\frac{1}{\frac{a_1}{a_1+a_2}\frac{1}{n_1^2} + \frac{a_2}{a_1+a_2}\frac{1}{n_2^2}}}. \tag{9.5}$$

Hence, by varying the duty cycle of the subwavelength grating it is, in principle, possible to synthesise all intermediate refractive index values between n_1 and n_2. In the following, we will use alternating layers of silicon and air in the x direction to generate a refractive index value in the grooves of the diffractive grating coupler that optimises its coupling efficiency.

9.3. Design

As opposed to the previous work on grating couplers, which focuses on TE polarisation, we will carry out our design for TM polarised light, which makes it particularly applicable to evanescent field waveguide sensing, where TM polarisation yields the best sensitivity [149]. The design wavelength here is $\lambda = 1.55\,\mu\mathrm{m}$.

Following the approach of [60], the width of grating (W) was adjusted to maximise the overlap between the lateral (x) profile of the waveguide's fundamental TM mode and the SMF-28 fibre mode (10.4 µm mode diameter at $1/e^2$ intensity), yielding a power overlap of 99 % for $W = 15\,\mu\mathrm{m}$. Since we are interested in TM polarisation, the

SPICUM servicio de publicaciones

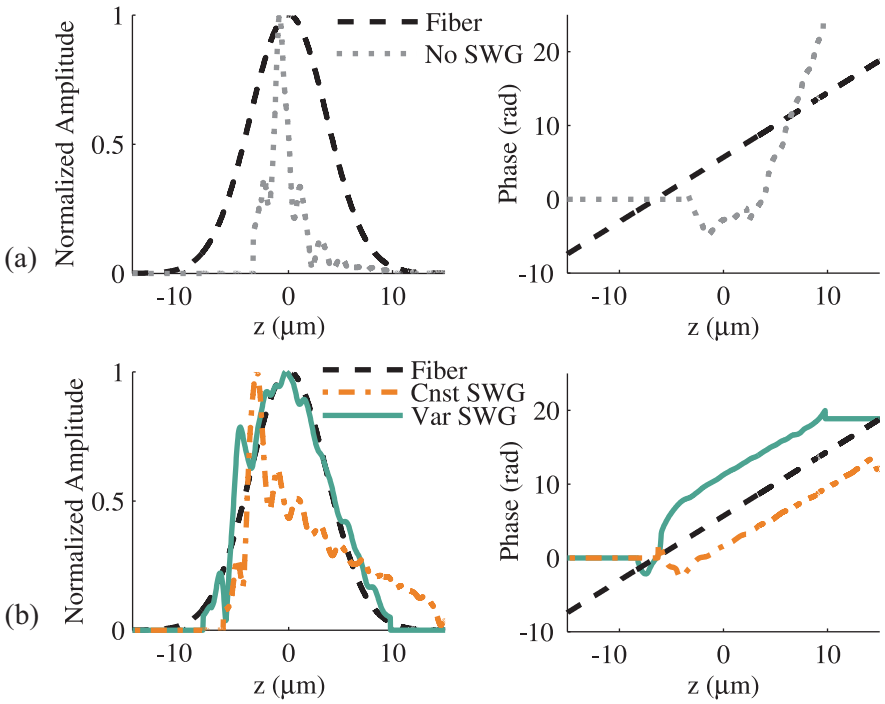

Figure 9.4.: Radiated H_x field at a plane $y = 1.5\mu$m over the grating surface, for different coupler configurations. (a) Without SWG; (b) With SWG. "Cnst SWG" stands for constant SWG, i.e., a non-apodised design; "Var SWG" stands for variable SWG, i.e., an apodised design. Fields have been shifted in the z direction for a maximum overlap with the fibre mode. The tilt angle of the fibre mode is 12° with respect to the grating normal (y) in the yz plane.

overlap was carried out with the H_x component instead of the E_x component used in [60]. The length of the taper required to create a transition with negligible loss between the 450 nm wide Si-wire waveguide and the grating was found to be 300 µm, using linear tapering.

9.3.1. Grating without SWG

A simple grating without sub-wavelength microstructures was first designed as a reference structure. The duty cycle and pitch of the reference grating were determined with two dimensional FDTD (Finite Difference Time Domain) simulations in the yz-plane using the RSoft simulator. The default choice for the duty cycle was 50 %. It was then optimised as a tradeoff between reducing back reflections and maximising the power radiated upwards, for a radiation angle close to the grating vertical. The pitch (Λ_z) was finally adjusted to yield radiation angle of ~ 10° with respect to the grating normal. This resulted in a duty cycle of 70 % and a pitch of $\Lambda_z = 0.95\mu$m.

With this simple initial design, the fraction of incident power that is radiated upwards is $P_u = 55\%$, while about 15% is coupled to the back-propagating waveguide fundamental mode. A comparatively small ($O_f = 35\%$) power overlap is obtained for this structure because of the large grating strength. As shown in figure 9.4(a), the

SPICUM servicio de publicaciones

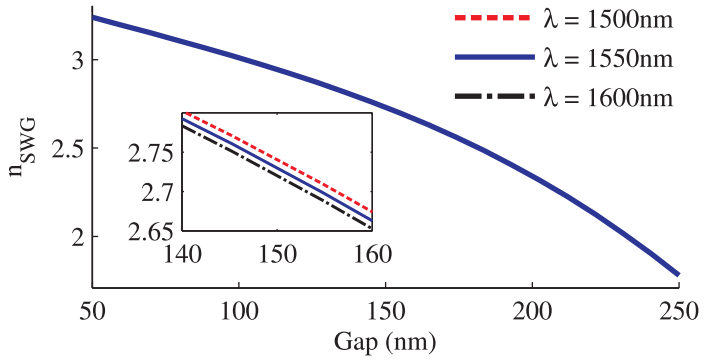

Figure 9.5.: Refractive index of the effective medium created by a silicon SWG with a pitch of $\Lambda_x = 300\,\text{nm}$, as a function of air gap. TM polarisation is assumed.

light is effectively radiated out of the waveguide within approximately 5 µm of propagation in the grating region. The overall coupling efficiency of this structure is only $C = 18\,\% = 7.5\,\text{dB}$.

9.3.2. Grating with uniform SWG

To reduce the grating strength, we introduce a sub-wavelength grating structure in the lateral (x) direction [figure 9.2(a)]. For our geometry, assuming that the pitch of the grating in the lateral direction is $\Lambda_x < \lambda_0 / \max(n_{\text{eff}})$, diffraction in the xz-plane is frustrated. Here λ_0 is the free-space wavelength and $\max(n_{\text{eff}})$ the maximum effective index encountered in the structure, which in this case is the effective index of the waveguide's fundamental TM mode ($n_{\text{eff}} = 2.26$).

Since the grating's width is much larger than its height, decoupled 2D models can be established in the vertical (y) and lateral (x) directions. As illustrated in figure 9.2(b), in the decoupled 2D model the sub-wavelength regions can then be approximated as effective media with effective indexes $N_{\text{SWG},i}$. Since N_{SWG} is an intermediate value between the refractive index of the cladding material (here air, $n = 1$) and silicon ($n = 3.476$), the SWG effectively reduces the coupling strength of the grating. Referring to the decoupled model for the lateral (x) direction in figure 9.2(c), the effective medium index of each SWG in the lateral (x) direction ($N_{\text{SWG},i}$) can be calculated as the effective index of the fundamental y-polarised (TM) mode of the corresponding multilayer slab [150]. We used a SWG with a rather conservative pitch of $\Lambda_x = 300\,\text{nm}$, and computed N_{SWG} as a function of the width of the air gap between the silicon teeth, using the commercial Fimmwave package. The resulting effective index is shown in figure 9.5, revealing that a wide range of effective indexes can be synthesised. It is also observed (figure 9.5, inset) that effective index dispersion is very low for this SWG medium.

Specifically, a gap size of 150 nm, which is attainable with both e-beam and 193 nm deep ultraviolet lithography, yields $N_{\text{SWG}} = 2.73$ for $\Lambda_x = 300\,\text{nm}$. Using this sub-wavelength effective medium, we next designed a uniform diffractive grating with 17 periods arrayed along the longitudinal (z) direction, consisting of alternating lines of silicon and the effective medium ($N_{\text{SWG}} = 2.73$), as illustrated in figure 9.2(b). Using

SPICUM servicio de publicaciones

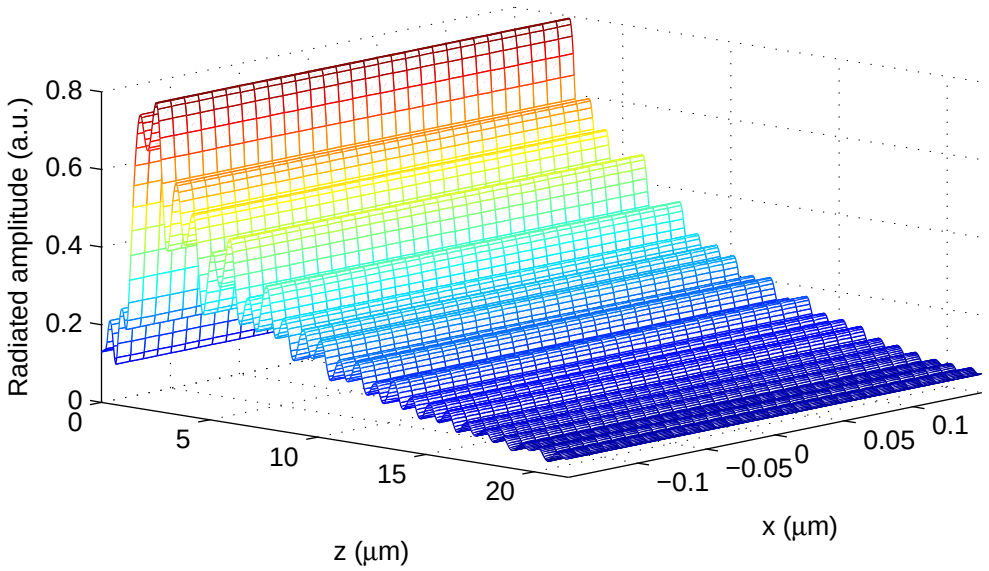

Figure 9.6.: Amplitude of the H_x field at a plane $y = 1.5\,\mu\text{m}$ over the grating surface, within one period of the SWG grating.

the criterion described before, a 70 % duty cycle was chosen in this case. The fibre mode overlap was increased to 73 % [figure 9.4(b)], which doubles the overlap attained without SWG. Since all grating teeth are identical, the radiated field is a plane wave and hence its phase increases linearly along the grating [see figure 9.4(b)]. The mode overlap remains though limited by the exponential near field profile along the z-direction for this non-apodised grating, whose maximum theoretical overlap with the Gaussian profile is 80 % [59]. The radiation angle for a pitch of $\Lambda_z = 0.84\,\mu\text{m}$ is 11.5°, and an improved coupler efficiency of 38 % = 4.2 dB is attained. Furthermore, since the Fresnel reflection coefficient at the silicon-SWG boundary is now reduced, the power coupled to the back propagating waveguide mode is < 1 %.

In order to validate the performance of this structure, a three dimensional FDTD simulation was carried out. Due to computational constraints it was not possible to simulate the entire grating region. Instead, we simulated one period of the lateral SWG along the full length of the coupler using periodic boundary conditions, as illustrated in figure 9.2(a). This mimics a structure extending infinitely in the lateral (x) direction, hence taking into account the effect of the SWG. As shown in figure 9.6 the radiated H_x field is virtually constant in the lateral (x) direction, so that the SWG can indeed be considered an effective medium. The calculated overlap with the fibre mode is 74 %, with a radiation angle of 11°, both being in excellent agreement with the 2D simulations.

9.3.3. Grating with apodised SWG

In the final step of coupler optimisation, we use the effective medium to continuously apodise the coupler in order to achieve a near-Gaussian out-coupled field matching

SPICUM servicio de publicaciones

the SMF-28 fibre. Using a variable SWG index along the grating requires that the pitch [$\Lambda_{z,i}$ in figure 9.2(b)] of each longitudinal (z) period be adjusted to eliminate phase errors, i.e. ensure that all elements radiate in the same direction [151]. To determine the correct pitch (Λ_z) for each value of the effective medium index (N_{SWG}), two dimensional FDTD simulations of non-apodised (uniform) gratings were carried out. For a specific value of N_{SWG}, the pitch was scanned, and the radiation angle as a function of pitch was determined from the radiated field.[1] The pitch that yielded the desired angle of 12° was then chosen. After obtaining a set of $N_{\mathrm{SWG}} \leftrightarrow \Lambda_z$ values, these were fitted to a cubic polynomial, yielding

$$\Lambda_z = 0.7993 + 0.407 N_{\mathrm{SWG}} - 0.1855 N_{\mathrm{SWG}}^2 + 0.0184 N_{\mathrm{SWG}}^3, \tag{9.6}$$

which allows for a direct calculation of Λ_z as a function of N_{SWG}. Using a linear variation from $N_{\mathrm{SWG}} = 3.3$ to $N_{\mathrm{SWG}} = 2$ along the 17 longitudinal (z) periods of the grating, we obtained a fibre mode overlap of 94 % [see figure 9.4(b)], with a radiation angle of 12° with respect to the grating normal. These results were again verified by 3D FDTD simulations, yielding an overlap of 92 % and a radiation angle of 11.5°. The phase of the radiated field is linear (see figure 9.4), which shows that the pitch of each period was adjusted properly. With the default duty cycle of 50 %, the coupler radiates P_u = 56 % of the incident power upwards, while only 0.1 % of light is reflected back in the waveguide. These improved values are attributed to the grating apodisation. Since in the design of the two previous grating structures we found that with the comparatively simple layer structure considered, achieving more than 55 % of upward power is difficult, no further duty cycle optimisation was carried out. The total estimated coupling efficiency of this design is $C = 50\,\% = 3\,\mathrm{dB}$.

While yielding an improved coupling efficiency with respect to the uniform coupler, the drawback of this apodised structure is that it requires rather small feature size of around 50 nm to implement the smallest and largest values of N_{SWG}, which makes it incompatible with DUV lithography. Increasing the pitch (Λ_x) of the SWG could solve this issue.

9.4. Measurements

Both the grating coupler with uniform and apodised SWG were fabricated using e-beam lithography at the National Research Council of Canada. The inset of Figure 9.7 shows the beginning of the apodised grating, with the SWGs in the horizontal (x) direction. Due to an error in mask layout it was, however, only possible to correctly characterise the uniform gratings. The measurement setup is similar to the setup used for the MMIs and the six-port described in section 8.3. However, here light is coupled in and out of the chip from above (see figure 9.7), using fibres mounted on goniometers to adjust their inclination.

To obtain the coupling efficiency of a single grating, the back-to-back structure shown in figure 9.7 was measured. This yields the insertion loss shown in the left hand side of figure 9.8. The two gratings are joined by a 3300 µm long waveguide,

[1] This information could also be obtained from a Bloch mode solver, which was, however, not at hand at the time of design.

SPICUM servicio de publicaciones

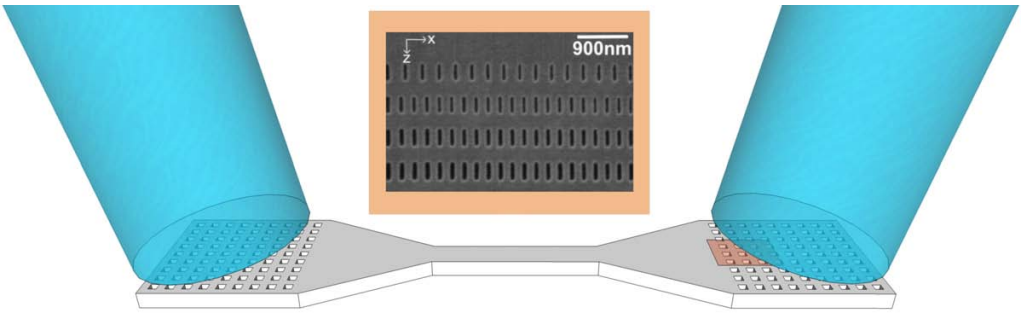

Figure 9.7.: Schematic view of the input and output coupling with grating couplers. The inset shows a SEM picture of a region of the apodised grating, approximately corresponding to the shaded area in the right hand grating.

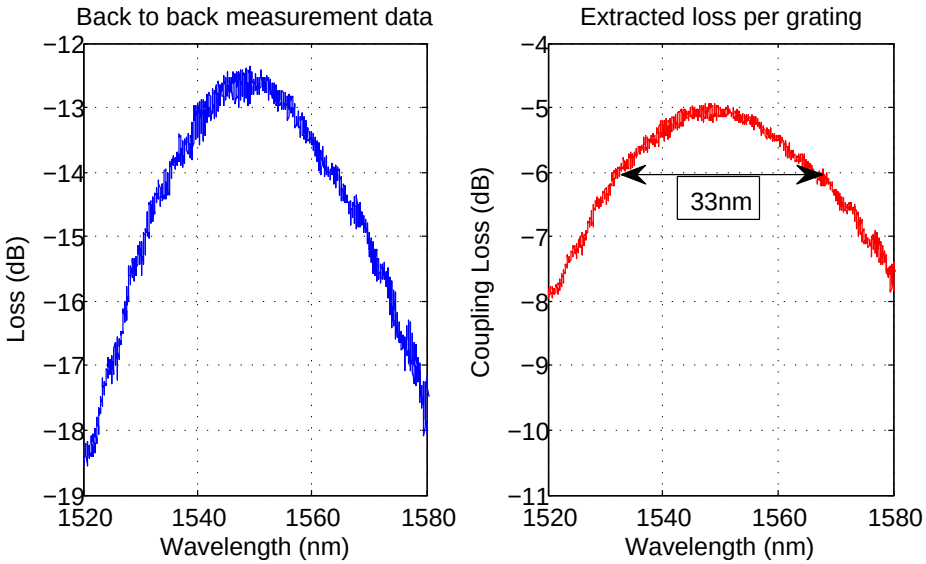

Figure 9.8.: Measured coupling efficiency of the grating coupler with uniform SWG.

SPICUM servicio de publicaciones

which, owing to the ~ 5 dB/cm propagation loss of the TM polarisation, introduces an attenuation of ~ 1.65 dB. By subtracting this value from the insertion loss, and assuming that both gratings exhibit the same efficiency, the coupling loss of an individual grating is readily computed. The result is shown on the right hand side of figure 9.8, from where a peak efficiency of about 5 dB is obtained, which is in reasonable agreement with the simulated 4.2 dB. The 1 dB bandwidth of the coupler is about 33 nm, which is typical value for this type of grating couplers [60].

9.5. Conclusion

In this chapter we have presented the design of a fibre to chip grating couplers which can be fabricated with a single etch step. With the conventional approach the simulated coupling loss of such a grating is 7.5 dB, because of the excessive strength of the grating. We have shown that the grating strength can be controlled through subwavelength structures in the lateral direction, that create an effective medium. Both a uniform grating with a DUV compatible minimum feature size of 150 nm and 4.2 dB simulated coupling efficiency and an apodised grating with 3 dB coupling efficiency were designed. Measurements on the uniform grating have shown a coupling efficiency of 5 dB with a 1 dB bandwidth of 33 nm. Work on the apodised version with increased feature size is currently being carried out.

SPICUM servicio de publicaciones

Every solution to a problem poses a new problem.
Johann Wolfgang von Goethe

10 Conclusions and prospects

THE MAIN achievements of this thesis are summarised here. We also outline some ongoing efforts that continue the work presented so far, and indicate some options for future research.

10.1. Conclusions

Two were the main goals of this thesis. First, and primarily, this work focused on the implementation and characterisation of an optical six-port reflectometer on silicon-on-insulator, using micrometric rib waveguides. Secondly, we have designed grating-to-chip couplers on silicon wire waveguides, that operate with TM polarisation and can be fabricated in a single etch step. Here we present the main conclusions of both investigations.

10.1.1. Optical reflectometer

An optical six-port reflectometer, once correctly calibrated, has the potential to measure the magnitude and phase response of optical devices with accuracies exceeding those offered by OFDR. The main goal of this thesis was the implementation and characterisation of a six-port reflectometer on Silicon-on-Insulator. The design is based on single-mode rib waveguides with a silicon height of $H = 1.5\,\mu m$, and operates with both TE and TM polarised light.

We started by thoroughly analysing the fabrication tolerances of bent, single-mode rib waveguides, both with rectangular and trapezoidal shape. The bending losses of both types of waveguides were found to be extremely sensitive to etch depth variations: for an etch-depth reduction of $0.1\,\mu m$ the minimum possible bending radius increases by a factor of 1.5 for rectangular waveguides, and by a factor 2 for trapezoidal waveguides. The final waveguide design for the six-port uses rectangular waveguides, with carefully chosen dimension to minimise the curvature radius, and maintain single-mode operation despite etch-depth variations. We have also highlighted the fact that coupling between waveguides is most critical when they carry the same power, which is the case at the output of MMIs.

SPICUM servicio de publicaciones

We have provided quantitative insight into the design of rib waveguide based MMIs, and have derived a simple design formula for the MMI access waveguides (Equation 5.39), that ensures high performance operation and good fabrication tolerances. A complete design procedure to optimise the remaining MMI dimensions has been proposed and applied to the design of a general and a paired interference 2×2 MMI and a 2×3 MMIs. An exhaustive fabrication tolerance analysis has shown that, as expected from theory, MMI width is the most critical dimensions, and that the paired interference device exhibits better tolerances. *S*-matrix based simulations of the interconnected MMIs show that the complete six-port reflectometer has an almost ideal performance for both TE and TM polarisation.

The phase response of a device that exhibits minimum phase can be directly computed from its magnitude response. This means that, for minimum phase devices, a simple power transmission measurement yields the same information that is obtained with a more complex OFDR like setup. We have established, for the first time, an analytical criterion to assess whether a certain photonic device is minimum phase or not (equation 7.10). MMIs have been shown to be minimum phase, and using this fact, we have been able to accurately characterise these devices in the presence of strong facet reflections. This is achieved by using the minimum phase information to compute the temporal impulse response, and filtering out the reflection artifacts, a technique that we have termed minimum phase temporal filtering (MPTF). A similar approach can be applied to measure the phase response of the six-port reflector.

Due to the complexity of the mask layout required for fabrication, an Autocad based function library, that automates the drawing of basic components, was developed. The devices were fabricated at the Canadian Photonic Fabrication Center. Characterisation of the waveguides yielded very low losses for TE polarisation (0.25 dB/cm), whereas about 2 dB/cm were measured for TM polarised light. We were able to demonstrate compact MMIs ($12.8\,\mu m \times 256\,\mu m$) with excess losses below 0.4 dB for both polarisations. We experimentally demonstrated that paired interference 2×2 MMIs are much more fabrication tolerant then general interference based devices. In a Mach-Zehnder configuration our devices maintain an extinction ratio well above 20 dB in the 1520 – 1580 nm band, for width variations in a range of $0.45\,\mu m$. To the best of our knowledge such a combination of high performance and relaxed tolerances had not been demonstrated before. Characterisation of the six-port reflectometer showed that it provides the magnitude and phase relations between the waves incident on and reflected from the device under test, with a deviation of less then ± 0.5 dB and $\pm 5°$ from their ideal values in a 90 nm bandwidth. This result is obtained for TE polarisation, with slightly higher deviations for the TM case, which is attributed to stress induced birefringence that was not taken into account in the design phase.

10.1.2. Grating coupler

A silicon-wire fibre-to-chip grating coupler that can be defined in the same etch step as the waveguides must be completely etched. However, this yields a very strong grating with a poor field match to the optical fibre. Here we have proposed, for the first time, the use of effective media, implemented with sub-wavelength gratings, to control the strength of the fibre-to-chip grating. Simulations have shown coupling

SPICUM servicio de publicaciones

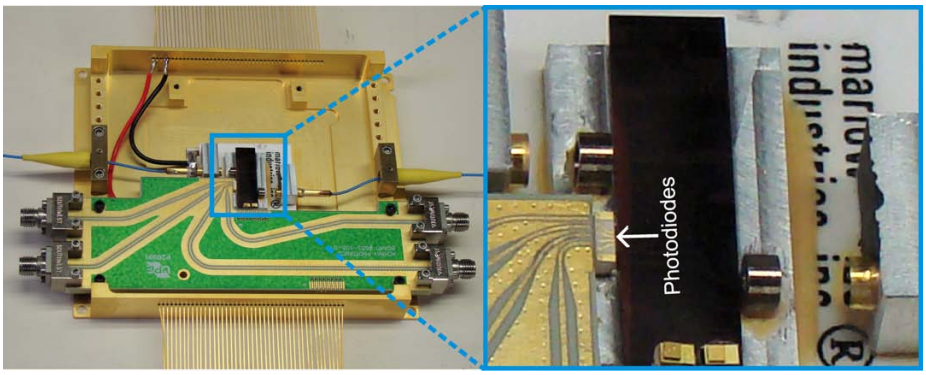

Figure 10.1.: A first prototype of the packaged six-port reflectometer, including photodiodes.

efficiencies of about 4.2 dB and 3 dB for uniform and apodised couplers, using the same layer structure as for the waveguides. First measurements have confirmed the validity of this approach: a 5 dB coupling efficiency with a 30 nm 1 dB bandwidth was experimentally demonstrated for a uniform grating.

10.2. Prospects

In this work we have covered several aspect of optical device design and characterisation, which provide incentives for future research. We will now detail some of these.

10.2.1. Six-port packaging and system testing

In the short term, packaging of the six-port PLC with photodiodes and fibre pigtails is a primary goal. Packaging of the device is done at an external company, and a first packaged prototype is shown in figure 10.1. It includes input and output fibres, as well as an array of four photodiodes at the output of the sixport (see enlarged picture). Unfortunately, the coupling losses between the chip and the output fibres were found to be unexpectedly high, an issue that we will hopefully be able to correct in the future. The prototype will allow us to perform calibration of the device and assess its actual performance in the measurement of photonic devices. This would include direct comparison of the measurement accuracy of the six-port based system and traditional OFDR based schemes, for different fibre devices, such as bragg gratings, couplers, etc.

10.2.2. Design and fabrication of high performance MMIs in other technologies

We have shown that with adequate design, high performance MMIs can be fabricated in silicon-on-insulator rib technology. Indium Phosphide rib waveguides are essentially subject to the same constraints as SOI rib waveguides, and high performance MMIs can indeed be fabricated in this technology using criteria very similar to those presented in this work. However, other technologies, such as Si-wire, exhibit rather

SPICUM servicio de publicaciones

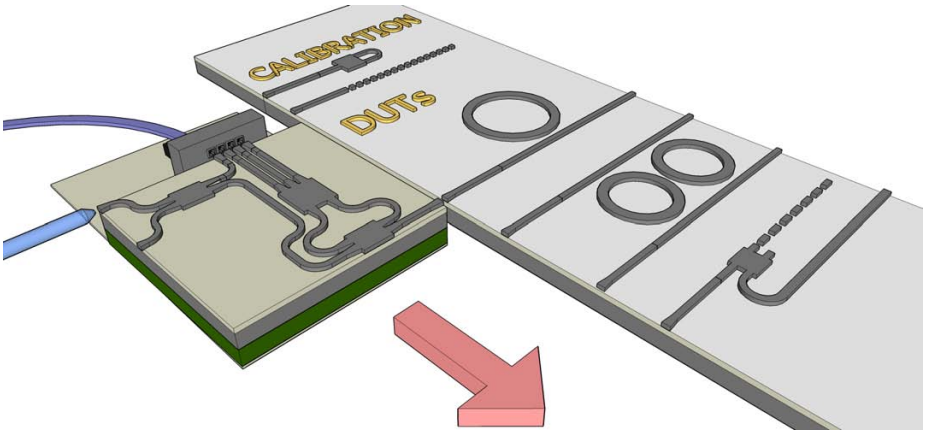

Figure 10.2.: Illustration of the concept of six-port based measurement head for direct on chip measurements.

different characteristics and may thus require other design approaches. By studying the particularities of the self-imaging in these technologies it should be possible to derive design methodologies that ensure high performance operation.

10.2.3. Extension of the MPTF technique

The minimum phase technique developed in this thesis enables accurate characterisation of MMIs and of the optical six-port. First results show that the technique should also be applicable to ring resonators, so that the general extension of the technique to narrowband devices can be an interesting topic of research. Of course, it will not be possible to characterise any narrowband device, but it may be feasible to establish some kind of analytical condition that ensures the applicability of the technique. On the other hand, application of this technique to non-minimum phase devices could be achieved by embedding them in test structures that *impose* the minimum phase condition (7.10).

10.2.4. Sub-wavelength grating based fibre-to-chip couplers

We have obtained very promising results regarding the control of the strength of single-etch step grating couplers via sub-wavelength structures. Future work on this topic is directed mainly toward increasing the minimum feature size of the sub-wavelength structure, in order to relax fabrication tolerances and enable fabrication with deep-UV lithography. Furthermore, fabrication of apodised couplers should provide increased coupling efficiency. It may also be possible to use the large birefringence of the sub-wavelength structure to design grating couplers with interesting behaviours for both TE and TM polarisation.

10.2.5. Direct characterisation of integrated optical devices

In a long term, it seems clear that more and more optical functionalities will be implemented in integrated photonics circuits. While the connection to the outside world

SPICUM servicio de publicaciones

will remain to be the optical fibre, the complexity of the system that are integrated on a chip will grow. In this sense, the evolution of the six-port technique towards the direct characterisation of integrated photonic devices is of interest. This concept is illustrated in figure 10.2, which shows a six-port based measurement head for the characterisation of on-chip devices. The idea is to have a six-port fabricated in the same technology as the devices under test, and including calibration structures in the vicinity of the DUTs. The measurement head is first calibrated, and then moved to the devices which we want to characterise. Of course, this requires the development of new calibration techniques that can be easily implemented with integrated photonics, and arouses questions about the feasibility of adequately aligning the measurement head and the chip that needs be tested.

SPICUM servicio de publicaciones

SPICUM
servicio de publicaciones

Appendices

SPICUM
servicio de publicaciones

SPICUM
servicio de publicaciones

A

Multiple self-imaging: complementary proofs.

This appendix contains some proofs and formulae which complement the Fourier series based derivation of image formation presented in section 5.2.4.

A.1. Proof of (5.19) and (5.20)

Let $g(x)$ be a continuous-space periodic function with period T and let $h[n]$ be a discrete-space periodic function with period N. Their Fourier series are given by

$$g(x) = \sum_{k=-\infty}^{+\infty} G[k] \exp\left(\mathrm{j}k\frac{2\pi}{T}x\right) \tag{A.1}$$

$$h[n] = \sum_{k=\langle N\rangle} H[k] \exp\left(\mathrm{j}k\frac{2\pi}{N}n\right), \tag{A.2}$$

where the Fourier coefficients are calculated as

$$G[k] = \frac{1}{T}\int_{\langle T\rangle} g(x) \exp\left(-\mathrm{j}k\frac{2\pi}{T}x\right)\mathrm{d}x \tag{A.3}$$

$$H[k] = \frac{1}{N}\sum_{n=\langle N\rangle} h[n] \exp\left(-\mathrm{j}k\frac{2\pi}{N}n\right). \tag{A.4}$$

Let $f(x)$ be another continuous function with period T and define

$$g(x) = f(x)\sum_{n=-\infty}^{+\infty}\delta\left(x-n\frac{T}{N}\right) = \sum_{n=-\infty}^{+\infty} f\left(n\frac{T}{N}\right)\delta\left(x-n\frac{T}{N}\right). \tag{A.5}$$

Here the Delta function property $f(x)\delta(x-x_0) = f(x_0)\delta(x-x_0)$ has been used. According to (A.3), and using the Delta function property $\int f(x)\delta(x-x_0)\mathrm{d}x = f(x_0)$, the Fourier coefficients of $g(x)$ are

$$G[k] = \frac{1}{T}\sum_{n=\langle N\rangle} f\left(n\frac{T}{N}\right)\exp\left(-\mathrm{j}k\frac{2\pi}{N}n\right). \tag{A.6}$$

SPICUM servicio de publicaciones

Note that $G[k]$ is periodic with period N. Now, by letting $h[n] = f\left(n\frac{T}{N}\right)$ and comparing (A.4) with (A.6) it is apparent that $H[k] = G[k]\,T/N$.

Thus, a continuous function $g(x)$, whose Fourier coefficients $G[k]$ are periodic with period N, is given by

$$g(x) = \sum_{n=-\infty}^{+\infty} h[n]\delta\left(x - n\frac{T}{N}\right) \tag{A.7}$$

$$h[n] = \frac{T}{N}\sum_{k=\langle N\rangle} G[k]\exp\left(\mathrm{j}k\frac{2\pi}{N}n\right) \tag{A.8}$$

A.2. Calculation of $\phi_Q[k]$

Here the calculation of the $\phi_Q[k]$ is described in detail. For convenience we repeat the expressions of $\Phi_Q[m]$ and $\phi_Q[k]$ here:

$$\Phi_Q[m] = \exp\left(\mathrm{j}\frac{\pi}{Q}\left(m^2-1\right)\right) \tag{A.9}$$

$$\phi_Q[k] = \frac{1+(-1)^{Q+k}}{2}\frac{T}{Q}\sum_{m=\langle Q\rangle}\Phi_Q[m]\exp\left(\mathrm{j}mk\pi/Q\right). \tag{A.10}$$

The factor $1+(-1)^{Q+k}$ implies that

$$\phi_Q[k]\neq 0 \quad \text{only if} \quad \begin{cases} Q\,\text{even} & \text{and} & k\,\text{even} \\ & \text{or} & \\ Q\,\text{odd} & \text{and} & k\,\text{odd} \end{cases}. \tag{A.11}$$

We will now examine these two cases separately.

A.2.1. Q even, k even

We now consider values of Q and k which are respectively of the form $Q = 2Q'$ and $k = 2k'$, with Q' and k' integers. Equation (A.10) then becomes

$$\phi_{2Q'}[2k'] = \frac{T}{2Q'}\sum_{m=\langle 2Q'\rangle}\Phi_{2Q'}[m]\exp\left(\mathrm{j}k'm\pi/Q'\right),$$

which after insertion of (A.9) and some algebra can be expressed as

$$\phi_{2Q'}[2k'] = \frac{T}{2Q'}\exp\left[-\mathrm{j}\frac{\pi}{2Q'}\left(k'^2+1\right)\right]\sum_{m=1}^{2Q'}\exp\left[\mathrm{j}\frac{\pi}{2Q'}\left(m+k'\right)^2\right]. \tag{A.12}$$

The sum in (A.12) is a Gaussian sum that can be solved using Schaar's identity (see appendix A.3 for further details):[1]

$$\sum_{m=0}^{2Q'-1}\exp\left(\mathrm{j}\frac{\pi}{2Q'}m^2\right) = \sqrt{2Q'}\exp\left(\mathrm{j}\frac{\pi}{4}\right). \tag{A.13}$$

[1] Remarkably, very similar equations also arise in quantum physics [152].

SPICUM servicio de publicaciones

Because the function $\exp\left(\mathrm{j}\frac{\pi}{2Q'}m^2\right)$ is periodic with period $2Q'$, its sum for $2Q'$ consecutive values of m does not depend on the interval of summation, so that (A.12) simplifies to

$$\phi_{2Q'}[2k'] = \frac{T}{\sqrt{2Q'}}\exp\left(\mathrm{j}\frac{\pi}{4}\right)\exp\left[-\mathrm{j}\frac{\pi}{2Q'}\left(k'^2+1\right)\right]. \tag{A.14}$$

A.2.2. *Q* odd, *k* odd

We now consider values of Q and k which are respectively of the form $Q = 2Q'-1$ and $k = 2k'-1$, with Q' and k' integers. Equation (5.22) then becomes

$$\phi_{2Q'-1}[2k'-1] = \frac{T}{2Q'-1}\sum_{m=\langle 2Q'-1\rangle}\Phi_{2Q'-1}[m]\exp\left(\mathrm{j}m\pi\frac{2k'-1}{2Q'-1}\right),$$

which is then expressed as

$$\phi_{2Q'-1}[2k'-1] = \frac{T}{2Q'-1}\exp\left[-\mathrm{j}\frac{\pi}{2Q'-1}\left(\left(\frac{2k'-1}{2}\right)^2+1\right)\right]\times\ldots$$
$$\sum_{m=\langle 2Q'+1\rangle}\exp\left[\mathrm{j}\frac{\pi}{2Q'+1}\left(m+\frac{2k'-1}{2}\right)^2\right]. \tag{A.15}$$

Although it is not apparent from Schaar's identity, it can be checked numerically that the sum in (A.15) is again given by $\sqrt{2Q'+1}\exp\left(\mathrm{j}\frac{\pi}{4}\right)$ so that (A.15) simplifies to

$$\phi_{2Q'-1}[2k'-1] = \frac{T}{\sqrt{2Q'-1}}\exp\left(\mathrm{j}\frac{\pi}{4}\right)\exp\left[-\mathrm{j}\frac{\pi}{2Q'-1}\left(\left(\frac{2k'-1}{2}\right)^2+1\right)\right]. \tag{A.16}$$

A.3. Schaar's identity

This identity states that for p and q integers of different parity, that is, one is even and the other is odd,[2]

$$\frac{1}{\sqrt{q}}\sum_{r=0}^{q-1}\exp\left(-\mathrm{j}\pi r^2\frac{p}{q}\right) = \frac{\exp\left(-\mathrm{j}\frac{\pi}{4}\right)}{\sqrt{p}}\sum_{r=0}^{p-1}\exp\left(\mathrm{j}\pi r^2\frac{q}{p}\right)$$

Substitution of $p = 2Q'$, and $q = 1$ yields the desired result.

[2] Weisstein, Eric W. "Schaar's Identity." From MathWorld–A Wolfram Web Resource. http://mathworld.wolfram.com/SchaarsIdentity.html

SPICUM servicio de publicaciones

SPICUM
servicio de publicaciones

B

Minimum phase condition

Here we derive a sufficient condition for a multi-path device to exhibit minimum phase. The transfer function, $M(s)$, of such a device is given by (7.9), which is reproduced here for convenience:

$$M(s) = \frac{1}{\Delta(s)} \left[\sum_{k=0}^{N} F_k(s)[1 + \sum_{q_k} P_{q_k}(s)] \right].$$

Using the same argument as in section 7.3.2, it is clear that the denominator of $M(s)$, $\Delta(s)$, does not introduce any non-minimum phase terms, so that we may focus solely on the numerator. Each of the $F_k(s)$ and $P_{q_k}(s)$ terms in 7.9 is a product of facet reflectivities, R_i, coupling coefficients,C_i, device transmission coefficients $S_{ij}(s)$, and waveguide transmissions$D_i(s)$. If we write the delays of the waveguides explicitly, the numerator of $M(s)$ becomes

$$V(s) = \exp(-s\tau_0) \left[F_0 + \sum_{k=1}^{N} F_k \exp(-s\tau_k) + \sum_{k=0}^{N} F_k \exp(-s\tau_k) \sum_{q_k} P_{q_k} \exp(-s\tau_{q_k}) \right], \quad \text{(B.1)}$$

where τ_0 is the delay of the shortest forward path and F_k and P_{q_k} do not depend on the waveguide delays. As discussed in section 7.3.2, $\exp(-s\tau_0)$ is an all-pass term, which will be lost when computing the minimum phase response, so we will drop it for the remainder of the discussion. The other delays involved in $V(s)$ must however be conserved when computing the minimum phase response, because they allow for the temporal separation of the direct transmission term from the other forward paths. Consequently, we need to establish a condition that ensures that $V(s)$ be a minimum phase function (with exception of the $\exp(-s\tau_0)$ term).

In many practical situation, including multi-mode interference couplers (see Section 7.4.1), the delay introduced by the waveguides is much larger than the impulse response of the device. Equivalently, the frequency response of the latter varies very slowly when compared to the former. Hence, for mathematical convenience we may approximate the S_{ij} parameters to be constants, so that F_k and P_{q_k} in (B.1) become constants, too. With this simplification $v(t)$, the impulse response function associated with $V(s)$, is simply a finite sequence of impulses with different amplitudes. Consequently, we may treat it as discrete time signal, i.e. as a sampled signal whose

SPICUM servicio de publicaciones

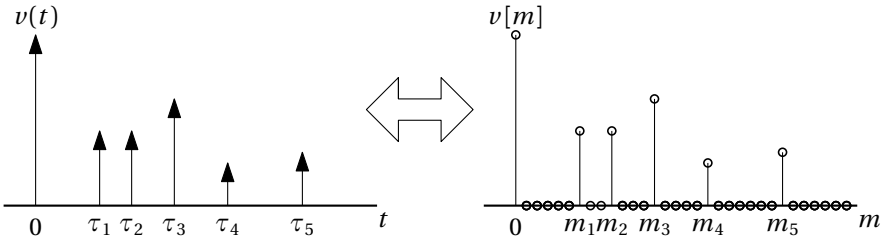

Figure B.1.: Discrete time representation of a sequence of impulses.

amplitude is non-zero only at the position of the impulses (see figure B.1). The sampled signal can then be z-transformed [130, Ch. 2] yielding $V(z)$, a polynomial in z^{-1}. Let m_M be the degree of this polynomial. For $V(z)$ to be a minimum phase function its zeros must lay inside in the unit circle $|z| = 1$ [130, Ch. 7]. Let us now define $U(z) = z^{m_M} V(z)$ which has the same zeros as $V(z)$ and is given by

$$U(z) = F_0 z^{m_M} + \sum_{k=1}^{N} F_k z^{m_M - m_k} + \sum_{k=0}^{N} F_k z^{m_M - m_k} \sum_{q_k} P_{q_k} z^{-m_{q_k}}. \tag{B.2}$$

Note that the degree of $U(z)$ is m_M so that it has exactly m_M zeros. We now define the functions

$$f(z) = F_0 z^{m_M} \tag{B.3}$$

$$g(z) = U(z) - f(z). \tag{B.4}$$

and invoke Rouché's theorem, which states [153]:

If two functions $f(z)$ and $g(z)$ are analytic inside and on some closed contour γ, and $|f(z)| > |g(z)|$ on γ, then $f(z)$ and $f(z) + g(z)$ have the same number of zeros inside γ.

The functions $f(z)$ and $g(z)$ defined in (B.3) and (B.4) are analytic because they are polynomials. Hence, if we impose that $|f(z)| > |g(z)|$ on $|z| = 1$, $U(z) = f(z) + g(z)$ has the same number of zeros inside $|z| = 1$ as $f(z)$. Since $f(z)$ has m_M zeros at $z = 0$, $U(z)$ has m_M zeros inside $|z| = 1$. But $U(z)$ only has m_M zeros in total, so that *all* zeros of $U(z)$ are inside the unit circle. Hence, if $|f(z)| > |g(z)|$ on $|z| = 1$ then $V(z)$ is a minimum phase function. Using the triangle inequality $|z_1 + z_2| < |z_1| + |z_2|$ we thus find that a sufficient condition for $V(z)$ to have all its zeros inside the unit circle is

$$|F_0| > \sum_{k=1}^{N} |F_k| + \sum_{k=0}^{N} |F_k| \sum_{q_k} |P_{q_k}|,$$

which is the expression we were looking for.

SPICUM servicio de publicaciones

C

Minimum phase computation and processing

THIS appendix to chapter 7 provides the theoretical background for the implementation of the algorithm that computes the minimum phase response from the power transmission measurements. While the optical devices discussed in chapter 7 are naturally modelled with continuous functions of time and frequency, both the measurement data as well as the computational implementation of the algorithm are discrete in nature. For example, the result of a power transmission measurement is sequence of length N of transmitted powers at certain wavelengths. Consequently, the treatment presented here is based on discrete time signals.

Some definitions and notation are given in section C.1 and the real part sufficiency of Fourier transforms is reviewed in section C.2. The relation between the magnitude and phase of the Fourier transform is detailed in section C.3, and implemented in Matlab in section C.4. Finally, section C.5 gives some detail on how to recover the maximum phase response, instead of the minimum phase response.

C.1. Definitions and Notation

We shall denote non-periodic (infinite) sequences as $x[n]$, whereas typewriter letters are used for periodic (finite length) sequences, i.e. $\mathtt{x}[n]$. The Fourier transform of non-periodic sequences is defined as

$$\begin{aligned}\mathscr{F}\{x[n]\} &= \sum_{n=-\infty}^{\infty} x[n]\exp\left(-\mathrm{j}\Omega n\right) = X(\Omega)\\ \mathscr{F}^{-1}\{X(\Omega)\} &= \frac{1}{2\pi}\int_{-\pi}^{\pi} X(\Omega)\exp(\mathrm{j}\Omega n)\mathrm{d}\Omega = x[n],\end{aligned}$$

and for periodic sequences of length N

$$\begin{aligned}\mathscr{F}_N\{\mathtt{x}[n]\} &= \sum_{n=0}^{N-1} \mathtt{x}[n]\exp\left(-\mathrm{j}\frac{2\pi}{N}nk\right) = \mathtt{X}[k]\\ \mathscr{F}_N^{-1}\{\mathtt{X}[k]\} &= \frac{1}{N}\sum_{k=0}^{N-1} \mathtt{X}[k]\exp\left(\mathrm{j}\frac{2\pi}{N}nk\right) = \mathtt{x}[n].\end{aligned}$$

SPICUM servicio de publicaciones

A range of discrete values is denoted with :, that is $n = 3,4,5,6,7$ is denoted as $n = 3:7$.

C.2. Real part sufficiency

Before discussing the computation of the minimum phase response from the measured power response, it is convenient to review the real part sufficiency of the Fourier transform. We will now briefly describe this propertie for non-periodic (infinite length) sequences, and periodic (finite length) sequences. For further details please see [135, Ch. 10].

C.2.1. Non-periodic sequences

Consider a real-valued, stable sequence $h[n]$, with Fourier transform $\mathscr{F}\{h[n]\} = H(\Omega)$, which is causal, i.e.,

$$h[n] \in \mathbb{R}; \qquad h[n] = 0 \quad n < 0. \tag{C.1}$$

The even part of $h[n]$ is given by

$$h_{\mathrm{E}}[n] = \frac{h[n] + h[-n]}{2}, \tag{C.2}$$

and since $h[n]$ is causal, $h[n]$ can be computed from $h_{\mathrm{E}}[n]$ as

$$h[n] = h_{\mathrm{E}}[n]\, u_+[n] \tag{C.3}$$

$$u_+[n] = \begin{cases} 2 & n > 0 \\ 1 & n = 0 \\ 0 & n < 0 \end{cases}. \tag{C.4}$$

On the other hand, the Fourier transform of the even part of $h[n]$ is the real part of the Fourier transform of $h[n]$, that is

$$\mathscr{F}\{h_{\mathrm{E}}[n]\} = H_{\mathrm{R}}(\Omega). \tag{C.5}$$

Hence, if $h[n]$ is causal, given only $H_{\mathrm{R}}(\Omega)$, the complete frequency response can be computed as

$$H(\Omega) = \mathscr{F}\left\{\mathscr{F}^{-1}\{H_{\mathrm{R}}(\Omega)\}\, u_+[n]\right\} = \mathscr{H}\{H_{\mathrm{R}}(\Omega)\}, \tag{C.6}$$

which is also known as Hilbert transformation.

C.2.2. Finite length or periodic discrete sequences

For sequences with a finite length of N samples and indexed between $n = 0$ and $n = N-1$, causality is defined as:

$$\mathtt{h}[n] = 0 \quad n = N/2+1 : N-1 \quad N \text{even}; \qquad \mathtt{h}[n] = 0 \quad n = (N+1)/2+1 : N-1 \quad N \text{odd}, \tag{C.7}$$

in the sense that $\mathtt{h}[n]$ can be recovered from $\mathtt{h}_{\mathrm{E}}[n]$, which is given by

$$\mathtt{h}_{\mathrm{E}}[n] = \frac{\mathtt{h}[n] + \mathtt{h}[-n \bmod N]}{2}. \tag{C.8}$$

SPICUM servicio de publicaciones

Analogously to the non-periodic case, the complete (discrete) frequency response $\mathtt{H}[k]$ can be computed from its real part $\mathtt{H}_\mathrm{R}[k]$ as

$$\mathtt{H}[k] = \mathscr{F}_N\left\{\mathscr{F}_N^{-1}\{\mathtt{H}_\mathrm{R}[k]\}\,\mathtt{u}_+[n]\right\} = \mathscr{H}_N\{\mathtt{H}_\mathrm{R}[k]\}\,, \tag{C.9}$$

where $\mathtt{u}_+[n]$ is given by

$$\mathtt{u}_+[n] = \begin{cases} 1 & n = 0, N/2 \\ 2 & n = 1 : N/2-1 \\ 0 & n = N/2+1 : N-1 \end{cases} \quad N\text{even}; \qquad \mathtt{u}_+[n] = \begin{cases} 1 & n = 0 \\ 2 & n = 1 : (N-1)/2 \\ 0 & n = (N+1)/2 : N-1 \end{cases} \quad N\text{odd}. \tag{C.10}$$

C.3. Minimum phase

Having reviewed the real part sufficiency, we can now discuss how the phase response can be recovered from the magnitude response. As before, we divide our discussion into non-periodic and periodic sequences.

C.3.1. Non-periodic sequences

In the previous section we have seen that if $h[n]$ is causal, it is completely characterised by the real part of its Fourier transform. On the other hand, the magnitude of the Fourier only gives a complete characterisation in the special case of minimum phase function. Consider the frequency response $H(\Omega)$, and its complex natural logarithm

$$\hat{H}(\Omega) = \ln H(\Omega) = \ln|H(\Omega)| + \mathrm{j}\angle H(\Omega) = \hat{H}_\mathrm{R}(\Omega) + \mathrm{j}\hat{H}_\mathrm{I}(\Omega), \tag{C.11}$$

$$\hat{h}[n] = \mathscr{F}^{-1}\left\{\hat{H}(\Omega)\right\}; \qquad \hat{h}[n] \in \mathbb{R} \tag{C.12}$$

which, in turn, is the Fourier transfrom of certain sequence $\hat{h}[n]$, which is often referred to as (complex) cepstrum. To avoid the 2π ambiguity of the phase term, $\angle H(\Omega)$ has to be defined such that it be a continuous function of Ω, i.e. the phase has to be "unwrapped". Note that since we are assuming $h[n]$ to be real, $H(\Omega)$ is conjugate-symmetric, i.e.,

$$H^*(\Omega) = H(-\Omega), \tag{C.13}$$

so that $|H(\Omega)| = |H(-\Omega)|$ and $\angle H(\Omega) = -\angle H(-\Omega)$. Consequently $\hat{H}(\Omega)$ is also conjugate-symmetric, meaning that $\hat{h}[n]$ is a real-valued sequence [135, Ch. 12.3]. The point is that *if* $\hat{h}[n]$ is causal, $\hat{H}(\Omega)$ is completely determined by $\hat{H}_\mathrm{R}(\Omega)$, and consequently, from (C.6) , $H(\Omega)$ is completely determined by $|H(\Omega)|$. Specifically, it may be computed as

$$H(\Omega) = \exp\left[\mathscr{H}\{\ln|H(\Omega)|\}\right]. \tag{C.14}$$

The cepstrum, $\hat{h}[n]$, is causal, if, and only if, $H(\Omega)$ is a minimum phase function. Equivalently, $H(z)$, the $\mathscr{Z}$-transform of $h[n]$ has to have no poles or zeros outside the unit circle, $|z| = 1$. This can be understood as follows: $\hat{H}(z) = \ln H(z)$ has singularities at both the poles and zeros of $H(z)$. The region of convergence of $\hat{H}(z)$ has to include the unit circle, because $\hat{h}[n]$ has to be stable ($\hat{H}(\Omega)$ has to exist). With this in mind we see that:

SPICUM servicio de publicaciones

- If $\hat{h}[n]$ is causal, i.e. right-handed, the region of convergence of $\hat{H}(z)$ is of the form $|z| > r$, meaning that $\hat{H}(z)$ cannot have singularities outside the unit circle, i.e. $H(z)$ cannot have poles nor zeros outside the unit circle.
- Conversely, if $H(z)$ has no poles and no zeros outside the unit circle, then $\hat{H}(z)$ has no singularities outside the unit circle either, meaning that $\hat{h}[n]$ is causal.

C.3.2. Finite length or periodic discrete sequences

For finite length sequences of length N, the cepstrum is defined through the discrete Fourier transform as:

$$\hat{\mathtt{H}}[k] = \ln \mathtt{H}[k] = \ln|\mathtt{H}[k]| + \mathrm{j}\angle \mathtt{H}[k] = \hat{\mathtt{H}}_{\mathrm{R}}[k] + \mathrm{j}\hat{\mathtt{H}}_{\mathrm{I}}[k], \tag{C.15}$$

$$\hat{\mathtt{h}}[n] = \mathscr{F}_N^{-1}\left\{\hat{\mathtt{H}}[k]\right\}; \qquad \hat{h}[n] \in \mathbb{R}. \tag{C.16}$$

With $\mathtt{h}[n]$ real, the discrete time Fourier transform exhibits a "circular" conjugate-symmetry given by

$$\mathtt{H}^*[k] = \mathtt{H}[-k \bmod N], \tag{C.17}$$

which translates into the cepstrum $\hat{\mathtt{h}}[n]$ also being real. Since $\hat{\mathtt{H}}[k]$ can be interpreted as a sampling of $\hat{H}(\Omega)$ at $\Omega = k2\pi/N$, $\hat{\mathtt{h}}[n]$ is an aliased version of $\hat{h}[n]$ [135, Ch. 12.7.3]

$$\hat{\mathtt{h}}[n] = \sum_{r=-\infty}^{\infty} \hat{h}[n - rN]. \tag{C.18}$$

Consequently, $\hat{\mathtt{h}}[n]$ will only be causal in the sense of equation. (C.7), if N is sufficiently large for $\hat{h}[n]$ to be negligible for $n \geq N/2$. In practice this can be achieved by making N sufficiently large, because it can be shown that $\hat{h}[n]$ decays at least as fast as $1/n$ [135, Ch. 12.5]. With $\hat{\mathtt{h}}[n]$ periodically causal, $\mathtt{H}[k]$ is readily computed from $|\mathtt{H}[k]|$ as

$$\mathtt{H}[k] = \exp\left[\mathscr{H}_N\left\{\ln|\mathtt{H}[k]|\right\}\right]. \tag{C.19}$$

Since the computation of $\mathscr{H}_N\{\ln|\mathtt{H}[k]|\}$ involves obtaining $\hat{\mathtt{h}}_{\mathrm{E}}[n]$, it can be checked that N is sufficiently large by inspecting the central part of $\hat{\mathtt{h}}_{\mathrm{E}}[n]$ which has to be negligibly small.

C.4. Implementation

Computational implementation of the minimum phase reconstruction is relatively straightforward using standard Fast Fourier Transform (FFT) algorithms and expressions (C.9) and (C.10). There are, however, some additional considerations which have to be taken into account.

In optical measurements normally power is recorded, so that the square root of the data has to be taken to obtain amplitude. Also, measurements are commonly recorded on a wavelength axis, whereas the Fourier transforms operates between frequency and time. Furthermore, use of the FFT requires equidistant samples, so that interpolation of the data from the wavelength axis to an evenly spaced frequency axis is required.

SPICUM servicio de publicaciones

All physical systems, including optical devices, have real-valued impulse response functions. As discussed in section C.3.2, this implies that $\mathtt{H}[k]$ be circular conjugate-symmetric, so that $|\mathtt{H}[k]| = |\mathtt{H}[-k \bmod N]|$. Note that the measurement data will not naturally fulfil this condition, because measurements are only taken on the positive part of the frequency axis. Suppose the measurement data is $\mathtt{M}[k]$ of length Q, then it easy to check that constructing $|\mathtt{H}[k]|$ of length $N = 2Q-2$ as

$$|\mathtt{H}[k]| = \begin{cases} \mathtt{M}[k] & k = 0:Q-1 \\ \mathtt{M}[2Q-2-k] & k = Q:2Q-2 \end{cases} \tag{C.20}$$

ensures the required symmetry [129]. As an example, if $\mathtt{M}[k] = [a,b,c,d,e]$ then $\mathtt{H}[k] = [a,b,c,d,e,d,c,b]$.

A Matlab implementation is given in Algorithm C.1 on the next page.

C.5. Maximum phase

In the complementary case of $H(z)$ being maximum phase, i.e. having no poles or zeros inside the unit circle, the same procedure may be used, but using $u_-[n] = u_+[-n]$. For finite-length sequences we have $\mathtt{u}_-[n] = \mathtt{u}_+[-n \bmod N]$:

$$\mathtt{u}_-[n] = \begin{cases} 1 & n = 0, N/2 \\ 0 & n = 1:N/2-1 \\ 2 & n = N/2+1:N-1 \end{cases} \quad N \text{ even;} \qquad \mathtt{u}_-[n] = \begin{cases} 1 & n = 0 \\ 0 & n = 1:(N-1)/2 \\ 2 & n = (N+1)/2:N-1 \end{cases} \quad N \text{ odd.}$$

SPICUM servicio de publicaciones

Algorithm C.1 Minimum phase computation in Matlab

```
function [Hmin,f,h,t]=MinimumPhase(lambda,power)
% function [Hmin,f,h,t]=MinimumPhase(lambda,power)
%
% Computes minimum phase response from swept power measurements.
% (c) 2009, Robert Halir, University of Málaga, robert.halir@ic.uma.es
%
% Inputs
% lambda:  measurement wavelengths (in meters) (length Q)
% power:  power samples (in Watts or milli-Watts) (length Q)
%
% Outputs
% Hmin:  minimum phase response on frequency axis (length N=2Q-2)
% f:  frequency axis
% h:  minimum phase impulse response
% t:  time axis
%
% Speed of light is set to c=3e8;

c=3e8; % speed of light

% make sure that both lambda and power are row vectors
lambda=lambda(:).';
power=power(:).';

% convert power to amplitude
amplitude=sqrt(power);

% interpolate to an evenly spaced frequency axis
f=linspace(c/lambda(end),c/lambda(1),length(lambda));
M=interp1(c./lambda,amplitude,f);

% construct |H[k]| as in Eq.(C.20)
H=[M fliplr(M(2:end-1))];

% compute even part of the cepstrum ĥ_E[n]
logh_E=ifft(log(H));

% construct the sequence u_+[n] [see Eq.(C.10)]
N=length(logh_E);
u=zeros(size(logh_E));
if mod(N,2)==0
   u([1,N/2+1])=1; u(2:N/2)=2;
else
   u(1)=1; u(2:(N+1)/2)=2;
end

% compute the minimum phase response
Hmin=exp(fft(u.*logh_E));

% transform to time domain
h=real(ifft(Hmin)); % real part removes numerical artifacts

% construct time axis
t=(((N-1)*(f(2)-f(1)))^-1)*(0:(N-1));
```


SPICUM servicio de publicaciones

D
Resumen en Español

ESTE apéndice ofrece un sucinto resumen de la presente tesis. El apartado D.1 da un panorámica general de la fotónica de silicio y presenta los principales objetivos y aportaciones de esta tesis. Las resultados más relevantes de la tesis se resumen en los apartados D.2 a D.6 y las conclusiones se exponen en la sección E.

D.1. Introducción

D.1.1. Antecedentes

Al igual que la electrónica abarca el desarrollo e integración de sistemas cuya partícula más fundamental es el electrón, la fotónica estudia sistemas basados en fotones, es decir, "partículas" de luz. La fotónica se presenta pues como una evolución natural de la óptica clásica, y generalmente se refiere a sistemas y componentes de fibra óptica, y componentes ópticos integrados, es decir realizados en un chip. Teniendo en cuenta que las comunicaciones basadas en fibra óptica constituyen la base tecnológica para el intercambio de información, sobre todo a través de Internet, que constituye ya una parte indispensable de nuestra sociedad, parece claro que el campo de la fotónica es de una apreciable relevancia. Buen ejemplo de ello es la concesión, en 2009, del premio Nobel de Física a Charles Kao, el padre de la fibra óptica.

Hoy en día la gran mayoría de los componentes electrónicos se fabrican con un mismo material: el silicio. Por ello existen técnicas y equipos disponibles comercialmente desde hace años que permiten la fabricación precisa y masiva (y por tanto económica) de componentes electrónicos en en este material. La fotónica es una disciplina mucho más joven que la electrónica, y no existe una tecnología de fabricación dominante. Sin embargo, el mismo silicio empleado para la realización de los circuitos electrónicos tiene propiedades ópticas muy interesantes: es transparente las longitudes de onda más comúnmente empleadas en comunicaciones ópticas ($\lambda = 1,55\,\mu$m y $\lambda = 1,3\,\mu$m), y presenta un índice de refracción muy elevado ($n_{\mathrm{Si}} \approx 3,5$), lo que permite un fuerte confinamiento de la luz, y, por tanto, la realización de circuitos sumamente compactos (del orden de cientos de micrómetros). No es de extrañar, por tanto, que la fotónica de silicio sea un campo de investigación extremadamente activo, en el que participa activamente la industria microelectrónica [13–16], y

SPICUM servicio de publicaciones

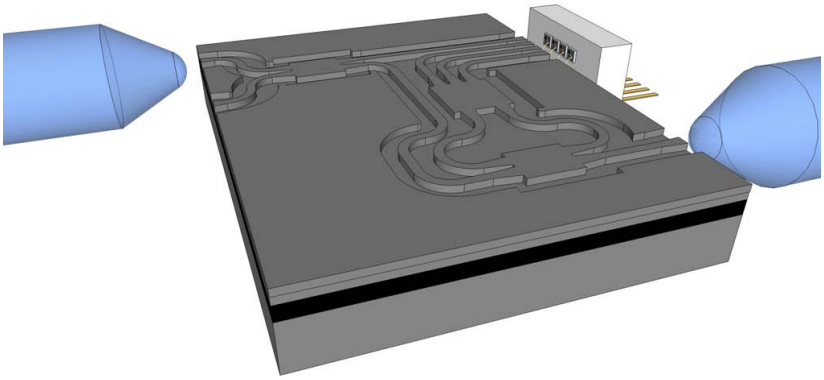

Figura D.1.: Illustración del seis puertos óptico integrado.

donde ya existen los primeros productos comerciales [19].

La complejidad de los dispositivos fotónico está en constante aumento. De la transmisión de pulsos a través de fibras ópticas a una única longitud de onda, se ha pasado a multiplexar más de cien longitudes de onda (portadores), y actualmente se están introduciendo sistemas coherentes, que utilizan modulaciones en fase y cuadratura, así como multiplexación por polarización [1–3]. Asimismo, el procesado todo óptico utilizando óptica integrada está cobran cada vez más importancia [23–25]. Por todo ello, se hace patente la necesidad de disponer de técnicas de medida ópticas, que permitan obtener una exacta caracterización, tanto en amplitud como en fase, de los dispositivos ópticos. A frecuencias de microondas una técnica de medida muy extendida, es la basado en el reflectómetro de seis puertos, que, gracias a sofisticadas técnicas de calibración, permite realizar medidas muy precisas aún con un hardware imperfecto [46]. Recientemente se ha propuesto, de manera teórica, la extensión de esta técnica al dominio óptico [32]. La implementación de un reflectómetro integrado en silicio permitiría la aplicación práctica de esta técnica, y se fija como principal objetivo de esta tesis.

D.1.2. Objetivos y aportaciones

En este tesis se plantean dos objetivos. El principal, como acabamos de mencionar, es el diseño, simulación, fabricación y caracterización de un reflectómetro óptico de seis puertos en silicio, concretamente en la plataforma Silicon-on-Insulator. La figura D.1 muestra una representación esquemática del dispositivo que se pretende implementar. La fibra óptica situada a su izquierda inyecta luz en el circuito, mientras que la situada a la derecha lo conecta al dispositivo bajo prueba. El funcionamiento del dispositivo se basa en hacer interferir, en cuatro detectores de potencia, muestras de la luz incidente y reflejada desde el dispositivo bajo prueba. A partir de las potencias detectadas, a una cierta longitud de onda, se puede calcular el coeficiente de reflexión complejo a esa longitud de onda. Puede apreciarse que el reflectómetro integrado se basa en guías con una geometría tipo “rib”, con dimensiones de $\sim 1,5\mu m \times 1,5\mu m$ (véase la figura D.2), ya que tienen una escasa dependencia de la polarización, y la

SPICUM servicio de publicaciones

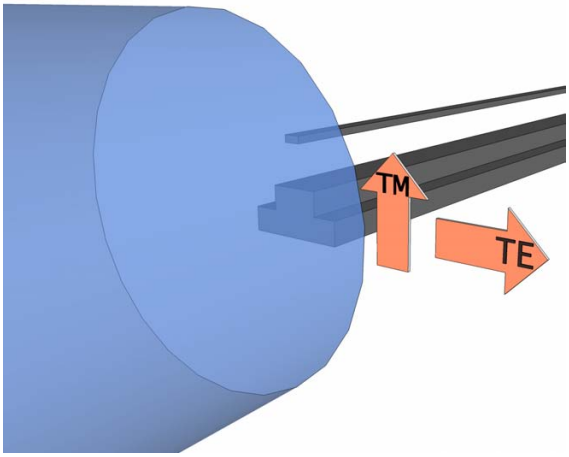

Figura D.2: Comparación del tamaño del núcleo de una fibra monomodo con una guía "silicon-wire" rectangular, y un guía rib micrométrica.

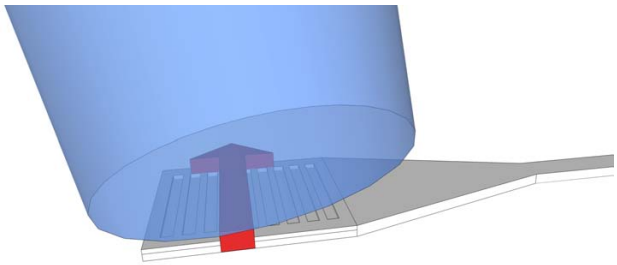

Figura D.3: Acoplo de luz con polarización TE a una guia "silicon-wire" mediante una red de difracción.

inyección de luz puede llevarse acabo de manera relativamente sencilla. El segundo objetivo de de este trabajo es el estudio de redes de acoplo chip fibra para guías de tipo "hilo de silicio", que presentan una sección transversal muy reducida ($\sim 450\,\text{nm} \times 250\,\text{nm}$), permitiendo una densidad de integración muy elevada. Sin embargo, como se puede observar en al figura D.2, la diferencia de tamaño entre una fibra óptica y un hilo de silicio es muy elevada, por lo que el acoplo de luz a estas guías es problemático. Las redes de acoplo resuelven este problema, ensanchando primero la guía, y luego difractando la luz fuera del plano del chip, como se ilustra en la figura D.3.

En cuanto a la implementación del reflectómetro de seis puertos, son varias las aportaciones que se han desarrollado en este trabajo. Por un lado, se han estudiado en detalle las características y tolerancias de fabricación de guías rib curvas [34, 35], que son un elemento esencial de cualquier circuito óptico integrado. Tal y como se muestra en la figura D.1 el reflectómetro se compone de varios acoplodores, basados en el mecanismo de interferencia multimodal (MMI), concretamente dos acopladores 2×2 y un acoplador 2×3. En esta tesis se ha propuesto una completa metodología de diseño para estos dispositivos, que da lugar a dispositivos con altas prestaciones y buenas tolerancias de fabricación [36, 37]. Se ha diseñado una compleja máscara para la fabricación de estructuras de prueba para los MMIs y del reflectómetro, que se han fabricado en el centro canadiense de fabricación fotónica (CPFC). La caracterización de los dispositivos fabricados plantea dos retos: en primer lugar, es necesario eliminar las fuertes reflexiones que se producen en los interfaces del chip con el aire, y, en segundo lugar se tiene que obtener la caracterización no sólo en amplitud sino también en fase del reflectómetro. Se ha desarrollado un técnica de fase míni-

SPICUM servicio de publicaciones

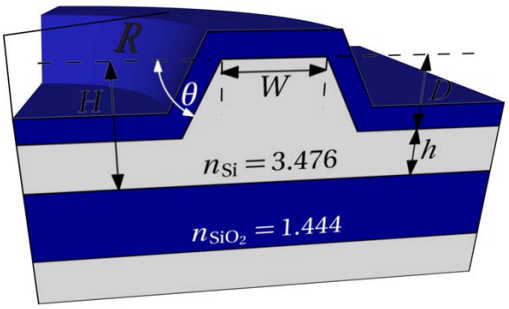

Figura D.4: Geometría de la guía de ondas curvada. Los índices de refracción corresponden la longitud de onda $\lambda = 1.55\,\mu m$. θ es 90° ó 54.74°.

ma, que da respuesta a ambas necesidades, al calcular la respuesta de fase a partir de las medidas de amplitud, y establecer un criterio analítico que permite saber si el dispositivo analizado tiene las características de fase necesarias para la aplicación de dicha técnica [38, 39]. Los MMIs fabricados presentan no sólo un tamaño muy compacto sino también unas prestaciones y tolerancias sin precedentes [40], y el seis puertos funciona prácticamente como un reflectómetro ideal en un ancho de banda de 90 nm [41].

El estudio de las redes de acoplo ha dado lugar a una novedosa red de difracción que emplea una estructura de tamaño inferior a la longitud de onda. Ésta controla la fuerza de la red, permitiendo adaptar el campo radiado el perfil del modo de una fibra óptica, usando un solo paso de grabado para la fabricación [42]. En esta tesis se presentan también los primeros resultados experimentales que demuestran el funcionamiento de la estructura.

En las siguientes secciones se describen brevemente las principales aportaciones de esta tesis.

D.2. Diseño de las guías de onda

La geometría general de la guía de onda con la que se trabaja en esta tesis se muestra en la figura D.4. La altura, H, de la guía está fijada de antemano ($H = 1,5\,\mu m$ en nuestro caso), y el ángulo, θ, de las paredes laterales es de 90° o 54,74° según las guías se definan mediante un proceso de grabado seco o húmedo. La anchura, W, la profundidad de grabado, D, y el radio de curvatura, R, pueden ajustarse libremente. El objetivo del diseño es determinar los parámetros óptimos para conseguir un funcionamiento monomodo, con el radio de curvatura más pequeño posible, y tolerante a las variaciones en el proceso de fabricación.

Un estudio sistemático revela que es preferible usar el grabado seco (con paredes laterales verticales), pues permite emplear radios de curvatura más pequeños, lo que reduce el tamaño del circuito final. Por otro lado, el funcionamiento monomodo y la reducción del radio de curvatura son objetivos opuestos, y ha de establecerse un compromiso entre ambos, máxime teniendo en cuenta que los radios de curvatura varían fuertemente con pequeñas cambios de la profundidad de grabado. Tras una extensa labor de análisis, se fija el ancho de la guía de $W = 1,3\,\mu m$ y su profundidad de grabado en $D = 0,7\,\mu m$, lo que permite emplear un radio de curvatura de $R = 900\,\mu m$ que mantiene un bajo nivel de pérdidas en todo el rango de fluctuaciones de la pro-

SPICUM servicio de publicaciones

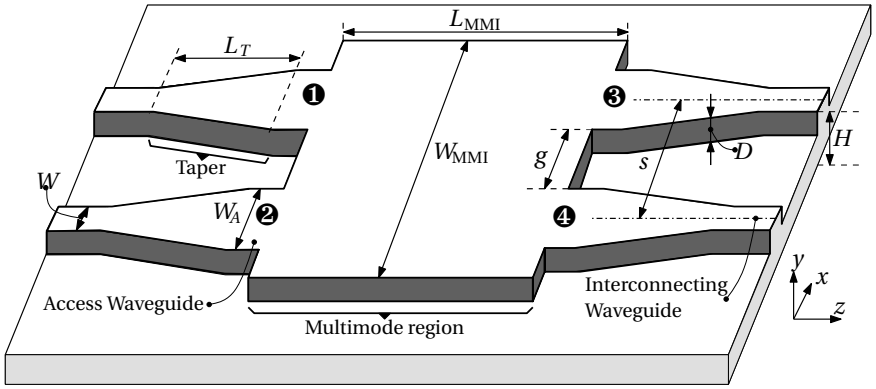

Figura D.5.: Geometria propuesta para el diseño del MMI.

fundidad de grabado que se producen en la fabricación.

Otro aspecto fundamental es el acoplo que se produce entre dos guías que transcurren paralelas a una separación de pocos micrómetros la una de la otra. Se determina que con una separación centro a centro de $s = 10\mu m$ dos guías paralelas se pueden considerar completamente desacopladas dentro del margen de distancias que se manejan en el circuito óptico integrado.

D.3. Diseño de los acopladores de interferencia multimodal y del seis puertos

Los acopladores de interferencia multimodal constituyen la base del reflectómetro de seis puertos, por lo que la optimización de sus prestaciones, y sus tolerancias resultan fundamentales. Es deseable fabricar los MMIs con mismo paso de grabado con que se definen las guías de interconexión, puesto que así se reduce el coste de los circuitos y, además, se minimizan los problemas de alineación de máscara que resultarían de usar dos pasos de grabado. La geometría general de un MMI se muestra en la figura D.5, donde se distinguen las guías de entrada y salida, y una zona central más ancha, que soporta múltiples modos. El funcionamiento de los MMIs se basa en inyectar luz en el dispositivo mediante una de las guías de acceso, excitándose múltiples modos en la zona ancha del dispositivo. Al propagarse, dichos modos se desfasan, y formas varias imágenes de la excitación de entrada, que se acoplan a las guías de salida. Sin embargo, dada la geometría de la guía rib, el diseño empleando un solo paso de grabado requiere un cuidadoso análisis. Por un lado, la zona multimodo soporta tanto modos “formadores” de imágenes [figura D.6(a)], como modos “interferentes” [figura D.6(b)]. Si se excitan estos últimos, las prestaciones del dispositivo se verán afectadas negativamente. Obsérvese que los modos formadores de imágenes son prácticamente simétricos en sentido vertical, mientras que los modos interferentes son antisimétricos. Por otro lado, como se muestra en la figura D.7(a) el modo fundamental de las guías de interconexión no es simétrico en sentido vertical, sino que presenta una forma de campana. Por tanto, este modo excitaría modos interferentes, que degradan apreciablemente las prestaciones de los MMIs. Para solventar este prob-

SPICUM servicio de publicaciones

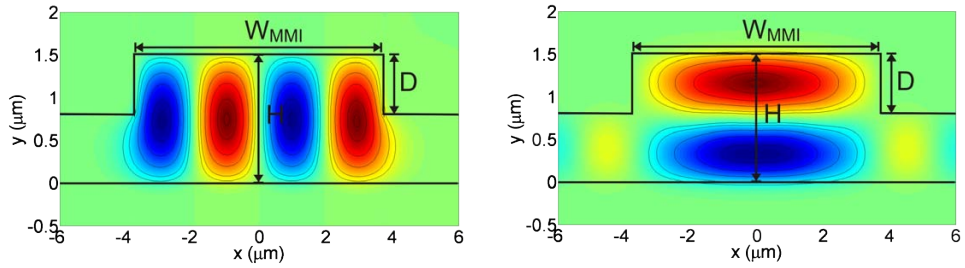

(a) Ejemplo de un modo formador de imágenes ($TE_{4,1}$).

(b) Ejemplo de un modo no formador de imágenes ($TE_{1,2}$).

Figura D.6.: Dos modos de una sección multimodo con poca profundidad de grabado ($W_{MMI} = 7.5\mu m,\ D = 0.7\mu m,\ H = 1.5\mu m$).

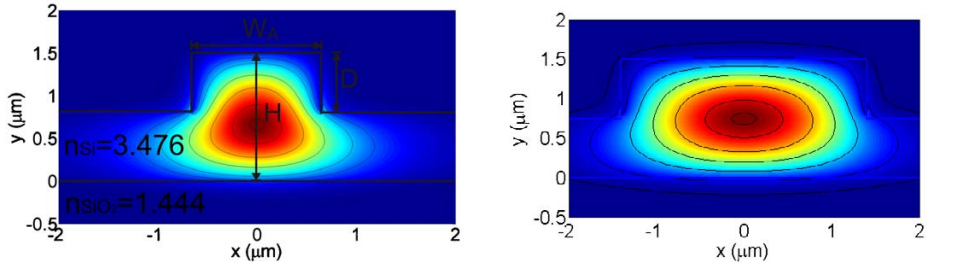

(a) $W_A = 1.3\mu m,\ D = 0.7\mu m,\ H = 1.5\mu m$

(b) $W_A = 2.4\mu m,\ D = 0.7\mu m,\ H = 1.5\mu m$

Figura D.7.: Modo TE_{11} de dos guías de acceso de tipo rib con diferentes relaciones de aspecto.

lema, se ensanchan las guías de acceso, consiguiéndose un modo más simétrico en sentido vertical [figura D.7(b)]. Gracias a un exhaustivo análisis de la simetría de los modos, así como del número de modos que soporta la zona multimodo, es posible establecer la expresión (5.39), que proporciona directamente la anchura necesaria, y que es uno de los resultados principales de este trabajo. Se ha desarrollado, asimismo, una metodología para diseñar todas las dimensiones restantes mostradas en la figura 5.6, teniendo en cuenta en todo momento las tolerancias del proceso con que los dispositivos van a ser fabricados. Esta metodología puede aplicarse tanto a los MMIs 2×2 y 2×3, como para configuraciones más complejas, como un 2×4.

Una vez establecidas las dimensiones de las guías de interconexión curvas y de los acopladores de interferencia multimodal, el diseño de la unión de seis puertos consiste en encontrar un layout que sea compacto, introduzca el mínimo desbalanceo entre las salidas, y sea compatible con el montaje de medida con que se va a caracterizar. El layout finalmente elegido es el que se muestra en la figura 6.1. Para simular el comportamiento global del circuito, una simulación electromagnética completa resulta poco práctica, por lo que se opta por concatenar simplemente los parámetros S de los diferentes elementos. Esto predice un muy buen comportamiento del seis puertos, que cumple su función de reflectómetro con errores de amplitud y fase menores que 1,5 dB y 10° en la banda de 1500 nm a 1600 nm.

SPICUM servicio de publicaciones

D.4. Técnica de media de fase mínima

La caracterización de los dispositivos fabricados plantea dos dificultados. La primera son las reflexiones espúreas que aparecen en los cantos del chip, donde el interfaz entre el aire y silicio forma un espejo con una reflectividad del 33 %. Por tanto, al medir los dispositivos, se obtiene su repuesta dentro de una cavidad resonante, lo cual imposibilita su correcta caracterización. La segunda radica en la necesidad de medir la respuesta en fase del seis puertos, cuando el montaje de medida sólo permite medir potencias. Ambas dificultades se resuelven con una nueva técnica de medida de fase mínima propuesta en esta tesis.

Los sistemas de fase mínima se caracterizan porque su respuesta en amplitud y fase están ligadas a través de una transformada de Hilbert. Por tanto, si el dispositivo es de fase mínima, conocida la potencia transmitida a través de él en función de la longitud de onda, es posible calcular directamente la información fase. A partir de la información de amplitud y fase se puede calcular la respuesta al impulso (o respuesta temporal) del sistema mediante una transformada de Fourier inversa. Esto permite identificar y eliminar fácilmente los ecos debidos a las reflexiones en los cantos del chip. Transformando de nuevo la respuesta al impulso al dominio de la frecuencia se obtiene la respuesta del dispositivo libre de reflexiones espúreas.

Evidentemente, esta técnica solamente proporciona resultados correctos si el dispositivo que se analiza es realmente de fase mínima. Por ello se ha desarrollado un criterio analítico, (7.9), que permite determinar si un dispositivo óptico cumple este requisito, y que constituye otra aportación clave de este trabajo. Asimismo, se dan una serie de reglas para la aplicación práctica de la técnica, en lo que a ancho de banda de medida y resolución espectral se refiere. La técnica ha sido verificada tanto mediante simulación como experimentalmente.

D.5. Fabricación y medida

La fabricación de los dispositivos se llevó a cabo en una “foundry” externa, concretamente en el Centro Canadiense de Fabricación Fotónica. El layout que se fabricó se muestra en la figura D.8, y consta de tres imágenes, que se distinguen como los tres rectángulos inscritos en el círculo a la izquierda de la figura. Cada una de estas imágenes da lugar a un chip, que a su vez está compuesto por multitud de estructuras de prueba para los diferentes elementos del reflectómetro, y un reflectómetro completo. Puede apreciarse que la máscara presenta una complejidad elevada, y de hecho fue necesario programar un biblioteca de funciones para Autocad para su realización.

El montaje de medida que se emplea para la caracterización de los dispositivos se muestra de manera esquemática en la figura D.9 y consta, esencialmente, de un láser de barrido y un controlador de polarización a la entrada del chip, y un polarizador y un detector de potencia a su salida. La luz se inyecta en los dispositivos posicionando una fibra terminada en una lenta delante de la guía correspondiente mediante una etapa de micro-posicionamiento. A la salida, se emplea un objetivo de microscopio para colectar la luz y dirigirla, en espacio libre, hacia el fotodetector.

Se caracterizó una serie de MMIs con diferentes anchos para estudiar, de manera experimental, sus tolerancias de fabricación, demostrándose que, tal y como se es-

SPICUM servicio de publicaciones

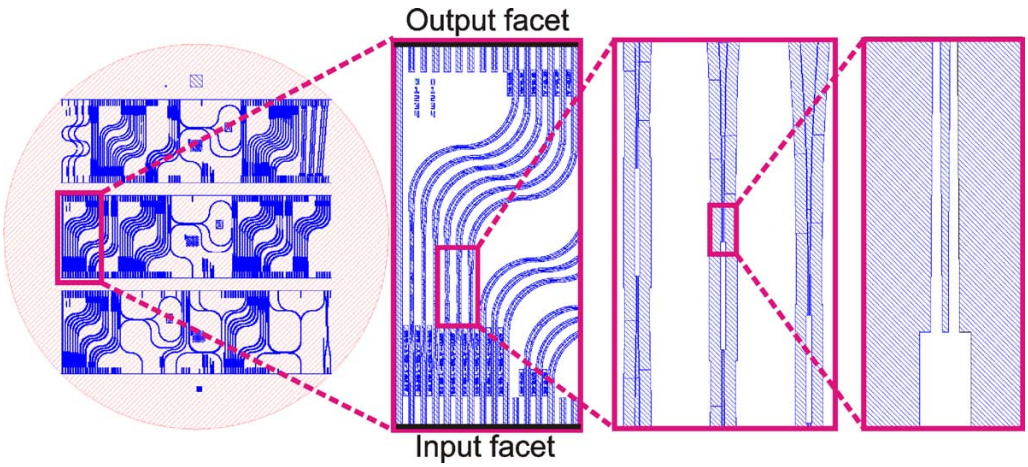

Figura D.8.: Diseño de la máscara para el seis puertos, los MMI y varias estructuras de prueba. Se muestran, de izquierda a derecha, diferentes niveles de ampliación de la máscara completa, tres MMI adyacentes, y las guías de salida de un MMI (se muestran como espacio blanco).

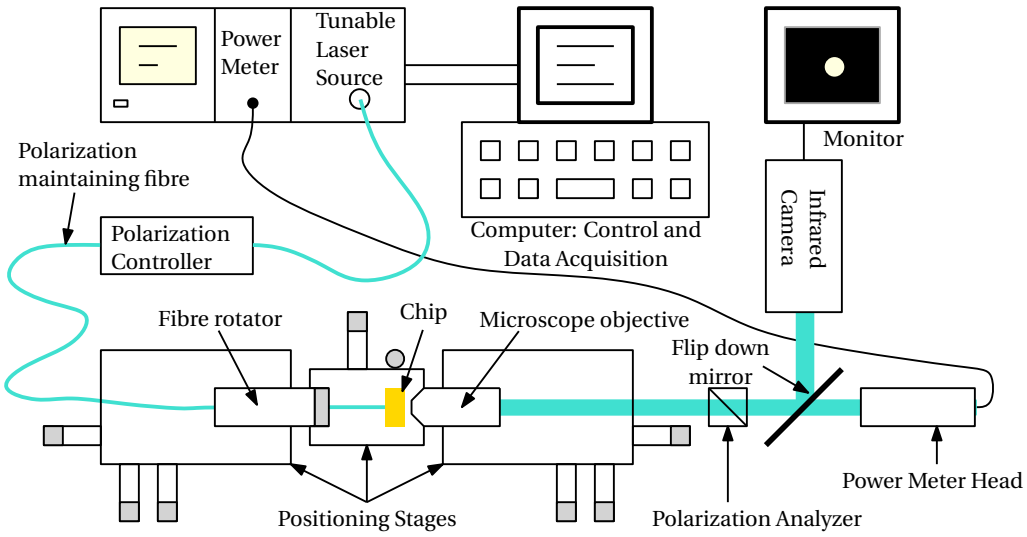

Figura D.9.: Esquema del montaje de medida empleado para la caracterización de los dispositivos.

SPICUM servicio de publicaciones

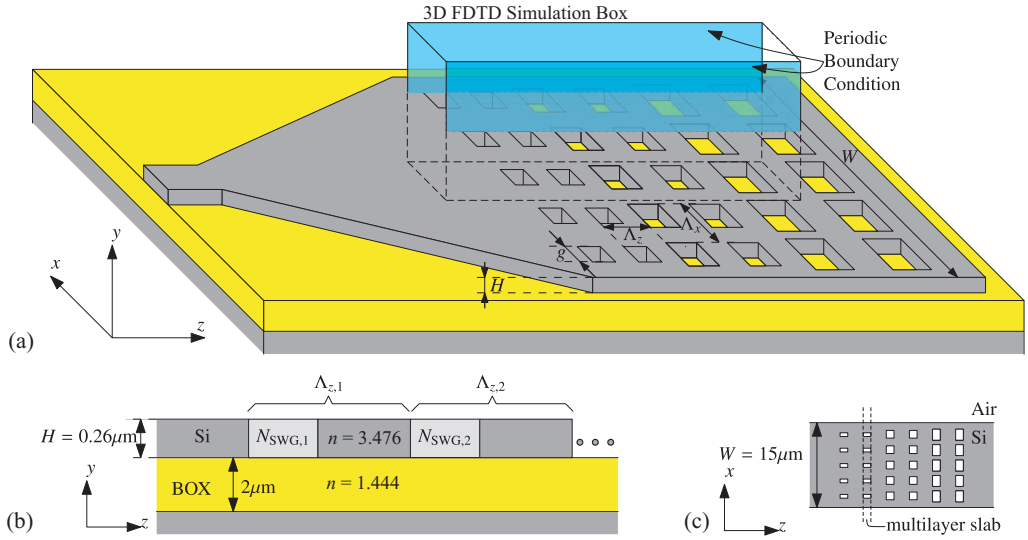

Figure D.10.: (a) Red de difracción para el acoplo chip fibra con una estructura con dimensiones menores a la longitud de onda en la dirección transversal. Se muestran asimismo modelos para la estructura en sentido vertical (b) y horizontal (c).

peraba de las simulaciones, estos dispositivos mantienen un desbalanceo y un error de fase inferiores a ~ 0,5 dB y ~ 5°, respectivamente, en un ancho de banda de 60 nm y para un rango de variación en el ancho del MMI 450 nm.

Para la caracterización del reflectómetro se aprovechó la reflexión en el canto del chip, ya que gracias a ella el dispositivo se comporta como si se estuviera midiendo un espejo de reflectividad conocida. Haciendo uso del procesado de fase mínima descrito en el apartado anterior se determinó que el reflectómetro combina las ondas incidentes el reflejadas del dispositivo bajo prueba con un error de fase menor que ±6° y un error de amplitud menor que ±0,5 dB en un ancho de banda de 90 nm. Esto lo convierte en un reflectómetro casi ideal, y que podrá aplicarse, en el futuro, a la caracterización de dispositivos ópticos.

D.6. Red de acoplo chip-fibra

Las redes de acoplo chip-fibra que se encuentran en la literatura habitualmente acoplan luz polarizada horizontalmente al circuito óptico integrado, y emplean dos pasos de grabado para controlar la fuerza de la red (véase la figura D.3). Sin embargo, en biosensores basados en campo evanescente, se emplea luz polarizada verticalmente, y para reducir el coste de los mismos, es preferible trabajar con un solo paso de grabado. Se planteó como objetivo el diseño de una red de acoplo que cumpliera las exigencias planteadas por estos biosensores.

El diseño de la red para acoplar luz verticalmente polarizada en vez de horizontalmente polarizada esencialmente solo implica cambiar adecuadamente su periodo. Por otro lado, conseguir una eficiencia de acoplo apropiada con un solo paso de grabado supone un cierto reto. Esto se debe a que al grabar completamente la red, se forma una discontinuidad muy abrupta entre la guía, de índice de refracción $n_{Si} \approx 3,5$

SPICUM servicio de publicaciones

y el aire. Esto provoca dos efectos. Por un lado, la potencia se radia en un haz muy estrecho, que no está bien adaptado al modo de la fibra, lo que aumenta las pérdidas de acoplo. Por otro lado, la discontinuidad produce una fuerte reflexión hacia atrás, que puede interferir con las medidas que se pretenden tomar. Ambos inconvenientes se solventan empleando la estructura que se muestra en la figura D.10(a). En vez de grabar franjas completas en dirección x, se graban agujeros con una cierta periodicidad, que es bastante inferior a la longitud de onda de la luz que se propaga por el dispositivo. De este modo, la onda luminosa no "ve" los agujeros, sino que percibe un medio homogéneo equivalente, cuyo índice de refracción puede ajustarse en un amplio rango variando el tamaño de los agujeros. Así es posible elegir un índice equivalente para que el haz radiado tengo una extensión (en dirección z) suficiente y se reduzcan las reflexiones. El ancho de la red es de $W = 15\,\mu\text{m}$ para adaptar el ancho del haz radiado al ancho del modo de una fibra, mientras que la altura de la capa de silicio es de $H = 0{,}26\,\mu\text{m}$. Debido a esta diferencia de escala, pueden establecerse sendos modelos 2D para describir el comportamiento de la estructura en la dirección vertical (y) y horizontal (x), que se muestran, respectivamente, en las figuras D.10(b) y D.10(c), y que facilitan en gran medida el diseño y la simulación de la red. Mediante el modelo mostrado en la figura D.10(c) se calcula el índice equivalente, simplemente como el modo fundamental del slab multicapa indicado. La simulación de la red de acoplo se lleva a cabo de acuerdo con el modelo de la figura 9.2(b), donde las franjas de agujeros se sustituyen por el índice equivalente. Este método de diseño se ha verificado con simulaciones 3D de la región de la red indicada en la figura 9.2(a). Asimismo, los primeros resultados experimentales obtenidos arrojan una eficiencia de acoplo de unos 5 dB, que concuerda con las simulaciones realizadas, y es solo ligeramente inferior a las eficiencias que se consiguen con redes que requieren dos pasos de grabado.

SPICUM servicio de publicaciones

E

Conclusiones y lineas futuras

En esta tesis se ha abordado el desarrollo y caracterización de dos dispositivos ópticos integrados en la plataforma Silicon-on-Insulator.

En primer lugar, y como objeto principal, se ha implementado un reflectómetro de seis puertos sobre guías rib de dimensiones micrométricas, que presentan un adecuado estado de madurez y permiten emplear técnicas estándar para el acoplo chip fibra. Para ello se han estudiado con detalle las propiedades de guiado de estas guías y se ha propuesta una completa metodología de diseño para acopladores de interferencia multimodal de altas prestaciones y relajadas tolerancias de fabricación, que pueden ser fabricados con un sólo paso de grabado. Además, se ha desarrollado una técnica de medida de fase mínima, que permite obtener la respuesta de fase de dispositivos ópticos integrados a partir de su respuesta en amplitud, que resulta sencilla de medir. Dicha técnica se ha aplicado para eliminar de las medidas reflexiones espúreas, procedentes de los cantos del chip, así como para determinar la fase relativa con la que el reflectómetro hace interferir las ondas incidentes y reflejadas del dispositivos bajo prueba. Se han demostrado experimentalmente tanto acopladores de interferencia multimodal de altas prestaciones y relajadas tolerancias como un reflectómetro integrado que funciona de manera casi ideal.

En segundo lugar, se han investigado las redes de difracción como mecanismo de acoplo de luz desde una fibra óptica a guías Silicon-wire, con dimensiones de unos cientos de nanómetros. Se ha propuesto una nueva técnica para controlar la fuerza de estas redes, basada en crear materiales equivalentes con estructuras de dimensiones inferiores a la longitud de onda. Esto permite fabricar redes de difracción con un solo paso de grabado, lo que supone una considerable ventaja sobre las redes existentes, que requieren de dos pasos de grabado. Se han medido eficiencias de acoplo similares a las que se consiguen con redes que requieren una fabricación más compleja.

Ya se dispone de una versión encapsulada del reflectómetro, conectorizada con fibras ópticas, y con la que se podrán hacer los primeros ensayos de medidas basadas en la técnica de seis puertos. A largo plazo, resulta de interés investigar la realización de un seis puertos que permita la caracterización directa de circuitos ópticos integrados, sin necesidad de contar con una fibra óptica para la conectorización. Asimismo, se podría estudiar la posibilidad de extender la técnica de fase mínima propuesta a dispositivos de banda estrecha. Finalmente, se continua trabajando en la mejora de las redes de acoplo propuestas en este trabajo.

SPICUM servicio de publicaciones

SPICUM
servicio de publicaciones

F

Curriculum Vitae

Robert Halir was born in Germany in 1981 and moved with his family to Spain in 1996. He earned his MSc in Telecommunications enginnering with first class honors from Málaga University in 2006. Funded by a national scholarship, he has since then been working towards his Ph.D. on the design of an integrated optical six-port reflectometer. This project is carried out in cooperation with the National Research Council of Canada, where the candidate has also worked on single etch-step fibre-to-chip grating couplers. During a stay at the INTEC-IMEC group (Belgium) he collaborated on polarization depend loss reduction in two-dimensional grating couplers. He is furthermore involved with the Heinrich Hertz Institute (Germany) in the design of coherent receivers in indium phosphide.

A complete list of his publications is given below.

International Journal Papers

1. R. Halir, A. Ortega-Moñux, J. G. Wangüemert-Pérez, Í. Molina-Fernández, P. Cheben, "Fabrication Tolerance Analysis of Bent Single-Mode Rib Waveguides on SOI", *Optical and Quantum Electronics*, Volume 38, Numbers, 9-11, July 2006

2. R. Halir, I. Molina-Fernández, A. Ortega-Moñux, J. G. Wangüemert-Pérez, Dan-Xia Xu, Pavel Cheben and Siegfried Janz, "A Design Procedure for High Performance, Rib Waveguide based Multimode Interference Couplers in Silicon-on-Insulator", *IEEE Journal of Lightwave Technology,* Volume 26, pages 2928-2936, August 2008

3. R. Halir, Í. Molina-Fernández, J.G.Wangüemert-Pérez, A. Ortega-Moñux, J. de-Oliva-Rubio, P. Cheben, "Characterization of integrated photonic devices with minimum phase technique", *Optics Express,* Volume 17, pages 8349-8361, May 2009

4. R. Halir, P. Cheben, S. Janz, D.-X. Xu, Í. Molina-Fernández, and J. G. Wangüemert-Pérez, "Waveguide grating coupler with subwavelength microstructures", *Optics Letters*, Volume 34, pages 1408–1410, May 2009

5. R. Halir, A. Ortega-Moñux, Í. Molina-Fernández, J. G. Wangüemert-Pérez, Pavel Cheben, Dan-Xia Xu, Boris Lamontagne, and Siegfried Janz, "Compact High

SPICUM servicio de publicaciones

Performance Multi-Mode Interference Couplers in Silicon-on-Insulator", *IEEE Photonics Technology Letters*, Volume 21, pages 1600-1602, November 2009

6. R. Halir, A. Ortega-Moñux, Í. Molina-Fernández, J. G. Wangüemert-Pérez, Pavel Cheben, Dan-Xia Xu, Boris Lamontagne, and Siegfried Janz, "Integrated Optical Six-Port Reflectometer in Silicon-on-Insulator", *IEEE Journal of Lightwave Technology*, Volume 27, pages 5405-5409, December 2009

7. Robert Halir, Diedrik Vermeulen, and Günther Roelkens, "Reducing Polarization Dependent Loss of Silicon-on-Insulator Fiber to Chip Grating Couplers", *IEEE Photonics Technology Letters*, Vol. 22, pp. 389-391, 2010

8. C. Alonso-Ramos, A. Ortega-Moñux, I. Molina-Fernández, P. Cheben, L. Zavargo-Peche, and R. Halir, "Efficient fiber-to-chip grating coupler for micrometric SOI rib waveguides," *Opt. Express*, Vol. 18, pp. 15189-15200, 2010

9. R. Halir, P. Cheben, J. Schmid, R. Ma, D. Bedard, S. Janz, D. Xu, A. Densmore, J. Lapointe, and Í. Molina-Fernández, "Continuously apodized fiber-to-chip surface grating coupler with refractive index engineered subwavelength structure," *Opt. Letters*, Vol. 35, pp. 3243-3245, 2010

International Conference Proceedings

1. R. Halir, A. Ortega-Moñux, J. G. Wangüemert-Pérez, I. Molina-Fernández, and P. Cheben, "Fabrication Tolerant Design of Bent Single Mode Rib Waveguides on SOI", in *XV International Workshop on Optical Waveguide Theory and Numercial Modelling*, A. Melloni, ed., (2006).

2. R. Halir, Í. Molina Fernández, A. Ortega Moñux, J. G. Wangüemert Pérez, D.-X. Xu, P. Cheben and S. Janz, "High performance, single etch step MMI design on SOI", in *European Conference on Integrated Optics* (Copenhagen, Denmark, April 25-27 2007), Paper ThG17.

3. L. Zavargo-Peche, C. A. Alonso-Ramos, A. Ortega-Moñux, R. Halir, J. G. Wangüemert-Pérez and Í. Molina-Fernández, "A Tool for Automatic Grating Design", in XVIIIth International Workshop on Optical Waveguide Theory and Numerical Modelling (Jena, Germany, April 17-18 2009), Poster 23

4. R. Kunkel, H.G. Bach, D. Hoffmann, C.M. Weinert, I. Molina-Fernandez and Robert Halir, "First Monolithic InP-Based 90°-Hybrid OEIC Comprising Balanced Detectors for 100GE Coherent Frontends", in *2009 International Conference on Indium Phosphide and Related Materials* (Newport Beach, CA, USA, May 10 - 14 2009)

5. Robert Halir, Íñigo Molina-Fernández, Alejandro Ortega-Moñux, Pavel Cheben, Siegfried Janz, Dan-Xia Xu, "Detecting Spurious Reflections in Integrated Photonic Devices", in *European Conference on Lasers and Electro-Optics* (Munich, Germany, June 14-19 2009), Paper CK.P.4

SPICUM servicio de publicaciones

6. Robert Halir, Diedrik Vermeulen, and Günther Roelkens, “Silicon-on-Insulator Tunable Wavelength Router with Minimized Polarization Dependent Loss”, in *Optical Fiber Conference* (San Diego, California, USA, March 21 - 25 2010), Paper OWJ1

7. I. Molina-Fernandez, A. Ortega-Moñux, R. Halir, J. G. Wangüemert-Pérez, and P. Perez-Lara, “Sixport technique for phase measurement of guided optical fields”, In *International Conferenceon Advanced phase measurement methods in optics and imaging*, AIP Conf. Proc., Volume 1236, pp. 314-319, 2010

SPICUM servicio de publicaciones

SPICUM
servicio de publicaciones

Bibliography

[1] P. Winzer, G. Raybon, H. Song, A. Adamiecki, S. Corteselli, A. Gnauck, D. Fishman, C. Doerr, S. Chandrasekhar, L. Buhl *et al.*, "100-Gb/s DQPSK transmission: From laboratory experiments to field trials," *J. Lightwave Technol.*, vol. 26, no. 20, pp. 3388–3402, 2008.

[2] J. Renaudier, G. Charlet, O. Bertran-Pardo, H. Mardoyan, P. Tran, M. Salsi, and S. Bigo, "Transmission of 100gb/s coherent pdm-qpskover 16x100km of standard fiber with allerbiumamplifiers," *Opt. Express*, vol. 17, no. 7, pp. 5112–5119, 2009. [Online]. Available: http://www.opticsexpress.org/abstract.cfm?URI=oe-17-7-5112

[3] R. Kunkel, H.-G. Bach, D. Hoffmann, C. Weinert, I. Molina-Fernandez, and R. Halir, "First monolithic inp-based 90°-hybrid oeic comprising balanced detectors for 100ge coherent frontends," in *Indium Phosphide & Related Materials, 2009. IPRM '09.* Newport Beach, CA, USA: IEEE Photonics Society, May 2009, pp. 167–170.

[4] C. F. Lam, "Optical network technologies for datacenter networks," in *Optical Fiber Communication Conference.* Optical Society of America, 2010, p. NWA3.

[5] A. B. et al, "Optics for high-performance servers and supercomputers," in *Optical Fiber Communication Conference*, 2010, p. OTuH1.

[6] A. Othonos, "Fiber bragg gratings," *Rev. Sci. Instrum.*, vol. 68, pp. 4309–4341, 1997.

[7] J. Schmitt, "Optical coherence tomography (oct): a review," *IEEE J. Sel. Top. Quantum Electron.*, vol. 5, no. 4, pp. 1205 –1215, jul/aug 1999.

[8] J. Bland-Hawthorn and P. Kern, "Astrophotonics: a new era for astronomical instruments," *Opt. Express*, vol. 17, no. 3, pp. 1880–1884, 2009. [Online]. Available: http://www.opticsexpress.org/abstract.cfm?URI=oe-17-3-1880

[9] "The silicon age? it's just dawning," Business Week, Dec. 1996. [Online]. Available: http://www.businessweek.com/1996/50/b350598.htm

[10] R. Soref, "The past, present, and future of silicon photonics," *IEEE J. Sel. Top. Quantum Electron.*, vol. 12, no. 6, pp. 1678–1687, Dec. 2006.

[11] D. Miller, "Device Requirements forOptical Interconnects to Silicon Chips," *Proceedings of the IEEE*, vol. 97, no. 7, pp. 1166–1185, 2009.

[12] G. T. Reed, "Device physics: The optical age of silicon," *Nature*, vol. 427, pp. 595–596, Feb. 2004.

SPICUM servicio de publicaciones

[13] A. Liu, R. Jones, L. Liao, D. Samara-Rubio, D. Rubin, O. Cohen, R. Nicolaescu, and M. Paniccia, "A high-speed silicon optical modulator based on a metal-oxide-semiconductor capacitor," *Nature*, vol. 427, pp. 615–618, Feb. 2004.

[14] W. M. Green, M. J. Rooks, L. Sekaric, and Y. A. Vlasov, "Ultra-compact, low rf power, 10 gb/s siliconmach-zehnder modulator," *Opt. Express*, vol. 15, no. 25, pp. 17 106–17 113, 2007. [Online]. Available: http://www.opticsexpress.org/abstract.cfm?URI=oe-15-25-17106

[15] Y. Kang, H. Liu, M. Morse, M. Paniccia, M. Zadka, S. Litski, G. Sarid, A. Pauchard, Y. Kuo, H. Chen *et al.*, "Monolithic germanium/silicon avalanche photodiodes with 340 GHz gain–bandwidth product," *Nature Photonics*, vol. 3, no. 1, pp. 59–63, 2008.

[16] S. Assefa, F. Xia, and Y. A. Vlasov, "Reinventing germanium avalanche photodetector for nanophotonic on-chip optical interconnects," *Nature*, vol. 464, pp. 80–85, 2010.

[17] A. Fang, H. Park, O. Cohen, R. Jones, M. Paniccia, and J. Bowers, "Electrically pumped hybrid AlGaInAs-silicon evanescent laser," *Opt. Express*, vol. 14, pp. 9203–9210, 2006.

[18] [Online]. Available: http://www.wadimos.eu/

[19] [Online]. Available: http://www.luxtera.com/

[20] P. Cheben, J. Schmid, A. Delâge, A. Densmore, S. Janz, B. Lamontagne, J. Lapointe, E. Post, P. Waldron, and D.-X. Xu, "A high-resolution silicon-on-insulator arrayed waveguide grating microspectrometer with sub-micrometer aperture waveguides," *Opt. Express*, vol. 15, pp. 2299–2306, 2007.

[21] D.-X. Xu, A. Densmore, A. Delâge, P. Waldron, R. McKinnon, S. Janz, J. Lapointe, G. Lopinski, T. Mischki, E. Post, P. Cheben, and J. H. Schmid, "Folded cavity SOI microring sensors for high sensitivity and real time measurement of biomolecular binding," *Opt. Express*, vol. 16, no. 19, pp. 15 137–15 148, 2008.

[22] M. Foster, R. Salem, D. Geraghty, A. Turner-Foster, M. Lipson, and A. Gaeta, "Silicon-chip-based ultrafast optical oscilloscope," *Nature*, vol. 456, no. 7218, pp. 81–84, 2008.

[23] S.-E. Ibrahim, L.-W. Luo, S. S. Djordjevic, C. B. Poitras, L. Zhou, N. K. Fontaine, B. Guan, S. Cheung, Z. Ding, K. Okamoto, M. Lipson, and S. J. Yoo, "Fully reconfigurable silicon photonic lattice filters with four cascaded unit cells," in *Optical Fiber Communication Conference*. Optical Society of America, 2010, p. OWJ5.

[24] F. Horst, "Silicon integrated waveguide devices for filtering and wavelength demultiplexing," in *Optical Fiber Communication Conference*. Optical Society of America, 2010, p. OWJ3. [Online]. Available: http://www.opticsinfobase.org/abstract.cfm?URI=OFC-2010-OWJ3

SPICUM servicio de publicaciones

[25] J. Brouckaert, W. Bogaerts, S. Selvaraja, P. Dumon, R. Baets, and D. Van Thourhout, "Planar concave grating demultiplexer with high reflective bragg reflector facets," *IEEE Photon. Technol. Lett*, vol. 20, no. 4, pp. 309–311, 2008.

[26] D. Derickson, *Fiber Optic Test and Measurement*, 1st ed. Prentice Hall, 1998.

[27] S. Dyer and K. Rochford, "Low-coherence interferometric measurements of the dispersion ofmultiple fiber Bragg gratings," *IEEE Photonics Technol. Lett.*, vol. 13, no. 3, pp. 230–232, 2001.

[28] M. Froggatt, M. Froggatt, E. Moore, and M. Wolfe, "Interferometric measurement of dispersion in optical components," in *Optical Fiber Communications Conference*. Optical Society of America, 2002, p. WK1. [Online]. Available: http://www.opticsinfobase.org/abstract.cfm?URI=OFC-2002-WK1

[29] M. Sarunic, M. A. Choma, C. Yang, and J. A. Izatt, "Instantaneous complex conjugate resolved spectral domain and swept-source oct using 3x3 fiber couplers," *Opt. Express*, vol. 13, no. 3, pp. 957–967, 2005. [Online]. Available: http://www.opticsexpress.org/abstract.cfm?URI=oe-13-3-957

[30] U. Wiedmann, P. Gallion, and G. Duan, "A generalized approach to optical low-coherence reflectometry including spectral filtering effects," *J. Lightwave Technol.*, vol. 16, no. 7, p. 1343, 1998.

[31] B. J. Soller, D. K. Gifford, M. S.Wolfe, and M. E. Froggatt, "High resolution optical frequency domain reflectometry for characterization of components and assemblies," *Opt. Express*, vol. 13, no. 2, pp. 666–674, Jan. 2005.

[32] I. Molina-Fernández, J. Wangüemert-Pérez, A. Ortega-Moñux, R. Bosisio, and K. Wu, "Planar lightwave circuit six port technique for optical measurement and characterization," *J. Lightwave Technol.*, vol. 23, no. 6, pp. 2148–2157, Jun. 2005.

[33] D. Taillaert, W. Bogaerts, P. Bienstman, T. F. Krauss, P. V. Daele, I. Moerman, S. Verstuyft, K. D. Mesel, and R. Baets, "An out-of-plane grating coupler for efficient butt-coupling between compact planar waveguides and single-mode fibers," *IEEE Journal of Quantum Electronics, IEEE J. Quantum Electron.*, vol. 38, no. 7, pp. 949–955, Jul. 2002.

[34] R. Halir, A. Ortega-Moñux, J. G. Wangüemert-Pérez, I. Molina-Fernández, and P. Cheben, "Fabrication tolerant design of bent single mode rib waveguides on soi," in *XV International Workshop on Optical Waveguide Theory and Numercial Modelling*, A. Melloni, Ed., 2006.

[35] ——, "Fabrication tolerance analysis of bent single-mode rib waveguides on SOI," *Opt. Quantum Electron.*, vol. 38, pp. 921–932, 2007.

[36] R. Halir, I. Molina-Fernández, A. O. Moñux, J. G. Wangüemert-Pérez, D.-X. Xu, P. Cheben, and S. Janz, "High performance, single etch step MMI design on SOI," in *European Conference on Integrated Optics*, Apr. 2007.

SPICUM servicio de publicaciones

[37] R. Halir, I. Molina-Fernández, A. Ortega-Moñux, J. G. Wangüemert-Pérez, D.-X. Xu, P. Cheben, and S. Janz, "A design procedure for high performance, rib waveguide based multimode interference couplers in silicon-on-insulator," *J. Lightwave Technol.*, vol. 26, no. 16, pp. 2928–2936, Aug. 2008.

[38] R. Halir, I. Molina-Fernández, J.G.Wangüemert-Pérez, A. Ortega-Moñux, J. de Oliva-Rubio, and P. Cheben, "Characterization of integrated photonic devices with minimum phase technique," *Opt. Express*, vol. 17, no. 10, pp. 8349–8361, May 2009.

[39] R. Halir, I. Molina-Fernandez, A. Ortega-Monux, P. Cheben, S. Janz, and D.-X. Xu, "Detecting spurious reflections in integrated photonic devices," in *European Conference on Lasers and Electro-Optics 2009 (Munich)*, Jun. 2009.

[40] R. Halir, A. Ortega-Moñux, I. Molina-Fernández, J. G. Wangüemert-Pérez, P. Cheben, D.-X. Xu, B. Lamontagne, and S. Janz, "Compact high performance multi-mode interference couplers in silicon-on-insulator," *IEEE Photonics Technol. Lett.*, vol. 21, pp. 1600–1602, Nov. 2009.

[41] R. Halir, A. Ortega-Moñux, I. Molina-Fernández, J. G. Wangüemert-Pérez, P. Cheben, D.-X. Xu, B. Lamontagne, and S. Janz, "Integrated optical six-port reflectometer in silicon-on-insulator," *J. Lightwave Technol.*, vol. 27, pp. 5405–5409, Dec. 2009.

[42] R. Halir, P. Cheben, S. Janz, D.-X. Xu, Íñigo Molina-Fernández, and J. G. Wangüemert-Pérez, "Waveguide grating coupler with subwavelength microstructures," *Opt. Lett.*, vol. 34, pp. 1408–1410, May 2009.

[43] A. V. Oppenheim, *Signals and Systems*. Prentice Hall, 1996.

[44] U. Glombitza and E. Brinkmeyer, "Coherent frequency-domain reflectometry for characterization ofsingle-mode integrated-optical waveguides," *J. Lightwave Technol.*, vol. 11, no. 8, pp. 1377–1384, 1993.

[45] "Luna ofdr data sheet," Jul 2004. [Online]. Available: http://lunatechnologies.com/products/ova/files/OFDR_description.pdf

[46] C. A. Hoer and K. C. Roe, "Using an arbitrary six-port junction to measure complex voltage ratios," *IEEE Trans. Microw. Theory Tech.*, vol. 23, no. 12, pp. 978–984, Dec. 1975.

[47] G. Engen, "The six-port reflectometer: An alternative network analyzer," *IEEE Trans. Microw. Theory Tech.*, vol. 25, no. 12, pp. 1075–1080, 1977.

[48] J. Li, R. Bosisio, and K. Wu, "Computer and measurement simulation of a new digital receiver operating directly at millimeter-wave frequencies," *IEEE Trans. Microw. Theory Tech.*, vol. 43, no. 12 Part 2, pp. 2766–2772, 1995.

[49] T. Hentschel, "The six-port as a communications receiver," *IEEE Trans. Microw. Theory Tech.*, vol. 53, no. 3 Part 2, pp. 1039–1047, 2005.

SPICUM servicio de publicaciones

[50] I. Molina-Fernández, P. Pérez-Lara, and J. Wangüemert-Pérez, "Simplified calibration strategy for an optical sixport reflectometer," *Opt. Express*, vol. 13, no. 20, pp. 8243–8255, 2005.

[51] I. Molina-Fernández and J. de Oliva-Rubio, "Effects of phase noise in an optical six-port measurement technique," *Opt. Express*, vol. 13, no. 7, pp. 2475–2486, Apr. 2005.

[52] P. P. Lara, "Aplicaciones avanzadas de la técnica de seis puertos a frecuencias ópticas y de microondas," Ph.D. dissertation, Universidad de Málaga, 2010.

[53] "Soitec thick soi general product characteristics," Apr. 2010. [Online]. Available: http://www.soitec.com/en/products/pdf/SOI_products_Thick.pdf

[54] B. Lamontagne, *Optical Waveguides: From Theory to Applied Technologies*, M. L. Calvo and V. Lakshminarayanan, Eds. CRC, 2007.

[55] X. Xu, J. M. Baribeau, P. Cheben, D. Dalacu, A. Delâge, B. Lamontagne, S. Janz, M. J. Picard, and W. N. Ye, "Prospects and challenges for microphotonic waveguide componentes based on Si and SiGe," in *ECS 2004*, 2004.

[56] M. Fournier, "ePIXfab the silicon platform, technology paper standard Leti_04," Leti, Tech. Rep., Sep. 2010. [Online]. Available: http://www.epixfab.eu/technology/

[57] W. Bogaerts, S. K. Selvaraja, and P. Dumon, "ePIXfab the silicon platform, technology paper IMEC_193_01," IMEC, Tech. Rep., Sep. 2008.

[58] V. Almeida, R. Panepucci, and M. Lipson, "Nanotaper for compact mode conversion," *Opt. Lett.*, vol. 28, no. 15, pp. 1302–1304, 2003.

[59] T. Tamir and S. Peng, "Analysis and design of grating couplers," *Appl. Phys.*, vol. 14, pp. 235–254, 1977.

[60] D. Taillaert, P. Bienstman, and R. Baets, "Compact efficient broadband grating coupler for silicon-on-insulator waveguides," *Opt. Lett.*, vol. 29, no. 23, pp. 2749–2751, Dec. 2004.

[61] G. Roelkens, D. Van Thourhout, and R. Baets, "High efficiency silicon-on-insulator grating coupler based on a poly-silicon overlay," *Opt. Express*, vol. 14, no. 14, pp. 11 622–11 630, Nov. 2006.

[62] D. Taillaert, R. Baets, P. Dumon, W. Bogaerts, D. V. Thourhout, B. Luyssaert, V. Wiaux, S. Beckx, and J. Wouters, "Silicon-on-insulator platform for integrated wavelength-selective components," in *Workshop on Fibres and Optical Passive Components (invited)*, 2005.

[63] T. Tsuchizawa, K. Yamada, H. Fukuda, T. Watanabe, J. ichi Takahashi, M. Takahashi, T. Shoji, E. Tamechika, S. ichi Itabashi, and H. Morita, "Microphotonics devices based on silicon microfabrication technology," *IEEE J. Sel. Top. Quantum Electron.*, vol. 11, no. 1, pp. 232–240, January 2005.

SPICUM servicio de publicaciones

[64] R. Halir, D. Vermeulen, and G. Roelkens, "Reducing polarization-dependent loss of silicon-on-insulator fiber to chip grating couplers," *IEEE Photonics Technol. Lett.*, vol. 22, no. 6, pp. 389 –391, march15, 2010.

[65] *ASML, PAS 5500/100 Step & Repeat i-Line System.* [Online]. Available: www.asml.com/asml/show.do?ctx=7077&rid=7099

[66] D.-X. Xu, A. Densmore, P. Waldron, J. Lapointe, E. Post, A. Delâge, S. Janz, P. Cheben, J. Schmid, and B. Lamontagne, "High bandwidth SOI photonic wire ring resonators using MMI couplers," *Opt. Express*, vol. 15, no. 6, pp. 3149–3155, 2007.

[67] L. Zimmermann, K. Voigt, G. Winzer, K. Petermann, and C. Weinert, "C -Band Optical 90° -Hybrids Based on Silicon-on-Insulator 4 $times$ 4 Waveguide Couplers," *IEEE Photonics Technol. Lett.*, vol. 21, no. 3, pp. 143–145, Feb.1, 2009.

[68] M. Harjanne and T. Aalto, "Design of tight bends in silicon-on-insulator," *Physica Scripta*, vol. T114, pp. 209–212, 2004.

[69] [Online]. Available: http://www.nrc-cnrc.gc.ca/cpfc-ccfdp/index.html

[70] R. A. Soref, J. Schmidtchen, and K. Peterman, "Large single-mode rib waveguides in GeSi-Si and Si-on-SiO_2," *IEEE J. Quantum Electron.*, vol. 27, no. 8, pp. 1971–1974, Aug. 1991.

[71] J. Lousteau, D. Furniss, A. Seddon, T. Benson, A. Vukovic, and P. Sewell, "The single-mode condition for silicon-on-insulator optical rib waveguides with large cross section," *J. Lightwave Technol.*, vol. 22, no. 8, pp. 1923–1929, 2004.

[72] S. P. Chan, C. E. Png, S. T. Lim, G. T. Reed, and V. Passaro, "Single mode and polarization-independent silicon-on-insulator waveguides with small cross section," *J. Lightwave Technol.*, vol. 23, no. 6, pp. 2103–2101, June 2005.

[73] O. Powell, "Single-mode condition for silicon rib waveguides," *J. Lightwave Technol.*, vol. 20, no. 10, pp. 1851–1855, October 2002.

[74] I. Kiyat, A. Aydinli, and N. Dagli, "High-Q silicon-on-insulator optical rib waveguide racetrack resonators," *Opt. Express*, vol. 13, no. 6, pp. 1900–1905, 2005.

[75] W. W. Lui, T. Hirono, K. Yokoyama, and W.-P. Huang, "Polarization rotation in semiconductor bending waveguides: A coupled-mode theory formulation," *J. Lightwave Technol.*, vol. 16, no. 5, pp. 929–936, May 1998.

[76] A. S. Sudbø, "Film mode matching: a versatile numerical method for vector mode field calculations in dielectric waveguides," *Pure Applied Optics*, vol. 2, pp. 211–233, 1993.

[77] T. Tamir, H. Kogelnik, W. Burns, A. Milton, R. Alferness, I. Kaminow, R. Tucker, F. Leonberger, and J. Donnelly, *Guided-Wave Optoelectronics*, T. Tamir, Ed. Springer Verlag, 1988, vol. 26.

SPICUM servicio de publicaciones

[78] H. F. Talbot, "Facts relating to Optical Science," *Philos. Mag.*, vol. 9, no. 4, pp. 401–407, Dec. 1836.

[79] R. Ulrich and G. Ankele, "Self-imaging in homogeneous planar optical waveguides," *Appl. Phys. Lett.*, vol. 27, p. 337, 1975.

[80] L. Rayleigh, "On copying diffraction-gratings, and on some phenomena connected therewith," *Philos. Mag.*, vol. 11, no. 67, pp. 196–205, Mar. 1880.

[81] O. Bryngdahl, "Image formation using self-imaging techniques," *J. Opt. Soc. Am*, vol. 63, no. 4, pp. 416–419, 1973.

[82] E. Pennings *et al.*, "Ultracompact, low-loss directional couplers on InP based on self-imaging by multimode interference," *Appl. Phys. Lett.*, vol. 59, no. 16, pp. 1926–1928, 1991.

[83] L. Soldano, F. Veerman, M. Smit, B. Verbeek, A. Dubost, and E. Pennings, "Planar monomode optical couplers based on multimode interference effects," *J. Lightwave Technol.*, vol. 10, no. 12, pp. 1843–1850, 1992.

[84] M. Schnarrenberger, L. Zimmermann, T. Mitze, J. Bruns, and K. Petermann, "Mach-Zehnder interferometer (MZI) with more than 20 db extinction ratio on silicon-on-insulator," in *2nd IEEE International Conference on Group IV Photonics*, Sept. 2005, pp. 132–133.

[85] D. Kim, A. Barkai, R. Jones, N. Elek, H. Nguyen, and A. Liu, "Silicon-on-insulator eight-channel optical multiplexer based on a cascade of asymmetric Mach-Zehnder interferometers," *Opt. Lett.*, vol. 33, no. 5, pp. 530–532, 2008.

[86] A. Al-Hetar, A. Mohammad, and I. Yulianti, "Multimode interference photonic switches," *Opt. Eng.*, vol. 47, p. 112001, 2008.

[87] S. Jeong and K. Morito, "Compact optical 90° hybrid employing a tapered 2× 4 MMI coupler serially connected by a 2× 2 MMI coupler," *Opt. Express*, vol. 18, no. 5, pp. 4275–4288, 2010.

[88] W. Shieh, H. Bao, and Y. Tang, "Coherent optical OFDM: theory and design," *Opt. Express*, vol. 16, pp. 841–859, 2008.

[89] M. Bachmann, P. Besse, and H. Melchior, "General self-imaging properties in $N \times N$ multimode interference couplers including phase relations," *Appl. Optics*, vol. 33, no. 18, pp. 3905–3911, Jun. 1994.

[90] L. B. Soldano and E. C. M. Pennings, "Optical multi-mode interference devices based on self-imaging: Principales and applications," *J. Lightwave Technol.*, vol. 13, no. 4, pp. 615–627, Apr. 1995.

[91] D. Khalil and A. Yehia, "Two-dimensional multimode interference in integrated optical structures," *Journal of Optics A: Pure and Applied Optics*, vol. 6, no. 1, p. 137, 2004. [Online]. Available: http://stacks.iop.org/1464-4258/6/i=1/a=025

SPICUM servicio de publicaciones

[92] G. T. Reed and A. P. Knights, *Silicon Photonics, an introduction*. John Wiley & Sons, 2004.

[93] M. Bachmann, P. Besse, and H. Melchior, "Overlapping-image multimode interference couplers with a reduced number of self-images for uniform and non-uniform power splitting," *Appl. Optics*, vol. 34, no. 30, pp. 6898–6910, 1995.

[94] C. Leuthold, J.; Joyner, "Multimode interference couplers with tunable power splitting ratios," *J. Lightwave Technol.*, vol. 19, no. 5, pp. 700–707, May 2001.

[95] P. Besse, E. Gini, M. Bachmann, and H. Melchior, "New 2×2 and 1×3 multimode interference couplers with free selection of power splitting ratios," *J. Lightwave Technol.*, vol. 14, no. 10, pp. 2286–2293, Oct 1996.

[96] J. Huang, M. Hu, J. Fujita, R. Scarmozzino, and J. Osgood, R.M., "High-performance metal-clad multimode interference devices for low-index-contrast material systems," *IEEE Photonics Technol. Lett.*, vol. 10, no. 4, pp. 561–563, Apr 1998.

[97] Y. Tang, W. Wang, Y. Wu, J. Yang, and Y. Wang, "Design and fabrication of multimode interference coupler with strong confinement structure on silicon-on-insulator," *Opt. Eng.*, vol. 43, no. 11, pp. 2495–2496, Nov. 2004.

[98] D. Dai, J.-J. He, and S. He, "Compact silicon-on-insulator-based multimode interference coupler with bilevel taper structure," *Appl. Optics*, vol. 44, no. 24, pp. 5036–5041, Aug. 2005.

[99] J. Huang, R. Scarmozzino, and R. Osgood, "A new design approach to large input/output number multimode interference couplers and its application to low-crosstalk wdm routers," *IEEE Photonics Technol. Lett.*, vol. 10, no. 9, pp. 1292–1294, Sep. 1998.

[100] R. Yin, X. Jiang, J. Yang, and M. Wang, "Structure with improved self-imaging in its graded-index multimode interference region," *J. Opt. Soc. Am. A*, vol. 19, no. 6, pp. 1301–1303, 2002.

[101] I. Molina-Fernández, A. Ortega-Moñux, and J. G. Wangüemert-Pérez, "Improving Multimode Interference Couplers Performance Through Index Profile Engineering," *J. Lightwave Technol.*, vol. 27, pp. 1307–1314, 2009.

[102] A. Ortega-Moñux, Í. Molina-Fernández, and J. Wangüemert-Pérez, "Index profile engineering of multimode interference couplers," in *Asia Communications and Photonics Conference and Exhibition*, 2009.

[103] M. T. Hill, X. J. M. Leijtens, G. D. Khoe, and M. K. Smit, "Optimizing imbalance and loss in 2 × 2 3-dB multimode interference couplers via access waveguide width," *J. Lightwave Technol.*, vol. 21, no. 10, pp. 2305–2313, Oct. 2003.

[104] Y. Shi, D. Dai, and S. He, "Improved performance of a silicon-on-insulator-based multimode interference coupler by using taper structures," *Opt. Commun.*, vol. 253, pp. 276–282, 2005.

SPICUM servicio de publicaciones

[105] D. Levy, R. Scarmozzino, and R. Osgood Jr, "Length reduction of tapered N×N MMI devices," *IEEE Photonics Technol. Lett.*, vol. 10, no. 6, pp. 830–832, 1998.

[106] K. A. Latunde-Dada and F. P. Payne, "Theory and design of adiabatically tapered multimode interference couplers," *J. Lightwave Technol.*, vol. 25, no. 3, pp. 834–839, Mar. 2007.

[107] C. Themistos, M. Rajarajan, B. Rahman, S. Obayya, and K. Grattan, "Rigorous Comparison of Parabolically Tapered and Conventional Multimode-Interference-Based 3-dB Power Splitters in InGaAsP/InP Waveguides," *Appl. Optics*, vol. 43, no. 27, pp. 5228–5235, 2004.

[108] D. Mackie and A. Lee, "Slotted multimode-interference devices," *Appl. Opt.*, vol. 43, no. 36, pp. 6609–6619, 2004.

[109] S. Tseng, "Diffraction engineering of multimode waveguides using computer-generated planar holograms," *Opt. Express*, vol. 17, pp. 21 465–21 471, 2009.

[110] J.-K. Hong, S.-S. Lee, and S.-D. Lee, "Extraneous self-imaging phenomenon with weak-guiding condition," *Opt. Lett.*, vol. 32, no. 10, pp. 1311–1313, 2007. [Online]. Available: http://ol.osa.org/abstract.cfm?URI=ol-32-10-1311

[111] Y. Tsai, A. Degiron, N. Jokerst, and D. Smith, "Plasmonic multi-mode interference couplers," *Opt. Express*, vol. 17, pp. 17 471–17 482, 2009.

[112] S. Zeng, Y. Zhang, and B. Li, "Self-imaging in periodic dielectric waveguides," *Opt. Express*, vol. 17, pp. 365–378, 2009.

[113] J. M. López-Doña, J. G. Wangüemert-Pérez, and I. Molina-Fernández, "Fast-fourier-based three-dimensional full-vectorial beam propagation method," *IEEE Photonics Technol. Lett.*, vol. 17, no. 11, pp. 2319–2321, Nov. 2005.

[114] A. W. Snyder and J. D. Love, *Optical Waveguide Theory*. Chapman and Hall, 1983.

[115] P. Besse, M. Bachmann, H. Melchior, L. Soldano, and M. Smit, "Optical bandwidth and fabrication tolerances of multimode interference couplers," *J. Lightwave Technol.*, vol. 12, no. 6, pp. 1004–1009, 1994.

[116] S. W. Wedge, R. Compton, A. Gerstlauer, and D. Rutledge, *Puff version 2.1 manual*, California Institute of Technology, 1999.

[117] R. G. Walker, "Simple and accurate loss measurement technique for semiconductor optical waveguides," *Electron. Lett.*, vol. 21, no. 13, pp. 581–583, Jun. 1985.

[118] W. J. Tomlinson, A. Shahar, and R. J. Deri, "Use and misuse of end-facet reflections in the characterization of optical waveguide directional couplers," *Appl. Opt.*, vol. 30, no. 21, pp. 2961–2969, Jul. 1991.

SPICUM servicio de publicaciones

[119] C. Vázquez, P. Baquero, and F. Hernández-Gil, "Fabry-perot method for the characterization of integrated optical directional couplers," *Appl. Opt.*, vol. 34, no. 30, pp. 6874–6886, Oct. 1995.

[120] Y. Gottesman, E. Rao, and D. Rabus, "New methodology to evaluate the performance of ring resonators using optical low-coherence reflectometry," *J. Lightwave Technol.*, vol. 22, no. 6, pp. 1566–1572, 2004.

[121] M. Muriel and A. Carballar, "Phase reconstruction from reflectivity in uniform fiber Bragg gratings," *Opt. Lett.*, vol. 22, no. 2, pp. 93–95, 1997.

[122] A. Carballar and M. Muriel, "Phase reconstruction from reflectivity in fiber Bragg gratings," *J. Lightwave Technol.*, vol. 15, no. 8, pp. 1314–1322, 1997.

[123] A. Ozcan, M. Digonnet, and G. Kino, "Characterization of Fiber Bragg Gratings Using Spectral Interferometry Based on Minimum-Phase Functions," *J. Lightwave Technol.*, vol. 24, no. 4, p. 1739, 2006.

[124] ——, "Minimum-phase-function-based processing in frequency-domain optical coherence tomography systems," *J. Opt. Soc. Am. A*, vol. 23, no. 7, pp. 1669–1677, 2006.

[125] ——, "Iterative processing of second-order optical nonlinearity depth profiles," *Opt. Express*, vol. 12, no. 15, pp. 3367–3376, 2004.

[126] J. Skaar and H. Engan, "Phase reconstruction from reflectivity in fiber Bragg gratings," *Opt. Lett.*, vol. 24, no. 3, pp. 136–138, 1999.

[127] L. Poladian, "Group-delay reconstruction for fiber Bragg gratings in ref lection and transmission," *Opt. Lett.*, vol. 22, no. 20, pp. 1571–1573, 1997.

[128] J. McDaniel and C. Clarke, "Interpretation and identification of minimum phase reflection coefficients," *J. Acoust. Soc. Am.*, vol. 110, pp. 3003–3010, 2001.

[129] K. Rochford and S. Dyer, "Reconstruction of minimum-phase group delay from fibre Bragg grating transmittance/reflectance measurements," *Electron. Lett.*, vol. 35, no. 10, pp. 838–839, 1999.

[130] A. V. Oppenheim and R. W. Schafer, *Digital Signal Processing*. Prentice Hall, 1975.

[131] J. Fienup, "Reconstruction of an object from the modulus of its Fourier transform," *Opt. Lett.*, vol. 3, no. 1, pp. 27–29, 1978.

[132] S. J. Mason, "Feedback theory — further properties of singal flow graphs," *Proc. IRE*, vol. 44, no. 7, pp. 920–926, July 1956.

[133] J. Victor, "Temporal impulse responses from flicker sensitivities: causality, linearity, and amplitude data do not determine phase," *J Opt Soc Am A*, vol. 6, no. 9, pp. 1302–3, 1989.

SPICUM servicio de publicaciones

[134] A. Ozcan, M. Digonnet, and G. Kino, "Quasi-phase-matched grating characterization using minimum-phase functions," *Opt. Commun.*, vol. 269, no. 1, pp. 199–205, 2007.

[135] A. V. Oppenheim and R. W. Schafer, *Discrete-Time Signal Processing*, A. V. Oppenheim, Ed. Prentice-Hall International, 1989.

[136] P. Cheben, D. Xu, S. Janz, and A. Delage, "Scaling down photonic waveguide devices on the SOI platform," in *Proc. SPIE*, vol. 5117, 2003, pp. 147–156.

[137] F. Payne, "Control of unwanted light in silicon waveguide circuits," *IEEE Photonics Technol. Lett.*, vol. 17, no. 12, pp. 2625–2627, Dec. 2005.

[138] K. Voigt, L. Zimmermann, G. Winzer, T. Mitze, J. Bruns, K. Petermann, B. Huttl, and C. Schubert, "Performance of 40-Gb/s DPSK Demodulator in SOI-Technology," *IEEE Photonics Technol. Lett.*, vol. 20, no. 8, pp. 614–616, 2008.

[139] D.-X. Xu, S. Janz, and P. Cheben, "Design of polarization-insensitive ring resonators in Silicon-on-Insulator using MMI couplers and cladding stress engineering," *IEEE Photonics Technol. Lett.*, vol. 18, no. 2, pp. 343–345, Jan. 2006.

[140] K. Solehmainen, M. Kapulainen, M. Harjanne, and T. Aalto, "Adiabatic and multimode interference couplers on Silicon-on-Insulator," *IEEE Photonics Technol. Lett.*, vol. 18, no. 21, pp. 2287–2289, Nov. 2006.

[141] W. Hong-Zhen, Y. Jinzhong, L. Zhong-Li, Z. Xiao-Feng, S. Wei, and F. Chang-Shui, "Silicon-On-Insulator based 2×2 multimode interference coupler with large tolerance," *Chin. Phys. Lett*, vol. 18, no. 2, pp. 245–247, 2001.

[142] F. Van Laere, G. Roelkens, J. Schrauwen, D. Taillaert, P. Dumon, W. Bogaerts, D. Van Thourhout, and R. Baets, "Compact grating couplers between optical fibers and Silicon-on-Insulator photonic wire waveguides with 69% coupling efficiency," in *Conference on Optical Fiber Communication (Washington, DC) PDP15*, 2006.

[143] P. Cheben, S. Janz, D.-X. Xu, B. Lamontagne, A. Delâge, and S. Tanev, "A broadband waveguide grating coupler with a subwavelength grating mirror," *IEEE Photonics Technol. Lett.*, vol. 18, no. 1, pp. 13–15, Jan. 2006.

[144] G. Roelkens, D. Thourhout, and R. Baets, "High efficiency grating coupler between silicon-on-insulator waveguides and perfectly vertical optical fibers," *Opt. Lett.*, vol. 32, no. 11, pp. 1495–1497, 2007.

[145] B. Wang, J. Jiang, and G. Nordin, "Embedded Slanted Grating for Vertical Coupling Between Fibers and Silicon-on-Insulator Planar Waveguides," *IEEE Photonics Technol. Lett.*, vol. 17, no. 9, pp. 1884–1886, 2005.

[146] D. Wiesmann, C. David, R. Germann, D. Emi, and G. Bona, "Apodized surface-corrugated gratings with varying duty cycles," *IEEE Photonics Technol. Lett.*, vol. 12, no. 6, pp. 639–641, 2000.

SPICUM servicio de publicaciones

[147] Y. Tang, Z. Wang, L. Wosinski, U. Westergren, and S. He, "Highly efficient nonuniform grating coupler for silicon-on-insulator nanophotonic circuits," *Opt. Lett.*, vol. 35, no. 8, pp. 1290–1292, 2010. [Online]. Available: http://ol.osa.org/abstract.cfm?URI=ol-35-8-1290

[148] S. M. Rytov, "The electromagnetic properties of finely layered medium," *Sov. Phys. JETP*, vol. 2, p. 466, 1956.

[149] A. Densmore, D. Xu, P. Waldron, S. Janz, P. Cheben, J. Lapointe, A. Delge, B. Lamontagne, J. Schmid, and E. Post, "A Silicon-on-Insulator Photonic Wire Based Evanescent Field Sensor," *IEEE Photonics Technol. Lett.*, vol. 18, no. 23, pp. 2520–2522, 2006.

[150] P. Lalanne and J. Hugonin, "High-order effective-medium theory of subwavelength gratings in classical mounting: application to volume holograms," *J. Opt. Soc. Am. A*, vol. 15, no. 7, pp. 1843–1851, 1998.

[151] P. Bock, P. Cheben, A. Delâge, J. H. Schmid, D.-X. Xu, S. Janz, and T. J. Hall, "Demultiplexer with blazed waveguide sidewall grating and subwavelength grating structure," *Opt. Express*, vol. 16, pp. 17 616–17 625, 2008.

[152] M. Berry and I. Marzoli, "Quantum carpets, carpets of light," physicsworld, Jun. 2001. [Online]. Available: http://physicsworld.com/cws/article/print/133

[153] R. V. Churchill and J. W. Brown, *Variable Compleja y Aplicaciones*. McGraw-Hill, 1990.

SPICUM servicio de publicaciones